

# On-surface synthesis of sandwich-molecular wires

I n a u g u r a l - D i s s e r t a t i o n

zur

Erlangung des Doktorgrades

der Mathematisch-Naturwissenschaftlichen Fakultät

der Universität zu Köln

vorgelegt von  
Stefan Kraus  
aus Aachen

Köln 2021

Erster Berichterstatter:	Prof. Dr. Thomas Michely
Zweiter Berichterstatter:	Priv.-Doz. Dr. Daniel E. Bürgler

Vorsitzender der Prüfungskommission:	Prof. Dr. Hans-Günther Schmalz
Tag der mündlichen Prüfung:	02.12.2021

Die vorliegende Dissertation wurde von der Mathematisch-Naturwissenschaftlichen Fakultät der Universität zu Köln angenommen.



# Abstract

In this thesis, the on-surface synthesis of sandwich-molecular wires — one-dimensional chains of metal atoms and cyclic molecules in an alternating sequence — is investigated. The use of a low-symmetry substrate for the global and uniaxial alignment of these wires is introduced, making them accessible to spatially averaging techniques. Further, the effects of different types of metal atoms and molecules on the organometallic synthesis and the resulting compounds are investigated as well as their influence on the electronic and magnetic properties.

First, the synthesis of a single-crystal sheet of graphene (Gr) on the two-fold symmetric substrate Ir(110) is demonstrated, which is achieved by thermal decomposition of  $\text{C}_2\text{H}_4$  at 1500 K. The structure of the Gr sheet is investigated using scanning tunnelling microscopy (STM) and low-energy electron diffraction (LEED). While the bare Ir(110) substrate is strongly reconstructed, the adsorbed Gr layer is found to suppress this reconstruction and large flat terraces are observed. The two-fold symmetry of the substrate is imprinted onto the moiré of Gr with Ir(110), resulting in a clear wave pattern of nm wavelength. A strong stripe-like modulation of the electronic properties and binding energies is observed. Complementary angle-resolved photoemission spectroscopy (ARPES) measurements and *ab initio* calculations show, that the Gr is strongly bound to the substrate and the characteristic Dirac cone in the electronic band structure is absent. This anisotropic pattern is demonstrated to enable uniaxial alignment of sandwich-molecular wires and templated adsorption of aromatic molecules. Furthermore, Gr/Ir(110) allows the on-surface synthesis of transition-metal dichalcogenide layers and the growth of epitaxial layers on unreconstructed Ir(110) under the Gr sheet.

Second, the introduced two-fold symmetric Gr/Ir(110) is used for the in-depth characterization of uniaxially aligned sandwich-molecular wires consisting of the lanthanide europium (Eu) and the eight-membered carbon ring cyclooctatetraene (Cot). Using STM and LEED, the alignment effect along the [001] direction of the Ir substrate is found to persist up to several multilayers of the organometallic film. The electronic band structure of the one-dimensional wires is investigated with ARPES. A flat band 1.85 eV below the Fermi energy is found, while no  $\pi$ -derived bands could be observed. Using complementary density-functional theory (DFT) calculations, X-ray photoelectron spectroscopy and by exchanging the Eu within the wires by the alkaline-metal barium (Ba), this flat band could be attributed to the localized Eu 4f states. By fitting the relative position of the 4f-derived band with respect to the lower-lying  $\sigma$  states in the DFT calculations to the ARPES measurements, the Hubbard  $U$  of the organometallic system is derived. X-ray absorption spectroscopy (XAS) and X-ray magnetic circular dichroism

(XMCD) are utilized to probe the magnetic behavior of the wire film at low temperatures. An electronic configuration of  $4f^7$  is found with a resulting magnetic spin moment of  $7\mu_B$  and an easy axis magnetization along the wires.

Third, the on-surface synthesis of organometallic compounds containing the rare-earth metal thulium (Tm) and Cot is reported, which are characterized using STM, XAS/XMCD and thermal desorption spectroscopy. On undoped Gr/Ir(111), a disperse phase of TmCot monomers is observed for low coverages, which for high coverages coexists with an additional island phase. Complementary DFT calculations find that the monomers bind to the substrate through charge transfer with a Tm electronic configuration of  $4f^{12}$ . This configuration is confirmed using XMCD measurements and an out-of plane easy axis anisotropy of the resulting magnetic moments is observed. Intriguingly, the chemical reaction pathway during the on-surface synthesis can be changed through the suppression of charge transfer into Gr by n-doping of the substrate. As a result, islands of parallelly aligned sandwich-molecular wires are formed. It is found, that the average wire length can be controlled by changing the Tm/Cot flux ratio during the organometallic synthesis, going from small wire fragments to wires exceeding 100 formula units.

Finally, the on-surface synthesis of metal–Cot sandwich-molecular wires is studied for metal atoms which are electronically similar to Eu and effects of modifications to the Cot ring as well as the growth on a metal oxide substrate are investigated using STM. Similar to Eu, also Ba and the rare-earth metal ytterbium (Yb) form sandwich-molecular wires on undoped Gr/Ir(111). In both cases, islands of interlocking and parallelly aligned wires of high crystalline quality are formed. Although the growth mechanism is the same as for Eu, differences in the morphology of the resulting islands are observed. The growth of sandwich-molecular wires consisting of rare-earth metals and tetramethyl-Cot was studied. In the case of Eu islands of parallel wires are found, though at a higher growth temperature compared to the synthesis using Cot. The wire islands show a strong height modulation which is explained by the additional methyl groups. Furthermore, tetramethyl-Cot leads to a weaker interaction with the substrate. Lastly, polar Eu oxide on Ir(111) was used as substrate for the synthesis of Eu–Cot wires. Although the resulting wire islands are less ordered compared to the growth on Gr/Ir(111), they were still found to be phase pure.

In the scientific appendix, the intercalation of Ba and Yb under Gr/Ir(111) is presented, both forming a  $(\sqrt{3}\times\sqrt{3})R30^\circ$  intercalation layer (for Ba with respect to Gr, and for Yb with respect to Ir). The mass spectrum of the Cot molecule and the thermal desorption spectrum of a multilayer of Cot adsorbed to Gr/Ir(111) are shown, together with STM data of an adsorbed monolayer film of Cot at low temperatures. The mass spectra of tetramethyl-Cot and Dibenzo-Cot are presented, together with thermal desorption spectra of multilayers adsorbed on Gr/Ir(111) for both molecules. Finally, the STM data of an adsorbed monolayer of Dibenzo-Cot molecules on Gr/Ir(111) are presented.

# Deutsche Kurzzusammenfassung

## (*German abstract*)

---

Die vorliegende Arbeit beschäftigt sich mit der Oberflächensynthese sandwich-molekularer Drähte — dies sind eindimensionale Ketten bestehend aus Metallatomen und zyklischen Molekülen in alternierender Abfolge. Es wird ein niedrigsymmetrisches Substrat zur globalen und uniaxialen Ausrichtung der Drähte vorgestellt, wodurch diese für räumlich mittelnende Verfahren zugänglich gemacht werden. Weiterhin wird der Einfluss verschiedener Metallatome und Moleküle auf die organometallische Synthese und die daraus entstehenden Verbindungen und ihre Konsequenz für die elektronischen und magnetischen Eigenschaften untersucht.

Zunächst wird die Synthese einer einkristallinen Lage Graphen (Gr) auf dem zweizählig symmetrischen Substrat Ir(110) beschrieben, welche mittels chemischer Gasphasenabscheidung von  $C_2H_4$  bei 1500 K hergestellt wird. Die Struktur der Graphenlage wurde mittels Rastertunnelmikroskopie und niederenergetischer Elektronenbeugung untersucht. Während das reine Ir(110)-Substrat stark rekonstruiert ist, wird diese Rekonstruktion durch die adsorbierte Graphenlage aufgehoben und es entstehen flache Terrassen. Die zweizählige Symmetrie des Substrats wird auf das Moiré von Gr mit Ir(110) übertragen und resultiert in einem eindeutigen Wellenmuster mit einer Wellenlänge der Größenordnung nm. Damit einhergehend wird eine streifenartige Modulation der elektronischen Eigenschaften und Bindungsenergien beobachtet. Ergänzende winkelaufgelöste Photoemissionsspektroskopiemessungen sowie *Ab-initio*-Berechnungen zeigen, dass die Graphenlage stark an das Substrat gebunden ist und der charakteristische Dirac-Kegel in der elektronischen Bandstruktur nicht beobachtet werden kann. Es wird demonstriert, dass dieses anisotrope Muster die uniaxiale Ausrichtung sandwich-molekularer Drähte ermöglicht und einen Templateffekt auf aromatische Moleküle hat. Weiterhin wird gezeigt, dass Gr/Ir(110) die Oberflächensynthese von Lagen aus Dichalcogeniden der Übergangsmetalle und das Wachstum epitaktischer Lagen auf unrekonstruiertem Ir(110) unterhalb des Graphens ermöglicht.

Im zweiten Manuskript wird das vorgestellte, zweizählig symmetrische Substrat Gr/Ir(110) zur ausführlichen Charakterisierung von uniaxial ausgerichteten sandwich-molekularen Drähten verwendet, welche aus dem Lanthanid Europium (Eu) und dem achthgliedrigen Kohlenstoffring Cyclooctatetraene (Cot) zusammengesetzt sind. Mittels Rastertunnelmikroskopie und niederenergetischer Elektronenbeugung wurde festgestellt, dass der Ausrichtungseffekt entlang der [001]-Richtung des Substrats auch auf mehrschichtige Lagen des organometallischen Films wirkt. Die elektronische Bandstruktur der eindimensionalen Drähte wurde mittels winkelaufge-

löster Photoemissionsspektroskopie untersucht. Dabei wird ein flaches Band 1.85 eV unterhalb der Fermi-Energie beobachtet, jedoch keine von den  $\pi$ -Zuständen abgeleiteten Bänder. Mittels *Ab-initio*-Berechnungen und Röntgenphotoelektronenspektroskopie und durch den Austausch von Eu innerhalb der Drähte durch das Erdalkalimetall Barium (Ba), konnte dieses Band den lokalisierten 4f-Zuständen von Eu zugeordnet werden. Durch die Anpassung der aus den Berechnungen bestimmten relativen Position des 4f-Bandes in Bezug auf die tieferliegenden  $\sigma$ -Zustände an die Messungen, konnte das effektive Hubbard- $U$  dieses organometallischen Systems bestimmt werden. Mittels der Methode des zirkularen magnetischen Röntgendifferenzismus wurde das magnetische Verhalten der Drähte bei tiefen Temperaturen untersucht. Dabei wurde eine elektronische Konfiguration von  $4f^7$  gemessen, sowie ein daraus resultierendes magnetisches Moment von  $7 \mu_B$  und eine bevorzugte Achse der Magnetisierung entlang der Drähte.

Im dritten Manuskript wird die Oberflächensynthese von organometallischen Verbindungen des Lanthanids Thulium (Tm) mit Cot-Molekülen beschrieben, welche mittels Rastertunnelmikroskopie, Thermodesorptions- und Röntgenabsorptionsspektroskopie sowie zirkularem magnetischen Röntgendifferenzismus charakterisiert wurden. Auf undotiertem Gr/Ir(111) entsteht eine disperse Phase aus TmCot-Monomeren, welche bei hohen Bedeckungen mit einer zweiten, aus Inseln bestehenden Phase koexistiert. *Ab-initio*-Berechnungen haben gezeigt, dass die Monomere durch Ladungstransfer an das Gr binden und eine elektronische Konfiguration von  $4f^{12}$  besitzen. Diese Konfiguration wurde mittels zirkularem magnetischen Röntgendifferenzismus bestätigt und es wurde eine magnetische Anisotropie mit bevorzugter Achse senkrecht zur Ebene der Graphenlage gemessen. Erstaunlicherweise konnte durch die Unterdrückung zusätzlichen Ladungstransfers in das Gr mittels n-Dotierung des Substrats der chemische Reaktionspfad der Oberflächensynthese gezielt verändert werden. Aufgrund dieser Substratdotierung gelang die Synthese von sandwich-molekularen Drähten, welche sich parallel in Inseln anordnen. Weiterhin kann durch Veränderung des Tm/Cot-Flussverhältnisses während der organometallischen Synthese die mittlere Drahtlänge kontrolliert werden, sodass kurze Drahtsegmente bis hin zu langen Drähten von über 100 Formeleinheiten entstehen.

Schließlich wurden mittels Rastertunnelmikroskopie Drähte mit modifizierten Cot-Molekülen untersucht und die Oberflächensynthese von Metall-Cot-Drähten wurde auf Metallatome erweitert, welche sich chemisch ähnlich verhalten wie Eu. Ebenfalls wurde die Synthese von sandwich-molekularen Drähten auf einer Metalloxid-Oberfläche untersucht. Ähnlich wie Eu, bilden auch Ba und das Seltenerdmetall Ytterbium (Yb) sandwich-molekulare Drähte auf undotiertem Graphen/Ir(111). In beiden Fällen ordnen sich die resultierenden Drähte parallel in Inseln von hoher struktureller Qualität an. Der Bildungsmechanismus ist für beide Metall-Cot-Drähte der selbe, allerdings wurden geringfügige Unterschiede in der Wachstumsmorphologie beobachtet. Weiterhin wurde das Wachstum von sandwich-molekularen Drähten untersucht, welche aus Seltenerdmetallen und Tetramethyl-Cot bestehen. Mit Eu haben sich bei der Synthese Eu-Tetramethyl-Cot-Drähte gebildet, welche sich parallel in Inseln anordnen, allerdings bei einer höheren Wachstumstemperatur verglichen mit der Synthese mit Cot. Die Eu-Tetramethyl-Drähte weisen eine

starke Höhenmodulation entlang der Drahtachse auf und sind schwächer an das Substrat gebunden als Eu–Cot-Drähte. Zuletzt wurde polares Eu-Oxid auf Ir(111) als Substrat für die Synthese von Eu–Cot-Drähten getestet. Obwohl die Ordnung der darauf synthetisierten Drähte geringer ist als auf Gr/Ir(111), ist eine phasenreine Synthese derselben möglich.

Im wissenschaftlichen Anhang wird die Interkalation von Ba und Yb unter Gr/Ir(111) gezeigt. Beide dieser Metalle bilden eine  $(\sqrt{3} \times \sqrt{3})R30^\circ$ -Überstruktur aus (für Ba bezogen auf Gr und für Yb bezogen auf Ir). Außerdem wird das Massenspektrum von Cot gezeigt, sowie das Thermodesorptionsspektrum einer Cot-Multilage auf Gr/Ir(111) und Rastertunnelmikroskopieaufnahmen eines adsorbierten Cot-Films auf Gr/Ir(111) bei tiefen Temperaturen. Die Massen- und Thermodesorptionsspektren von Tetramethyl-Cot und Dibenzo-Cot werden gezeigt, sowie Rastertunnelmikroskopieaufnahmen einer adsorbierten Monolage von Dibenzo-Cot auf Gr/Ir(111).



## Frequently used acronyms and abbreviations

<b>0D</b>	-	zero-dimensional
<b>1D</b>	-	one-dimensional
<b>2D</b>	-	two-dimensional
<b>ARPES</b>	-	angle-resolved photoemission spectroscopy
<b>Bz</b>	-	benzene
<b>Cot</b>	-	cyclooctatetraene
<b>Cp</b>	-	cyclopentadien
<b>CVD</b>	-	chemical vapor deposition
<b>DFT</b>	-	density functional theory
<b>(P)DOS</b>	-	(projected) density of states
<b>Gr</b>	-	graphene
<b>h-BN</b>	-	hexagonal boron nitride
<b>LEED</b>	-	low-energy electron diffraction
<b>MBE</b>	-	molecular beam epitaxy
<b>ML</b>	-	monolayer (with respect to Ir(111) if not stated otherwise)
<b>STM</b>	-	scanning tunneling microscopy
<b>TDS</b>	-	thermal desorption spectroscopy
<b>UHV</b>	-	ultrahigh vacuum
<b>XAS</b>	-	X-ray absorption spectroscopy
<b>XMCD</b>	-	X-ray magnetic circular dichroism
<b>XPS</b>	-	X-ray photoelectron spectroscopy





# Contents

<b>Abstract</b>	<b>iii</b>
<b>Deutsche Kurzzusammenfassung (<i>German abstract</i>)</b>	<b>v</b>
<b>Frequently used acronyms and abbreviations</b>	<b>ix</b>
<b>1 Motivation</b>	<b>1</b>
<b>2 Scientific background</b>	<b>5</b>
2.1 2D layers on low-symmetry substrates . . . . .	5
2.2 Organometallic compounds . . . . .	9
2.3 On-surface synthesis . . . . .	14
<b>3 Manuscript 1: Single-crystal graphene on Ir(110)</b>	<b>19</b>
<b>4 Manuscript 2: Uniaxially aligned 1D sandwich-molecular wires: electronic structure and magnetism</b>	<b>53</b>
<b>5 Manuscript 3: From dots to wires: doping-dependent on-surface synthesis of thulium-cyclooctatetraene compounds on graphene</b>	<b>79</b>
<b>6 Reactant and substrate variation in on-surface synthesis</b>	<b>109</b>
6.0.1 Barium-cyclooctatetraene wires on graphene/Ir(111) . . . . .	110
6.0.2 Ytterbium-cyclooctatetraene wires on graphene/Ir(111) . . . . .	111
6.0.3 Europium-ytterbium-cyclooctatetraene wires on graphene/Ir(111) . . . . .	113
6.0.4 Europium-tetramethyl-cyclooctatetraene wires on graphene/Ir(111) . . . . .	114
6.0.5 Terbium-tetramethyl-cyclooctatetraene wires on graphene/Ir(111) . . . . .	118
6.0.6 Europium-cyclooctatetraene wires on polar europium oxide on Ir(111) . . . . .	119
<b>7 Discussion</b>	<b>123</b>
7.1 Irradiation damage . . . . .	123
7.2 On-surface synthesis . . . . .	127
7.3 Magnetic ordering . . . . .	133

## Contents

---


<b>8 Summary and outlook</b>	<b>135</b>
<b>A Scientific appendix</b>	<b>139</b>
A.1 Ytterbium intercalation under graphene/Ir(111) . . . . .	139
A.2 Barium intercalation under graphene/Ir(111) . . . . .	141
A.3 Cyclooctatetraene . . . . .	142
A.4 Tetramethyl-cyclooctatetraene . . . . .	143
A.5 Dibenzo-cyclooctatetraene . . . . .	144
<b>B List of publications (<i>Liste der Teilpublikationen</i>)</b>	<b>146</b>
<b>Bibliography</b>	<b>149</b>
<b>Acknowledgements (<i>Danksagung</i>)</b>	<b>159</b>
<b>Lebenslauf (<i>Curriculum Vitae</i>)</b>	<b>165</b>

# CHAPTER 1

## Motivation

Organometallic chemistry is a comparatively recent field of research which can be considered as the intersection of organic chemistry and inorganic chemistry. As organic chemistry is the study of carbon complexes and inorganic chemistry deals with non-carbon based compounds, organometallic chemistry focuses on the interaction of both components and their resulting properties. The organometallic compounds investigated in this thesis — sandwich-molecular compounds — became popular when the structure of ferrocene was discovered [1,2]. Ferrocene consists of an iron dication sandwiched by two cyclopentadienyl anions, shown as side/top view model in Figure 1.1a/b. At the time it was found surprising that ferrocene is highly stable, does not decompose at temperatures up to 400 °C and is unaffected by air and water [3].

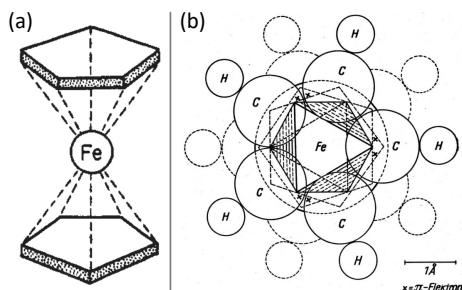


**Figure 1.1:** (a) Side view and (b) top view of ferrocene structure model in the original publications. Adapted with permission from: (a) ref. [1] © 1952 ACS. (b) Ref. [2] .

As it turns out, the reason for this remarkable stability is the charge transfer from the central iron atom to the surrounding molecules, creating two aromatic cyclopentadienyl anions ( $C_5H_5^-$ ). This finding triggered its own field of research, the study of metallocenes, which is relevant for catalysis today [4]. For their pioneering work in uncovering the sandwich structure of ferrocene, Ernst Otto Fischer and Geoffrey Wilkinson were later awarded the Nobel Prize for chemistry in 1973. It was quickly realized that these metal- $C_5H_5$  complexes are just one example of a much broader category of sandwich compounds, like the soon-after discovered di-benzene-chromium [5] and uranocene [6]. Benzene ( $C_6H_6$ , abbreviated to Bz) is a six-membered carbon ring which is aromatic in its neutral state and therefore binds to the central metal atom via covalent binding. In contrast, the eight-membered carbon ring cyclooctatetraene ( $C_8H_8$ , abbreviated to Cot) becomes aromatic upon accepting two electrons and forms strong ionic bonds to the encapsulated metal atom.

The same type of binding mechanism has allowed the synthesis of one-dimensional (1D) sandwich-molecular wires, which are central to this thesis. Sandwich-molecular wires are 1D

chains of metal atoms and cyclic molecules arranged in an alternating sequence. Historically, sandwich-molecular wires were first produced in the liquid phase [7] and more recently in the gas phase [8], limiting the types of experiments that can be conducted on these systems. From an electronic standpoint, their most interesting feature is the interaction of the metal atom with the surrounding ligand field of the molecules. In this thesis, lanthanide–Cot wires are investigated, in which the interaction of the localized 4f states of the lanthanide with the extended  $\pi$  orbitals of Cot holds the promise of magnetic coupling between the robust 4f-generated moments through electronic hybridization. Theoretical investigations have predicted high spin filter efficiencies for such systems [9], making them promising candidates for spintronic applications [10, 11].

Spintronics makes use of the electronic spin — in addition to its charge — for information processing and promises lower power consumption, higher storage and transistor densities as well as higher processing frequencies [12]. One technological example making use of this is the common hard disk drive, which utilizes the giant magnetoresistance effect. The relevance of this effect and its real-world applications was acknowledged when Peter Grünberg and Albert Fert were awarded the Nobel Prize for physics in 2007 for its discovery [13, 14]. However, a fundamental problem for the research and development of future spintronic devices is the spin diffusion length over which the electronic spin is conserved. Only if the diffusion length is of the order of the device dimension, the spin can be a useful quantity for computation. Building molecular spintronic devices is therefore a logical next step, since molecular structures inherently have a low dimensionality. Not limited to this, they can also be precisely controlled and by proper choice of the reactants, be formed via self assembly. 1D sandwich-molecular wires are thus promising to contribute to this field, with theoretical predictions of spin valves for short wire segments [15, 16], spintronic and magnetic switches [17, 18] and high spin-filter efficiencies for sandwich-molecular wires containing Bz [19–25], Cp [26–28] and Cot [9, 29–31].

In this thesis, the *in situ* growth of sandwich-molecular wires under controlled ultrahigh vacuum conditions is studied, using the recently developed on-surface synthesis method [32]. From a synthesis perspective, different types of metal reactants and molecules are combined and the influence of the substrate is studied. Scanning tunnelling microscopy and low-energy electron diffraction were employed for structure determination. The magnetic properties and 4f electronic configurations within the wires were investigated by X-ray absorption spectroscopy and X-ray magnetic circular dichroism — surface sensitive and element-specific techniques. In addition, complementary *ab initio* calculations are presented to explore the formation mechanism of the wires, as well as their binding character and hybridization.

---

This thesis is structured as follows: Chapter 2 introduces the scientific background for the presented work, *i.e.* 2D materials on low-symmetry substrates, organometallic compounds and their on-surface synthesis. In the next three chapters, manuscripts are presented which are either submitted for publication or still in preparation phase. They form the central part of this thesis. The manuscript in chapter 3 describes the preparation and characterization of the inert and two-fold symmetric substrate Gr/Ir(110). Additionally, the use of this substrate as a uniaxial nanotemplate for organic and organometallic species, *i.e.* sandwich-molecular wires is demonstrated in this manuscript. Building on these findings, the manuscript in chapter 4 makes use of this new substrate for the uniaxial alignment of Eu–Cot sandwich-molecular wires. The synthesized wires are a true 1D organometallic species and the electronic and magnetic properties are investigated. The organometallic synthesis combining thulium (Tm) and Cot is presented in the manuscript of chapter 5. It is shown that by n-doping the substrate — Gr/Ir(111) in this case — the chemical reaction pathway can be changed going from a disperse phase of TmCot monomers on the undoped substrate to sandwich-molecular wires on the n-doped substrate. Chapter 6 presents the on-surface synthesis of sandwich-molecular wires, in which both reactants — metal atoms and molecules — as well as the substrate were varied. The main outcomes of the experimental results are discussed in chapter 7 and finally the thesis is concluded with a summary and outlook to future experiments in chapter 8.



## CHAPTER 2

---

### Scientific background

*In this chapter, the scientific background relevant to the experimental results is explained. First, previous work on 2D layer growth on two-fold and four-fold symmetric substrates is presented. The quality and phase purity of these layers as well as the resulting moiré with their substrates are described. Following this, organometallic compounds are introduced, including 0D single-molecule magnets, 1D sandwich-molecular wires and 2D metal-organic networks and previous findings on their properties are described. Finally, the idea of organometallic on-surface synthesis is presented and different types of synthesis routes are explained.*

#### 2.1 2D layers on low-symmetry substrates

##### Graphene

The growth of graphene (Gr) on metal surfaces has been studied extensively, with a heavy focus on symmetry-matching substrates [33]. Depending on the interaction strength with the substrate, the properties of Gr are modified more or less strongly. For weakly interacting substrates, such as Cu(111) [34] or Pt(111) [35], multiple domains are found after epitaxial growth because the energy barrier between the different domains is low. Gr on these weakly interacting substrates can be regarded as close to freestanding. If the interaction with the substrate is significantly higher, as is the case for Ru(0001) [36], single-crystal Gr can be formed, but at the cost of higher chemical interaction, strong corrugation of the 2D layer and the loss of Gr's freestanding properties [37]. Only if the interaction with the metal substrate is just high enough, single-crystal Gr can be grown while maintaining the freestanding character of Gr, which is unique to the growth of Gr/Ir(111) [38, 39].

Far less investigations have been conducted on the growth of Gr on low-symmetry substrates, *i.e.* of four-fold or two-fold symmetry. A common theme for these systems is that the low symmetry of the surface is imprinted onto the moiré of Gr with its substrate if the interaction is strong enough. The only single-domain (but not single-crystal) growth of Gr on a low-symmetry metal substrate was reported for the quasihexagonal bcc(110) surface of Fe [40], which is of two-fold symmetry. As depicted in Figure 2.1a, a sheet of single-domain Gr is formed, except for

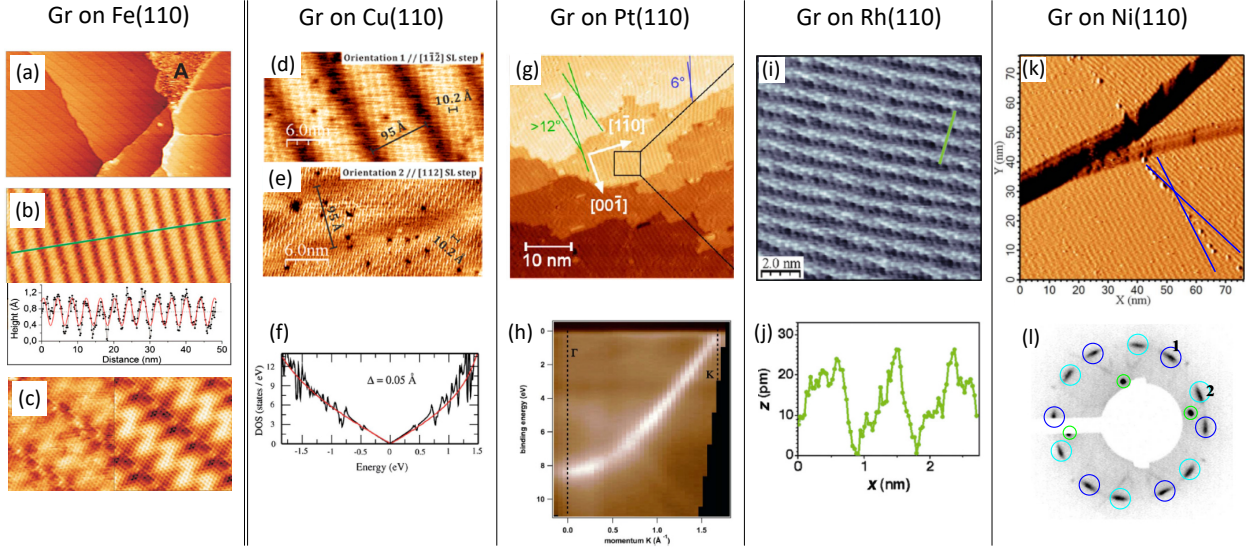


**Figure 2.1:** Gr/Fe(110): (a) STM topograph ( $650 \times 1150 \text{ \AA}^2$ ) of single-domain Gr and disordered phase **A**. (b) STM topograph ( $200 \times 500 \text{ \AA}^2$ ) of stripe-like moiré with corresponding height profile along green line. (c) High-resolution STM topograph ( $75 \times 150 \text{ \AA}^2$ ) of moiré with two imaging contrasts, zigzag motif along stripe direction is visible. Gr/Cu(110): (d)–(e) STM topographs ( $150 \times 300 \text{ \AA}^2$ ) of two Gr domains with corresponding wave periodicities of  $\approx 100 \text{ \AA}$  in (d) and  $\approx 10 \text{ \AA}$  in (e). (f) DFT-calculated DOS of Gr/Cu(110). Gr/Pt(110): (g) STM topograph ( $500 \times 500 \text{ \AA}^2$ ) with four domains visible indicated by green and blue lines, in each domain a weak stripe pattern is visible. (h) ARPES data corresponding to (g), with a linear dispersion around the K point, consistent with freestanding Gr. Gr/Rh(110): (i) STM topograph ( $111 \times 111 \text{ \AA}^2$ ) of one Gr domain, stripe pattern with  $\approx 10 \text{ \AA}$  periodicity. (j) Height profile indicated by green line in (i), corrugation of  $\approx 0.2 \text{ \AA}$  is observed. Gr/Ni(110): (k) STM topograph ( $760 \times 760 \text{ \AA}^2$ ) of two-domain Gr/Ni(110), directions indicated by blue lines. (l) LEED pattern corresponding to (k), Ni(110) reflection encircled in green, the two Gr domains are encircled blue/cyan. Adapted with permission from: (a)–(c) ref. [40] © 2012 APS. (d)–(e) Ref. [41] © 2020 ACS. (f) Ref. [42] © 2016 APS. (g)–(h) Ref. [43] © 2018 IOP. (i)–(j) Ref. [44] © 2018 Springer. (k)–(l) Ref. [45] © 2008 APS.

the small disordered patch marked by **A** (the disordered area covers about 5 – 10 % of the surface). Due to the two-fold symmetry, a stripe-like wave pattern of  $\approx 4 \text{ nm}$  periodicity is imposed onto the moiré visible in Figure 2.1b, with the wave crests along the [001] direction of the substrate. The corresponding height profile in Figure 2.1b shows a corrugation of  $\approx 0.9 \text{ \AA}$ , which is ascribed to a strong chemisorption to the Fe(110) surface [40]. The strong Gr–substrate interaction also explains the fact that single-domain islands can be grown. While on the length scale of Figure 2.1a the moiré appears purely stripe-like, a closer look reveals that the wave pattern is not strictly linear, but follows a zigzag pattern along the stripe direction (compare Figure 2.1c).

Graphene has also been grown on several fcc(110) surfaces. On the Cu(110) surface it was found that, similar to Cu(111), the interaction with Gr is very weak. Depending on the growth conditions, this leads to the formation of at least two [41] or more [42] Gr domains on Cu(110). In Figure 2.1d/e STM topographs of the two Gr domains reported in ref. [41] are shown. Also



here, a stripe-like wave pattern is observed with periodicities ranging from  $\approx 10 \text{ \AA}$  to  $\approx 100 \text{ \AA}$ , depending on the orientation of Gr to the Cu(110) surface. The calculated density of states (DOS) for Gr/Cu(110) in Figure 2.1f (shown in black) agrees with the DOS of freestanding Gr (shown in red), consistent with a weak Gr–substrate binding [42], which explains why single-orientation Gr growth is not possible on Cu(110). Similarly, on the Pt(110) surface several Gr domains are found in ref. [43]. In the topograph of Figure 2.1g, four coexisting domains are observed, indicated by the green and blue lines. Each domain shows a weak stripe-like wave pattern in the Gr layer and a high defect density is observed. The formation of multiple domains again indicates a weak Gr–substrate binding, which is confirmed in the ARPES measurement of Figure 2.1h. At the K point of the Brillouin zone a linear dispersion is found, consistent with the band structure of freestanding Gr. Also on the Rh(110) surface the formation of multiple Gr domains was reported [44]. Figure 2.1i shows the topograph of one such domain. A wave pattern with  $10 \text{ \AA}$  periodicity is observed with a corrugation of  $\approx 0.2 \text{ \AA}$  (compare Figure 2.1j), significantly lower compared to the stronger interacting Gr/Fe(110) surface [40]. Finally, on the Ni(110) surface at least two Gr domains are reported [45, 46], and shown in the topograph of Figure 2.1k. The two Gr orientations are indicated by the blue lines at the boundary of two domains. The corresponding LEED pattern in Figure 2.1l shows the first order Ni(110) reflections encircled in green, and the two domains of Gr encircled in cyan and blue. Also visible in the LEED pattern is that the Gr reflections are smeared out over a certain range, *i.e.* the domain orientation is not very strict.

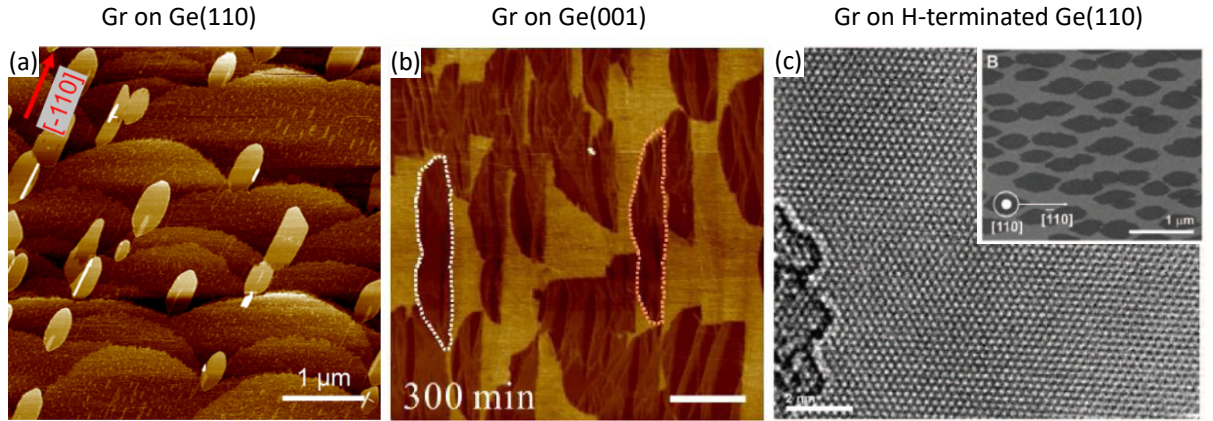


**Figure 2.2:** (a) AFM topograph ( $4.6 \times 4.6 \mu\text{m}^2$ ) of single-domain Gr islands on Ge(110). (b) AFM topograph ( $4000 \times 4000 \text{ \AA}^2$ ) of single-domain Gr islands on Ge(001). (c) HR-TEM image ( $95 \times 130 \text{ \AA}^2$ ) of single-crystal Gr sheet on H-terminated Ge(110). Inset: SEM image ( $3.0 \times 3.5 \mu\text{m}^2$ ) of single-domain Gr islands on H-terminated Ge(110) before the full Gr layer is closed. Adapted with permission from: (a) ref. [47] © 2016 ACS. (b) Ref. [48] © 2011 Elsevier. (c) Ref. [49] © 2014 AAAS.

As apparent from Figure 2.1 — and in analogy to fcc(111) metal surfaces — it is non-trivial to find a (110) metal surface with a suitable interaction strength, which combined with proper growth conditions, yields the growth of single-domain single-crystal Gr sheets. In principle,

it is plausible that the Gr layers in Figure 2.1 could be used as anisotropic templates for the adsorption of *e.g.* a molecular layer. However, in order to globally template a uniaxial alignment of adsorbed layers, a closed single-crystal Gr sheet is needed.

Gr on low-symmetry substrates also has other possible uses besides the templating of adsorbed species. For example, a Gr sheet has been used as a layer to protect the Pt(001) surface from oxidation and to preserve its surface reconstruction [50,51]. Another example is the use of low-symmetry surfaces of the semiconductor Ge for the growth of wafer-size single-crystal Gr sheets. In ref. [47] single-domain Gr islands were grown on the Ge(110) surface shown in Figure 2.2a. In this case, the orienting effect is explained by the strong chemical binding to the substrate and alignment of the Gr armchair direction along the Ge atomic steps in the  $[\bar{1}10]$  direction of the substrate. On a vicinal surface of Ge(001) it was additionally found that Gr islands can be uniaxially aligned through the vicinal steps [48] of the substrate (see Figure 2.2b), which can be stitched together to form a wafer-scale single-crystal Gr sheet [48]. The growth of a single-crystal Gr sheet was also achieved on the H-terminated Ge(110) surface [49]. As apparent from the inset of the topograph in Figure 2.2c, the nucleation of Gr islands happens along one direction, and through further growth, the islands merge to a wafer-scale single-crystal Gr sheet. The Gr atomic lattice is well visible in Figure 2.2c, but there is no apparent moiré with the substrate. The reason is that the Ge(110) surface is fully passivated by the H termination, resulting in very weak binding to the adsorbed Gr sheet. In fact, the Gr sheet is so weakly bound that it can be transferred by dry transfer. In all examples of Gr growth in Figure 2.2, no apparent moiré is observed, which means that these Gr sheets are not feasible for uniaxial templating, but are only applicable for the synthesis of wafer-scale Gr sheets. A further practical drawback is that the Gr growth on Ge surfaces is conducted close to the Ge melting temperature. If the growth temperature in these cases is not controlled properly, Gr growth results in severe faceting of the Ge surface [52–54].

In summary, the growth of Gr on low-symmetry substrates has so far been limited to multiple-domain [41–46] or phase-impure [40] growth. Single-crystal growth was achieved only in the absence of an anisotropic moiré [48,49], making it unsuitable for the use as a template.

### Hexagonal boron nitride

While single-crystal growth on a low-symmetry surface with an anisotropic moiré has not yet been realized for Gr, it has been achieved with the isostructural and isoelectric material hexagonal boron nitride (h-BN). In ref. [43] the growth of single-domain h-BN/Pt(110) was first reported, though with a high defect density. By increasing the temperature during growth above the roughening temperature of Pt, a single-crystal of h-BN/Pt(110) could be grown [55], though at the expense of a complex surface reconstruction. The resulting topography in Figure 2.3a shows a clear stripe-like wave pattern with a periodicity of 21 Å. The only example of a 2D layer with anisotropic moiré used as template for molecular adsorption was h-BN/Rh(110) [56]. On

Rh(110), h-BN forms two domains which exhibit a clear wave pattern with  $13\text{ \AA}$  periodicity shown in the topograph of Figure 2.3b. In ref. [56] it was demonstrated that the anisotropic moiré is able to impose uniaxial alignment of an adlayer of molecules, while maintaining their electric properties.

In conclusion, h-BN sheets with a two-fold symmetric moiré were achieved with multiple domains, each of which was demonstrated to template molecular adsorption, or as single-crystal layer at the cost of complex surface reconstructions.

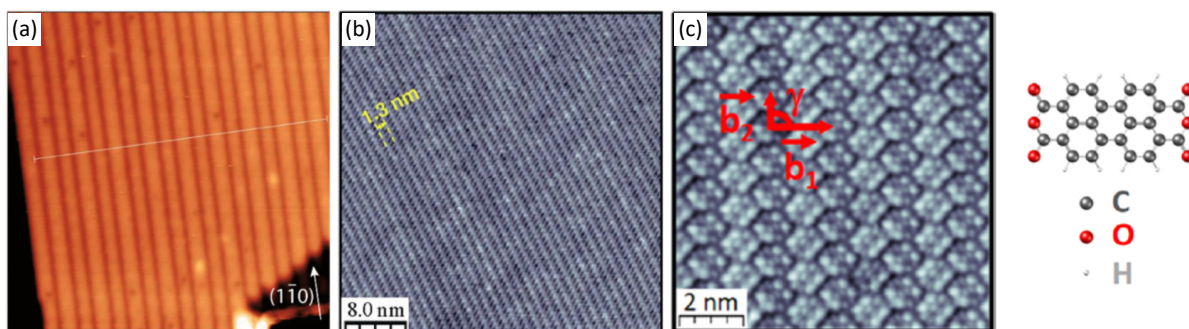


**Figure 2.3:** (a) STM topograph ( $435 \times 435\text{ \AA}^2$ ) of single-domain h-BN on Pt(110) with a wave pattern of  $\approx 21\text{ \AA}$  periodicity. (b) STM topograph ( $420 \times 420\text{ \AA}^2$ ) of h-BN on Rh(110) with a wave pattern of  $\approx 13\text{ \AA}$  periodicity. (c) STM topograph ( $95 \times 95\text{ \AA}^2$ ) of an oriented molecular layer on Gr/Rh(110) with the atomic model of the molecule (3,4,9,10-perylene tetracarboxylic dianhydride). Adapted with permission from: (a) ref. [55] © 2019 ACS. (b) Ref. [56] © 2018 Springer. (c) Ref. [56] © 2019 ACS.

## 2.2 Organometallic compounds

Organometallic compounds are promising candidates for future applications in molecular spintronic devices [10, 11], for which the fundamental understanding of the involved interactions is necessary. There are three main categories of organometallic compounds in this context, which are 0D single-molecule magnets, 1D sandwich-molecular wires and 2D metal-organic networks. To understand what sets the sandwich-molecular wires introduced in chapter 1 apart from other organometallic compounds, the properties and previous experimental findings for the three types of systems are described in the following.

Key interests are the electronic and magnetic properties which emerge from the interaction of the molecular  $\pi$  system with the metal 3d or 4f orbitals. The focus of this thesis is on the investigation of rare-earth elements, which have an occupied 4f shell. In contrast to transition metals, in which the outer 3d shell is directly involved in the interactions with the local environment, the 4f shell is closer to the core and thus more isolated, along with its 4f-generated magnetic moment. The main techniques used for magnetic investigations of these systems are X-ray absorption spectroscopy (XAS) [57, 58] and X-ray magnetic circular dichroism (XMCD) [59, 60] due to their surface sensitivity and element specificity.

## 0D single-molecule magnets and 2D metal–organic networks

Single-molecule magnets are small units consisting of one or few magnetic atoms bound to or encapsulated by a molecular structure. While at the macroscopic level, magnetic properties such as hysteretic behavior of the magnetization within an external field, emerge from the coupling between many magnetic units and their resulting long range order, this is not the case for single-molecule magnets which are essentially 0D complexes. In single-molecule magnets solely the local interaction of the magnetic atoms with the surrounding ligand field determines the behavior of the magnetic moment. As an example the emergence of a magnetic hysteresis can be considered [61]. In macroscopic systems three conditions must be fulfilled: (i) long-range ferromagnetic (or ferrimagnetic) coupling between the magnetic moments must be present, (ii) the temperature must be below the Curie temperature such that thermal fluctuations are insignificant, and (iii) the systems must have a large enough magnetic anisotropy to prevent the moments to simply follow the external magnetic field. In single-molecule magnets (i) is irrelevant due to the low dimensionality. (ii) Thermal fluctuations are even more important. The temperature below which fluctuations are insignificant is called blocking temperature [62] in 0D systems. Below the blocking temperature, switching of the magnetic moment is explained by quantum tunnelling of the magnetization [63,64]. (iii) The anisotropy is provided only by the ligand field and hence comparably weak, typically leading to very low blocking temperatures.

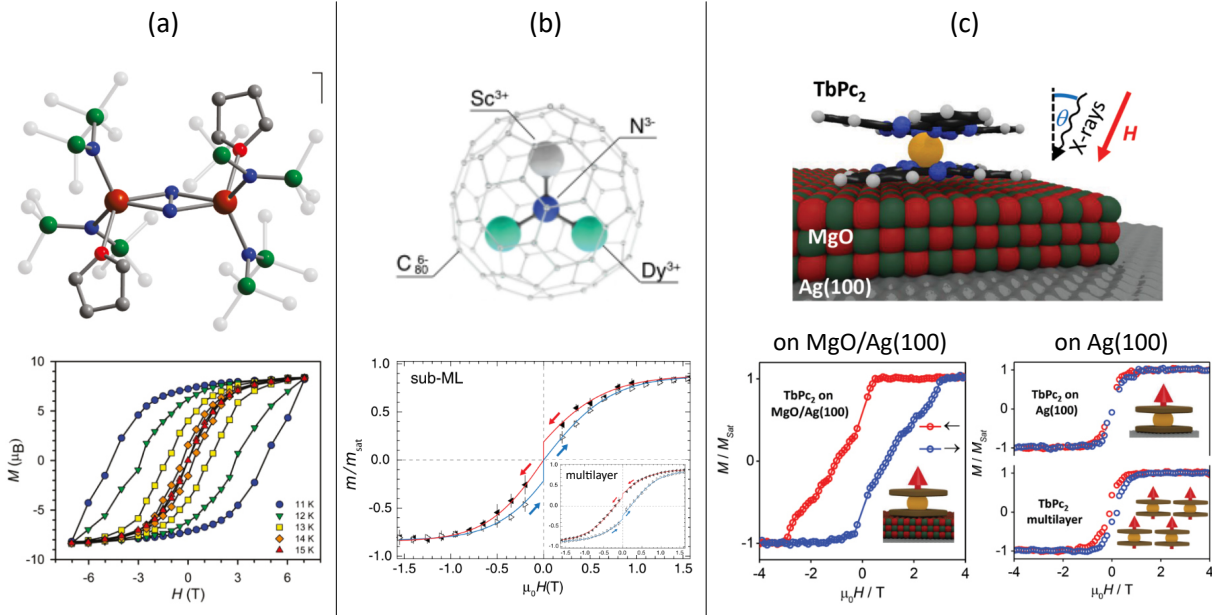


**Figure 2.4:** (a)–(c): Atomic models of single-molecule magnets with corresponding magnetization curves. (a) Radical-bridged Tb complex from ref. [65]. (b) Endohedral  $Dy_2ScN$  complex from ref. [66]. (c)  $TbPc_2$  double-decker from ref. [67]. Adapted with permission from: (a) ref. [65] © 2011 APS. (b) Ref. [66] © 2015 APS. (c) Ref. [67] © 2015 WILEY.



Up to now, mainly three different types of single-molecule magnets have been investigated. One category is shown in Figure 2.4a from ref. [65] in which the magnetic atoms are directly build into the molecular structure and a magnetic hysteresis is observed below 15 K. Similar systems were reported in refs. [64, 68–72]. In the type of system shown in Figure 2.4b from ref. [66] the magnetic atoms are enclosed within endohedral fullerenes isolating them from the environment. This architecture leads to a magnetic hysteresis below 4 K and blocking temperatures of up to 28 K have been reported in a similar system [73]. Figure 2.4c from ref. [67] shows the most common type of single-molecule magnet, in which the magnetic atom is sandwiched (or half-sandwiched) by one or two molecules. The common use of these systems is explained by the fact that they are easy to produce and also easy to modify by changing the metal atom and molecules as basic building blocks. The most used molecules are porphyrins [74–76] or phthalocyanines [67, 77–80]. A key question that is also relevant for the 1D and 2D systems is the influence of the substrate and the interaction of the 4f orbital with the molecular  $\pi$  system. For the single-molecule magnet in Figure 2.4c a hysteresis is reported when adsorbed on the insulating substrate MgO/Ag(100). This hysteresis is suppressed when the magnetic units are directly deposited on the Ag(100) metal surface, which is explained by the strong interaction with the metal substrate [67]. Only in the second layer — in which the interaction with the first molecular layer is weak — the hysteresis is observed again. This example shows that the local environment of the organometallic species has a strong effect on the electronic and magnetic properties. Another important question also relevant to 1D and 2D systems, is whether there is a significant interaction of the 4f orbital with the surrounding ligand field. It was reported in ref. [78] that the 4f states are directly involved in the electrical transport through bis-phthalocyaninato-neodymium molecular units adsorbed to Cu(100), while the 4f-generated magnetic moments are preserved. This interaction holds the promise of the electronic control of magnetic moments for future spintronic devices [78].

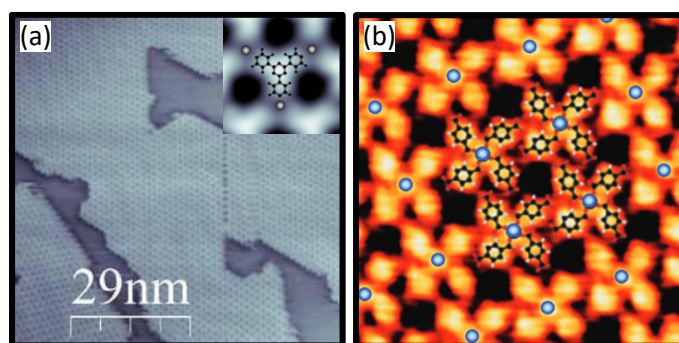


**Figure 2.5:** (a) STM topograph ( $800 \times 800 \text{ Å}^2$ ) of metal-organic network consisting of Fe centers coordinated by linker molecules from ref. [81]. Inset: STM topograph ( $25 \times 25 \text{ Å}^2$ ) with atomic structure model of Fe atoms and molecule. (b) STM topograph ( $62 \times 62 \text{ Å}^2$ ) of Fe-benzenedicarboxylate network on Cu(100) from ref. [82]. Adapted with permission from: (a) ref. [81] © 2012 APS. (b) Ref. [82] © 2009 APS.

Also 2D metal–organic networks have been investigated with respect to their electronic and magnetic properties, mostly on metal substrates. One example shown in Figure 2.5a is the self-assembled network of Fe centers coordinated by linker molecules [81]. In the first layer, the metal–organic structure consists of units shown in the inset of Figure 2.5a. In the second layer each Fe atom is covered by one additional linker molecule. The corresponding XMCD measurements show an out-of-plane easy-axis magnetization and ferromagnetic coupling between the Fe atoms. Since the substrate is non-magnetic, the interaction between the Fe atoms is explained by super-exchange coupling, meaning purely through the organic network, indicating a significant hybridization between the atomic and molecular orbitals. Another example of an Fe–organic network adsorbed on Cu(100) is shown in Figure 2.5b, overlaid with an atomic model of the Fe centers and molecules. In this system, a strong in-plane magnetic anisotropy is observed which is explained by mixing the ground and first excited molecular states [82]. When O<sub>2</sub> is adsorbed the Fe centers, the easy axis of magnetization is switched from in-plane to out-of-plane, once again underlining the effect of the local environment on the interaction within metal–organic networks.

In conclusion, single-molecule magnets feature a magnetic hysteresis without long-range order and are confined to 0D with corresponding low blocking temperatures. Metal–organic networks can show ferromagnetic coupling throughout the surface plane, in which the strong interaction of magnetic moments with the surrounding ligand field of molecular films was observed.

### 1D sandwich-molecular wires

Sandwich-molecular wires are 1D chains of metal atoms and cyclic molecules in an alternating sequence, as shown in Figure 2.6a for a metal–Cot wire. In contrast to the organometallic systems described above, they have the unique feature of electronic interactions between the metal atoms and the  $\pi$  molecular orbitals in just one dimension. Therefore, 1D long-range magnetic ordering is possible within these wires. The magnetic atoms are relatively well isolated from the environment through the encapsulation by cyclic molecules.

Many theoretical investigations have been conducted on sandwich-molecular wires for various combinations of atoms and molecules. Early investigations were made for wires consisting of the 3d metal vanadium (V) and the aromatic Bz molecule. Due to the aromaticity of Bz, the intra-wire coupling is covalent [85, 86]. V–Bz wires are predicted to be a ferromagnetic half metals [19], which means they obey spin filter properties. Modifications of these wires were investigated, in which Bz was replaced by borazine [87] or borata-Bz [22]. Both modifications influence the binding strength and magnetic coupling. Several metal–Bz wires were investigated in which effects on the electronic structure [86] and wire geometry [88] were reported. In ref. [24] the synthesis of half-metallic molybdenum–borine wires on a Si substrate was theoretically pro-

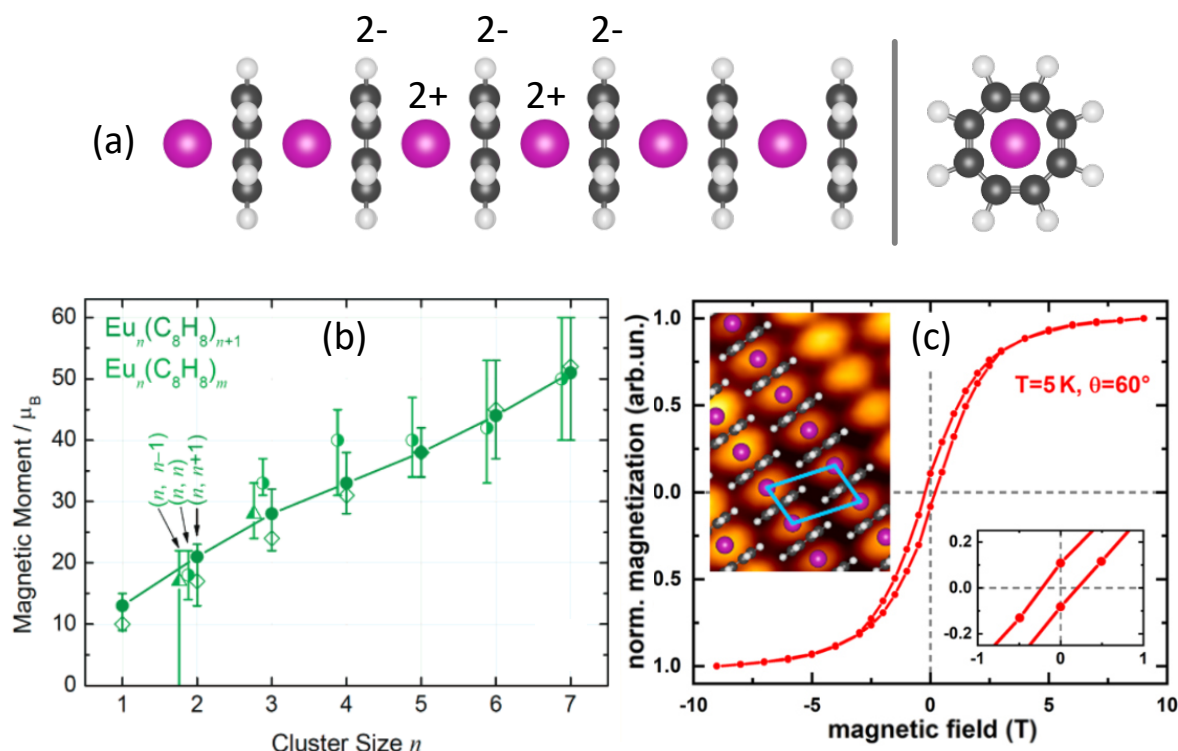


**Figure 2.6:** (a) Atomic structure model of a metal–Cot sandwich-molecular wire as side view (left) and view along the wire axis (right). Pink: metal atoms. Black: C atoms. White: H atoms. (b) Wire length dependence of total magnetic moment for EuCot wires from ref. [83]. (c) Magnetization curve of EuCot wires on Gr/Ir(111) along wire axis from ref. [84]. Inset: STM topograph of EuCot wires on Gr/Ir(111) overlaid with atomic structure model, the wire carpet unit cell is indicated by cyan rhomboid. Adapted with permission from: (a) ref. [83] © 2008 ACS. (b) Ref. [84] © 2019 ACS.

posed [24]. Experimentally, V–Bz wires were produced in the gas phase by laser vaporization and found to be ferromagnetic [89], confirming the theoretical predictions.

By choosing a cyclic molecule which can accept additional electrons into its  $\pi$  system, ionically bound sandwich-molecular wires can be formed. For example, the Cp molecule introduced in chapter 1 becomes an aromatic  $\text{Cp}^-$  anion within organometallic compounds. Many metal–Cp wires were theoretically predicted to be ferromagnetic half metals [17, 27, 90–92]. Further, theoretical studies have been conducted on 1D wires consisting of Bz and Cp combined with metal atoms [26, 48, 93, 94]. Up to now, no experimental investigations of the electronic and magnetic properties of metal–Cp wires have been conducted.

For the coordination of lanthanide (Ln) atoms within sandwich-molecular wires the already described Cot molecule is used (abbreviated to LnCot wires). While the neutral Cot molecule is antiaromatic [95] and has a tub-like shape [96], it becomes aromatic and planar upon accepting two additional electrons into its  $\pi$  system. Combined with Ln atoms, this results in a periodic  $\text{Ln}^{2+}$ – $\text{Cot}^{2-}$  ionic binding motif of the LnCot wires as shown in Figure 2.6a. This binding motif is energetically highly favorable, allowing the growth of much longer wires compared to

the covalently bound transition-metal–Bz wires. First *ab initio* calculations were conducted for short EuCot wires, in which a hybridization of the Eu 4f states with the Cot  $\pi$  orbitals was found [97]. The magnetic moment per formula unit of  $7\mu_B$  in EuCot wires has been predicted to increase linearly with the wire length. Further, EuCot wires were predicted to be semiconducting ferromagnets with high spin-filter efficiencies [9]. In ref. [29], the modified Eu–borata-Cot wires were predicted to be half-metallic [29] instead of semiconducting.

Experimentally, a magnetic moment of  $7\mu_B$  per Eu atom in EuCot wires was found in Stern-Gerlach type experiments [83,98]. As shown in Figure 2.6b, the total magnetic moment increases linearly with the wire length, confirming the theoretical predictions. Recently, the on-surface synthesis of EuCot wires on Gr/Ir(111) was introduced [32]. Using this new method, EuCot wires on Gr/Ir(111) were investigated with XMCD measurements in ref. [84]. It was found that the EuCot wires are indeed ferromagnetic semiconductors, in agreement with the theoretical calculations. Within the EuCot wire carpets the magnetic moments couple ferromagnetically along the wire axis and a magnetic hysteresis is observed below 7 K shown in Figure 2.6c. For sandwich-molecular wires containing terbium (Tb), thulium (Tm) and holmium (Ho), Stern-Gerlach type experiments were conducted [83,98]. It was found that the total magnetic moment of LnCot (Ln=Tb, Tm, Ho) wires tends to increase with wire length, although not strictly linear as in EuCot wires. The on-surface synthesis of other LnCot wires would greatly benefit electronic and magnetic investigations using surface-sensitive experimental techniques.

### 2.3 On-surface synthesis

On-surface synthesis is widely used for the growth of 0D up to 2D organic and metal–organic structures. There are different on-surface synthesis routes, and it can be distinguished between growth on reactive metal surfaces — which play an essential role during synthesis due to their catalytic character — and the growth on non-reactive substrates. Both routes have in common that they rely on distinct building blocks or precursor molecules for the on-surface reactions.

One exemplary synthesis route on a metal substrate is shown in Figure 2.7a–c from ref. [99]. There, Ullmann coupling [100] is used for the formation of a 2D network. First, precursor molecules are deposited on a metal surface, in this case Ag(111), which form a layer of independently adsorbed molecules via self-assembly (see Figure 2.7a). Through a mild annealing step to 125 °C a porous organometallic network is formed, in which the precursor molecules are linked via Ag atoms from the substrate (compare Figure 2.7b). A final annealing step to 250 °C forms a covalent organic network, in which the precursor molecules are linked via covalent bonding assisted by the catalytic Ag(111) substrate. This is a general growth scheme as explained in ref. [101]. The intriguing feature of this growth scheme is that many different resulting structures can be synthesized based on the type of precursor molecule, substrate reactivity and symmetry. There are many other examples of 2D networks, either covalently bonded [102–104] or metal-coordinated molecular networks [81, 82, 105, 106]. For many of the systems the different



annealing steps of Ullmann coupling are not necessary, and the resulting networks simply form by self assembly of the provided atomic and molecular species.

In ref. [105] a metal–organic network was constructed by two steps. First, a self-assembled organic network on Ag(111) was formed, for which precursor molecules were evaporated onto the substrate by sublimation from a Knudsen cell. In a second step, a metal–organic network was synthesized by metalation of the pre-assembled organic network. Through the metalation step, magnetic coupling in the 2D layer was induced. In ref. [107], Fe- and Mn-containing phthalocyanine molecules were sublimated from a powder and deposited on a Co surface, which resulted in a self-assembled metal–organic 2D network.

On-surface synthesis can also be used to grow 1D structures on metal surfaces, such as Gr nanoribbons [108] or metal–ligand chains [109]. In ref. [110], the formation of 1D chains was reported, which connect to a 2D network for higher coverage. Also, low-symmetric substrates can be used to template uniaxial alignment of molecular chains, *e.g.* on Au(110) [111] shown in Figure 2.7d. In this case, the uniaxial Au(110) surface pattern causes the alignment effect on the anisotropic molecules. In ref. [76], the on-surface synthesis of 0D bis(porphyrinato)cerium double-decker complexes was reported. This was achieved by deposition of elemental cerium under ultrahigh vacuum conditions into a film of pre-adsorbed tetraphenylporphyrin molecules on Ag(111). In a subsequent annealing step the double-deckers formed via self assembly while surplus molecules were re-evaporated into the vacuum. The result was a self-assembled 2D pattern of the double decker units.

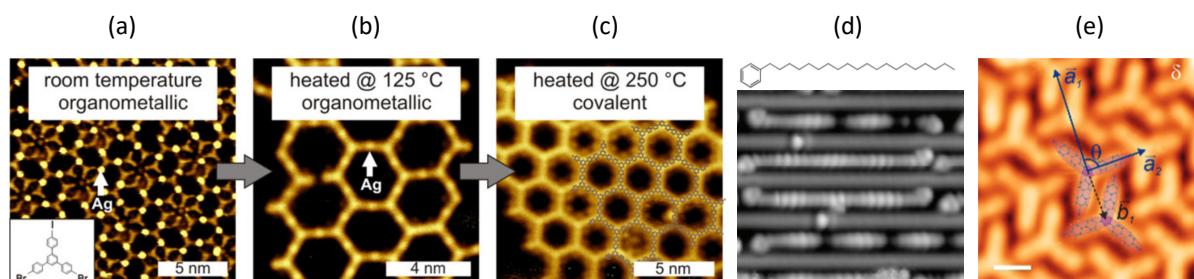


**Figure 2.7:** (a)–(c): Ullmann coupling via organometallic intermediates on Ag(111). (a) STM topograph ( $165 \times 165 \text{ \AA}^2$ ) of self-assembled network of precursor molecules. (b) STM topograph ( $110 \times 110 \text{ \AA}^2$ ) of metal–organic network after 125 °C annealing step of network in (a). (c) STM topograph ( $140 \times 140 \text{ \AA}^2$ ) of covalently bound molecular network after 250 °C annealing of network in (b). (d) Molecular model and STM topograph ( $60 \times 70 \text{ \AA}^2$ ) of molecules adsorbed to the Au(110) surface. (e) STM topograph ( $63 \times 63 \text{ \AA}^2$ ) of self-assembled Dy–organic network on Gr/Ir(111), molecule: 1,3,5-tris(40-biphenyl-400-carbonitrile) benzene. Adapted with permission from: (a)–(c) ref. [99] © 2015 WILEY. (d) Ref. [111] © 2011 AAAS. (e) Ref. [112]

Since the reactive metal surfaces are essential for the assembly of the described networks, it is inevitable that these networks directly interact with the metal substrate. This means that the adsorbed molecules or molecular structures are electronically coupled to the substrate and the magnetic moments are influenced by the interaction with the underlying crystal field. In order

to reduce the interaction with the underlying surface, one can choose a more inert substrate. A perfect example is the inert substrate Gr/Ir(111) [38,39] which has already been used for the on-surface growth of a EuO(001) films [113], transition metal dichalcogenide layers [114,115] and as adsorption platform for aromatic molecules [116]. One example where Gr/Ir(111) has been used as substrate for the synthesis of a metal–organic network is reported in ref. [112]. There, a dysprosium–supramolecular network was synthesized by depositing the dysprosium (Dy) atoms into an adsorbed molecular film on Gr/Ir(111) at 338 K with a subsequent post-annealing step at 473 K. The result is the Dy–organic network shown in the topograph of Figure 2.7e, which is decoupled from the substrate through the quasi-freestanding Gr sheet.

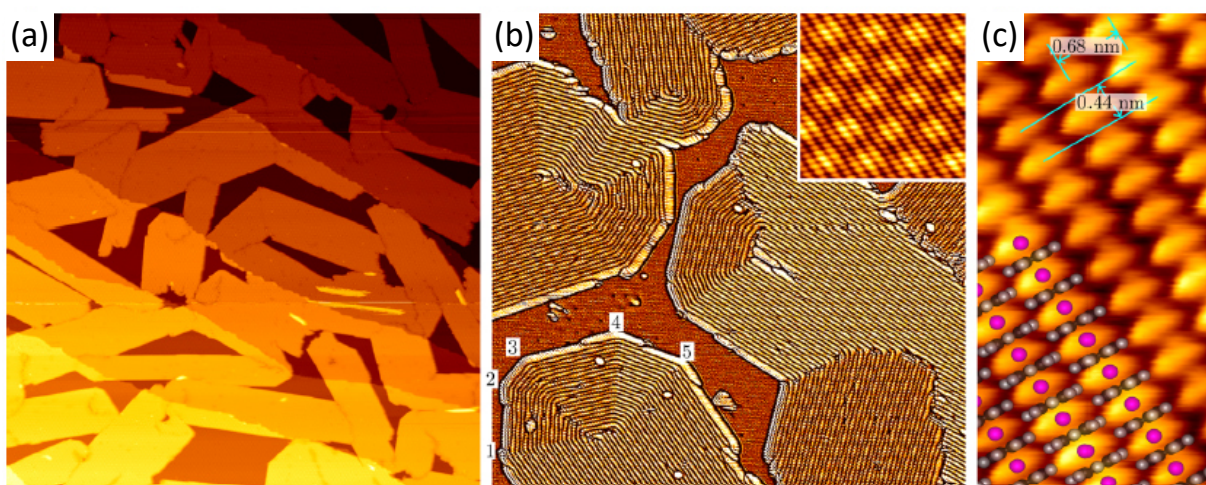


**Figure 2.8:** (a)–(c) STM topographs of a submonolayer film of EuCot nanowires on Gr on Ir(111). (a) ( $3300 \times 3300 \text{ \AA}^2$ ) overview of EuCot islands on Gr/Ir(111). (b) ( $820 \times 820 \text{ \AA}^2$ ), Laplacian-filtered to reveal the 1D chain structure within the islands. Inset: ( $100 \times 100 \text{ \AA}^2$ ), the moiré of Gr with Ir(111) is visible through the wire islands. (c) ( $51 \times 25 \text{ \AA}^2$ ), molecular resolution of interlocking and parallelly aligned EuCot wires within an island, overlaid with a structure model of the wires. Adapted with permission from ref. [32] © 2017 ACS.

**Sandwich-molecular wires:** While in the previous examples of 2D networks and 1D chains the binding relies on covalent coupling and generally needs the catalytic activity of the substrate, the on-surface synthesis of sandwich-molecular wires introduced in ref. [32] requires the inert substrate Gr as an essential part of the synthesis. Therein, elemental Eu is deposited onto Gr/Ir(111) in a background pressure of Cot molecules. The high mobility of Eu and Cot on Gr/Ir(111) leads to the formation of high-quality EuCot islands shown in Figure 2.8a. The islands have a close-to-random orientation with respect to the substrate and are formed by parallelly aligned EuCot wires within the islands, visible in Figure 2.6b. In the inset of Figure 2.6b the moiré of Gr with Ir(111) is visible through the wire film, which interacts weakly with the substrate through van der Waals interactions. As visible in the molecular resolution topograph in Figure 2.8b, neighboring EuCot wires are shifted by half a formula unit and interlock with

each other, as indicated by the overlaid structure model. The wires have an intra-wire periodicity of  $(4.4 \pm 0.2) \text{ \AA}$  and an inter-wire distance of  $(6.7 \pm 0.5) \text{ \AA}$ .

Distinctive to this system is the upright standing orientation of the Cot molecules with respect to the surface, while all other molecular systems described before are adsorbed flat onto the substrate. This is enabled by the ionic binding between the  $\text{Eu}^{2+}$  cations and  $\text{Cot}^{2-}$  anions within the wires. Due to the reactivity of the wire ends, which are terminated by an Eu cation or a Cot anion [117], wire lengths of  $1 \mu\text{m}$  or more are obtained using this method, greatly exceeding the lengths achieved by other methods. It should be mentioned, that although 2D carpets of interlocking EuCot wires are formed, they still maintain their 1D character. The reason is that while the ionic intra-wire binding is very strong, the inter-wire binding is only of van-der-Waals type and therefore negligible [32]. Up to now, EuCot wires are the only sandwich-molecular species synthesized by on-surface synthesis. However, the variety of wires produced in gas phase experiments promises to also allow on-surface synthesis of sandwich-molecular wires using other rare-earth elements.



## CHAPTER 3

---

# Manuscript 1: Single-crystal graphene on Ir(110)

*This chapter wholly consists of the above-named manuscript and its supplement. The manuscript is currently submitted to Physical Review B and available as preprint [118].*

*S.K., F.H., J.F., T.K. and K.B. conducted the syntheses and the STM and LEED experiments. S.K., M.B., R.-M.S., A.J.H. and A.H. conducted the ARPES experiments. N.A., S.T. and V.C. conducted the theoretical calculations. S.K. wrote the manuscript in close collaboration with T.M. and with contributions from N.A.*

*Some of the results shown in this chapter can be found in the doctoral thesis of F. Huttmann.*

# Single-crystal graphene on Ir(110)

Stefan Kraus<sup>\*1</sup>, Felix Huttmann<sup>1</sup>, Jeison Fischer<sup>1</sup>, Timo Knispel<sup>1</sup>, Ken Bischof<sup>1</sup>,  
Alexander Herman<sup>2</sup>, Marco Bianchi<sup>3</sup>, Raluca-Maria Stan<sup>3</sup>, Ann Julie Holt<sup>3</sup>, Vasile  
Caciuc<sup>4</sup>, Shigeru Tsukamoto<sup>4</sup>, Heiko Wende<sup>2</sup>, Philip Hofmann<sup>3</sup>, Nicolae Atodiresei<sup>†4</sup>, and  
Thomas Michely<sup>1</sup>

<sup>1</sup>*II. Physikalisches Institut, Universität zu Köln, Zùlpicher Str. 77, 50937 Köln, Germany*

<sup>2</sup>*Faculty of Physics and Center for Nanointegration Duisburg-Essen (CENIDE), University of  
Duisburg-Essen, Lotharstraße 1, 47048 Duisburg, Germany*

<sup>3</sup>*Department of Physics and Astronomy, Interdisciplinary Nanoscience Center (iNANO), Aarhus  
University, 8000 Aarhus C, Denmark*

<sup>4</sup>*Peter Grünberg Institute and Institute for Advanced Simulation, Forschungszentrum Jùlich,  
Wilhelm-Johnen-StraÙe, 52428 Jùlich, Germany*

## Abstract

A single-crystal sheet of graphene is synthesized on the low-symmetry substrate Ir(110) by thermal decomposition of C<sub>2</sub>H<sub>4</sub> at 1500 K. Using scanning tunneling microscopy, low-energy electron diffraction, angle-resolved photoemission spectroscopy, and *ab initio* density functional theory the structure and electronic properties of the adsorbed graphene sheet and its moiré with the substrate are uncovered. The adsorbed graphene layer forms a wave pattern of nm wave length with a corresponding modulation of its electronic properties. This wave pattern is demonstrated to enable the templated adsorption of aromatic molecules and the uniaxial growth of organometallic wires. Not limited to this, graphene on Ir(110) is also a versatile substrate for 2D-layer growth and makes it possible to grow epitaxial layers on unreconstructed Ir(110).

---

<sup>\*</sup>kraus@ph2.uni-koeln.de (experiment)

<sup>†</sup>n.atodiresei@fz-juelich.de (theory)

# 1 Introduction

*In situ* grown graphene (Gr) is an excellent inert substrate for subsequent growth and van der Waals epitaxy. Examples are the growth of EuO(001) on Gr/Ir(111) [1], or the van der Waals epitaxy of transition metal dichalcogenide layers on bilayer Gr/6H-SiC(0001) [2, 3] or on Gr/Ir(111) [4, 5]. Due to its inertness, Gr is also well suited as substrate when investigating the properties of molecular layers in the absence of strong molecule-substrate hybridization [6, 7]. Similarly, its inertness makes it an ideal substrate for organometallic chemistry with the function to confine the reactant diffusion to two dimensions [8]. In case of Gr forming a moiré with its growth substrate, also templating of molecular layers [9] and of atom or cluster superlattices has been reported [10, 11].

Gr growth also has a substantial effect on its substrate: step edges are moved [12], step bunches and facets are formed [13, 14], or vicinal growth substrates become faceted [15]. A layer of Gr was shown to protect a surface against oxidation, e.g. for Ni(111) [16] or Pt(100) [17], or to prevent the lifting of a reconstruction [18]. Noteworthy, the protection of a metal surface against the formation of a surface reconstruction has not yet been reported.

Up to now mostly symmetry-matching substrates were used for *in situ* growth of Gr, e.g. fcc(111) or hcp(0001) surfaces [19]. Depending on the strength of interaction between Gr and the substrate, either single-domain Gr could be grown, e. g. for Ru(0001) [20] (good orientation due to strong interaction) or multidomain structures result, e.g. for Pt(111) [21] or Cu(111) [22]. For strongly interacting substrates forming a moiré with Gr the corrugation is often substantial due to the spatial variation of binding within the moiré unit cell [23]. Gr/Ir(111) is a unique case, in which the interaction is still weak, but due to proper selection of growth conditions, a well-oriented single-crystal Gr sheet can still be grown [24, 25].

Far less work has been conducted for Gr growth on non-symmetry-matching substrates of fourfold [17] and twofold symmetry [26, 27, 28, 29, 30]. Gr on fcc(110) metal surfaces displays domain formation or multiple orientations. This holds for Ni(110), Cu(110) and Pt(110), irrespective of whether the interaction with the substrate is strong or weak [26, 27, 28]. Up to now, among the metals only the quasihexagonal dense-packed bcc(110) surface of Fe, still only of twofold symmetry, was shown to enable Gr growth with unique orientation [29]. Intense research was triggered by the finding that on the (110) face of the semiconductor Ge growth of large Gr single-crystal layers is possible [31, 30], though at the risk of growth close to substrate melting. Also for the isostructural and isoelectric hexagonal boron nitride (h-BN) monolayers, the growth of single-domain phase-pure layers on only twofold-symmetric substrates was not feasible on metals [32, 33, 34, 35]. The exception is the growth of h-BN on Pt(110), where the adlayer imposes a complex reconstruction change of the substrate [36].

Here, we introduce Gr on the low-symmetry substrate Ir(110), which displays single-domain single-crystal growth when choosing the proper growth conditions. The perfection by which the Gr layer can be fabricated is surprising, when considering that the clean Ir(110) surface is heavily

reconstructed at room temperature. Unreconstructed Ir(110) forms a ridge pattern of (331) and (33 $\bar{1}$ ) nano-facets with a corrugation in the nm range [37]. Under the Gr cover, however, Ir(110) remains unreconstructed.

Using scanning tunneling microscopy (STM) and low-energy electron diffraction (LEED) the moiré of Gr with Ir(110) is determined. Density functional theory (DFT) calculations reveal a strong modulation of binding and charge transfer to Gr associated with the moiré wave pattern along the  $[\bar{1}10]$  direction of the substrate with a periodicity of 10 Å.

The use of this wave pattern for templated adsorption is directly demonstrated here. In DFT calculations naphthalene is used as a paradigm for an aromatic molecule to explore the anisotropic energy landscape of physisorption induced by the wave pattern. Based on these insights, uniaxial alignment of sandwich-molecular wires during organometallic on-surface synthesis [8, 38] is experimentally demonstrated.

Inert single-crystal substrates are rare, but attractive for the growth of quasi-freestanding 2D layers. The application potential of Gr/Ir(110) for 2D-layer growth is exemplified through molecular beam epitaxy of monolayer NbS<sub>2</sub>. As a last example of versatility, we show that through Gr intercalation thermodynamically stable epitaxial layers can be grown on *unreconstructed* Ir(110).

## 2 Methods

Gr on Ir(110) was synthesized with identical results on two different crystals in the ultrahigh vacuum systems ATHENE (base pressure below  $1 \cdot 10^{-10}$  mbar, STM imaging at 300 K) and M-STM (base pressure in preparation chamber  $3 \cdot 10^{-10}$  mbar, in STM chamber below  $1 \cdot 10^{-11}$  mbar, STM imaging temperature 1.7 K). Gases are delivered through a gas dosing tube giving rise to a pressure enhancement by a factor of 80 compared to the pressure measured through a distant ion gauge specified here. Sample cleaning was accomplished by exposure to  $1 \cdot 10^{-7}$  mbar oxygen at 1200 K when needed, cycles of noble gas sputtering (Ar, Xe), and brief annealing to 1500 K. Closed layers of Gr on Ir(110) were grown by exposure to  $2 \cdot 10^{-7}$  mbar ethylene for 210 s at 1500 K for the single-domain Gr phase. For the two-domain Gr phase briefly mentioned in the manuscript and discussed in the SI, the ethylene exposure was at 1300 K. EuCot sandwich-molecular wires were grown at a sample temperature of 300 K by sublimation of Eu from a Knudsen cell with a deposition rate of  $1.1 \cdot 10^{17} \frac{\text{atoms}}{\text{m}^2\text{s}}$  in a background pressure of  $1 \cdot 10^{-8}$  mbar Cot [8]. The software *WSxM*[39] was used for STM data processing.

To ensure Gr quality and for structural characterization LEED was used in an energy range of 30 – 150 eV. The LEED patterns shown are contrast-inverted for better visibility.

Angle-resolved photoemission spectroscopy (ARPES) measurements have been conducted at the SGM-3 beamline at the synchrotron ASTRID2 in Aarhus, Denmark. The samples were grown in situ in an ultrahigh vacuum chamber (base pressure  $3 \cdot 10^{-10}$  mbar) connected to the beamline, and using the recipe described above. Sample cleaning has been accomplished by noble gas sputtering using Ne. The samples have been checked in situ using the Aarhus STM mounted at



the endstation to check for consistency with the homelab results.

Our *ab initio* density functional theory (DFT) [40, 41] were carried out using the projector augmented wave method (PAW) [42] as implemented in the VASP code [43, 44, 45]. The van der Waals interactions present in the Gr/Ir(110) system were taken into account by employing the non-local correlation energy functional vdW-DF2 [46] together with a re-optimized [47] Becke (B86b) exchange energy functional [48]. Gr on Ir(110) was modeled by a slab containing three Ir layers and a vacuum region of  $\approx 21 \text{ \AA}$  amounting to 350 C and 264 Ir atoms, respectively. The ground-state geometry and its electronic structure of this system have been obtained for a kinetic energy cut-off of 500 eV and a threshold value of the calculated Hellmann-Feynman forces of  $\approx 0.005 \text{ eV/\AA}$ . Furthermore, for the structural relaxation the Brillouin zone integrations were performed using the  $\Gamma$  point while the density of states (DOS) was obtained with the help of a  $2 \times 2$   $k$  mesh.

### 3 Results and discussion

**Superstructure – experiment:** Gr is grown on carefully cleaned Ir(110) through exposure to ethylene at 1500 K. After cooldown to 300 K, STM finds large flat terraces, separated by plateaus with flat top levels and elongated along the  $[1\bar{1}0]$  direction. The profile in Figure 1a shows a plateau height of several nm. The plateau top level and the surrounding base level are flat. There is no indication for a ridge pattern of  $(331)$  and  $(3\bar{3}\bar{1})$  nano-facets with a corrugation in the nm range [37], as it is observed after cooldown in the absence of a Gr cover [compare Figure S1 of the Supporting Information (SI)]. A zoom into a flat terrace area makes a twofold symmetric moiré visible, as shown in Figure 1b. We define the rectangular moiré cell as well as the moiré vectors  $\vec{m}_1$  and  $\vec{m}_2$  as indicated in Figure 1b. The moiré leads to a well visible wave pattern with wave vector in the direction of  $\vec{m}_2$ , i.e. along the  $[1\bar{1}0]$  direction. The wave crests and troughs are consequently oriented along the  $[001]$  direction. The additional, larger wavelength periodicity with wave vector in the direction of  $\vec{m}_1$  is less pronounced.

Both periodicities can be recognized in the profile of Figure 1b. With the profiles taken on the wave pattern crests and under the tunneling conditions chosen, the corrugation is  $0.08 \text{ \AA}$  for the long wavelength periodicity with wave vector along  $\vec{m}_1$  (cyan line in Figure 1b), while it is  $0.17 \text{ \AA}$  for the wave pattern with wave vector along  $\vec{m}_2$  (blue line in Figure 1b). It can be seen in Figure 1b that on some wave crests an additional corrugation with a wavelength of about  $\frac{1}{4}$  of the moiré periodicity is present. By visually analyzing this extra corrugation along the wave crests highlighted by black arrows in Figure 1b it is obvious that (i) this extra corrugation varies along the wave crests and that (ii) neighboring wave crests differ in the amplitude of this corrugation, being almost absent or quite pronounced. While (i) suggests the presence of small tilts in the orientation of the two lattices, (ii) indicates that the moiré is not commensurate along  $\vec{m}_2$ . The large wavelength periodicity with wave vector in the direction of  $\vec{m}_1$  is also not perfectly uniform and affected by the presence of defects. This is apparent for the vertical crests at the right of

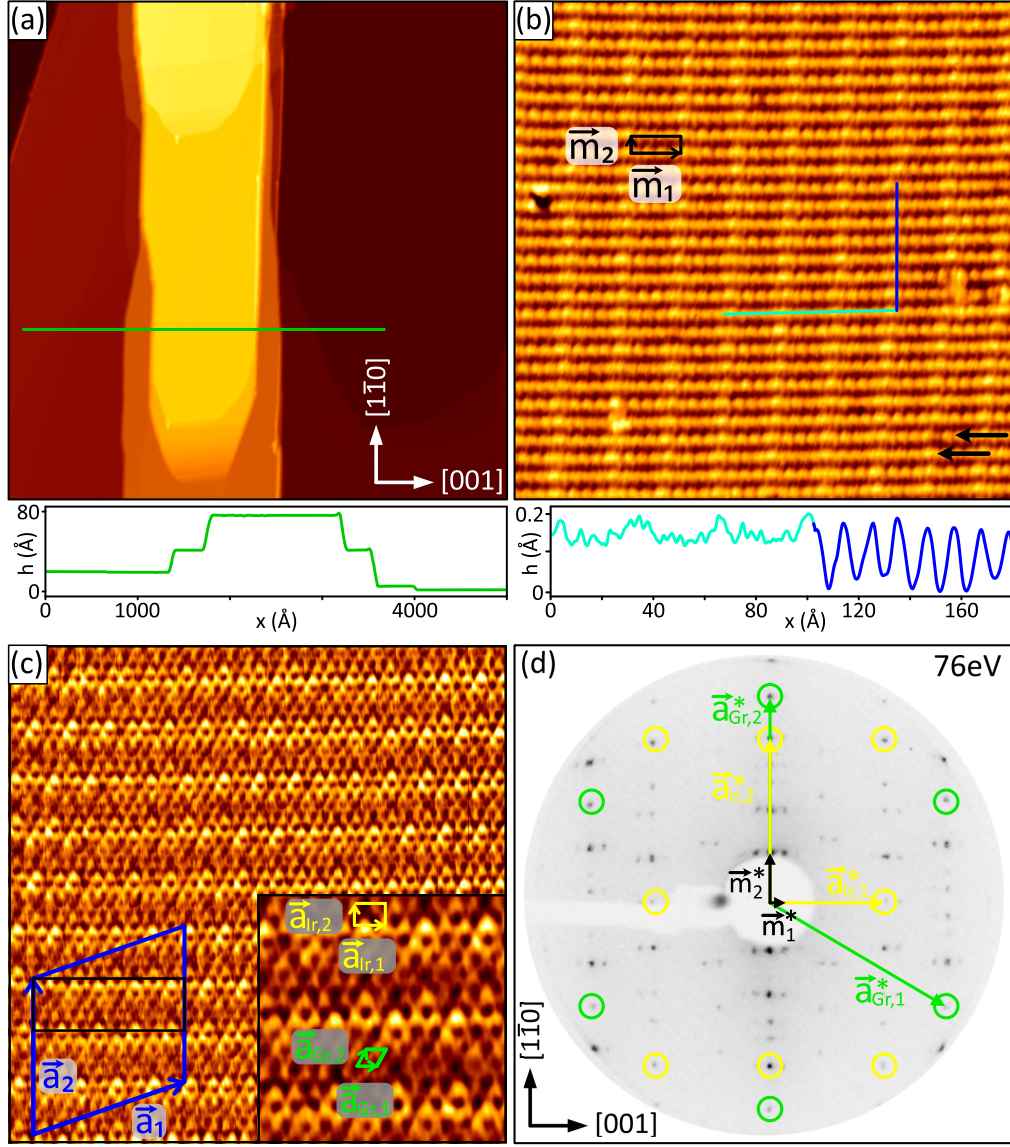


Figure 1: (a) Large scale STM topograph ( $7000 \times 7000 \text{ \AA}^2$ ) of Gr/Ir(110) grown at  $T = 1500 \text{ K}$ . The [001] and  $[1\bar{1}0]$  directions specified in the lower right corner are valid also for (b), (c) and (d). STM height profile along the green line is shown below the topograph. (b) STM topograph ( $300 \times 300 \text{ \AA}^2$ ) of flat terrace area. Black rectangle indicates the moiré unit cell. Black arrows highlight varying appearance of wave crests. STM height profile along path of cyan and blue line is shown below topograph. (c) Atomic resolution STM topograph ( $100 \times 100 \text{ \AA}^2$ ) with commensurate superstructure cell and primitive translations  $\vec{a}_1$  and  $\vec{a}_2$  indicated in blue. Moiré unit cell is shown in black. Inset: magnified view ( $30 \times 30 \text{ \AA}^2$ ) with centers of Gr rings visible as dark depressions. Gr and Ir(110) unit cells and primitive translations are indicated. (d) 76 eV LEED pattern of Gr/Ir(110). First order Ir and Gr reflections are encircled yellow and green, respectively. Reciprocal moiré, Gr and Ir primitive translations are indicated. See text. STM imaging temperatures are 300 K in (a) and (b), and 1.7 K in (c). Tunneling parameters are (a)  $U_{\text{bias}} = -1.33 \text{ V}$  and  $I_t = 0.8 \text{ nA}$ , (b)  $U_{\text{bias}} = -1.33 \text{ V}$  and  $I_t = 1.1 \text{ nA}$ , (c)  $U_{\text{bias}} = -0.05 \text{ V}$  and  $I_t = 20.0 \text{ nA}$ .

Figure 1b, where the crests slightly change orientation due to the defect in the middle right of the topograph. Again, this indicates the presence of small tilts and shears of the Gr lattice.

We note that depending on the tunneling parameters and tip condition the corrugation may differ substantially from the apparent corrugation found for the topograph of Figure 1b. Corrugations of up to  $0.4 \text{ \AA}$  for the long wavelength periodicity with wave vector along  $\vec{m}_1$  and up to  $0.8 \text{ \AA}$  for the wave pattern with wave vector along  $\vec{m}_2$  are found. The corrugation along  $\vec{m}_1$  is generally found to be smaller than the one along  $\vec{m}_2$ . Elastic effects of tip-surface interaction at very low tunneling resistances, and at somewhat larger resistances a distance dependence of the corrugation on the local density of states are most likely the origin of this variation.

In the atomically resolved STM topograph of Figure 1c, the centers of the Gr honeycombs are well visible as dark depressions. The Gr zigzag rows are close to perfectly aligned with the  $[001]$  direction. The moiré periodicity  $m_2$  along the  $[1\bar{1}0]$  direction is well visible and caused by the superposition of the  $2.715 \text{ \AA}$  periodicity of Ir(110) and the zigzag row spacing of Gr. Application of the moiré construction for the case of aligned periodicities as outlined in [49] results in  $m_2 = (9.94 \pm 0.15) \text{ \AA}$  and a zigzag row spacing of  $(2.133 \pm 0.007) \text{ \AA}$ . This row spacing implies a Gr lattice parameter of  $a_{\text{Gr}} = (2.463 \pm 0.008) \text{ \AA}$ . The Gr lattice parameter agrees within the limits of error with the in-plane lattice parameter of relaxed graphite  $a_{\text{graphite}} = 2.4612 \text{ \AA}$  [50]. Gr on Ir(110) appears to be unstrained. The determination of the periodicity  $m_1$  is more difficult, since it is not clearly visible in the atomically resolved topograph of Figure 1c and similar ones, presumably due to the low tunneling resistance conditions needed to obtain atomic resolution. However, the observation of the ratio of  $m_1$  to  $m_2$  is possible in STM topographs without atomic resolution and allows one to estimate  $m_1 = (33 \pm 2) \text{ \AA}$ . Finally, the Fourier transform of Figure 1c displays spots corresponding to the Ir(110) and Gr lattices simultaneously (compare Figure S2 in the SI). Its analysis confirms the absence of significant strain in Gr and the magnitude of the Gr primitive translations  $\vec{a}_{\text{Gr},1}$  and  $\vec{a}_{\text{Gr},2}$  to deviate less than 0.5 %.

The LEED pattern of Gr/Ir(110) shown in Figure 1d can be decomposed into reflections of *unreconstructed* Ir(110) encircled yellow and first order reflections of a single Gr domain encircled green. All other reflections are linear combinations of the Ir(110) and Gr reciprocal lattice vectors. The moiré periodicity along  $[001]$  corresponds to the difference  $\vec{m}_1^* = 2 \cdot \vec{a}_{\text{Gr},1}^* + \vec{a}_{\text{Gr},2}^* - 3 \cdot \vec{a}_{\text{Ir},1}^*$  and along  $[1\bar{1}0]$  to  $\vec{m}_2^* = \vec{a}_{\text{Gr},2}^* - \vec{a}_{\text{Ir},2}^*$ . The vectors  $\vec{m}_i^*$ ,  $\vec{a}_{\text{Gr},i}^*$  and  $\vec{a}_{\text{Ir},i}^*$  indicated in Figure 1d are the reciprocal vectors to  $\vec{m}_i$ ,  $\vec{a}_{\text{Gr},i}$  and  $\vec{a}_{\text{Ir},i}$  (compare Figures 1b and 1c). The moiré periodicities derived from LEED are  $m_1 = (31 \pm 2) \text{ \AA}$  and  $m_2 = (9.8 \pm 0.3) \text{ \AA}$ . They agree within the limits of error well with our STM analysis. The same holds for the real space Gr lattice parameter  $a_{\text{Gr}} = (2.49 \pm 0.04) \text{ \AA}$  derived from the LEED pattern.

On a side note, we also observed the formation of a two-domain Gr phase, but at a lower growth temperature of 1300 K. Compare Figure S3 of the SI for details.

Summarizing our analysis, STM and LEED suggest an incommensurate moiré of unstrained or marginally strained Gr with Ir(110). In fact, assuming unstrained Gr with its graphite lattice parameter  $a_{\text{graphite}} = 2.4612 \text{ \AA}$  and the zigzag rows parallel to the  $[001]$  direction, as observed in

STM and LEED, would result in  $m_1 = 32.02 \text{ \AA}$  and  $m_2 = 9.91 \text{ \AA}$ . These numbers agree very well with our STM and LEED analysis. In order to be able to conduct DFT calculations, we need to approximate the experimental situation through a commensurate superstructure cell. The smallest commensurate unit cell with negligible Gr strain is indicated as blue rhomboid in Figure 1c and in the ball model of Figure 2a. The unit cell is spanned by the primitive translations  $\vec{a}_1$  and  $\vec{a}_2$  of lengths  $a_1 = 32.58 \text{ \AA}$  and  $a_2 = 29.87 \text{ \AA}$ , corresponding to 12.5 Gr units on 8 Ir units in  $[001]$  direction and 14 Gr rows on 11 Ir units along the  $[1\bar{1}0]$  direction. The triple length of  $\vec{a}_2$  compared to  $\vec{m}_2$  takes into account, that along the  $[1\bar{1}0]$  direction approximate commensurability is only achieved after three moiré periods  $m_2$ . In matrix notation the commensurate superstructure can be expressed as  $\begin{pmatrix} 8 & 4 \\ 0 & 11 \end{pmatrix}$  with respect to Ir(110) and  $\begin{pmatrix} 10 & 5 \\ -7 & 14 \end{pmatrix}$  with respect to Gr (compared Figure S4 in the SI). The Gr lattice parameters  $a_{\text{Gr},1} = 2.457 \text{ \AA}$  and  $a_{\text{Gr},2} = 2.463 \text{ \AA}$  in the commensurate superstructure unit cell are close to the in-plane lattice parameters of relaxed graphite  $a_{\text{graphite}} = 2.4612 \text{ \AA}$  [50] and to our measurements. They are only slightly compressed by 0.17 % or stretched by 0.07 % with respect  $a_{\text{graphite}}$ .

**Superstructure – *ab initio* calculations:** For our DFT calculations we used a slab consisting of 3 layers of Ir, the Gr layer, and 21  $\text{\AA}$  of vacuum in  $z$  direction. The DFT supercell shown in Figure 2a is based on the superstructure unit cell defined by  $\vec{a}_1$  and  $\vec{a}_2$  (compare Figure 1c).

The adsorption energy per C atom amounts to  $E_{\text{ads}} = -140.2 \text{ meV}$ , about twice the value obtained for Gr/Ir(111) with the same exchange-correlation functional [51]. Side views of the supercell are presented as Figure 2b with the direction of view along  $[001]$ , normal to the dense-packed Ir rows and along a Gr zigzag direction, and Figure 2c with the direction of view along  $[1\bar{1}0]$ , i.e. along the dense-packed Ir rows and a Gr armchair direction. The view along  $[001]$  displays a clear wave pattern of the Gr layer with wave vector along the direction of  $\vec{a}_2$  or the  $[1\bar{1}0]$  direction. The wave crests are labeled  $c_1, c_2, c_3$  and the wave troughs are labeled  $t_1, t_2, t_3$ . Close inspection reveals that the three wave crests and the three wave troughs are not equivalent in symmetry: while a zigzag row is either precisely aligned to an Ir atom row along  $[001]$  for  $t_1$  or between two Ir atom rows for  $c_2$ , this alignment is only approximate for the other two crests and troughs. Consequently, the corrugation of the wave pattern is non-uniform ranging from 0.32  $\text{\AA}$  to 0.46  $\text{\AA}$ . The view along  $[1\bar{1}0]$  displays no clear corrugation pattern of the Gr layer.

These DFT results are in good agreement with the experimental observation of a pronounced wave pattern with crests along  $[001]$  with the same periodicity as in DFT. The experimental corrugation of this wave pattern (blue in the height profile of Figure 1b) is generally larger than the corrugation in the direction normal to it (cyan in the height profile of Figure 1b), again in qualitative agreement with our DFT calculation. The DFT calculated corrugation of up to 0.46  $\text{\AA}$  is well within the range of experimentally measured corrugations of 0.15  $\text{\AA}$  to 0.8  $\text{\AA}$  along the  $[1\bar{1}0]$  direction.

**Binding – *ab initio* calculations:** Already the side views of Figure 2b and 2c suggest that the binding configurations of the C atoms to the Ir(110) substrate vary substantially. On a global level this is evident by noting that the C-Ir bond length, i.e. the distance between a C atom

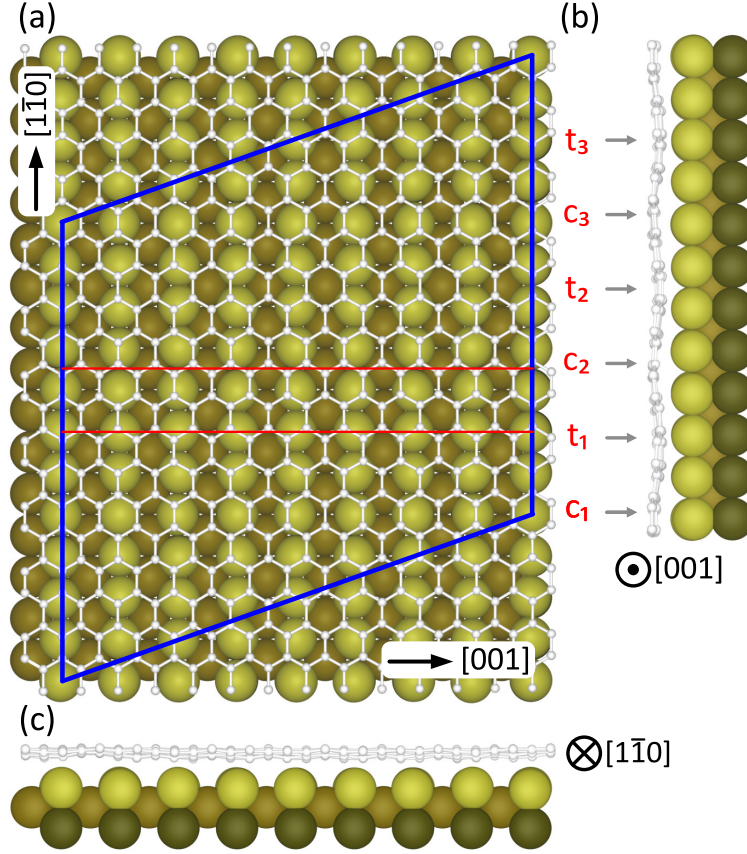


Figure 2: Ball model representations of relaxed DFT geometries for Gr/Ir(110). Ir atoms: light (top layer) to dark (bottom layer) brown spheres. C atoms: small light grey dots connected by light grey lines. (a) Top view with DFT supercell indicated by blue rhomboid. The  $[1\bar{1}0]$  and  $[001]$  directions are also shown. (b) Side view with  $[001]$  direction out of drawing plane as indicated. A pattern of crests  $c_1$ - $c_3$  and troughs  $t_1$ - $t_3$  in the Gr layer is visible along  $[1\bar{1}0]$  with their positions highlighted by arrows. (c) Side view with  $[1\bar{1}0]$  direction into drawing plane as indicated.

of Gr and the nearest Ir substrate atom, varies between 2.11 Å and 3.10 Å, i.e. from a strong chemisorption to a weak chemisorption bond length. This large variation is primarily caused by the large corrugation of the Ir substrate with its hill and valley structure. A manifestation of the binding heterogeneity is the Gr wave pattern as apparent in the side view of Figure 2b. To obtain insight into the underlying physics and associated wavelike variation of Gr's properties, charge-density difference plots along the red lines in Figure 2a in the trough  $t_1$  and the crest  $c_2$  are compared in Figures 3a and 3b, respectively. In the cut through the trough  $t_1$  shown in Figure 3a charge accumulation (red) between the Ir and the C atoms signals the formation of chemical bonds. These chemical bonds to the substrate cause the C atoms of Gr to acquire partial  $sp^3$  character. Moreover, charge accumulates in the  $\pi$  system above the C atom plane. In the cut through the crest  $c_2$  shown in Figure 3b essentially no charge accumulation between the C atoms and the distant Ir atoms is present – chemical bonds are weak. Therefore, contrary to the troughs, in the crests little charge is injected into the  $\pi$  system above the C atoms. Besides



a variation in local work function, the variation of the local charge transfer into the Gr  $\pi$  system implies also a variation of the van der Waals interactions of the Gr layer with physisorbed species. As outlined in [52], the strength of the van der Waals interactions is larger where the charge cloud of the  $\pi$  system spreads out into the vacuum further away from the C nuclei. The modulation of the binding character and electronic properties with the wave pattern is also apparent in Figure 3c, which shows the charge-density difference average over the entire superstructure unit cell and projected onto a plane along the  $[1\bar{1}0]$  direction. There, the variation of binding character and charge donation to the Gr  $\pi$  system is well visible through the variation of strong charge accumulation above and below the C atom plane.

The charge density difference plots normal to the wave pattern along the Gr armchair direction ( $[1\bar{1}0]$  direction of the Ir substrate) also display a variation of electronic properties. However, on all cuts the dominant wave pattern is superimposed, causing a considerable heterogeneity along the direction of cut. Compare also Figure S5 of the SI.

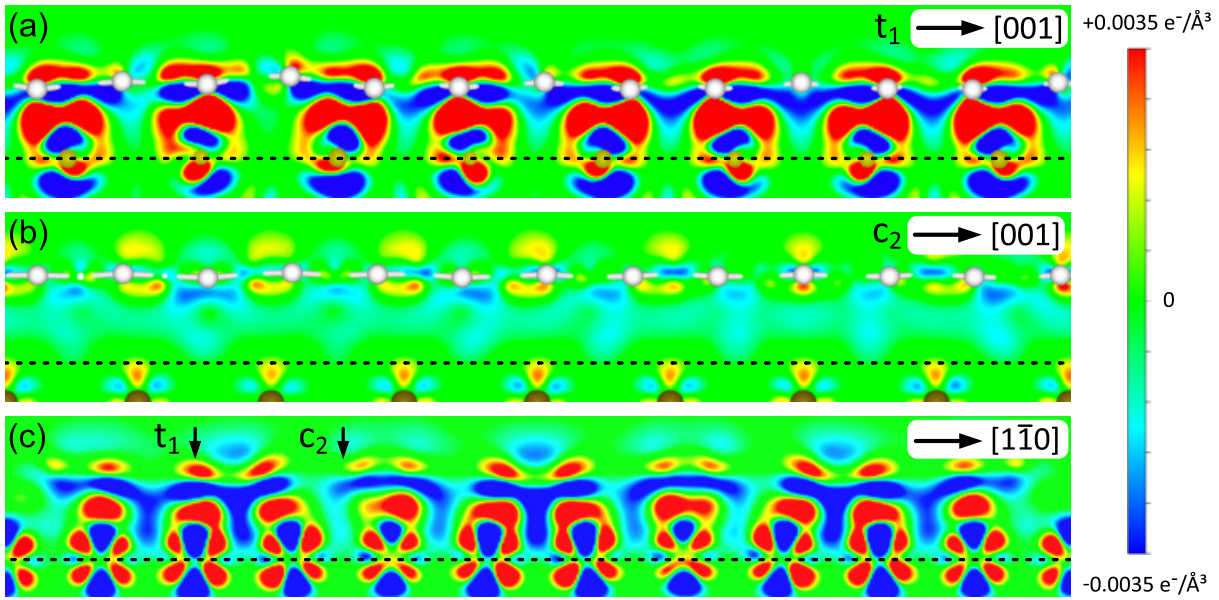


Figure 3: (a), (b) Charge-density difference plots in the (a) trough and (b) crest locations indicated in Figure 2b as  $t_1$  and  $c_2$  and in Figure 2a by horizontal red lines. (c) Charge-density difference average over the entire superstructure unit cell and projected onto a plane along the  $[1\bar{1}0]$  direction corresponding to the view of Figure 2b. The positions of the cuts along  $t_1$  and  $c_2$  are indicated by arrows. The black dotted lines indicate the position of the top level Ir atoms. See text. Color scale for all plots ranges from charge accumulation in red ( $+0.0035 \text{ electrons}/\text{\AA}^3$ ) to depletion in blue ( $-0.0035 \text{ electrons}/\text{\AA}^3$ ).

**Electronic structure of Gr on Ir(110):** Figure 4a compares the characteristic V-shaped freestanding Gr density of states (red line) with the Gr partial DOS when adsorbed to Ir(110) (black line). The V-shape of the freestanding Gr DOS signals electronically intact Gr with a Dirac cone formed by the Gr  $\pi$  and  $\pi^*$  bands that touch at the Dirac point, where the DOS vanishes. This feature is characteristic for freestanding or physisorbed Gr layers and corresponds to an  $sp^2$  hybridization of its electronic states. The absence of this feature and the substantial partial

Gr DOS of Gr/Ir(110) in the entire energy range of a few eV around the Fermi energy signifies considerable modification of the Gr electronic structure when adsorbed to Ir(110), similar e.g. to the case of Gr on Ni(111) [53]. The diversity of C-Ir bonds noticed already in Figure 2 gives rise to a diversity of C-Ir hybridizations, which together with the variation of the local charge transfer visible in Figure 3, gives rise to the smeared out partial DOS of Gr. The blue curve in Figure 4a represents the partial Gr DOS projected onto the carbon  $p_z$  atomic-like orbitals that originally form the Gr  $\pi$  system. The difference between this projection and the entire partial Gr DOS is small, but indicates a non-negligible  $sp^3$  character of bonding due to the local chemical interactions between the corrugated Gr and Ir(110) as depicted in Figure 3.

The detailed electronic structure of the adsorption system has been determined by ARPES [54]. Figure 4b shows the photoemission intensity as a function of binding energy and  $k_{\parallel}$  in the  $\Gamma - K$  direction of the Gr Brillouin zone. The ARPES data show no sign of a Dirac cone nor any feature that could be related to the Gr  $\pi$  band, fully consistent with the DFT calculations. See Figure S6 in the SI and the related discussion for a more detailed analysis.

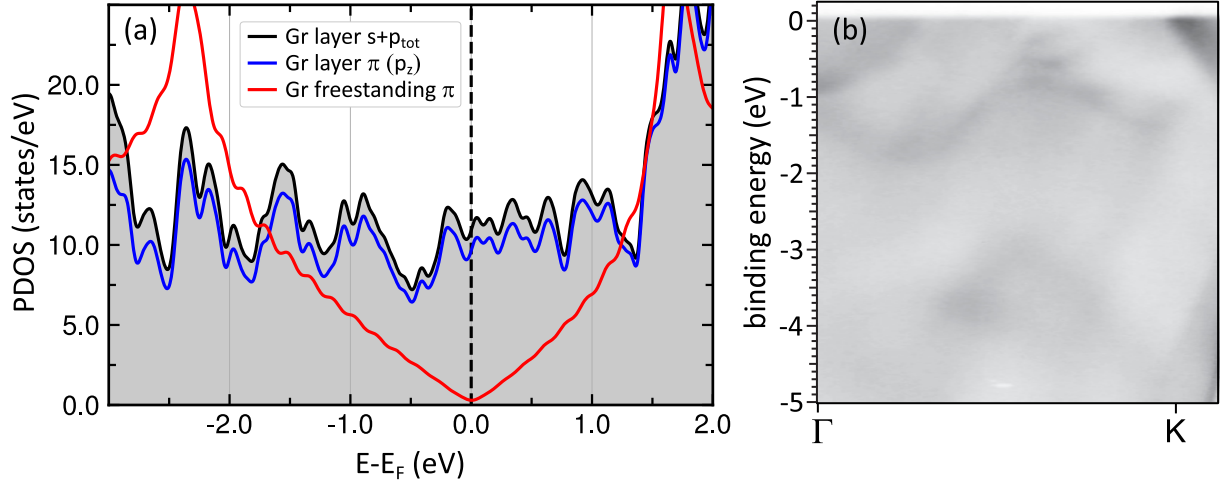


Figure 4: (a) Red line: Density of states (DOS) of freestanding Gr. Black line and gray-shaded area: Gr partial DOS when on Ir(110). Blue line: Gr partial DOS projected on the Gr  $\pi$  system consisting of  $p_z$  atomic-like orbitals. See text. (b) Angle-resolved photo emission spectrum along  $\Gamma - K$ , recorded at a photon energy of 100 eV and a temperature of  $T = 35$  K. There is no Dirac cone at the K point and there are no features that could be related to the Gr  $\pi$  bands in agreement with the DFT calculations.

**A naphthalene molecule as sensor for the energy landscape of adsorption on Gr/Ir(110):** To obtain insight to whether the modulation associated to the wave pattern of Gr/Ir(110) can be used to template molecular adsorption, a naphthalene molecule was employed as sensor in DFT calculations of still feasible computational effort. Using different starting configurations for  $C_{10}H_8$  adsorbed to the crest  $c_2$  and trough  $t_1$  of Gr/Ir(110) (compare Figure 2) several local minima of adsorption energy were identified.

Figure 5a displays the minimum energy adsorption geometry, where the molecule resides in the trough, as also obvious from the side view cuts of the charge-density difference plots of Figure 5b

and 5c. Adsorption takes place with the long molecular axis along the trough. No energy minimum could be found for the molecule in different orientations, e. g. with the long axis normal to the trough. The adsorption energy  $E_{\text{ads}}$  is -947 meV, lower by 168 meV compared to the best-bound configuration on a crest. The minimum energy adsorption site in the trough corresponds to the locations where the charge accumulation above Gr is highest (compare Figure 3). Thus these results are in qualitative agreement with experiments and DFT calculations for naphthalene adsorbed to Gr/Ir(111) [52], where the strength of the van der Waals interactions was found to increase with the charge donated to Gr (n-doping). For the minimum energy configuration shown in Figure 5, the average naphthalene-graphene distance is 3.27 Å, a distance typical for a physisorbed molecule, while for all other local adsorption energy minima the distances are larger. Compare Figure S7 and Table S1 of the SI for additional calculations and more details.

Our calculations make plain that despite Gr’s strong interaction with the Ir(110) substrate, it is still an inert substrate for molecular adsorption, acting as a spacer effectively separating the metal from the molecule. The situation is not unexpected, when considering that also other ‘strongly’ interacting Gr layers act still as inert spacer between molecules and the underlying metal. To give an example, the peak desorption temperature of benzene from ‘strongly’ interacting Gr on Ru(0001) [19] is within the limits of error identical to the one from graphite [55].

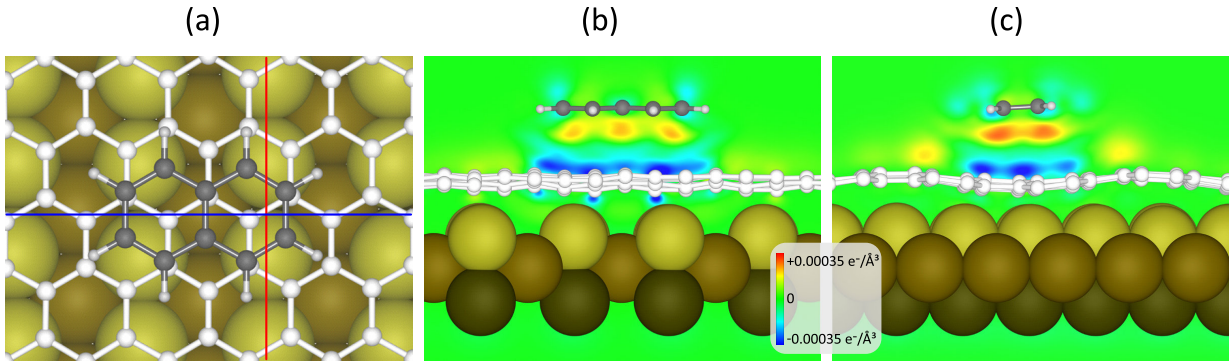


Figure 5: (a) Top view ball model for minimum energy adsorption geometry of C<sub>10</sub>H<sub>8</sub> in trough  $t_1$  on Gr/Ir(110) (compare Figure 2). (b) Charge-density difference plot along blue line in (a) of combined system compared to sum of isolated C<sub>10</sub>H<sub>8</sub> molecule and Gr/Ir(110). (c) Same as (b), but along red line in (a). Color scale in (b) and (c) is the same as in Figure 3, but used for one order of magnitude smaller charge density-differences ranging from +0.00035 electrons/Å<sup>3</sup> for charge accumulation in red to -0.00035 electrons/Å<sup>3</sup> for charge depletion in blue.

**Use of Gr/Ir(110) as nanotemplate for alignment in on-surface synthesis:** Our theoretical calculations for C<sub>10</sub>H<sub>8</sub> adsorbed to Gr/Ir(110) imply that this substrate displays an anisotropic physisorption energy landscape and is thereby able to template adsorption and to impose uniaxial alignment. Here, we use the example of on-surface synthesis of sandwich-molecular wires to demonstrate these properties. A sandwich-molecular wire is an organometallic compound consisting of an alternation of metal atoms with ring-shaped aromatic molecules [56, 57]. When Eu atoms and cyclooctatetraene (Cot, C<sub>8</sub>H<sub>8</sub>) molecules (eight-membered carbon rings) are combined in room temperature on-surface synthesis on Gr/Ir(111), Eu is evaporated



onto the substrate in a background pressure of Cot, of which the excess re-evaporates at 300 K [8]. Because of van der Waals interaction between the wires, they interlock and form monolayer high, *randomly* oriented islands of parallel wires resulting in diffraction rings rather than spots in LEED [8, 38]. The lack of island orientation was found not to depend on coverage.

As obvious from Figure 6, successful on-surface synthesis of EuCot is also possible on Gr/Ir(110). This observation implies directly the mobility of reaction intermediates to wire ends and the re-evaporation of the Cot excess at room temperature. This underpins the inertness of the Gr/Ir(110) substrate and the physisorbed state of the unreacted molecules. In contrast to the random orientation of the wire carpet islands on Gr/Ir(111), growth on the anisotropic Gr/Ir(110) substrate gives rise to thin and long wire islands all oriented along the [001] direction as visible in Figure 6a. For larger coverages a well-oriented, coalesced monolayer results, as shown in Figure 6b. Only step edges along  $[1\bar{1}0]$  may cause a deviation from the global [001] alignment in small patches, e.g. in the lower right of Figure 6b. Figure 6c displays the corresponding LEED pattern. It exhibits clear diffraction spots of the wire lattice encircled in dotted-blue. The rhomboidal reciprocal unit cell is indicated in green. Because LEED is a spatially averaging technique, the diffraction pattern implies a global alignment of the wires along the [001] direction. Highlighted by the two black arrows in Figure 6c,  $3 \times 1$  superstructure reflections can be identified in the direction normal to the wires, of which the origin is explained below. In the molecular resolution STM topograph of Figure 6d the parallel wires are shown together with a ball model overlay of the molecular structure and the wire lattice unit cell. Close inspection of the STM topograph reveals a beating of the wire height (brightness) along  $[1\bar{1}0]$ , where about every third wire appears to be higher. It is this height variation of the wires that gives rise to the  $3 \times 1$  superstructure spots in LEED, which is thus a global feature of wire ordering. The intensity variation can be explained by the mismatch of the interwire distance and the moiré periodicity of the underlying substrate in this direction. Based on the crest spacing of  $\approx 10 \text{ \AA}$  and the wire spacing of  $\approx 6.8 \text{ \AA}$  measured on Gr/Ir(111) [8], three wires fit on two moiré periodicities along  $\vec{m}_2$ . Apparently two thirds of the wires are located close to the trough positions, while one third is located close to a crest position. Furthermore, faint vertical lines of brighter contrast spaced by  $m_1$  reflect the bending of the horizontally aligned wires over the moiré periodicity along [001].

Based on the successful on-surface synthesis using the same parameters as for EuCot wire growth on Gr/Ir(111) [8, 38], it is evident that also on Gr/Ir(110) the wires are bound through van der Waals interactions to the substrate. The upright standing aromatic Cot-dianions are in contact with Gr only through their peripheral H-atoms. Bound to the cyclic carbon ring, they are unable to interact chemically with Gr. For a single wire, our DFT calculation shown above suggests adsorption to a trough location, where the van der Waals interaction is stronger than on the crests. However, due to substantial interwire van der Waals interaction, single wires are not realized even for smaller coverages. Nevertheless, consistent with a preferential binding to the troughs, two thirds of the wires are adsorbed close to the troughs rather than to the crests, as noticed above when discussing the  $3 \times 1$  wire superstructure.

Elastic energy considerations are also in favor of adsorption along the wave pattern, i.e. the [001] direction, rather than vertically to the wave pattern. In order to maximize the binding to the substrate, the wires need to adhere conformal to the Gr-sheet in an optimum distance defined by Pauli repulsion and van der Waals interactions. For a 1D-wire oriented perpendicular to the wave pattern along the  $[1\bar{1}0]$  direction this would imply substantially more bending with shorter periodicity to conform to the wave pattern than for a wire oriented along the [001] direction with substantially less corrugation and larger periodicity  $m_1$ . Thus, the elastic energy penalty for wire orientation along the [001] direction is lower, also favoring its orientation along this direction.

It is remarkable that physisorbed species – the 1D sandwich-molecular wires – are perfectly oriented through the Gr/Ir(110) template at temperatures as high as room temperature. However, even if the charge modulation and elastic energy effects are presumably small per formula unit – possibly as low as 10 meV – the wires are composed of hundreds of formula units. Thereby, energy differences for wires adsorbed in different orientations and at different adsorption sites become large.

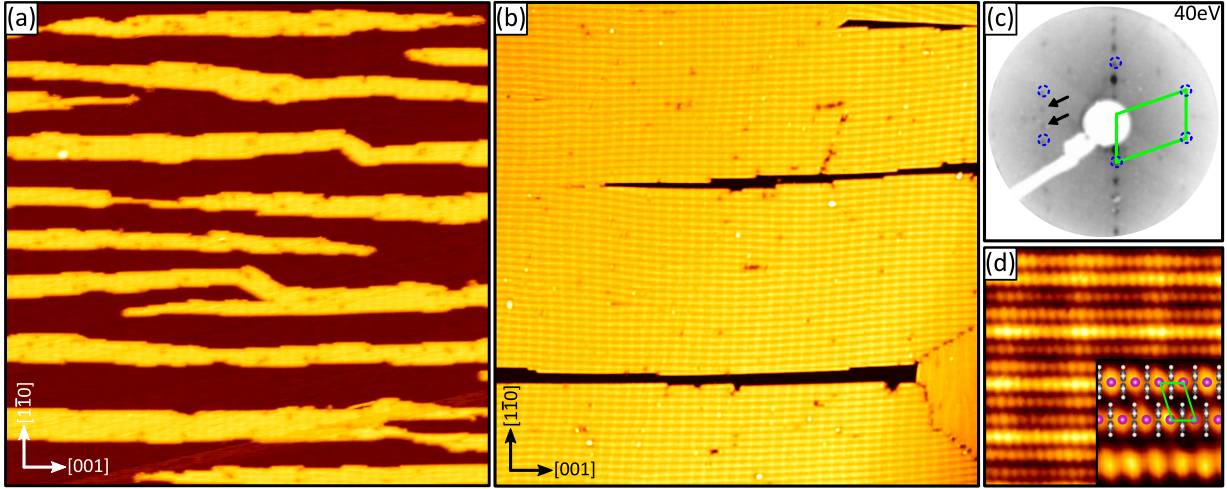


Figure 6: (a), (b) STM topographs ( $1500 \times 1500 \text{ \AA}^2$ ) of (a) elongated EuCot wire carpet islands and (b) of a full layer on Gr/Ir(110) oriented along the [001] direction. (c) 40 eV LEED pattern of the same sample as in (b). The unit cell of the EuCot wire carpet is indicated by green lines, with the corresponding first order reflections encircled dashed-blue.  $3 \times 1$  superstructure reflections are highlighted by black arrows. Note that different LEED set-ups cause different sizes of LEED patterns. (d) STM topograph ( $100 \times 100 \text{ \AA}^2$ ) of EuCot/Gr/Ir(110) with a  $3 \times 1$  intensity variation along the  $[1\bar{1}0]$  direction resulting from the lattice mismatch of the substrate moiré and the wire carpet. Inset: molecular resolution STM topograph ( $25 \times 25 \text{ \AA}^2$ ) overlayed with a wire model. Magenta dots: Eu atoms. White and black dots: H atoms and C atoms of Cot. The wire carpet unit cell is indicated as green rhomboid. STM topographs taken at 300 K. Tunneling parameters are (a)  $U_{\text{bias}} = -2.0 \text{ V}$  and  $I_t = 0.03 \text{ nA}$ , (b)  $U_{\text{bias}} = -1.74 \text{ V}$  and  $I_t = 0.08 \text{ nA}$ , and (d)  $U_{\text{bias}} = -1.82 \text{ V}$  and  $I_t = 0.35 \text{ nA}$ .

**Additional uses of Gr/Ir(110) as substrate:** Figure 7a displays monolayer NbS<sub>2</sub> islands of excellent structural quality grown on Gr/Ir(110) through MBE following the method described in [58]. Besides Gr/SiC(0001) [2] and Gr/Ir(111) [4], Gr/Ir(110) is thus a third inert Gr system

suitable for the MBE growth of 2D layers and 2D layer heterostructures. The orientation of the transition metal dichalcogenide (TMD) islands is close to random after room temperature growth and mild annealing, not different to TMD growth on the other Gr substrates. The random orientation indicates a weak interaction of the TMD with Gr/Ir(110).

Figure 7b displays Fe islands intercalated underneath Gr on Ir(110). The unique feature here is that the Gr cover enables epitaxial growth on unreconstructed Ir(110) which has not been possible before. A pseudomorphic Fe monolayer on Ir(110) as realized here could offer magnetic properties similarly exciting as those of the Fe monolayer on Ir(111) [59].

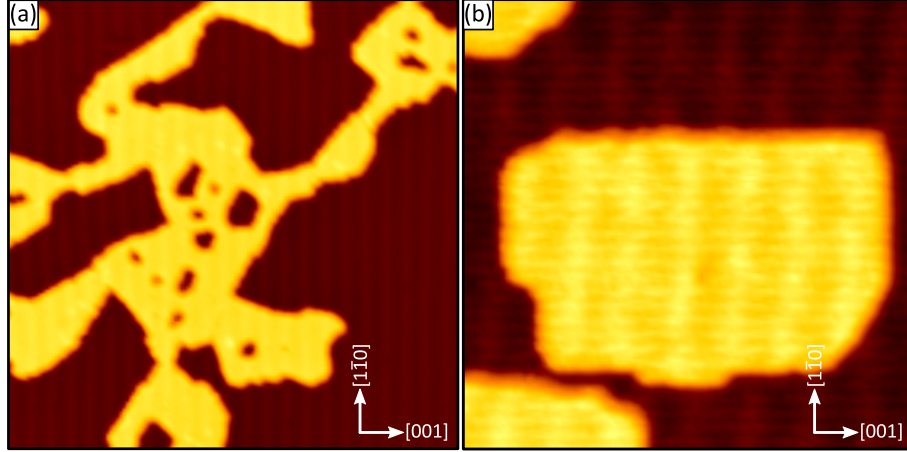


Figure 7: (a) STM topograph ( $750 \times 750, \text{\AA}^2$ ) taken after MBE growth of monolayer NbS<sub>2</sub> islands on Gr/Ir(110) at 150 K and additional annealing to 825 K. (b) STM topograph ( $300 \times 300 \text{\AA}^2$ ) of a pseudomorphic Fe intercalation island underneath Gr on unreconstructed Ir(110). STM topographs taken at 1.7 K. Tunneling parameters are (a)  $U_{\text{bias}} = 2.0 \text{ V}$  and  $I_t = 0.1 \text{ nA}$  and (b)  $U_{\text{bias}} = 1.0 \text{ V}$  and  $I_t = 0.5 \text{ nA}$ .

**Discussion:** Instead of forming the nano-facet reconstruction, Ir(110) remains unreconstructed upon cooldown to room temperature when Gr has been grown on it at 1500 K. To explain this remarkable observation we note that the surface reconstructions of Ir(110) are driven by the temperature-dependent minimization of surface free energy  $\gamma$  which itself is linked to the surface stress [60]. The Ir(110) surface was shown to run through a sequence of reconstructions upon cooling with a  $(2 \times 1)$  missing row reconstruction being present at 800 K–900 K, a  $(3 \times 1)$  missing row reconstruction being dominant at 500 K–600 K, while eventually upon cooling the  $(331)/(33\bar{1})$  nano-facet reconstruction forms [61, 62]. The surface structure of Ir(110) at the Gr growth temperature of 1500 K is unknown, but based on the results for the same surface orientation of the parent element Pt [63], at 1500 K Ir(110) is presumably above the roughening temperature and will display fast surface profile fluctuations due to high mobility. Knowing that a Gr membrane replicates the surface morphology at the growth temperature [13], the morphology observed at 300 K by STM is close to the morphology at the end of growth at 1500 K. Therefore, we tentatively conclude that Gr grows on unreconstructed Ir(110). The calculated binding energy of 140.2 meV per C atom is of similar magnitude as the Ir surface free energy, which can

be estimated to be of the order of 300 meV for Ir(110) if normalized to the Gr atomic density [64]. It is therefore plausible that upon cooling, reconstructions that lower the surface energy in the clean case, are suppressed as they would diminish the adhesion between Gr and the Ir(110) substrate. In fact, any of the known Ir(110) reconstructions make the surface rougher and thus either would reduce the number of binding substrate atoms or force large deformations in Gr to conform to the substrate. In brief and somewhat coarse, the adhering Gr layer shifts the binding of Ir(110) surface atoms to a more bulk-like situation due to the formation of Ir-C bonds, largely relieving the driving force for surface reconstruction.

Gr on Ir(110) is a single crystal, if grown at 1500 K, while two domains are found for growth at 1300 K (compare Figure S3 of the SI). The situation is similar for the growth of Gr on Ir(111), where upon increasing the growth temperature the situation changes from multiple domain orientations to a single crystal of Gr [24, 25]. The lack of strain in the  $\begin{pmatrix} 8 & 4 \\ 0 & 11 \end{pmatrix}$  commensurate approximation of the high-temperature superstructure suggests that in fact the low-temperature two-domain structure which is considerably strained (compare Figure S3 of the SI and related discussion) reflects kinetic limitations of the Gr growth process rather than a change in the orientation-dependent adsorption energy. To substantiate such speculations systematic growth temperature dependent studies would be necessary, which are beyond the scope of this work. Nevertheless, we speculate that if the growth temperature can be raised sufficiently, also on other fcc(110) surfaces single-crystal Gr layers could be grown.

Lastly, one might ask why Gr on Ir(110) is so different from Gr on Ir(111), with a much higher binding energy and an electronic structure lacking a Dirac cone. As a first remark it should be noted that although the binding energy of graphene to Ir(110) is with 140.2 meV per C atom much larger than the 69 meV per C atom to Ir(111) [51], it is still much lower than typical chemisorption energies of several eV per molecule or the 7.6 eV cohesive energy of Gr [65]. The binding energy of Gr to Ir(110) is comparable to the binding energy of Gr to Ni(111) [66], which is considered as weak chemisorption [67]. We also note, that the electronic structure of Gr is especially sensitive to the environment because of the low density of states close to the Dirac point. Therefore a loss of the Dirac cone, as also observed for Ni(111) [53] does not imply a loss of the predominant  $sp^2$  bonding character, as obvious from the projected DOS in Figure 4.

Compared to Ir(111), which is smooth and where all surface atoms are 9-fold coordinated, Ir(110) is a more open and a corrugated surface, with the surface atoms in the protruding rows being only 6-fold coordinated, whereas the surface atoms in the troughs are 1.36 Å below the level of the row atoms and 11-fold coordinated. Evidently, on Ir(110) the surface atoms with lower coordination are more reactive. For instance, DFT calculations show that the CO binding energy on Ir(110) is larger by 410 meV compared to Ir(111) in the low coverage limit [68], a difference much larger than the 71 meV difference in binding energy of Gr to Ir(110) and Ir(111).

We speculate that the overall van der Waals interaction pulls Gr towards the surface such that the protruding atoms on Ir(110) start to hybridize with the Gr layer, while the recessed atoms do not. On the flat Ir(111) surface, Pauli repulsion stops the approach prior to the onset

of significant hybridization of specific substrate orbitals with the Gr sheet [69]. Based on this proposed scenario, we speculate that a similar difference in binding also holds for Gr on other metal surfaces, e.g. for Pt.

## 4 Conclusion

Single-domain Gr on Ir(110) forms upon low-pressure CVD growth at 1500 K, displays a rectangular moiré pattern with periodicities  $m_1 = 33 \text{ \AA}$  in [001] direction and  $m_2 = 10 \text{ \AA}$  in  $[\bar{1}10]$  direction, and can be approximated as a  $\begin{pmatrix} 8 & 4 \\ 0 & 11 \end{pmatrix}$  superstructure with respect to Ir(110). The Gr layer is chemisorbed to Ir(110) with an adsorption energy of  $-140.2 \text{ meV}$  per C atom. Due to strong and locally varying interaction with the substrate it lacks a Dirac cone.

The Gr layer displays a wave pattern with wave vector in [001] direction and corrugation of  $\approx 0.4 \text{ \AA}$  according to our *ab initio* calculations. This wave pattern implies a modulation in charge transfer to the Gr  $\pi$  system and in the Gr-Ir hybridization, both being most pronounced in the trough of the wave pattern. The effect of this property modulation on the physisorption of aromatic molecules is explored through *ab initio* calculations for a naphthalene molecule. The adsorption energy landscape is found to be highly anisotropic with the maximum binding energy for molecules with their long axis adsorbed along the troughs, where the van der Waals interaction is strongest because of the larger transferred charge to Gr. The same property modulation is shown experimentally to enable the alignment of EuCot sandwich-molecular wires along troughs at 300 K. The successful on-surface synthesis – requiring re-evaporation of excess Cot molecules and the diffusion of reaction intermediates – also documents the inertness of the substrate. This property is also at the heart of the successful use of Gr/Ir(110) as a substrate for the growth of the quasi-freestanding transition metal dichalcogenide layer NbS<sub>2</sub> through reactive MBE.

Under the Gr cover, Ir(110) remains unreconstructed down to the lowest temperatures. It is argued that the strong adhesion between Gr and Ir(110) suppresses the formation of the nano facets,  $(2 \times 1)$ , and  $(3 \times 1)$  reconstructions. By intercalation thereby epitaxial layers can be grown on unreconstructed Ir(110) as exemplified for a pseudomorphic Fe monolayer.

## Data availability statement

The data that support the findings of this study are available from the corresponding author upon reasonable request.

## Acknowledgements

This work was funded by the Deutsche Forschungsgemeinschaft (DFG, German Research Foundation) within the project 'Sandwich molecular nanowires: on-surface synthesis, structure and magnetism' (MI 581/23-1, AT 109/5-1 and WE 2623/17-1). V. C., N. A., J. F., T. K., and T. M

acknowledge additional DFG support within CRC1238, project no. 277146874 - CRC 1238 (sub-projects C01 and B06). We gratefully acknowledge the Gauss Centre for Supercomputing (GCS) for providing computing time through the John von Neumann Institute for Computing (NIC) on the GCS share of the supercomputer JURECA at Jülich Supercomputing Centre (JSC). This work was also supported by VILLUM FONDEN via the Centre of Excellence for Dirac Materials (Grant No. 11744).

## Conflict of interest

The authors declare that they have no competing financial interests.

## Author contributions

S.K., F.H., J.F., T.K. and K.B. conducted the syntheses and the STM and LEED experiments. S.K., M.B., R.-M.S., A.J.H. and A.H. conducted the ARPES experiments. N.A., S.T. and V.C. conducted the theoretical calculations. S.K., N.A. and T.M. wrote the manuscript with contributions from all authors. All authors contributed to the scientific discussion.

## Supporting information available

The supporting information provides data for pristine reconstructed Ir(110) (Figure S1), the Fourier transform of Figure 1c (Figure S2), data and a structure model for the  $T = 1300$  K two-domain phase of Gr/Ir(110) (Figure S3), an illustration (Figure S4) and explanation for the matrix notation of the approximate commensurate superstructure cell, additional charge-density difference plots (Figure S5), and additional ARPES data in Figure S6 with further evidence for the absence of a Gr Dirac cone. Figure S7 displays the geometries of all adsorption energy minima found for  $C_{10}H_8$  on Gr/Ir(110), and Table S1 the details of adsorption in these minima.

## References

- [1] J. Klinkhammer, D. F. Förster, S. Schumacher, H. P. Oepen, T. Michely and C. Busse, ‘Structure and magnetic properties of ultra thin textured EuO films on graphene’, *Appl. Phys. Lett.* **103**, 131601 (2013).
- [2] M. M. Ugeda, A. J. Bradley, S.-F. Shi, F. H. da Jornada, Y. Zhang, D. Y. Qiu, W. Ruan, S.-K. Mo, Z. Hussain, Z.-X. Shen, F. Wang, S. G. Louie and M. F. Crommie, ‘Giant bandgap renormalization and excitonic effects in a monolayer transition metal dichalcogenide semiconductor’, *Nat. Mater.* **13**, 1091 (2014).
- [3] M. M. Ugeda, A. J. Bradley, Y. Zhang, S. Onishi, Y. Chen, W. Ruan, C. Ojeda-Aristizabal, H. Ryu, M. T. Edmonds, H.-Z. Tsai, A. Riss, S.-K. Mo, D. Lee, A. Zettl, Z. Hussain, Z.-X. Shen and M. F. Crommie, ‘Characterization of collective ground states in single-layer NbSe2’, *Nat. Phys.* **12**, 92 (2016).

- [4] J. Hall, B. Pielic, C. Murray, W. Jolie, T. Wekking, C. Busse, M. Kralj and T. Michely, ‘Molecular beam epitaxy of quasi-freestanding transition metal disulphide monolayers on van der Waals substrates: a growth study’, *2D Mater.* **5**, 025005 (2018).
- [5] C. Murray, W. Jolie, J. A. Fischer, J. Hall, C. van Efferen, N. Ehlen, A. Grüneis, C. Busse and T. Michely, ‘Comprehensive tunneling spectroscopy of quasifreestanding MoS<sub>2</sub> on graphene on Ir(111)’, *Phys. Rev. B* **99**, 115434 (2019).
- [6] M. Garnica, D. Stradi, S. Barja, F. Calleja, C. Díaz, M. Alcamí, N. Martín, A. L. Vázquez de Parga, F. Martín and R. Miranda, ‘Long-range magnetic order in a purely organic 2D layer adsorbed on epitaxial graphene’, *Nat. Phys.* **9**, 368 (2013).
- [7] S. K. Hämäläinen, M. Stepanova, R. Drost, P. Liljeroth, J. Lahtinen and J. Sainio, ‘Self-assembly of cobalt-phthalocyanine molecules on epitaxial graphene on Ir(111)’, *J. Phys. Chem. C* **116**, 20433 (2012).
- [8] F. Huttmann, N. Schleheck, N. Atodiresei and T. Michely, ‘On-surface synthesis of sandwich molecular nanowires on graphene’, *J. Am. Chem. Soc.* **139**, 9895 (2017).
- [9] J. Mao, H. Zhang, Y. Jiang, Y. Pan, M. Gao, W. Xiao and H.-J. Gao, ‘Tunability of supramolecular kagome lattices of magnetic phthalocyanines using graphene-based moiré patterns as templates’, *J. Am. Chem. Soc.* **131**, 14136 (2009).
- [10] R. Baltic, M. Pivetta, F. Donati, C. Wäckerlin, A. Singha, J. Dreiser, S. Rusponi and H. Brune, ‘Superlattice of single atom magnets on graphene’, *Nano Lett.* **16**, 7610 (2016).
- [11] T. Hartl, M. Will, D. Čapeta, R. Singh, D. Scheinecker, V. Boix de la Cruz, S. Dellmann, P. Lacovig, S. Lizzit, B. V. Senkovskiy, A. Grüneis, M. Kralj, J. Knudsen, J. Kotakoski, T. Michely and P. Bampoulis, ‘Cluster superlattice membranes’, *ACS Nano* **14**, 13629 (2020).
- [12] V. Borovikov and A. Zangwill, ‘Step-edge instability during epitaxial growth of graphene from SiC(0001)’, *Phys. Rev. B* **80**, 121406 (2009).
- [13] J. Kraus, S. Böcklein, R. Reichelt, S. Günther, B. Santos, T. O. Menteş and A. Locatelli, ‘Towards the perfect graphene membrane? – Improvement and limits during formation of high quality graphene grown on Cu-foils’, *Carbon* **64**, 377 (2013).
- [14] J. Bao, O. Yasui, W. Norimatsu, K. Matsuda and M. Kusunoki, ‘Sequential control of step-bunching during graphene growth on SiC(0001)’, *Appl. Phys. Lett.* **109**, 081602 (2016).
- [15] I. Šrut Rakić, M. Kralj, W. Jolie, P. Lazić, W. Sun, J. Avila, M.-C. Asensio, F. Craes, V. M. Trontl, C. Busse and P. Pervan, ‘Step-induced faceting and related electronic effects for graphene on Ir(332)’, *Carbon* **110**, 267 (2016).
- [16] Y. S. Dedkov, M. Fonin, U. Rüdiger and C. Laubschat, ‘Graphene-protected iron layer on Ni(111)’, *Appl. Phys. Lett.* **93**, 022509 (2008).
- [17] L. Nilsson, M. Andersen, J. Bjerre, R. Balog, B. Hammer, L. Hornekær and I. Stensgaard, ‘Preservation of the Pt(100) surface reconstruction after growth of a continuous layer of graphene’, *Surf. Sci.* **606**, 464 (2012).
- [18] L. Nilsson, M. Andersen, R. Balog, E. Lægsgaard, P. Hofmann, F. Besenbacher, B. Hammer, I. Stensgaard and L. Hornekær, ‘Graphene coatings: probing the limits of the one atom thick protection layer’, *ACS Nano* **6**, 10258 (2012).
- [19] M. Batzill, ‘The surface science of graphene: metal interfaces, CVD synthesis, nanoribbons, chemical modifications, and defects’, *Surf. Sci. Rep.* **67**, 83 (2012).
- [20] S. Marchini, S. Günther and J. Wintterlin, ‘Scanning tunneling microscopy of graphene on Ru(0001)’, *Phys. Rev. B* **76**, 075429 (2007).
- [21] T. A. Land, T. Michely, R. J. Behm, J. C. Hemminger and G. Comsa, ‘Direct observation of surface reactions by scanning tunneling microscopy: Ethylene→ethynidyne→carbon particles→graphite on Pt(111)’, *J. Chem. Phys.* **97**, 6774 (1992).

- [22] L. Gao, J. R. Guest and N. P. Guisinger, ‘Epitaxial graphene on Cu(111)’, *Nano Lett.* **10**, 3512 (2010).
- [23] D. Martoccia, M. Björck, C. M. Schlepütz, T. Brugger, S. A. Pauli, B. D. Patterson, T. Greber and P. R. Willmott, ‘Graphene on Ru(0001): a corrugated and chiral structure’, *New J. Phys.* **12**, 043028 (2010).
- [24] E. Loginova, S. Nie, K. Thürmer, N. C. Bartelt and K. F. McCarty, ‘Defects of graphene on Ir(111): rotational domains and ridges’, *Phys. Rev. B* **80**, 085430 (2009).
- [25] H. Hattab, A. T. N’Diaye, D. Wall, G. Jnawali, J. Coraux, C. Busse, R. van Gastel, B. Poelsema, T. Michely, F.-J. Meyer zu Heringdorf and M. Horn-von Hoegen, ‘Growth temperature dependent graphene alignment on Ir(111)’, *Appl. Phys. Lett.* **98**, 141903 (2011).
- [26] A. Fedorov, A. Varykhalov, A. Dobrotvorskii, A. Chikina, V. Adamchuk and D. Usachov, ‘Structure of graphene on the Ni(110) surface’, *Phys. Solid State* **53**, 1952 (2011).
- [27] O. Duggerjav, G. Duvjir, L. Tapasztó and C. Hwang, ‘Growth of graphene on the Cu(110) surface’, *J. Phys. Chem. C* **124**, 12106 (2020).
- [28] S. Achilli, E. Cavaliere, T. H. Nguyen, M. Cattelan and S. Agnoli, ‘Growth and electronic structure of 2D hexagonal nanosheets on a corrugated rectangular substrate’, *Nanotechnology* **29**, 485201 (2018).
- [29] N. A. Vinogradov, A. A. Zakharov, V. Kocevski, J. Ruzs, K. A. Simonov, O. Eriksson, A. Mikkelsen, E. Lundgren, A. S. Vinogradov, N. Mårtensson and A. B. Preobrajenski, ‘Formation and structure of graphene waves on Fe(110)’, *Phys. Rev. Lett.* **109**, 026101 (2012).
- [30] J. Dai, D. Wang, M. Zhang, T. Niu, A. Li, M. Ye, S. Qiao, G. Ding, X. Xie, Y. Wang, P. K. Chu, Q. Yuan, Z. Di, X. Wang, F. Ding and B. I. Yakobson, ‘How graphene islands are unidirectionally aligned on the Ge(110) surface’, *Nano Lett.* **16**, 3160 (2016).
- [31] J.-H. Lee, E. K. Lee, W.-J. Joo, Y. Jang, B.-S. Kim, J. Y. Lim, S.-H. Choi, S. J. Ahn, J. R. Ahn, M.-H. Park, C.-W. Yang, B. L. Choi, S.-W. Hwang and D. Whang, ‘Wafer-scale growth of single-crystal monolayer graphene on reusable hydrogen-terminated germanium’, *Science* **344**, 286 (2014).
- [32] M. Corso, T. Greber and J. Osterwalder, ‘h-BN on Pd(110): a tunable system for self-assembled nanostructures?’, *Surf. Sci.* **577**, L78 (2005).
- [33] T. Greber, L. Brandenberger, M. Corso, A. Tamai and J. Osterwalder, ‘Single layer hexagonal boron nitride films on Ni(110)’, *e-J. Surf. Sci. Nanotechnol.* **4**, 410 (2006).
- [34] M. P. Allan, S. Berner, M. Corso, T. Greber and J. Osterwalder, ‘Tunable self-assembly of one-dimensional nanostructures with orthogonal directions’, *Nanoscale Res. Lett.* **2**, 94 (2007).
- [35] A. J. Martínez-Galera and J. M. Gómez-Rodríguez, ‘Influence of metal support in-plane symmetry on the corrugation of hexagonal boron nitride and graphene monolayers’, *Nano Res.* **11**, 4643 (2018).
- [36] D. Steiner, F. Mittendorfer and E. Bertel, ‘Quasiliquid layer promotes hexagonal boron nitride (h-BN) single-domain growth: h-BN on Pt(110)’, *ACS Nano* **13**, 7083 (2019).
- [37] R. Koch, M. Borbonus, O. Haase and K. H. Rieder, ‘New aspects on the Ir(110) reconstruction: surface stabilization on mesoscopic scale via (331) facets’, *Phys. Rev. Lett.* **67**, 3416 (1991).
- [38] F. Huttmann, N. Rothenbach, S. Kraus, K. Ollefs, L. M. Arruda, M. Bernien, D. Thonig, A. Delin, J. Fransson, K. Kummer, N. B. Brookes, O. Eriksson, W. Kuch, T. Michely and H. Wende, ‘Europium cyclooctatetraene nanowire carpets: a low-dimensional, organometallic, and ferromagnetic insulator’, *J. Phys. Chem. Lett.* **10**, 911 (2019).
- [39] I. Horcas, R. Fernández, J. M. Gómez-Rodríguez, J. Colchero, J. Gómez-Herrero and A. M. Baro, ‘WSXM: A software for scanning probe microscopy and a tool for nanotechnology’, *Rev. Sci. Instrum.* **78**, 013705 (2007).
- [40] P. Hohenberg and W. Kohn, ‘Inhomogeneous electron gas’, *Phys. Rev.* **136**, B864 (1964).
- [41] W. Kohn and L. J. Sham, ‘Self-consistent equations including exchange and correlation effects’, *Phys. Rev.* **140**, A1133 (1965).



- [42] P. E. Blöchl, ‘Projector augmented-wave method’, *Phys. Rev. B* **50**, 17953 (1994).
- [43] G. Kresse and J. Hafner, ‘*Ab initio* molecular dynamics for liquid metals’, *Phys. Rev. B* **47**, 558 (1993).
- [44] G. Kresse and J. Furthmüller, ‘Efficient iterative schemes for *ab initio* total-energy calculations using a plane-wave basis set’, *Phys. Rev. B* **54**, 11169 (1996).
- [45] G. Kresse and D. Joubert, ‘From ultrasoft pseudopotentials to the projector augmented-wave method’, *Phys. Rev. B* **59**, 1758 (1999).
- [46] K. Lee, E. D. Murray, L. Kong, B. I. Lundqvist and D. C. Langreth, ‘Higher-accuracy van der Waals density functional’, *Phys. Rev. B* **82**, 081101(R) (2010).
- [47] I. Hamada, ‘van der Waals density functional made accurate’, *Phys. Rev. B* **89**, 121103(R) (2014).
- [48] A. D. Becke, ‘On the large gradient behavior of the density functional exchange energy’, *J. Chem. Phys.* **85**, 7184 (1986).
- [49] A. T. N'Diaye, J. Coraux, T. N. Plasa, C. Busse and T. Michely, ‘Structure of epitaxial graphene on Ir(111)’, *New J. Phys.* **10**, 043033 (2008).
- [50] P. Eckerlin and H. Kandler, ‘Group III: Condensed Matter (Landolt–Börnstein: numerical data and functional relationships in science and technology - New Series)’, **6**, 626 (1971).
- [51] F. H. Farwick zum Hagen, D. M. Zimmermann, C. C. Silva, C. Schlueter, N. Atodiresei, W. Jolie, A. J. Martínez-Galera, D. Dombrowski, U. A. Schröder, M. Will, P. Lazić, V. Caciuc, S. Blügel, T.-L. Lee, T. Michely and C. Busse, ‘Structure and growth of hexagonal boron nitride on Ir(111)’, *ACS Nano* **10**, 11012 (2016).
- [52] F. Huttman, A. J. Martínez-Galera, V. Caciuc, N. Atodiresei, S. Schumacher, S. Standop, I. Hamada, T. O. Wehling, S. Blügel and T. Michely, ‘Tuning the van der Waals interaction of graphene with molecules via doping’, *Phys. Rev. Lett.* **115**, 236101 (2015).
- [53] Q. Wang, L. Wei, M. Sullivan, S.-W. Yang and Y. Chen, ‘Graphene layers on Cu and Ni(111) surfaces in layer controlled graphene growth’, *RSC Adv.* **3**, 3046 (2013).
- [54] S. V. Hoffmann, C. Søndergaard, C. Schultz, Z. Li and P. Hofmann, ‘An undulator-based spherical grating monochromator beamline for angle-resolved photoemission spectroscopy’, *Nucl. Instrum. Methods Phys. Res. A* **523**, 441 (2004).
- [55] A. Chakradhar, K. Trettel and U. Burghaus, ‘Benzene adsorption on Ru(0001) and graphene/Ru(0001)—how to synthesize epitaxial graphene without STM or LEED?’, *Chem. Phys. Lett.* **590**, 146 (2013).
- [56] N. Hosoya, R. Takegami, J.-i. Suzumura, K. Yada, K. Miyajima, M. Mitsui, M. B. Knickelbein, S. Yabushita and A. Nakajima, ‘Formation and electronic structures of organoeuropium sandwich nanowires’, *J. Phys. Chem. A* **118**, 8298 (2014).
- [57] A. Nakajima and K. Kaya, ‘A novel network structure of organometallic clusters in the gas phase’, *J. Phys. Chem. A* **104**, 176 (2000).
- [58] J. Hall, N. Ehlen, J. Berges, E. van Loon, C. van Efferen, C. Murray, M. Rösner, J. Li, B. V. Senkovskiy, M. Hell, M. Rolf, T. Heider, M. C. Asensio, J. Avila, L. Plucinski, T. Wehling, A. Grüneis and T. Michely, ‘Environmental control of charge density wave order in monolayer 2H-TaS<sub>2</sub>’, *ACS Nano* **13**, 10210 (2019).
- [59] S. Heinze, K. von Bergmann, M. Menzel, J. Brede, A. Kubetzka, R. Wiesendanger, G. Bihlmayer and S. Blügel, ‘Spontaneous atomic-scale magnetic skyrmion lattice in two dimensions’, *Nat. Phys.* **7**, 713 (2011).
- [60] R. Shuttleworth, ‘The surface tension of solids’, *Proc. Phys. Soc. A* **63**, 444 (1950).
- [61] A. Ney, J. Schulz, M. Sturmat and R. Koch, ‘Stress-driven self-assembly on Ir(110): stripes, droplets, and missing-row-type reconstructions’, *Surf. Sci.* **519**, 192 (2002).

- [62] J. J. Schulz, M. Sturmat and R. Koch, ‘Illuminating structural transformation of Ir(110): a high-temperature scanning tunneling microscopy study’, *Phys. Rev. B* **62**, 15402 (2000).
- [63] I. K. Robinson, E. Vlieg and K. Kern, ‘Structure and roughening of the Pt(110) surface’, *Faraday Discuss. Chem. Soc.* **89**, 159 (1990).
- [64] R. Tran, Z. Xu, B. Radhakrishnan, D. Winston, W. Sun, K. A. Persson and S. P. Ong, ‘Surface energies of elemental crystals’, *Sci. Data* **3**, 160080 (2016).
- [65] K. H. Hellwege, O. Madelung, M. Schulz and H. Weiss, ‘Semiconductors, physics of group IV elements and III-V compounds. Landolt-Börnstein, New Series, Group III’, **17 Pt. A**, (1982).
- [66] P. L. Silvestrelli and A. Ambrosetti, ‘van der Waals corrected DFT simulation of adsorption processes on transition-metal surfaces: Xe and graphene on Ni(111)’, *Phys. Rev. B* **91**, 195405 (2015).
- [67] F. Mittendorfer, A. Garhofer, J. Redinger, J. Klimeš, J. Harl and G. Kresse, ‘Graphene on Ni(111): strong interaction and weak adsorption’, *Phys. Rev. B* **84**, 201401 (2011).
- [68] C. Liu, L. Zhu, P. Ren, X. Wen, Y.-W. Li and H. Jiao, ‘High-coverage CO adsorption and dissociation on Ir(111), Ir(100), and Ir(110) from computations’, *J. Phys. Chem. C* **123**, 6487 (2019).
- [69] C. Busse, P. Lazić, R. Djemour, J. Coraux, T. Gerber, N. Atodiresei, V. Caciuc, R. Brako, A. T. N’Diaye, S. Blügel, J. Zegenhagen and T. Michely, ‘Graphene on Ir(111): physisorption with chemical modulation’, *Phys. Rev. Lett.* **107**, 036101 (2011).

# Supporting information:

## single-crystal graphene on Ir(110)

Stefan Kraus<sup>\*1</sup>, Felix Huttmann<sup>1</sup>, Jeison Fischer<sup>1</sup>, Timo Knispel<sup>1</sup>, Ken Bischof<sup>1</sup>,  
Alexander Herman<sup>2</sup>, Marco Bianchi<sup>3</sup>, Raluca-Maria Stan<sup>3</sup>, Ann Julie Holt<sup>3</sup>, Vasile  
Caciuc<sup>4</sup>, Shigeru Tsukamoto<sup>4</sup>, Heiko Wende<sup>2</sup>, Philip Hofmann<sup>3</sup>, Nicolae Atodiresei<sup>†4</sup>, and  
Thomas Michely<sup>1</sup>

<sup>1</sup>*II. Physikalisches Institut, Universität zu Köln, Zùlpicher Str. 77, 50937 Köln, Germany*

<sup>2</sup>*Faculty of Physics and Center for Nanointegration Duisburg-Essen (CENIDE), University of  
Duisburg-Essen, Lotharstraße 1, 47048 Duisburg, Germany*

<sup>3</sup>*Department of Physics and Astronomy, Interdisciplinary Nanoscience Center (iNANO), Aarhus  
University, 8000 Aarhus C, Denmark*

<sup>4</sup>*Peter Grünberg Institute and Institute for Advanced Simulation, Forschungszentrum Jùlich,  
Wilhelm-Johnen-StraÙe, 52428 Jùlich, Germany*

---

<sup>\*</sup>kraus@ph2.uni-koeln.de (experiment)

<sup>†</sup>n.atodiresei@fz-juelich.de (theory)

**Figure S1: Surface reconstruction of Ir(110)**

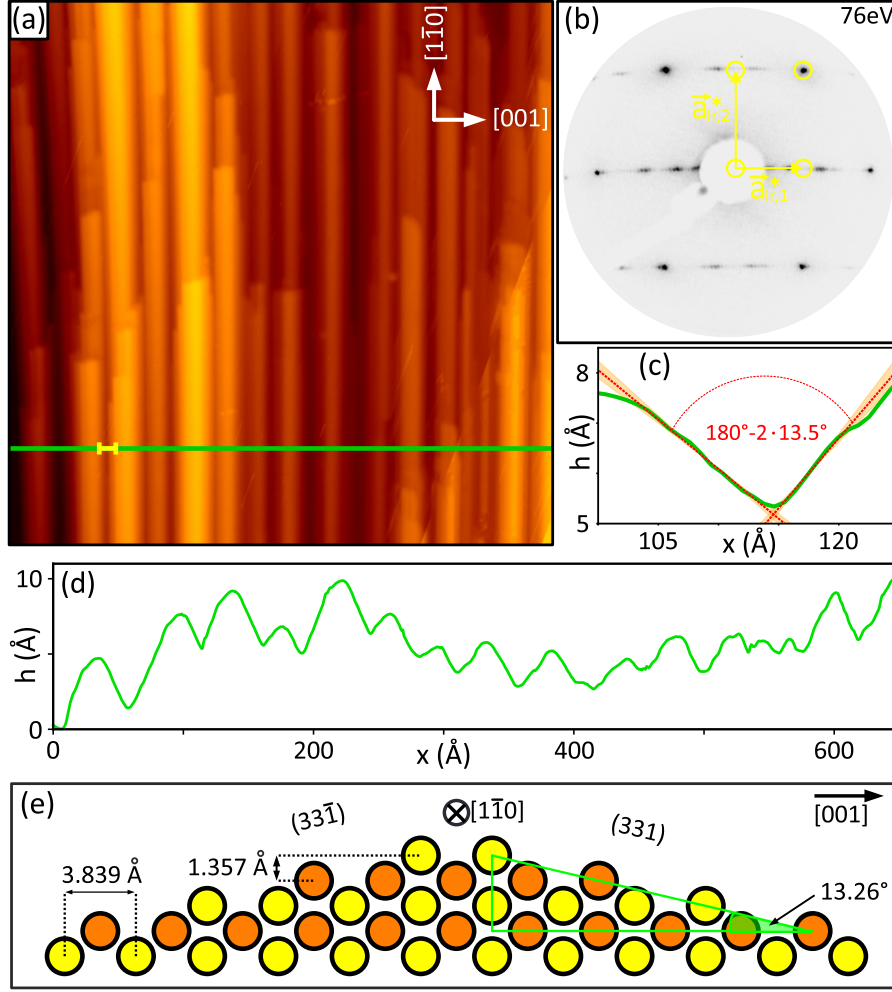


Figure S1: (a) STM topograph ( $650 \times 650 \text{ \AA}^2$ ) of faceted, clean Ir(110) without Gr. The  $[001]$  and  $[1\bar{1}0]$  directions are specified in the upper right corner and hold also for (b). (b) 76 eV contrast-inverted LEED pattern of sample in (a). Locations of Ir reflections for unreconstructed Ir(110) are encircled yellow. First order reflections are split due to facetting. (c) Height profile along yellow line segment in (a). The slopes are indicated by dotted-red lines, the corresponding uncertainties as orange cones. The angle between the slopes is  $153^\circ$  and agrees well with the  $(331)$  and  $(33\bar{1})$  nano-facets being inclined by  $13.26^\circ$  with respect to the  $(110)$  plane. (d) Height profile along green line in (a). (e) Side view ball model of surface displaying  $(331)$  and  $(33\bar{1})$  nano-facets consistent with the profiles of (c) and (d). STM imaging temperature in (a) is 300 K, tunneling parameters in (a) are  $U_{\text{bias}} = -1.80 \text{ V}$  and  $I_t = 0.35 \text{ nA}$ .

We have investigated the reconstructed surface of an iridium (110) single crystal as previously discussed in Refs. [1, 2]. Figure S1a shows an STM topograph, in which the reconstruction is visible. The surface is not flat, but forms elongated ridges along the  $[1\bar{1}0]$  direction. In the LEED pattern of Fig. S1b the Ir(110) reflections and reciprocal lattice translations are indicated in yellow. The first order reflections are split into pairs of two spots centered around the regular positions along the  $[001]$  direction, while the second order reflections are not split. Figure S1c

shows the contact point of two ridges as indicated by the yellow line in Fig. S1a. The measured contact angle is  $(13.5 \pm 0.5)^\circ$ . The profile in Fig. S1d shows height variations between the ridges of less than  $10 \text{ \AA}$  and distinct contact angles between these ridges. The formation of  $(331)$  and  $(3\bar{3}1)$  facets reduces the surface energy and leads to an angle of  $13.26^\circ$  with respect to the  $(110)$  surface [1].

**Figure S2: Fourier transform of atomic resolution STM topograph of Gr/Ir(110)**

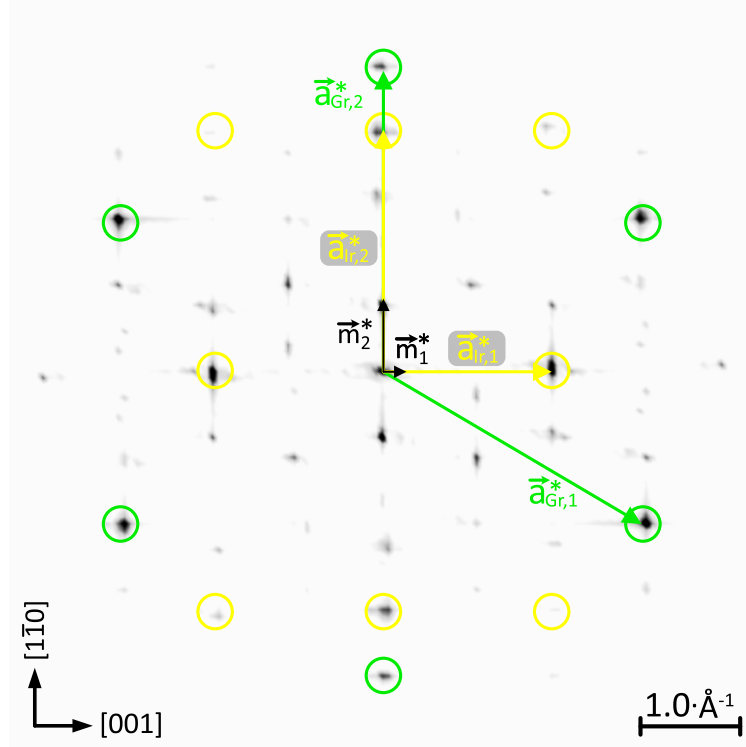


Figure S2: Contrast-inverted Fourier transform of atomic resolution STM topograph of Gr/Ir(110). The reciprocal lattice points of the Ir(110) surface are encircled in yellow, the reciprocal lattice points of the single graphene domain are encircled in green. All corresponding reciprocal lattice vectors are indicated in the respective colors.

The contrast-inverted Fourier transform in Fig. S2 shows the reciprocal lattice points of the Ir(110) substrate and the single-domain Gr. Comparing their locations allows one to conclude that Gr is undistorted, i.e. the lattice parameters  $a_{\text{Gr},1}$  and  $a_{\text{Gr},2}$  agree with each other with an error margin below 0.5 %. Additionally, the reciprocal lattice points of the rectangular moiré lattice are present in the Fourier transform, and agree with the values from the STM and LEED analysis within the margin of error.

**Figure S3: Two-domain Gr on Ir(110)**

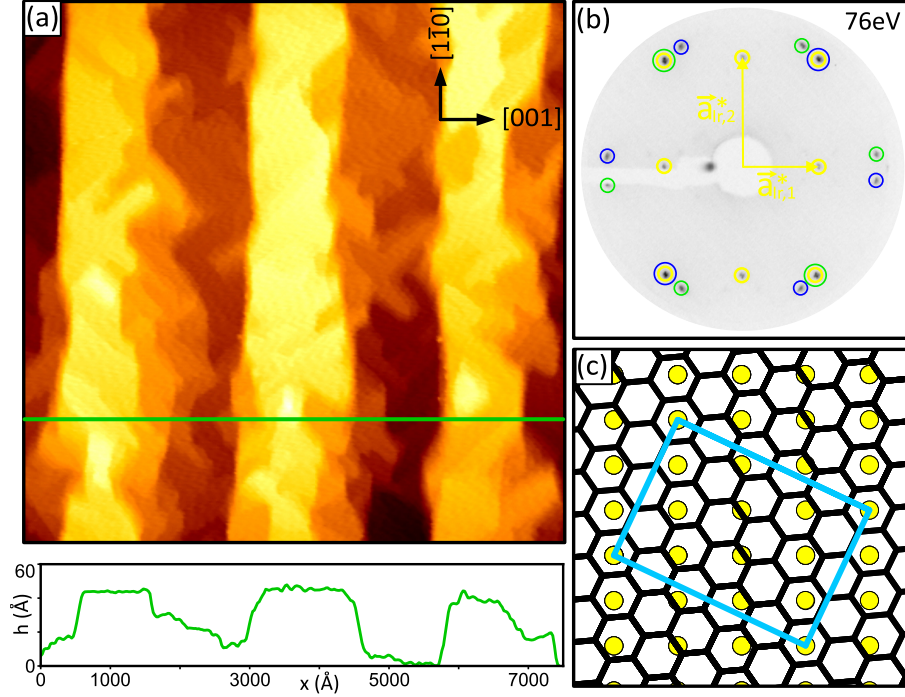


Figure S3: a) STM topograph ( $7500 \times 7500 \text{ \AA}^2$ ) of Gr/Ir(110) grown at  $T = 1300 \text{ K}$ . The  $[001]$  and  $[1\bar{1}0]$  directions specified in the upper right corner are valid also for (c). STM height profile along green line in (a) is shown below the topograph. (b) Contrast-inverted 76 eV LEED pattern of sample in (a). The first order Ir reflections are encircled yellow, the first order Gr reflections related to the two Gr domains encircled green and blue, respectively. (c) Ball model of Gr domain on Ir(110), corresponding to Gr reflections encircled blue in (b). A commensurate unit cell is indicated by the cyan rectangle. STM imaging temperature in (a) is 300 K, tunneling parameters in (a) are  $U_{\text{bias}} = -1.01 \text{ V}$  and  $I_t = 0.97 \text{ nA}$ .

We have also observed a two-domain Gr layer when ethylene exposure was conducted at the lower temperature of 1300 K. In the large scale STM topograph in Fig. S3a taken after Gr growth, a rough surface of ill-defined plateaus along the  $[1\bar{1}0]$  direction is visible. The profile of Fig. S3a shows a height variation of the order of few nm along the  $[001]$  direction. The corresponding contrast-inverted LEED pattern in Fig. S3b displays the Ir first order reflections encircled yellow, along with two groups of six additional first order reflections due to Gr, encircled green and blue, respectively. Each group forms an approximate hexagon, as expected for the diffraction pattern of Gr. We assign each of these groups to a distinct Gr domain. For each domain, two Gr reflections coincide with either the (1,1) and (-1,-1) or with the (1,-1) and (-1,1) reflections of Ir(110). This coincidence determines the orientation and domain structure of the Gr. It implies a substantial tensile strain in Gr of about 4% along the direction of coincidence. Both other directions are also under tensile strain of about 1.6% compared to relaxed graphite. Figure S3c shows an atomic model of the graphene domain indicated in blue in Fig. S3b, the cyan rectangle is the commensurate superstructure unit cell. From this model, the Gr lattice parameters are

2.54 Å in two directions, and 2.48 Å in the remaining direction. These numbers agree well with our experiment. This low growth temperature two-domain Gr layer is not well suited as a growth substrate due to its two-domain structure and the large substrate roughness that evolves during Gr growth.



**Figure S4: Matrix notation of the approximate commensurate superstructure cell**

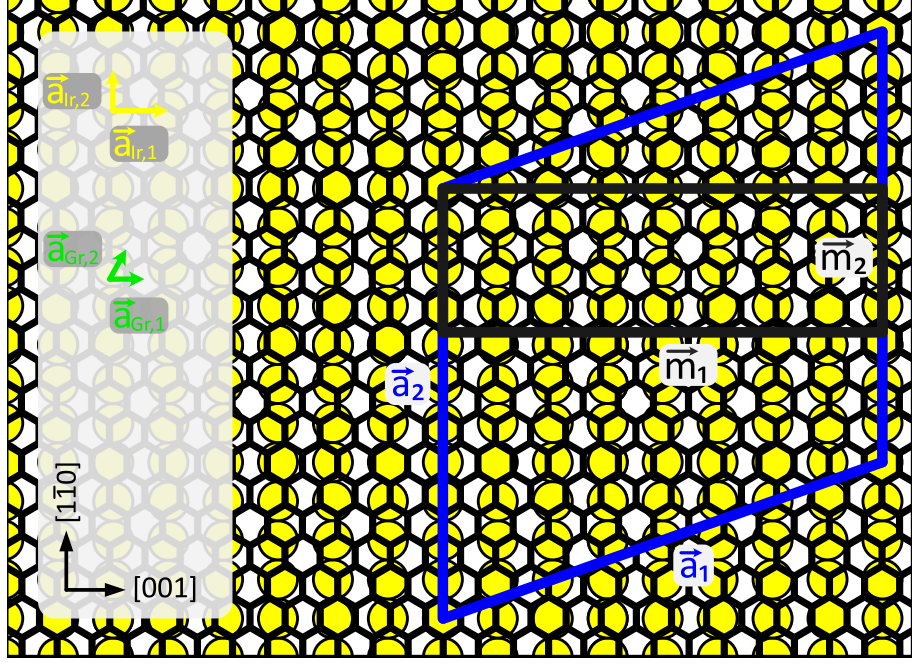


Figure S4: Atomic model of the single-domain Gr phase on Ir(110). The approximate superstructure unit cell is shown as blue rhomboid, the moiré cell as black rectangle, the corresponding lattice vectors and side lengths are indicated. The Ir(110) and Gr lattice vectors are defined on the left hand side, as used for the matrix notation of the superstructure cell.

Figure S4 shows an atomic model of the single-domain Gr on unreconstructed Ir(110). The superstructure and moiré cells are shown as blue rhomboid and black rectangle, respectively. Equation 1 summarizes the relation between the superstructure lattice vectors, the Ir(110) and Gr lattice vectors and is expressed in the matrix notation. All vectors are defined as shown in Fig. S4.  $\vec{a}_{\text{Ir},1}$  is the Ir lattice vector in  $[001]$  direction, and  $\vec{a}_{\text{Ir},2}$  along the  $[1\bar{1}0]$  direction with lengths  $a_{\text{Ir},1} = 3.839 \text{ \AA}$  and  $a_{\text{Ir},2} = 2.715 \text{ \AA}$ . The Gr lattice vectors in the commensurate model have lengths  $a_{\text{Gr},1} = 2.457 \text{ \AA}$  and  $a_{\text{Gr},2} = 2.463 \text{ \AA}$ , with  $\vec{a}_{\text{Gr},1}$  along  $[001]$  and  $\vec{a}_{\text{Gr},2}$  rotated by close to  $60^\circ$ . The resulting superstructure lattice vectors have lengths  $a_1 = 32.58 \text{ \AA}$  and  $a_2 = 29.87 \text{ \AA}$ .

$$\begin{pmatrix} \vec{a}_1 \\ \vec{a}_2 \end{pmatrix} = \begin{pmatrix} 8 & 4 \\ 0 & 11 \end{pmatrix} \cdot \begin{pmatrix} \vec{a}_{\text{Ir},1} \\ \vec{a}_{\text{Ir},2} \end{pmatrix} = \begin{pmatrix} 10 & 5 \\ -7 & 14 \end{pmatrix} \cdot \begin{pmatrix} \vec{a}_{\text{Gr},1} \\ \vec{a}_{\text{Gr},2} \end{pmatrix} \quad (1)$$

**Figure S5: Charge-density difference plots: cuts along  $[1\bar{1}0]$  direction and average along  $[001]$**

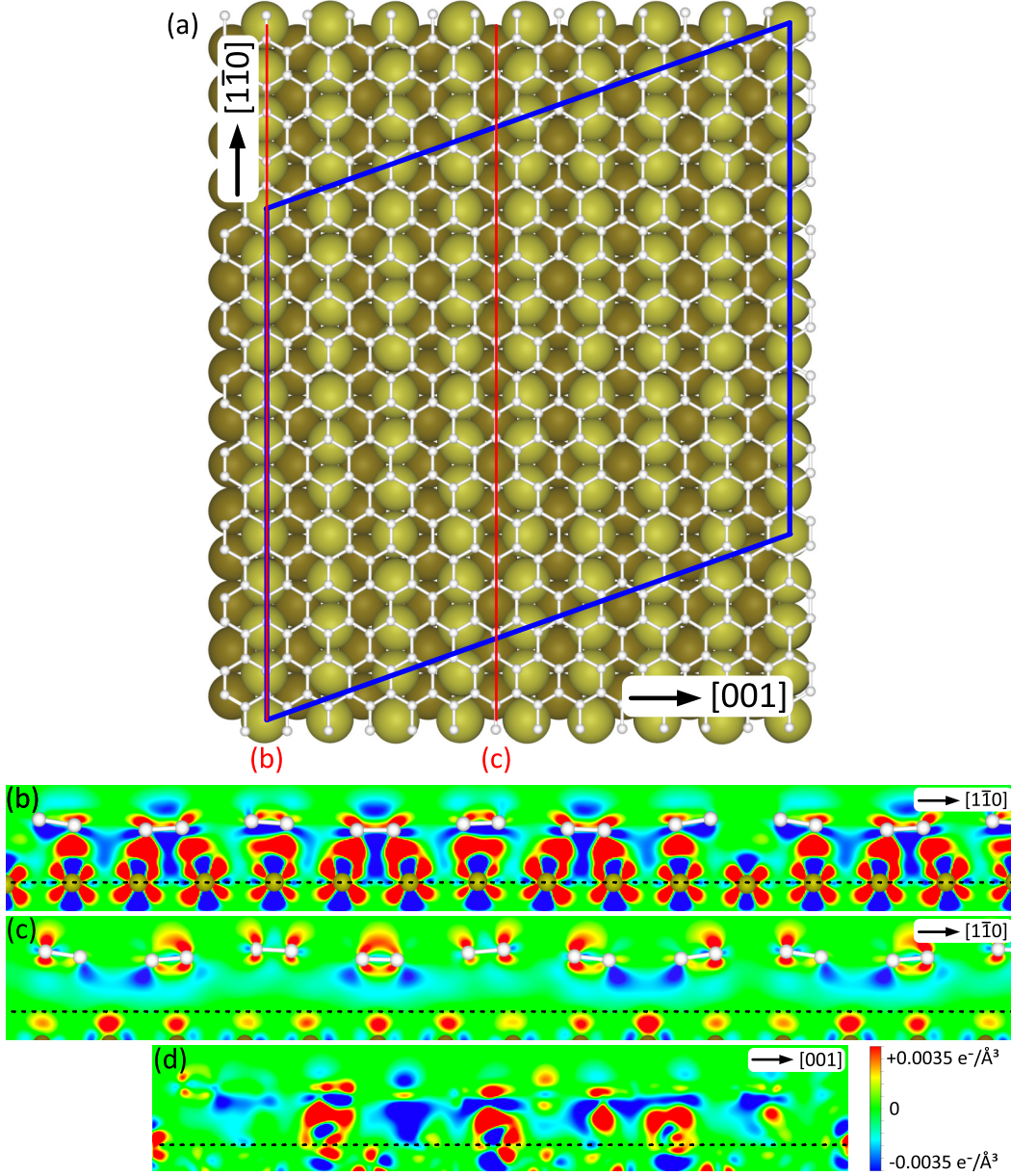


Figure S5: (a) Top view of ball model representations of relaxed DFT geometries for Gr/Ir(110). Ir atoms: light (top layer) to dark (bottom layer) brown spheres; C atoms: small light grey dots connected by light grey lines. The DFT supercell is indicated by the blue rhomboid. (b),(c) Charge-density difference plots along  $[1\bar{1}0]$ -direction on top of a dense-packed Ir row (b) and between two dense-packed rows (c), as indicated by the red lines in (a). (d) Charge-density difference average over the entire superstructure unit cell and projected onto a plane along the  $[001]$  direction. The dotted lines in (b)-(d) indicate the vertical position of the top level Ir atoms. Color scale for (b)-(d) ranges from charge accumulation in red ( $+0.0035$  electrons/ $\text{\AA}^3$ ) to depletion in blue ( $-0.0035$  electrons/ $\text{\AA}^3$ ).

**Figure S6: Absence of Gr signal in ARPES on Gr/Ir(110)**

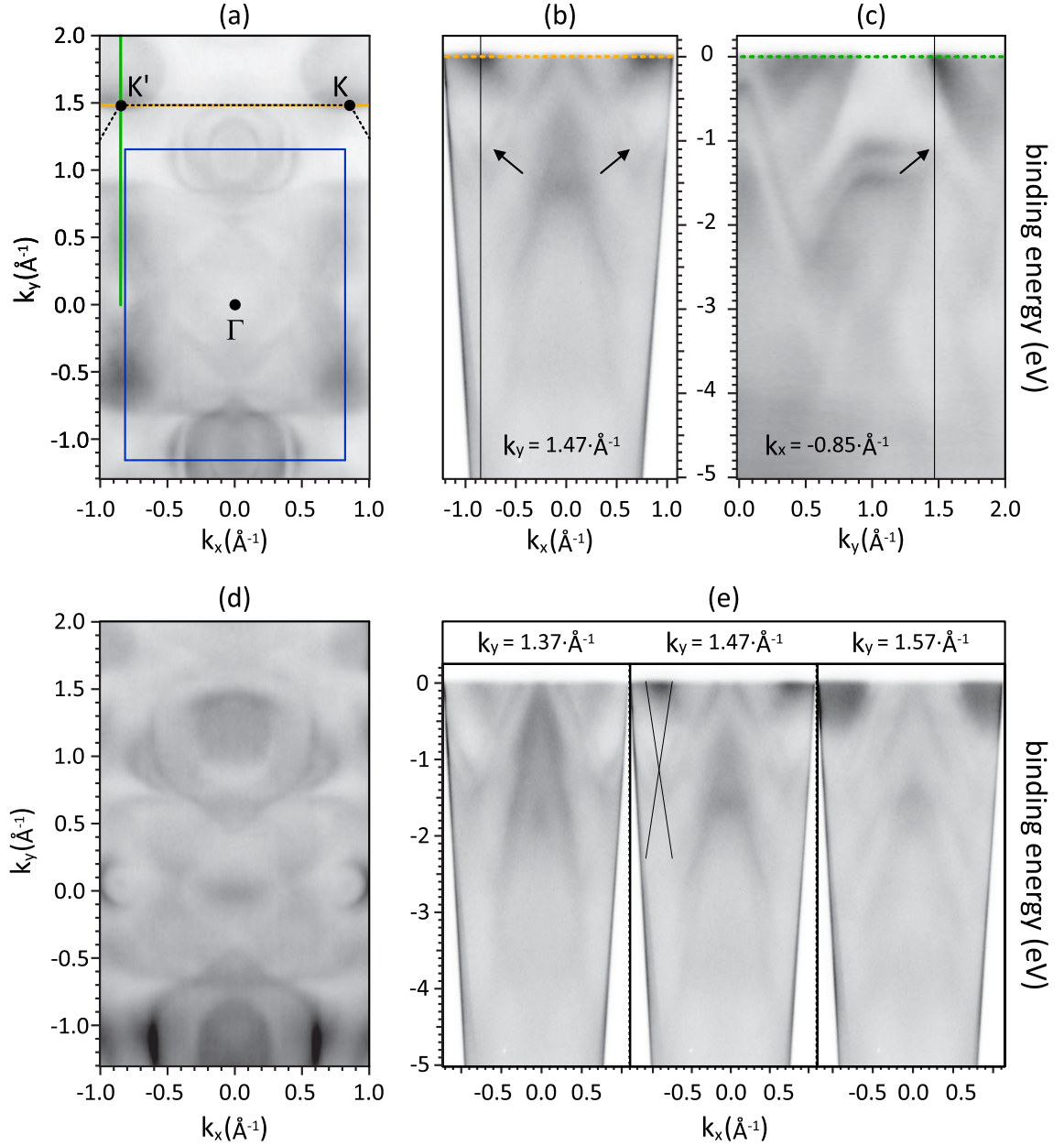


Figure S6: (a) Fermi surface of Gr/Ir(110) measured by ARPES. The Ir(110) Brillouin zone is indicated by the blue rectangle and part of the Gr Brillouin zone boundary indicated by the black dotted lines. (b) ARPES scan along  $k_y$  for fixed  $k_y = 1.47 \text{ \AA}^{-1}$  as indicated by the orange line in (a). Expected position of Gr Dirac cone is indicated by arrows and additionally by the vertical black line for negative  $k_x$ . (c) ARPES scan along  $k_y$  with fixed  $k_y = -0.85 \text{ \AA}^{-1}$ , along the green line indicated in (a). The expected position of the Gr Dirac cone indicated by vertical line and arrow. (d) ARPES constant energy slice at a binding energy of  $E_{\text{bind}} = -1 \text{ eV}$ , no conical sections at the K points are visible. (e) ARPES scans with  $\pm 0.1 \text{ \AA}^{-1}$  larger or smaller  $k_x$  as compared to  $k_y = 1.47 \text{ \AA}^{-1}$  used also for (b). The theoretical dispersion is shown in the center plot. All data have been recorded at a sample temperature of  $T = 35 \text{ K}$  and a photon energy of  $100 \text{ eV}$ .



**Figure S7: Local adsorption minima for a naphthalene molecule on Gr/Ir(110)**

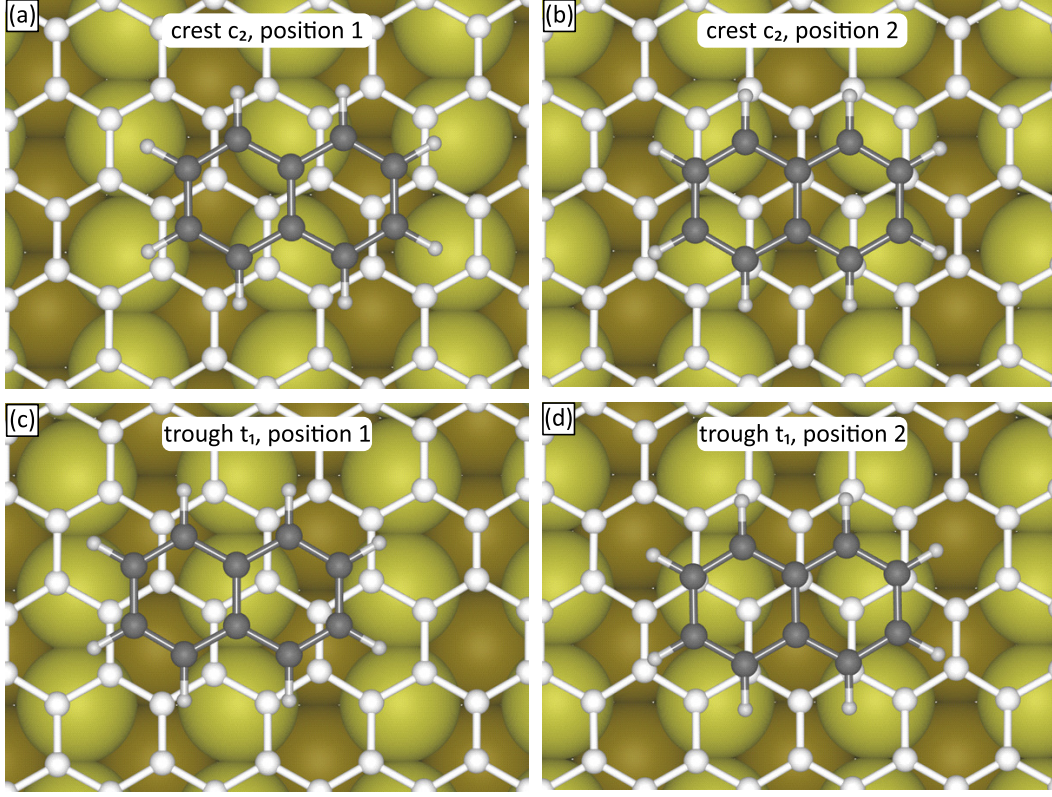


Figure S7: Figures (a) to (d) display in top view ball models the local minimum energy adsorption geometries on (a)/(b) crest  $c_2$  and (c)/(d) trough  $t_1$ . The parameters of adsorption are given in Table S1.

Following the methodology developed in [3], the adsorption energy  $E_{\text{ads}}$  can be decomposed into a term  $E_{\text{ads}}^{\text{vdW}}$  originating from purely non-local correlation effects and the so-called DFT contribution  $E_{\text{ads}}^{\text{DFT}}$  covering the remaining interaction. For all adsorption configurations  $E_{\text{ads}}^{\text{vdW}}$  is negative (attractive) while  $E_{\text{ads}}^{\text{DFT}}$  is positive (repulsive). For the minimum adsorption energy case shown in Fig. S7 the numbers are  $E_{\text{ads}}^{\text{vdW}} = -1500$  meV per molecule (150 meV per C atom) and  $E_{\text{ads}}^{\text{DFT}} = 553$  meV per molecule (55 meV per C atom). This implies that binding is through purely non-local correlations, superseeding Pauli repulsion and ionic interactions by far.

**Table S1: DFT-calculated adsorption energies of naphthalene molecule adsorbed onto Gr/Ir(110)**

	$E_{\text{diff}}$ (meV)	$E_{\text{ads}}$ (meV)	$E_{\text{ads}}^{\text{vdW}}$ (meV)	$E_{\text{ads}}^{\text{DFT}}$ (meV)	Nph-Gr dist. ( $\text{\AA}$ )
t <sub>1</sub> pos. 1	73.02	-873.62	-1389.21	515.60	3.319
t <sub>1</sub> pos. 2	0.00	-946.64	-1499.66	553.03	3.272
c <sub>2</sub> pos. 1	211.57	-735.07	-1202.80	467.72	3.423
c <sub>2</sub> pos. 2	167.74	-778.90	-1272.93	464.03	3.392

Table S1: DFT-calculated adsorption energies of naphthalene molecule adsorbed onto Gr/Ir(110). For both locations t<sub>1</sub> and c<sub>2</sub> two local minima are found (position 1 and 2).  $E_{\text{diff}}$  denotes the energy difference of the different local minima compared to t<sub>1</sub> (pos. 2),  $E_{\text{ads}}$  is the total binding energy,  $E_{\text{ads}}^{\text{vdW}}$  is the binding energy due to non-local correlation effects and  $E_{\text{ads}}^{\text{DFT}}$  contains the other DFT contribution to the total binding energy  $E_{\text{ads}}$ . Nph-Gr indicates the distance in  $\text{\AA}$  between naphthalene and substrate.

## References

- [1] R. Koch, M. Borbonus, O. Haase and K. H. Rieder, ‘New aspects on the Ir(110) reconstruction: surface stabilization on mesoscopic scale via (331) facets’, *Phys. Rev. Lett.* **67**, 3416 (1991).
- [2] J. Kuntze, S. Speller and W. Heiland, ‘The Ir(110) surface studied by STM’, *Surf. Sci.* **402-404**, 764 (1998).
- [3] F. Huttmann, A. J. Martínez-Galera, V. Caciuc, N. Atodiresei, S. Schumacher, S. Standop, I. Hamada, T. O. Wehling, S. Blügel and T. Michely, ‘Tuning the van der Waals interaction of graphene with molecules via doping’, *Phys. Rev. Lett.* **115**, 236101 (2015).



## CHAPTER 4

---

# Manuscript 2: Uniaxially aligned 1D sandwich-molecular wires: electronic structure and magnetism

*This chapter wholly consists of the above-named manuscript and its supplement. The manuscript is currently submitted to the Journal of Physical Chemistry C.*

*S.K., F.H. and K.B. conducted the syntheses and the STM and LEED experiments. S.K., M.B., R.-M.S., A.J.H. and A.H. conducted the ARPES experiments. S.K. and A.H. conducted the XPS experiments. S.K., A.H., N.R. and K.O. conducted the XAS/XMCD experiments. N.A. and S.T. conducted the theoretical calculations. S.K. wrote the manuscript in close collaboration with T.M. and with contributions from N.A.*

# Uniaxially aligned 1D sandwich-molecular wires: electronic structure and magnetism

Stefan Kraus<sup>\*1</sup>, Alexander Herman<sup>2</sup>, Felix Huttmann<sup>1</sup>, Marco Bianchi<sup>3</sup>, Raluca-Maria Stan<sup>3</sup>, Ann Julie Holt<sup>3</sup>, Shigeru Tsukamoto<sup>4</sup>, Nico Rothenbach<sup>2</sup>, Katharina Ollefs<sup>2</sup>, Jan Dreiser<sup>5</sup>, Ken Bischof<sup>1</sup>, Heiko Wende<sup>2</sup>, Philip Hofmann<sup>3</sup>, Nicolae Atodiresei<sup>†4</sup>, and Thomas Michely<sup>1</sup>

<sup>1</sup>*II. Physikalisches Institut, Universität zu Köln, Zùlpicher Str. 77, 50937 Köln, Germany*

<sup>2</sup>*Faculty of Physics and Center for Nanointegration Duisburg-Essen (CENIDE), University of Duisburg-Essen, Lotharstraße 1, 47048 Duisburg, Germany*

<sup>3</sup>*Department of Physics and Astronomy, Interdisciplinary Nanoscience Center (iNANO), Aarhus University, 8000 Aarhus C, Denmark*

<sup>4</sup>*Peter Grünberg Institute and Institute for Advanced Simulation, Forschungszentrum Jùlich, Wilhelm-Johnen-StraÙe, 52428 Jùlich, Germany*

<sup>5</sup>*Swiss Light Source, Paul Scherrer Institute, Forschungsstrasse 111, 5232 Villigen PSI, Switzerland*

## Abstract

Sandwich-molecular wires consisting of europium and cyclooctatetraene were grown *in situ* on the moiré of graphene with Ir(110). The moiré templates a uniaxial alignment of monolayer EuCot nanowire carpets and multilayer films with the EuCot wire axis along the [001] direction of the Ir substrate. Using angle-resolved photoemission spectroscopy we investigate the band structure of the wire carpet films. While  $\pi$ -derived bands were not observed experimentally, we find a flat band 1.85 eV below the Fermi energy. Using density-functional theory, X-ray photoelectron spectroscopy, and by replacing europium through barium in the sandwich-molecular wires, it is concluded that the flat band represents localized Eu 4f states. Comparison to DFT calculations allows one to derive the relevant Hubbard  $U$  in the organometallic compound. X-ray magnetic circular dichroism is employed to characterize the magnetic properties of the EuCot wire carpet films at low temperatures. Clear evidence for an easy axis magnetization along the wires is found.

---

<sup>\*</sup>kraus@ph2.uni-koeln.de (experiment)

<sup>†</sup>n.atodiresei@fz-juelich.de (theory)



# 1 Introduction

On-surface organometallic chemistry investigates the interaction of a wide variety of metal atoms with organic molecules on a supporting layer. Due to the relevance for spintronic applications [1], the interaction of magnetic metal atoms — such as transition or rare-earth metals — with the surrounding ligand field of the molecules, is of specific interest. The most studied systems to date are zero-dimensional single-molecule magnets [2, 3, 4, 5, 6, 7, 8, 9, 10] showing a magnetic hysteresis without long-range order, and two-dimensional (2D) metal–organic networks [11, 12, 13, 14, 15], some of which have been shown to mediate magnetic interaction within the surface plane [16, 17, 18, 19, 20].

Far less investigated are one-dimensional (1D) organometallic systems. Sandwich-molecular wires — chains of metal atoms and cyclic molecules in alternating sequence — are a class of such 1D organometallic systems. One example are transition-metal-benzene complexes, some of which have been theoretically predicted to be ferromagnetic half metals [21, 22, 23, 24], i.e. they can act as spin filters. Half-metal and spin-filter properties have also been discussed by theory for transition-metal-cyclopentadienyl complexes [25, 26, 27], or complexes containing larger molecules such as cyclononatetraenyl [28] or metallofullerenes [29]. Recently, also cyclopentadienyl-titanium-cyclooctatetraene double deckers have even been discussed in the context of molecular spin qubits [30].

Here, we focus on sandwich-molecular wires consisting of an alternating sequence of lanthanide (Ln) atoms and the eight-membered carbon ring cyclooctatetraene ( $\text{C}_8\text{H}_8$ , Cot) [31, 32, 33]. While the charge-neutral Cot molecule is anti-aromatic and non-planar, it becomes aromatic and planar upon accepting two electrons. By forming a 1D chain of alternating  $\text{Ln}^{2+}$  cations and  $\text{Cot}^{2-}$  anions, elongated LnCot sandwich-molecular wires can grow. Using europium (Eu) as lanthanide metal, in gas-phase experiments wire lengths of up to 30 formula units were reported [34]. To uncover the binding mechanism, angle-integrated photoelectron spectroscopy of gas phase wires was conducted [31, 32, 34], while Stern-Gerlach experiments revealed a magnetic moment of  $7\mu_{\text{B}}$  per Eu atom, and the total magnetic moment increases linearly with the chain length [33]. Theory has investigated the electronic and magnetic structure of short and long EuCot wires [35, 36, 37, 38] or versions with a slightly modified Cot ring [39]. These theoretical investigations agree in the prediction of ferromagnetic coupling and a semiconducting nature of the EuCot wires.

*In situ* on-surface synthesis of EuCot wires has been recently demonstrated on Gr/Ir(111) [40]. This synthesis method yields wire lengths of the order of 1000 formula units. The wires interlock to form wire carpets or wire spirals. Wires on graphene (Gr) were confirmed to be ferromagnetic semiconductors [41] and are a first case of a 1D organometallic structure coupling only through van der Waals interaction to their substrate. The orientation of the EuCot wire carpet islands on Gr/Ir(111) is random in-plane. This randomness hindered not only the full determination of magnetic anisotropies, but also a measurement of the band structure of the wires which is

expected to show dispersion along the wire axis.

With the present work we provide a new twist to the problem and thereby advance previous investigations on the magnetic and electronic structure of EuCot nanowires [41]. Using the uniaxial moiré of graphene on Ir(110) [42] to template a unique orientation of the EuCot nanowire carpets, access to the full anisotropic electronic and magnetic properties of these 1D objects and their 2D arrangement in wire carpets is obtained.

In previous angle-resolved photoemission spectroscopy (ARPES) investigations of organic single crystals [43, 44, 45, 46, 47, 48] and  $\pi$ -conjugated covalently bonded 1D polymers resting on vicinal Ag or Au surfaces [49, 50] the relevance of radiation damage was noted [48]. Radiation damage is also found in the present work to be inescapable for ARPES of 1D organometallic systems, which had not yet been investigated with this method.

## 2 Methods

Scanning tunneling microscopy (STM) measurements and *in situ* sample synthesis were conducted in Cologne in the ultrahigh vacuum system ATHENE with a base pressure below  $1 \cdot 10^{-10}$  mbar. In this system Gr on Ir(110) or Ir(111) was synthesized *in situ*. Gases are delivered through a gas dosing tube giving rise to a pressure enhancement by a factor of 80 compared to the pressure measured through a distant ion gauge and specified here. Sample cleaning was accomplished by exposure to  $1 \cdot 10^{-7}$  mbar oxygen at 1200 K when needed, cycles of noble gas sputtering (Ar, Xe), and brief annealing to 1500 K. Closed layers of the single-domain Gr phase were grown on Ir(110) by exposure to  $2 \cdot 10^{-7}$  mbar ethylene at 1500 K for 210 s. On Ir(111), Gr was grown by room temperature exposure to ethylene until saturation coverage was reached and subsequent thermal decomposition at 1500 K, resulting in well-oriented Gr islands, which are grown to a complete layer through an additional exposure  $1 \cdot 10^{-7}$  mbar ethylene for 600 s at 1200 K [51]. EuCot sandwich-molecular wires were grown on Gr/Ir(110) by sublimation of elemental Eu from a Knudsen cell with a deposition rate of  $1.1 \cdot 10^{17} \frac{\text{atoms}}{\text{m}^2\text{s}}$  in a background pressure of  $1 \cdot 10^{-8}$  mbar Cot for 30 s.

STM imaging was conducted at 300 K with a sample bias and tunneling current in the order of  $U_{\text{bias}} \approx -2$  V and  $I_t \approx 0.1$  nA. For STM image processing the software *WSxM* [52] was applied. To ensure Gr quality and for structural characterization low-energy electron diffraction (LEED) was used in an energy range of 30 – 150 eV. LEED patterns are contrast-inverted for better visibility.

ARPES measurements were conducted at the SGM-3 beamline at the synchrotron ASTRID2 in Aarhus [53], Denmark at a sample temperature of 35 K. The samples were grown *in situ* in an ultrahigh vacuum chamber (base pressure  $3 \cdot 10^{-10}$  mbar) connected to the beamline, and using the recipe as described above. Sample cleaning was accomplished by noble gas sputtering using Ne. The samples were checked *in situ* using the Aarhus STM mounted at the endstation for consistency with the homelab results. For the ARPES measurements, an approximate photon

(ph) flux of  $5 \cdot 10^{12} \frac{\text{ph}}{\text{s}}$  was used. The total photon exposure in  $\frac{\text{ph}}{\text{nm}^2}$  is specified for each data set shown and calculated as the product of photon flux, beam size on the sample ( $190 \times 90 \mu\text{m}^2$ ) and total irradiation time.

X-ray photoelectron spectroscopy (XPS) measurements were conducted at the University Duisburg-Essen for samples grown *in situ* using the recipe described above. EuCot (BaCot) multilayers on Gr/Ir(111) were grown by sublimation of elemental Eu (Ba) from a Knudsen cell with a deposition rate of  $1.3 \cdot 10^{15} \frac{\text{atoms}}{\text{m}^2\text{s}}$  ( $3.1 \cdot 10^{15} \frac{\text{atoms}}{\text{m}^2\text{s}}$ ) in a background pressure of  $5 \cdot 10^{-7}$  mbar Cot (without gas dosing tube) for 2700 s (1380 s). For the XPS measurements of the multilayer films a photon energy of 1486.6 eV (Al K- $\alpha$ ) was used. The EuCot and BaCot monolayer films on Gr/Ir(111) were checked with LEED and display diffraction rings consistent with the formation of sandwich-molecular wire carpets [40].

X-ray absorption spectroscopy (XAS) and X-ray magnetic circular dichroism (XMCD) measurements have been conducted at the X-Treme beamline and endstation at the Swiss Light Source synchrotron in Villigen, Switzerland [54]. The samples were prepared *in situ* in an ultrahigh vacuum chamber with a base pressure of  $4 \cdot 10^{-10}$  mbar directly connected to the endstation and using the recipe described above. During syntheses, sample cleaning was achieved by oxygen etching and noble-gas sputtering using argon. For consistency with homelab results, the prepared samples were checked with LEED and a variable-temperature STM. The presented XAS data were recorded at a sample temperature of 3 K and using circularly polarized light in the energy range of 1110 – 1250 eV, using the *total electron yield* detection mode. In order to reduce irradiation damage during measurements, the beam spot size on the sample was defocussed to  $0.3 \times 2.5 \text{ mm}^2$  and the approximate photon flux was  $\approx 3 \cdot 10^{-3} \frac{\text{ph}}{\text{nm}^2\text{s}}$ .

Our first-principles spin-polarized calculations were performed using the density functional theory (DFT) [55] and the projector augmented plane wave method [56] as implemented in the VASP code [57, 58]. For the plane wave expansion of the Kohn-Sham wave functions [59] we used a cut-off energy of 500 eV. For the EuCot monolayer, the Brillouin zone was sampled with a  $(46 \times 8 \times 1)$  k-point mesh, i.e. 46 k-points in the direction of the EuCot wire and 8 k-points in the direction perpendicular to the EuCot (BaCot) wires. We carried out the structural relaxation using the vdW-DF2 [60] with a revised Becke (B86b) exchange [61, 62, 63] functional to properly account for the nonlocal correlation effects like van der Waals interactions. The analysis of the electronic structures was done using the PBE exchange-correlation energy functional [64]. We used the GGA + U approach [65] to correctly account for the orbital dependence of the Coulomb and exchange interactions of the Eu 4f states. We performed several simulations in which we varied systematically the Hubbard parameter ( $U_{\text{eff}}$ ) from 3.5 – 7.2 eV. The supercell contained 15 Å of vacuum in the z direction. The EuCot and BaCot monolayers were modelled with an intra-wire periodicity of 4.35 Å and an inter-wire spacing of 6.80 Å.

### 3 Results and discussion

**Structure of wire carpet films:** Figure 1a displays an STM topograph of an oriented monolayer EuCot wire carpet grown on Gr/Ir(110), with the wires along the [001] direction. In the inset a ball model of the interlocking wires and the unit cell (green rhomboid) are overlaid on a molecular resolution topograph. In the corresponding LEED pattern of Figure 1b the first order reflections of the wire carpet are encircled blue and the reciprocal lattice vectors  $\vec{b}_1$  and  $\vec{b}_2$  are indicated by black arrows. The other visible LEED reflections stem from the Gr/Ir(110) substrate. A topograph of an EuCot carpet with second layer islands is shown in Figure 1c. A preferential

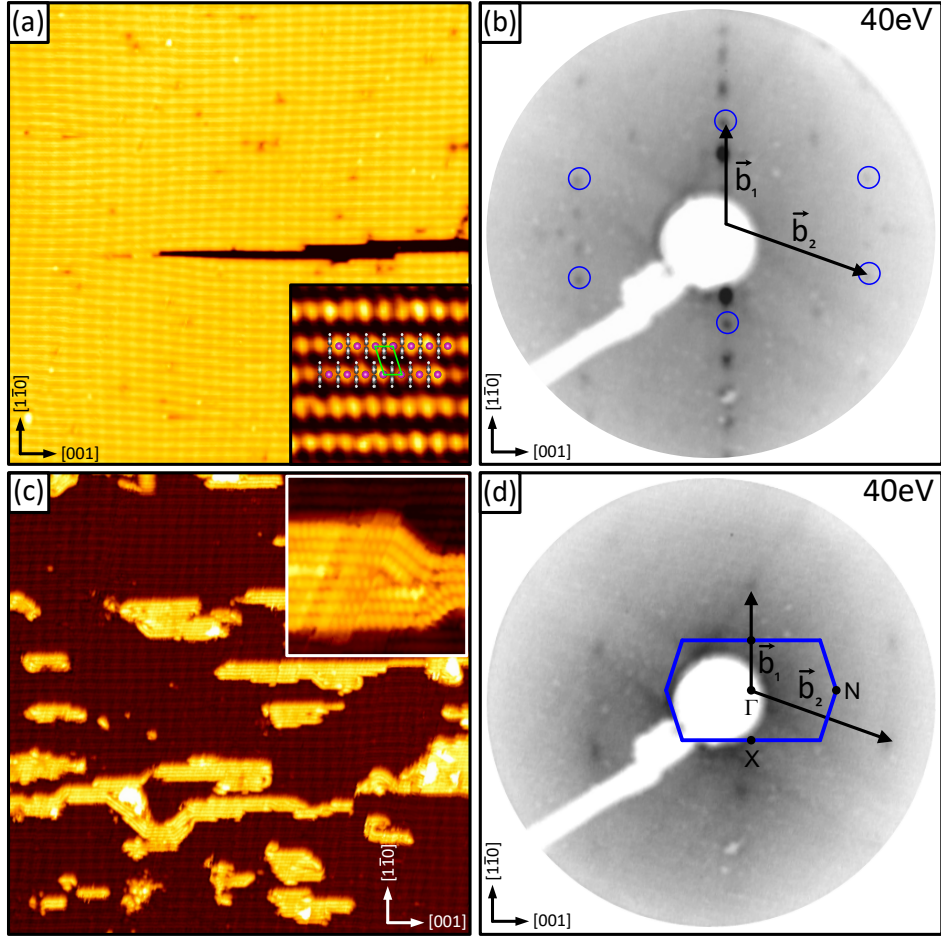


Figure 1: (a) STM topograph ( $900 \times 900 \text{ \AA}^2$ ) of a ML EuCot wire carpet on Gr/Ir(110) with global wire orientation along [001]. Inset: corresponding molecular resolution STM topograph ( $30 \times 30 \text{ \AA}^2$ ) with ball model and wire carpet unit cell indicated by green rhomboid. (b) 40 eV LEED pattern corresponding to (a). First order EuCot carpet reflections are encircled blue, reciprocal lattice vectors  $\vec{b}_1$  and  $\vec{b}_2$  are indicated by black arrows. (c) STM topograph ( $900 \times 900 \text{ \AA}^2$ ) of EuCot wire carpet on Gr/Ir(110) with second layer wire islands still aligned along the [001] direction. Inset: molecular resolution STM topograph ( $100 \times 100 \text{ \AA}^2$ ) of second layer wire island. (d) 40 eV LEED pattern of a 5 ML EuCot film on Gr/Ir(110). The first Brillouin zone of the 2D wire carpet with high symmetry points  $X$ ,  $\Gamma$  and  $N$  is indicated in blue. Tunneling parameters are (a)  $U_{\text{bias}} = -1.74 \text{ V}$  and  $I_t = 0.08 \text{ nA}$ , (c)  $U_{\text{bias}} = -2.60 \text{ V}$  and  $I_t = 0.03 \text{ nA}$ .

orientation of the wires in the second layer along the  $[001]$  direction is still present as underlined by the molecular resolution topograph of intact wires in the inset. STM topographs of thicker EuCot wire carpet films could not be obtained due to the poor conductivity of the film, resulting in tip-induced film changes. Figure 1d displays the LEED pattern of an  $\approx 5$  ML thick EuCot wire film. Although less sharp than in Figure 1b, the first order EuCot film reflections are present, while due to the thick EuCot film the substrate reflections are no more visible.

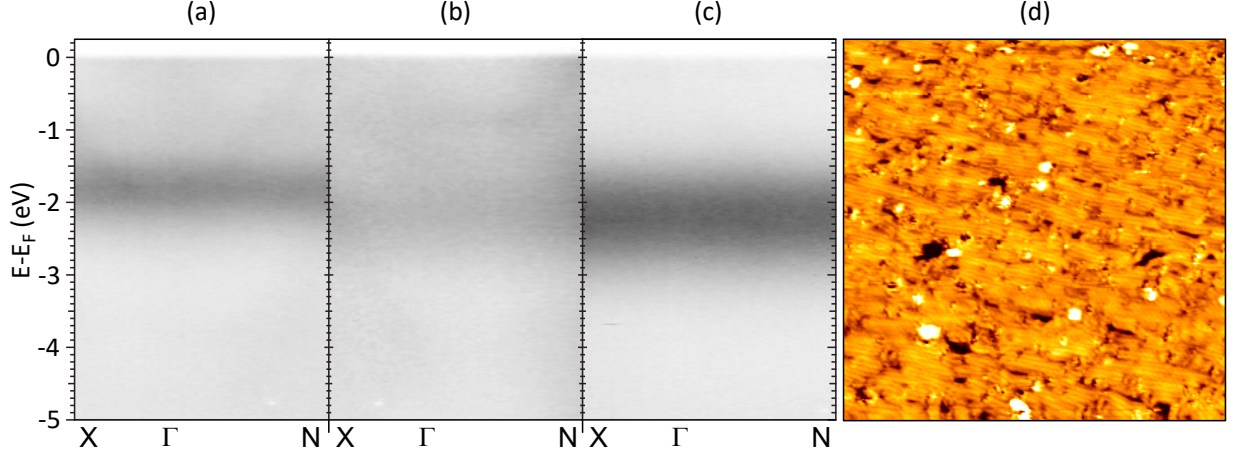


Figure 2: (a) Angle-resolved photo emission spectrum along  $X - \Gamma - N$  for a 1 ML EuCot film recorded at a photon energy of 110 eV. The photon beam is moved over the sample limiting the photon dose at each location to  $\approx 6 \cdot 10^3 \frac{\text{ph}}{\text{nm}^2}$ . A flat band is visible at  $-1.85$  eV. (b) ARPES spectrum along  $X - \Gamma - N$  for a 1 ML EuCot film recorded at a photon energy of 100 eV. The flat band appears more blurred and is located in energy  $-2.25$  eV. The photon beam is not moved over the sample and the integrated photon dose at the measurement location is  $\approx 3 \cdot 10^5 \frac{\text{ph}}{\text{nm}^2}$ . (c) ARPES spectrum along  $X - \Gamma - N$  for a 4 ML EuCot film recorded at a photon energy of 100 eV. The flat band is pronounced and located in energy also at  $-2.25$  eV. The photon beam is not moved over the sample and the integrated photon dose at the measurement location is  $\approx 1.2 \cdot 10^7 \frac{\text{ph}}{\text{nm}^2}$ . (d) STM topograph ( $500 \times 500 \text{ \AA}^2$ ) of a 1 ML thick EuCot wire carpet after a photon dose of  $\approx 6 \cdot 10^3 \frac{\text{ph}}{\text{nm}^2}$  in each sample location. Tunneling parameters are  $U_{\text{bias}} = -2.12$  V and  $I_t = 0.14$  nA.

**ARPES measurements of wire carpet films:** ARPES measurements of globally aligned wire carpet films were conducted with the goal to measure the band structure of the wire carpet islands. Specifically along the wire axis, i.e. along the  $\Gamma - N$  direction, dispersion could be expected. Figure 2a displays the measured band structure for a 1 ML thick EuCot film along the wires in  $\Gamma - N$  direction and normal to the wires in  $\Gamma - X$  direction. The spectrum displays a single and flat band at  $-1.85$  eV with a full width at half maximum (FWHM) of  $(1.0 \pm 0.2)$  eV. The entire  $E(\vec{k})$  slice represented in Figure 2a is composed of  $\approx 30$  energy-scans, each at fixed polar angle  $\theta$ . In order to minimize the effects of radiation damage, after each scan the beam (dimension  $190 \times 90 \mu\text{m}^2$ ) was moved to a fresh, non-illuminated sample position. The photon dose at each location is  $\approx 6 \cdot 10^3 \frac{\text{ph}}{\text{nm}^2}$ .

When the photon beam is not moved over the sample surface, but resides in the same location

for an extended measurement, the situation changes. Figure 2b displays the same  $E(\vec{k})$  slice for a sample of the same EuCot film thickness as shown in Figure 2a, but without scanning and with an integrated photon dose larger by a factor of 50 at the location of measurement. The flat band is shifted down in energy to  $-2.25$  eV and appears blurred. For a thicker 4 ML EuCot film without scanning of the beam the  $E(\vec{k})$  slice is represented in Figure 2c. The dispersionless band becomes more pronounced and remains at  $-2.25$  eV. The FWHM of  $(1.5 \pm 0.3)$  eV is increased compared Figure 2a. The integrated photon dose at the location of photoemission is larger by factor of 2000 compared to Figure 2a.

Figure 2d displays an STM topograph of a sample where by moving the illuminating photon beam over the entire sample, to good approximation each location has been subject to a photon dose of  $\approx 6 \cdot 10^3 \frac{\text{ph}}{\text{nm}^2}$ . Clear signs of degradation of the EuCot carpet are already visible, namely dark holes and bright spots that are present in larger concentration than prior to illumination with photons (compare Figure 1a). Still in most areas the wires are intact, but display a shorter length due to the defects. We tentatively conclude that the ARPES slice represented in Figure 2a is from a marginally damaged still 'close to intact' EuCot film as represented by Figure 2d, while the downshift and broadening of the flat band as found for much larger photon doses in Figures 2b and 2c are attributed to radiation damage effects. This topic will be analyzed in more detail in the discussion.

**Electronic structure calculations compared to experiments:** To understand the origin of the flat band, we conducted DFT calculations and additional XPS measurements. The calculated band structure for a 1 ML EuCot carpet is shown in Figure 3a along  $X - \Gamma - N$ . Comparison with Figure 3b makes obvious that in the occupied states between  $-3$  eV and  $-1.5$  eV an Eu 4f band without dispersion and carbon  $\pi$  bands with weak dispersion along  $\Gamma - N$  are present. The absence of dispersion for the 4f band at  $-1.85$  eV is consistent with the localized nature of the 4f wave functions, which are close to the Eu nucleus and do not overlap. In the larger scale representation of the PDOS in Figure 3c it is apparent that the 4f peak at  $-1.85$  eV dominates the DOS and should give rise to the strongest signal in the experiment. Figure 3d shows the angle-integrated ARPES data of the 1 ML EuCot film with a strong peak at  $-1.9$  eV, which is in correspondence with the flat band at  $-1.85$  eV of the ARPES data shown in Figure 2a. It can be attributed to the 4f states shown in the PDOS, as highlighted by the green dotted line. Also the two lower lying peaks of the angle integrated ARPES data shown in Figure 3d centered at  $-6.4$  eV and  $-8.9$  eV agree with the position of the  $\pi$  and  $\sigma$  states in the PDOS as highlighted by the grey dotted lines.

The set of three peaks in the angle-integrated ARPES data at  $-1.9$  eV,  $-6.4$  eV and  $-8.9$  eV was used to map out the proper choice of the Hubbard  $U$ , which was systematically varied from  $3.5$  eV to  $8.2$  eV (compare Figure S1 of the SI). The value of  $U = 3.5$  eV of the calculated PDOS agrees best with the experimentally observed peaks.

In Figure 3e, we show the calculated band structure for a 1 ML BaCot wire carpet films, which looks similar to the one for EuCot (STM and LEED of BaCot wire carpets on Gr/Ir(111) can

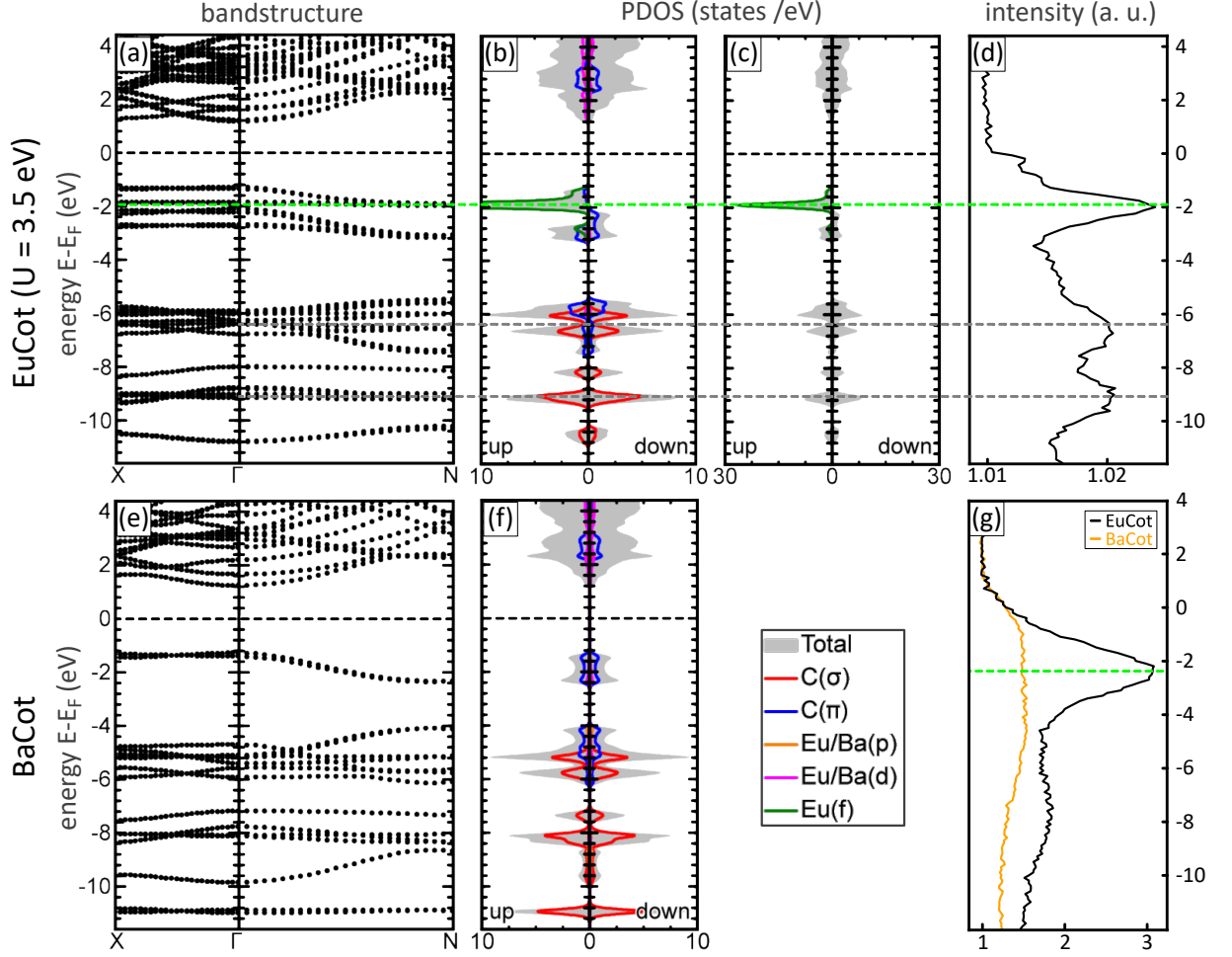


Figure 3: EuCot ML: (a) DFT band structure of 1 ML EuCot film along  $X - \Gamma - N$ . (b) Spin-polarized PDOS. (c) Larger scale spin-polarized PDOS. (d) Angle-integrated ARPES data of a 4 ML EuCot film. Position of 4f peak is indicated by dotted green line in (a)-(d). (e) DFT band structure of 1 ML BaCot film along  $X - \Gamma - N$ . (f) Spin-polarized PDOS. (g) XPS data of EuCot (black) and BaCot (orange) multilayer film with thickness of  $\approx 10$  ML. The position of the 4f peak is indicated by dotted green line. An effective Hubbard  $U$  of 3.5 eV ( $U = 4.4$  eV and  $J = 0.9$  eV) was used in the calculations. ARPES data were obtained at a photon energy  $E_{h\nu} = 130$  eV at  $T = 35$  K. XPS data were obtained at a photon energy  $E_{h\nu} = 1486.6$  eV (Al K- $\alpha$ ) at  $T = 300$  K. Photon exposure for (d) is  $\approx 6 \cdot 10^4 \frac{\text{ph}}{\text{nm}^2}$  at a photon energy of 130 eV.

be found in Figure S2 of the SI). In the corresponding PDOS in Figure 3f the 4f peak is missing, while the  $\pi$  and  $\sigma$  states are just slightly shifted in energy. Further, we also measured XP spectra on 10 ML EuCot and BaCot films shown in Figure 3g. For the EuCot spectrum (black line) we observe a large peak at  $-2.2$  eV, while this peak is missing in the BaCot spectrum, which is clear evidence that the flat band in ARPES at energies between  $-1.85$  eV and  $-2.25$  eV is due to the Eu 4f states.

**Hybrid electronic states and energetic position of 4f band:** The electronic configuration of Ba ( $5p^6 4f^0 5d^0 6s^2$ ) and Eu ( $5p^6 4f^7 5d^0 6s^2$ ) differs only in the occupation of 4f states. While the 4f shell is empty in Ba, it is half filled for Eu. Therefore, by comparison of the binding



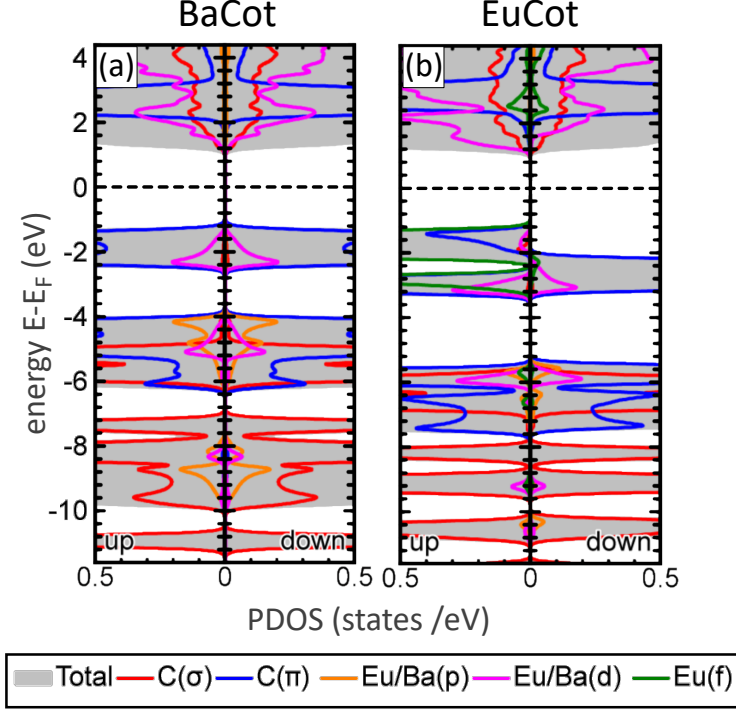


Figure 4: Detailed plot of spin-polarized PDOS (a) BaCot and (b) EuCot monolayers. Projections of the total DOS (shaded grey) onto the specified bands of C, Eu, and Ba are indicated in the legend. An effective Hubbard  $U$  of 3.5 eV ( $U = 4.4$  eV and  $J = 0.9$  eV) to describe the Eu 4f states was used in the calculations.

in EuCot and BaCot wires an insight into the effect of the 4f orbitals on the electronic structure and related energetic levels is gained.

In a simplified chemical picture, when Ba and Eu atoms interact with the cyclooctatetraene ( $C_8H_8$ , Cot) molecules, the two 6s electrons are transferred to the organic ligand. As a consequence, the binding within the BaCot and EuCot wires can be described as being of electrostatic nature and within this standard ionic picture a formal oxidation state of “2+” is expected for the metal atoms (i. e.  $Ba^{2+}$ ,  $Eu^{2+}$ ) and “2-” for the organic ligand (i.e.  $Cot^{2-}$ ). For an  $Eu^{2+}$  ion, one would expect the electrons in the  $4f^7$  channel to localize closer to the atomic core and therefore to lie at lower energies (as compared to charge-neutral Eu atoms) and be purely atomic-like.

However, our theoretical simulations performed on BaCot and EuCot monolayers demonstrate that the specific chemical environment introduced by the  $\pi$ -electron cloud of the Cot ligands around the metallic atoms changes the Ba and Eu valence electronic configurations. The binding is not purely of electrostatic nature but contains also a hybridization component between the  $\pi$ -electron cloud and the metal orbitals. This hybridization results in an uplift of the energetic position of the 4f states, as outlined below.

Figure 4 shows a magnified view of the spin-polarized PDOS for BaCot and EuCot ML films. As apparent from Figure 4a, for the BaCot ML film in both spin-channels the hybrid electronic states at about  $-2$  eV are dominated by the carbon  $\pi$ -like orbitals (blue), but also include a small



contribution of Ba 5d states (cyan). Similarly, also for the EuCot ML film in the spin-down channel the hybrid electronic states at  $\approx -3$  eV are dominated by the carbon  $\pi$ -like orbitals (blue), but with a small contribution of Eu 5d states (cyan, , compare Figure 4b). In the spin-up channel, additionally Eu 4f states (green) are energetically aligned with these EuCot hybrid electronic states, i.e. some hybrid states have a large 4f and small  $\pi$  contribution while other hybrid states have a larger  $\pi$  and smaller 5d and 4f character.

The projection of the total charge density in a sphere around the metal atom onto the s, p, d and f atomic-like orbitals leads to the following electronic occupation numbers: 0.08 in s, 5.64 in p, 0.43 in d and 0.00 in f for Ba and 0.04 in s, 5.85 in p, 0.44 in d and 6.88 in f for Eu, respectively. The magnetic moment per atom is  $0.00 \mu_B$  for Ba and  $6.95 \mu_B$  for Eu atoms (5p:  $-0.01 \mu_B$ , 6s:  $+0.01 \mu_B$ , 5d:  $+0.07 \mu_B$  and 4f:  $6.88 \mu_B$ ).

Thus, the partial occupancies together with the energetic alignment of  $\pi$ , 5d, and 4f states indicate that in addition to the electrostatic interaction a hybridization occurs between Cot and Ba as well as between Cot and Eu. For Ba it is due to the overlap of the Cot  $\pi$  orbitals and Ba 5d states that have long tails extending further away from the metal ion. For Eu this hybridization is mediated through atomic hybrid orbitals with mixed 5d and 4f character rather than pure 5d character as for Ba. In other words, around the Eu atom, the local chemical environment provided by the Cot ligand is modified so that the atomic 5d and 4f states are allowed to mix while this is forbidden for an isolated atom. These atomic-like d-f states have a large 4f atomic character close to the nucleus and long tails extending further away from the nucleus, originating from the Eu 5d atomic-like orbitals. As a consequence of the long spatial extent, these Eu atomic-like d-f orbitals can overlap and hybridize with the Cot  $\pi$  orbitals.

**XAS measurements:** To further access the electronic and magnetic properties of EuCot nanowires on Gr/Ir(110), XAS and XMCD data have been measured at the Eu  $M_{5,4}$  edges, probing the properties of the 4f states. Figure 5a displays the averaged XAS of the Eu  $M_{5,4}$  edges. Comparison of the spectral shape to literature data[66] and multiplet calculations prove a  $4f^7$  electronic configuration of the Eu in the EuCot nanowires. The spectrum is nearly identical to the one obtained from EuCot wire carpet islands grown on Gr/Ir(111) [41]. The normalized XMCD signal in Figure 5b provides information about the magnetic moment of the Eu. By applying sum-rule analysis [67, 68] the spin and orbital magnetic moment of the Eu can be extracted. Here, we obtain a spin moment of  $\mu_S = (7.2 \pm 0.6) \mu_B$  and orbital moment of  $\mu_L = (0.0 \pm 0.4) \mu_B$ . The dipolar term  $\langle T_z \rangle$  is approximated to be zero, based on the half-filled 4f shell [68, 69, 70]. The resulting moments are in good agreement with the expectation for atomic Eu with  $\mu_S = 7 \mu_B$  and  $\mu_L = 0 \mu_B$  and the results for EuCot wire carpets adsorbed on Gr/Ir(111) in ref. [41]. Figure 5c displays the field-dependent XMCD signal at the  $M_5$  edge normalized to the pre-edge, which is proportional to the magnetic moment. For a better overview, the up and down branches of each orientation are averaged. The magnetization curves of EuCot nanowires on Gr/Ir(110) are measured for normal ( $\theta = 0^\circ$ ) and grazing ( $\theta = 60^\circ$ ) incidence at  $T = 3$  K. Saturation is reached at  $\approx 4$  T for both orientations. The zero field susceptibility for grazing incidence along

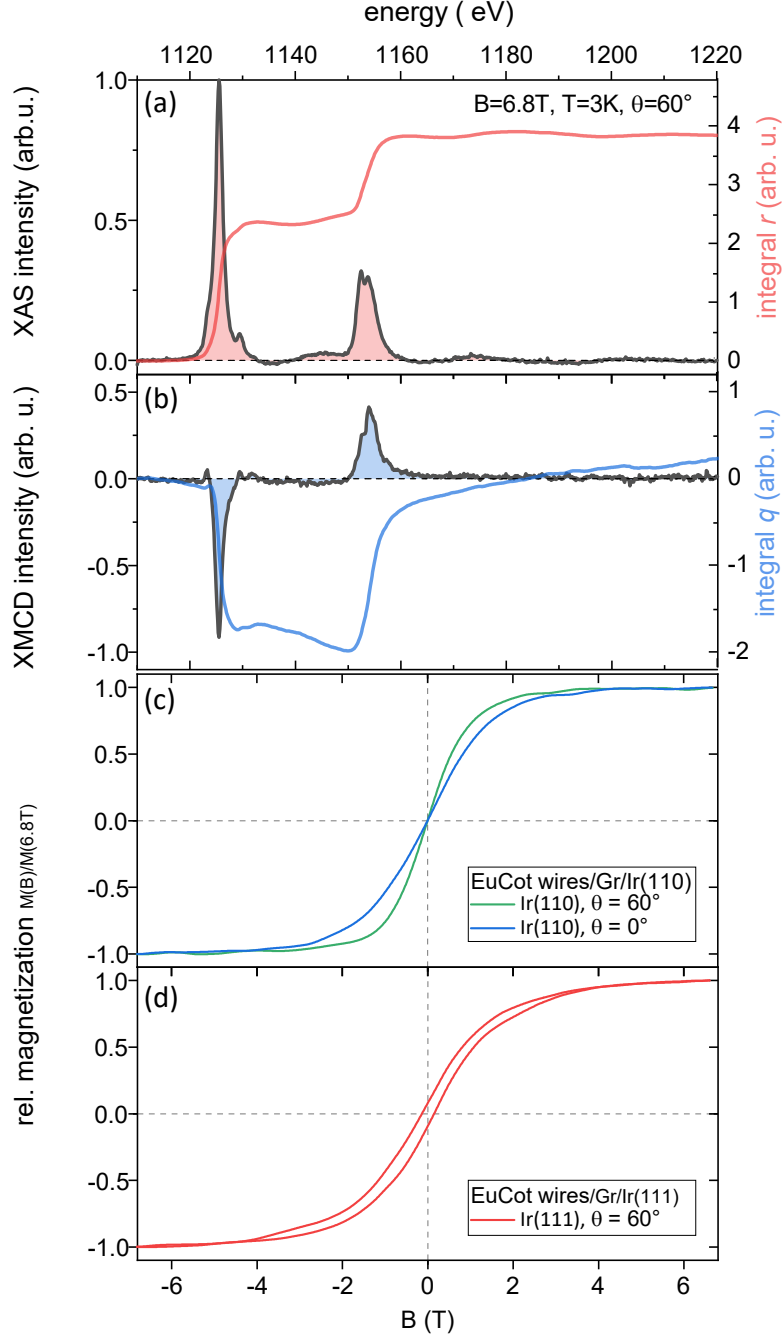


Figure 5: (a) Average XAS  $\frac{1}{2}(\mu_+ + \mu_-)$  of the Eu  $M_5$  and  $M_4$  edges measured at grazing incidence  $\theta = 60^\circ$  off surface normal tilted into the  $[001]$  direction,  $T = 3$  K, and  $B = 6.8$  T (grey line). The red line represents the integral over the averaged XAS. (b) Normalized XMCD  $(\mu_+ - \mu_-)$  (black line) and its integral (blue line). (c) Averaged and smoothed magnetization curves based on the field dependent XMCD signal of the Eu  $M_5$  edge for grazing and normal incidence at  $T = 3$  K. Grazing incidence is along the  $[001]$  direction, i.e. along the wire axis. (d) Comparison to the averaged and smoothed XMCD magnetization curves of EuCot nanowires/Gr/Ir(111) at grazing incidence and  $T = 3$  K.

the  $[001]$  direction is  $\chi_{60^\circ-[001]} = (7.3 \pm 0.6) \frac{\mu_B}{T}$  which is larger by a factor of 1.6 compared to the one at normal incidence of  $\chi_{0^\circ} = (4.6 \pm 0.4) \frac{\mu_B}{T}$ . In comparison, the zero field susceptibility  $\chi_{60^\circ-[1\bar{1}0]}$  measured at grazing incidence along the  $[1\bar{1}0]$  direction — i.e. normal to the wire axis — is close to  $\chi_{0^\circ}$ , only larger by a factor of 1.2. Thus the easy axis of magnetization is along the  $[001]$  direction.

Neither for grazing nor for normal X-ray incidence the magnetization curves for EuCot wire carpets on Gr/Ir(110) in Figure 5c display a hysteresis. This is surprising in view of the fact that for EuCot/Gr/Ir(111) represented by Figure 5d hysteresis is found at grazing incidence. The EuCot/Gr/Ir(111) data shown were measured subsequently with the same set-up under the same conditions as the EuCot/Gr/Ir(110) data. The data for EuCot/Gr/Ir(111) in Figure 5d agree well with the results of ref. [41]. In previous work we established that through radiation damage, the hysteresis loop for EuCot wire carpets on Gr/Ir(111) disappears and additional changes in the spectral shape of the XAS take place, which are absent here. Therefore, the observed hysteresis in the EuCot wire carpet on Gr/Ir(111) indicates the absence of significant radiation damage during XAS in the present measurements for both substrates.

**Discussion:** One of the goals of this work was to measure the band structure of the EuCot wires. Band structure measurements of 1D organometallic systems have not been conducted before and our measurements provide evidence that the determination of band structures of organometallic films built from 1D objects is demanding. In fact, the organometallic EuCot wires are subject to radiation damage: a LEED pattern taken with a conventional LEED set-up, rather than with a microchannelplate-LEED, fades away within a minute and the STM and ARPES data shown in Figure 2 document also a fluence-dependent damage under photoemission conditions. It is obvious that low-energy electrons in the energy range at and below 100 eV cause radiation damage. Whether this is the exclusive effect or whether also X-rays themselves cause damage cannot be answered on the basis of the present data. STM data after scanning the sample with a photon fluence  $\approx 6 \cdot 10^3 \frac{\text{ph}}{\text{nm}^2}$  exhibit already first signs of damage. However, extended wire segments are still visible and therefore we are convinced that the spectrum displayed in Figure 2a is still close to a situation without radiation damage. In any case, scanning the X-ray beam over the sample turned out to be an effective tool to limit radiation damage.

There is no single obvious explanation for the downshift and broadening of 4f states due to radiation damage. We speculate that decomposition of EuCot leads to the formation of metallic Eu, which is known to locally n-dope Gr, i.e. to locally move the Fermi level in Gr up (or its work function down) [71]. This would imply a corresponding shift of the Fermi level within the semiconducting EuCot wires. Because of the low density of states in Gr, one donated electron per 200 C atoms would be sufficient to explain the observed Fermi level shift of about 0.4 eV [72], a number that seems to be compatible with the defect pattern visible in the STM topograph of Figure 2d. The local variation of the doping level would then give a simple explanation for the observed broadening of the 4f states.

The position of the 4f states about -1.85 eV below the Fermi level is within the range of what has

been found for Eu metal [73] and Eu oxide systems [74]. One of the nice features of our experiments is the experimental determination of the proper Hubbard  $U$  to be used in organometallic compounds with Eu. Tuning the relative position of the 4f peak and the lower-lying peaks of the PDOS to the ARPES data through varying the value of  $U$  (shown in Figure S1 in the SI) is a straightforward way to access the magnitude of this quantity, which is otherwise difficult to obtain. It should also be noted here that the detailed PDOS in Figure 4b shows a slight hybridization of the Eu 4f states with the Eu 5d and the carbon  $\pi$  states, aligning their positions. The absence of dispersing  $\pi$ -derived bands in our ARPES data can be rationalized simply when considering the relative weights of the different states in the PDOS as presented in Figure 3b and 3c. The 4f-related peak in the PDOS is about a factor 30 higher than any peak related to  $\pi$  states within the energy range investigated by ARPES. Therefore, the lack of a dispersing  $\pi$ -derived band could simply be an intensity problem. A careful evaluation of polarization-dependent matrix elements for both the f states and the  $\pi$  system together with the experimental possibility to change the polarization conditions, ideally with the option to change both the light polarization and the angle of incidence, could possibly improve this intensity ratio to some degree.

EuCot wire carpets on Gr/Ir(111) were shown to be ferromagnetic insulators with an open magnetization loop at 7 K [41]. On Gr/Ir(111) the EuCot carpet islands form in close-to-random orientation, averaging out any in-plane anisotropy and reducing the maximum susceptibility. Therefore, one expects for a globally aligned EuCot wire carpet film an (i) increased susceptibility when the projection of magnetic field onto the surface is along the easy axis and (ii) consequently for the same orientation of the magnetic field also a larger hysteresis of the magnetization as compared to a film of randomly oriented EuCot wire carpet islands.

In the experiment we indeed find that with respect to (i) the measured susceptibility becomes anisotropic in-plane. While the susceptibility  $\chi_{60^\circ-[1\bar{1}0]}$  is close to  $\chi_{0^\circ}$ ,  $\chi_{60^\circ-[001]}$  is larger by a factor of  $\approx 1.6$ . This is clear evidence for an easy magnetic axis along the wire, as it would for instance be favored by dipolar interactions [41].

With respect to our expectation (ii) we do not find a larger hysteresis. To the contrary, the hysteresis vanishes as shown in Figure 5 and only paramagnetic behavior is observed at 3 K. We speculate, that this suppression of the magnetic hysteresis is caused by the interaction of the wire carpet with the substrate. In order to avoid misunderstandings, we point out that also Gr on Ir(110) is an inert substrate, in this respect comparable to Gr on Ir(111). Binding of the wires to the substrate is due to van der Waals interactions while hybridization of the upright standing Cot molecules in the wires with Gr can be ruled out. Nevertheless, three features differ for the wires on Gr/Ir(110) compared to Gr/Ir(111).

First, wires on Gr/Ir(111) are bent with a periodicity of 2.5 nm and a corrugation of 0.35 Å or more [75], while the corrugation along the [001] direction on Gr/Ir(110) is marginal and below 0.1 Å. Although the absolute curvature is small, it implies a variation in the coupling of neighboring Eu atoms through the Cot molecule and thereby might affect magnetic properties.

Second, the density of states within Gr will affect the binding situation with the EuCot wires.

The binding within EuCot wires is largely of ionic type, between positively charged  $\text{Eu}^{2+}$  and negatively charged  $\text{Cot}^{2-}$  ions. Besides the van der Waals interaction also the electrostatic field around the ionically bound wires causes them to interlock. A variation of the density of states in Gr around the Fermi level will modify the screening of the electrostatic interactions between the wire ions. Thus the binding strength within the EuCot wire is affected, which in turn may modify the magnetic coupling of Eu ions through the Cot molecules.

Lastly, also charge transfer from the substrate to the EuCot wires — which due to the higher density of states at the Fermi level is more likely for the case of chemisorbed Gr on Ir(110) than for physisorbed Gr on Ir(111) — will also affect binding and magnetism within the EuCot wires. In DFT model calculations we found a clear effect of charge-donating and charge-withdrawing side groups of the Cot molecules within the EuCot wires on magnetic ordering.

Based on the last two arguments, one might speculate that electronically intact, but strongly n-doped or p-doped 'metallic' Gr, could suppress the open magnetization loop in a similar way as found on Gr/Ir(110). Indeed, when Gr/Ir(111) is intercalated by Yb, a strong n-dopant for Gr due to its two 6s electrons, the open magnetization curve is also suppressed (compare Figure S3 in the SI). Still, the disappearance of the hysteresis cannot unequivocally be traced back to a single physical reason.

## 4 Conclusion

Uniaxial alignment of EuCot wires on Gr along the [001] direction of the Ir(110) substrate is imposed by the Gr moiré and persists from submonolayer islands up to multilayer films. This alignment provides access to the structural, electronic, and magnetic properties of such wire systems using spatially-averaging techniques.

Contrary to expectation, ARPES could not detect dispersing  $\pi$ -derived bands, but only a flat band 1.85 eV below the Fermi energy. Using complementary DFT calculations and XPS measurements we attribute this flat band to the Eu 4f states. By comparing the position of the 4f states with the lower-lying  $\sigma$  bands we pinpoint the Hubbard  $U$  of this system to be close to  $U = 3.5$  eV. A detailed PDOS analysis indicates hybridization of the  $\pi$  and 4f states, which effectively lifts the 4f band up in energy. The absence of dispersing  $\pi$ -derived bands may be due to their much lower DOS, which in combination with quick decomposition through radiation damage leaves them unobservable. Our results are yet another example that radiation damage must be carefully considered, when investigating organometallic systems with energetic electrons or photons.

For the magnetic properties of the oriented EuCot wire sample we find —consistent with EuCot/Gr/Ir(111)— that the Eu ion has  $[\text{Xe}]4f^7 6s^0$  configuration, resulting in a magnetic moment of  $7 \mu_B$ . Magnetization close to the wire axis displays the highest susceptibility, making plain that the easy magnetization axis is along the wires. Magnetic hysteresis observed on Gr/Ir(111) vanishes for the EuCot wire carpet on Gr/Ir(110). We speculate that enhanced screening for the

more 'metallic' Gr/Ir(110) substrate affects the ionic binding of the wires which in turn might influence their subtle magnetic ordering.

## Supporting information available

Figure S1: Comparison of EuCot ML theoretical band structure and DOS with angle-integrated ARPES data for different values of Hubbard  $U$ . Figure S2: STM topograph and LEED pattern of BaCot wire carpets on Gr/Ir(111). Figure S3: Magnetization curve of EuCot wires on Gr/Yb/Ir(111) at grazing incidence.

## Acknowledgements

This work was funded by the Deutsche Forschungsgemeinschaft (DFG, German Research Foundation) within the project 'Sandwich molecular nanowires: on-surface synthesis, structure and magnetism' (MI 581/23-1, AT 109/5-1 and WE 2623/17-1). V. C. and N. A. acknowledge additional DFG support within CRC1238, project no. 277146874 - CRC 1238 (subproject C01). We gratefully acknowledge the Gauss Centre for Supercomputing (GCS) for providing computing time through the John von Neumann Institute for Computing (NIC) on the GCS share of the supercomputer JURECA at Jülich Supercomputing Centre (JSC). This work was also supported by VILLUM FONDEN via the Centre of Excellence for Dirac Materials (Grant No. 11744).

## References

- [1] S. Sanvito, 'Molecular spintronics', *Chem. Soc. Rev.* **40**, 3336 (2011).
- [2] J. D. Rinehart, M. Fang, W. J. Evans and J. R. Long, 'A  $N_2^{3-}$  radical-bridged terbium complex exhibiting magnetic hysteresis at 14 K', *J. Am. Chem. Soc.* **133**, 14236 (2011).
- [3] R. Westerström, A.-C. Uldry, R. Stania, J. Dreiser, C. Piamonteze, M. Muntwiler, F. Matsui, S. Rusponi, H. Brune, S. Yang, A. Popov, B. Büchner, B. Delley and T. Greber, 'Surface aligned magnetic moments and hysteresis of an endohedral single-molecule magnet on a metal', *Phys. Rev. Lett.* **114**, 087201 (2015).
- [4] C. Wäckerlin, F. Donati, A. Singha, R. Baltic, S. Rusponi, K. Diller, F. Patthey, M. Pivetta, Y. Lan, S. Klyatskaya, M. Ruben, H. Brune and J. Dreiser, 'Giant hysteresis of single-molecule magnets adsorbed on a nonmagnetic insulator', *Adv. Mater.* **28**, 5195 (2016).
- [5] R. Baltic, F. Donati, A. Singha, C. Wäckerlin, J. Dreiser, B. Delley, M. Pivetta, S. Rusponi and H. Brune, 'Magnetic properties of single rare-earth atoms on graphene/Ir(111)', *Phys. Rev. B* **98**, 024412 (2018).
- [6] K. Diller, A. Singha, M. Pivetta, C. Wäckerlin, R. Hellwig, A. Verdini, A. Cossaro, L. Floreano, E. Vélez-Fort, J. Dreiser, S. Rusponi and H. Brune, 'Magnetic properties of on-surface synthesized single-ion molecular magnets', *RSC Adv.* **9**, 34421 (2019).
- [7] F. Donati, S. Rusponi, S. Stepanow, L. Persichetti, A. Singha, D. M. Juraschek, C. Wäckerlin, R. Baltic, M. Pivetta, K. Diller, C. Nistor, J. Dreiser, K. Kummer, E. Velez-Fort, N. A. Spaldin, H. Brune and P. Gambardella, 'Unconventional spin relaxation involving localized vibrational modes in Ho single-atom magnets', *Phys. Rev. Lett.* **124**, 077204 (2020).

- [8] G. Serrano, L. Poggini, M. Briganti, A. L. Sorrentino, G. Cucinotta, L. Malavolti, B. Cortigiani, E. Otero, P. Saintavit, S. Loth, F. Parenti, A.-L. Barra, A. Vindigni, A. Cornia, F. Totti, M. Mannini and R. Sessoli, ‘Quantum dynamics of a single molecule magnet on superconducting Pb(111)’, *Nat. Mater.* **19**, 546 (2020).
- [9] C.-H. Chen, L. Spree, E. Koutsouflakis, D. S. Krylov, F. Liu, A. Brandenburg, G. Velkos, S. Schimmel, S. M. Avdoshenko, A. Fedorov, E. Weschke, F. Choueikani, P. Ohresser, J. Dreiser, B. Büchner and A. A. Popov, ‘Magnetic hysteresis at 10 K in single molecule magnet self-assembled on gold’, *Adv. Sci.* **8**, 2000777 (2021).
- [10] J. Dreiser, C. Wäckerlin, M. Buzzi, K. S. Pedersen and J. Bendix, ‘Island formation of Er(trensal) single-ion magnets on graphene observed on the micrometer scale’, *RSC Adv.* **11**, 9421 (2021).
- [11] S. Stepanow, N. Lin, D. Payer, U. Schlickum, F. Klappenberger, G. Zoppellaro, M. Ruben, H. Brune, J. Barth and K. Kern, ‘Surface-assisted assembly of 2D metal–organic networks that exhibit unusual threefold coordination symmetry’, *Angew. Chem. Int. Ed.* **46**, 710 (2007).
- [12] S. Vijayaraghavan, D. Eciija, W. Auwärter, S. Joshi, K. Seufert, M. Drach, D. Nieckarz, P. Szabelski, C. Aurisicchio, D. Bonifazi and J. V. Barth, ‘Supramolecular assembly of interfacial nanoporous networks with simultaneous expression of metal–organic and organic-bonding motifs’, *Chem. Eur. J.* **19**, 14143 (2013).
- [13] J. I. Urgel, B. Cirera, Y. Wang, W. Auwärter, R. Otero, J. M. Gallego, M. Alcamí, S. Klyatskaya, M. Ruben, F. Martín, R. Miranda, D. Eciija and J. V. Barth, ‘Surface-supported robust 2D lanthanide-carboxylate coordination networks’, *Small* **11**, 6358 (2015).
- [14] C. Wäckerlin and K.-H. Ernst, ‘Autocatalytic surface explosion chemistry of 2D metal-organic frameworks’, *J. Phys. Chem. C* **125**, 13343 (2021).
- [15] Z. Yang, C. Lotze, K. J. Franke and J. I. Pascual, ‘Metal–organic superlattices induced by long-range repulsive interactions on a metal surface’, *J. Phys. Chem. C* **125**, 18494 (2021).
- [16] T. R. Umbach, M. Bernien, C. F. Hermanns, A. Krüger, V. Sessi, I. Fernandez-Torrente, P. Stoll, J. I. Pascual, K. J. Franke and W. Kuch, ‘Ferromagnetic coupling of mononuclear Fe centers in a self-assembled metal-organic network on Au(111)’, *Phys. Rev. Lett.* **109**, 267207 (2012).
- [17] K. Schouteden, T. Ivanova, Z. Li, V. Iancu, E. Janssens and C. Van Haesendonck, ‘Probing magnetism in 2D molecular networks after *in situ* metalation by transition metal atoms’, *J. Phys. Chem. Lett.* **6**, 1048 (2015).
- [18] G. E. Pacchioni, M. Pivetta, L. Gagnaniello, F. Donati, G. Autès, O. V. Yazyev, S. Rusponi and H. Brune, ‘Two-orbital kondo screening in a self-assembled metal–organic complex’, *ACS Nano* **11**, 2675 (2017).
- [19] M. Blanco-Rey, A. Sarasola, C. Nistor, L. Persichetti, C. Stamm, C. Piamonteze, P. Gambardella, S. Stepanow, M. M. Otrokov, V. N. Golovach and A. Arnau, ‘Magnetic properties of metal–organic coordination networks based on 3d transition metal atoms’, *Molecules* **23**, (2018).
- [20] S. Schulz, I. A. Nechaev, M. Güttler, G. Poelchen, A. Generalov, S. Danzenbächer, A. Chikina, S. Seiro, K. Kliemt, A. Y. Vyazovskaya, T. K. Kim, P. Dudin, E. V. Chulkov, C. Laubschat, E. E. Krasovskii, C. Geibel, C. Krellner, K. Kummer and D. V. Vyalikh, ‘Emerging 2D-ferromagnetism and strong spin-orbit coupling at the surface of valence-fluctuating  $\text{EuIr}_2\text{Si}_2$ ’, *npj Quantum Mater.* **4**, 26 (2019).
- [21] L. Wang, Z. Cai, J. Wang, J. Lu, G. Luo, L. Lai, J. Zhou, R. Qin, Z. Gao, D. Yu, G. Li, W. N. Mei and S. Sanvito, ‘Novel one-dimensional organometallic half metals: vanadium-cyclopentadienyl, vanadium-cyclopentadienyl-benzene, and vanadium-anthracene wires’, *Nano Lett.* **8**, 3640 (2008).
- [22] X. Zhang, M. Cao, L. Liu and Y. Liu, ‘Tunable electronic and magnetic properties of boron/nitrogen-doped  $\text{BzTMCP}^*\text{TMBz/CpTMCP}^*\text{TMCP}$  clusters and one-dimensional infinite molecular wires’, *J. Phys. Chem. C* **118**, 11620 (2014).

- [23] K. Lu, W. Gao, M. Xu, Y. Sun, J. Li, X. Yao, Y. Liu and X. Zhang, ‘Spin Transport Properties of One-Dimensional Benzene Ligand Organobimetallic Sandwich Molecular Wires’, *ACS Omega* **5**, 5534 (2020).
- [24] T. Masubuchi and A. Nakajima, in ‘Theoretical chemistry for advanced nanomaterials: functional analysis by computation and experiment’, , *Springer* 313 (2020).
- [25] L. Zhou, S.-W. Yang, M.-F. Ng, M. B. Sullivan, Tan and L. Shen, ‘One-dimensional iron-cyclopentadienyl sandwich molecular wire with half metallic, negative differential resistance and high-spin filter efficiency properties’, *J. Am. Chem. Soc.* **130**, 4023 (2008).
- [26] L. Shen, S.-W. Yang, M.-F. Ng, V. Ligatchev, L. Zhou and Y. Feng, ‘Charge-transfer-based mechanism for half-metallicity and ferromagnetism in one-dimensional organometallic sandwich molecular wires’, *J. Am. Chem. Soc.* **130**, 13956 (2008).
- [27] Y. Li, G. Zhou, J. Li, J. Wu, B.-L. Gu and W. Duan, ‘*Ab initio* study of half-metallicity and magnetism of complex organometallic molecular wires’, *J. Phys. Chem. C* **115**, 7292 (2011).
- [28] M. Joshi and T. K. Ghanty, ‘Prediction of a nine-membered aromatic heterocyclic 1,4,7-triazacyclononatetraenyl anion and its sandwich complexes with divalent lanthanides’, *Chemistry-Select* **4**, 9940 (2019).
- [29] X. Zhang, X. Gong, Y. Sun, M. Xu, B. Xi, X. Zhao, X. Ye, X. Yao, M. He, L. Liu and Y. Liu, ‘3d transition metal-metallofullerene-ligand molecular wires: robust one-dimensional antiferromagnetic semiconductors’, *J. Phys. Chem. C* **123**, 30571 (2019).
- [30] L. C. de Camargo, M. Briganti, F. S. Santana, D. Stinghen, R. R. Ribeiro, G. G. Nunes, J. F. Soares, E. Salvadori, M. Chiesa, S. Benci, R. Torre, L. Sorace, F. Totti and R. Sessoli, ‘Exploring the organometallic route to molecular spin qubits: the [CpTi(cot)] case’, *Angew. Chem. Int. Ed.* **60**, 2588 (2021).
- [31] T. Kurikawa, Y. Negishi, F. Hayakawa, S. Nagao, K. Miyajima, A. Nakajima and K. Kaya, ‘Multiple-decker sandwich complexes of lanthanide-1,3,5,7-cyclooctatetraene [Ln<sub>n</sub>(C<sub>8</sub>H<sub>8</sub>)<sub>m</sub>] (Ln = Ce, Nd, Eu, Ho, and Yb); localized ionic bonding structure’, *J. Am. Chem. Soc.* **120**, 11766 (1998).
- [32] N. Hosoya, R. Takegami, J.-i. Suzumura, K. Yada, K. Koyasu, K. Miyajima, M. Mitsui, M. B. Knickelbein, S. Yabushita and A. Nakajima, ‘Lanthanide organometallic sandwich nanowires: formation mechanism’, *J. Phys. Chem. A* **109**, 9 (2005).
- [33] K. Miyajima, M. B. Knickelbein and A. Nakajima, ‘Stern-Gerlach Study of Multidecker Lanthanide-Cyclooctatetraene Sandwich Clusters’, *J. Phys. Chem. A* **112**, 366 (2008).
- [34] N. Hosoya, R. Takegami, J.-i. Suzumura, K. Yada, K. Miyajima, M. Mitsui, M. B. Knickelbein, S. Yabushita and A. Nakajima, ‘Formation and electronic structures of organoeuropium sandwich nanowires’, *J. Phys. Chem. A* **118**, 8298 (2014).
- [35] N. Atodiresei, P. H. Dederichs, Y. Mokrousov, L. Bergqvist, G. Bihlmayer and S. Blügel, ‘Controlling the magnetization direction in molecules via their oxidation state’, *Phys. Rev. Lett.* **100**, 117207 (2008).
- [36] X. Zhang, M.-F. Ng, Y. Wang, J. Wang and S.-W. Yang, ‘Theoretical studies on structural, magnetic, and spintronic characteristics of sandwiched Eu<sub>n</sub>COT<sub>n+1</sub> (n = 1-4) clusters’, *ACS Nano* **3**, 2515 (2009).
- [37] K. Xu, J. Huang, S. Lei, H. Su, F. Y. C. Boey, Q. Li and J. Yang, ‘Efficient organometallic spin filter based on europium-cyclooctatetraene wire’, *J. Chem. Phys.* **131**, 104704 (2009).
- [38] X. Liu, Y. Tan, G. Zhang and Y. Pei, ‘Electronic structure and spin transport properties of a new class of semiconductor surface-confined one-dimensional half-metallic [Eu-(C<sub>n</sub>H<sub>n-2</sub>)]<sub>N</sub> (n = 7-9) sandwich compounds and molecular wires: first principle studies’, *J. Phys. Chem. C* **122**, 16168 (2018).
- [39] X. Yao, S. Yuan and J. Wang, ‘Theoretical studies of sandwich molecular wires with europium and boratacyclooctatetraene ligand and the structure on a H-Ge(001)-2x1 surface’, *J. Phys. Chem. C* **120**, 7088 (2016).



- [40] F. Huttmann, N. Schleheck, N. Atodiresei and T. Michely, ‘On-surface synthesis of sandwich molecular nanowires on graphene’, *J. Am. Chem. Soc.* **139**, 9895 (2017).
- [41] F. Huttmann, N. Rothenbach, S. Kraus, K. Ollefs, L. M. Arruda, M. Bernien, D. Thonig, A. Delin, J. Fransson, K. Kummer, N. B. Brookes, O. Eriksson, W. Kuch, T. Michely and H. Wende, ‘Europium cyclooctatetraene nanowire carpets: a low-dimensional, organometallic, and ferromagnetic insulator’, *J. Phys. Chem. Lett.* **10**, 911 (2019).
- [42] S. Kraus, F. Huttmann, J. Fischer, T. Knispel, K. Bischof, A. Herman, M. Bianchi, R.-M. Stan, A. J. Holt, V. Caciuc, S. Tsukamoto, H. Wende, P. Hofmann, N. Atodiresei and T. Michely, ‘Single-crystal graphene on Ir(110)’, *arXiv:2109.04198* (2021).
- [43] S.-i. Machida, Y. Nakayama, S. Duhm, Q. Xin, A. Funakoshi, N. Ogawa, S. Kera, N. Ueno and H. Ishii, ‘Highest-occupied-molecular-orbital band dispersion of rubrene single crystals as observed by angle-resolved ultraviolet photoelectron spectroscopy’, *Phys. Rev. Lett.* **104**, 156401 (2010).
- [44] Y. Nakayama, Y. Urugami, S. Machida, K. R. Koswattage, D. Yoshimura, H. Setoyama, T. Okajima, K. Mase and H. Ishii, ‘Full picture of valence band structure of rubrene single crystals probed by angle-resolved and excitation-energy-dependent photoelectron spectroscopy’, *Appl. Phys. Express* **5**, 111601 (2012).
- [45] J. Nitta, K. Miwa, N. Komiya, E. Annese, J. Fujii, S. Ono and K. Sakamoto, ‘The actual electronic band structure of a rubrene single crystal’, *Sci. Rep.* **9**, 9645 (2019).
- [46] Y. Nakayama, Y. Mizuno, M. Hikasa, M. Yamamoto, M. Matsunami, S. Ideta, K. Tanaka, H. Ishii and N. Ueno, ‘Single-crystal pentacene valence-band dispersion and its temperature dependence’, *J. Phys. Chem. Lett.* **8**, 1259 (2017).
- [47] Y. Nakayama, R. Tsuruta, N. Moriya, M. Hikasa, M. Meissner, T. Yamaguchi, Y. Mizuno, T. Suzuki, T. Koganezawa, T. Hosokai, T. Ueba and S. Kera, ‘Widely dispersed intermolecular valence bands of epitaxially grown perfluoropentacene on pentacene single crystals’, *J. Phys. Chem. Lett.* **10**, 1312 (2019).
- [48] Y. Nakayama, S. Kera and N. Ueno, ‘Photoelectron spectroscopy on single crystals of organic semiconductors: experimental electronic band structure for optoelectronic properties’, *J. Mater. Chem. C* **8**, 9090 (2020).
- [49] I. Piquero-Zulaica, A. Garcia-Lekue, L. Colazzo, C. K. Krug, M. S. G. Mohammed, Z. M. Abd El-Fattah, J. M. Gottfried, D. G. de Oteyza, J. E. Ortega and J. Lobo-Checa, ‘Electronic structure tunability by periodic meta-ligand spacing in one-dimensional organic semiconductors’, *ACS Nano* **12**, 10537 (2018).
- [50] A. Basagni, G. Vasseur, C. A. Pignedoli, M. Vilas-Varela, D. Peña, L. Nicolas, L. Vitali, J. Lobo-Checa, D. G. de Oteyza, F. Sedona, M. Casarin, J. E. Ortega and M. Sambi, ‘Tunable band alignment with unperturbed carrier mobility of on-surface synthesized organic semiconducting wires’, *ACS Nano* **10**, 2644 (2016).
- [51] R. van Gastel, A. T. N’Diaye, D. Wall, J. Coraux, C. Busse, N. M. Buckanie, F.-J. Meyer zu Heringdorf, M. Horn von Hoegen, T. Michely and B. Poelsema, ‘Selecting a single orientation for millimeter sized graphene sheets’, *Appl. Phys. Lett.* **95**, 121901 (2009).
- [52] I. Horcas, R. Fernández, J. M. Gómez-Rodríguez, J. Colchero, J. Gómez-Herrero and A. M. Baro, ‘WSXM: A software for scanning probe microscopy and a tool for nanotechnology’, *Rev. Sci. Instrum.* **78**, 013705 (2007).
- [53] S. V. Hoffmann, C. Søndergaard, C. Schultz, Z. Li and P. Hofmann, ‘An undulator-based spherical grating monochromator beamline for angle-resolved photoemission spectroscopy’, *Nucl. Instrum. Methods. Phys. Res. B* **523**, 441 (2004).
- [54] C. Piamonteze, U. Flehsig, S. Rusponi, J. Dreiser, J. Heidler, M. Schmidt, R. Wetter, M. Calvi, T. Schmidt, H. Pruchova, J. Krempasky, C. Quitmann, H. Brune and F. Nolting, ‘X-Treme beamline at SLS: X-ray magnetic circular and linear dichroism at high field and low temperature’, *J. Synchrotron Radiat.* **19**, 661 (2012).

- [55] P. Hohenberg and W. Kohn, ‘Inhomogeneous electron gas’, *Phys. Rev.* **136**, B864 (1964).
- [56] P. E. Blöchl, ‘Projector augmented-wave method’, *Phys. Rev. B* **50**, 17953 (1994).
- [57] G. Kresse and J. Hafner, ‘*Ab initio* molecular dynamics for liquid metals’, *Phys. Rev. B* **47**, 558 (1993).
- [58] G. Kresse and J. Furthmüller, ‘Efficient iterative schemes for *ab initio* total-energy calculations using a plane-wave basis set’, *Phys. Rev. B* **54**, 11169 (1996).
- [59] W. Kohn and L. J. Sham, ‘Self-consistent equations including exchange and correlation effects’, *Phys. Rev.* **140**, A1133 (1965).
- [60] K. Lee, E. D. Murray, L. Kong, B. I. Lundqvist and D. C. Langreth, ‘Higher-accuracy van der Waals density functional’, *Phys. Rev. B* **82**, 081101 (2010).
- [61] A. D. Becke, ‘On the large gradient behavior of the density functional exchange energy’, *J. Chem. Phys.* **85**, 7184 (1986).
- [62] I. Hamada, ‘Van der Waals density functional made accurate’, *Phys. Rev. B* **89**, 121103 (2014).
- [63] F. Huttmann, A. J. Martínez-Galera, V. Caciuc, N. Atodiresei, S. Schumacher, S. Standop, I. Hamada, T. O. Wehling, S. Blügel and T. Michely, ‘Tuning the van der Waals interaction of graphene with molecules via doping’, *Phys. Rev. Lett.* **115**, 236101 (2015).
- [64] J. P. Perdew, K. Burke and M. Ernzerhof, ‘Generalized gradient approximation made simple’, *Phys. Rev. Lett.* **77**, 3865 (1996).
- [65] V. I. Anisimov, F. Aryasetiawan and A. I. Lichtenstein, ‘First-principles calculations of the electronic structure and spectra of strongly correlated systems: the LDA + U method’, *J. Condens. Matter Phys.* **9**, 767 (1997).
- [66] J. B. Goedkoop, B. T. Thole, G. van der Laan, G. A. Sawatzky, F. M. F. de Groot and J. C. Fuggle, ‘Calculations of magnetic X-ray dichroism in the 3d absorption spectra of rare-earth compounds’, *Phys. Rev. B* **37**, 2086 (1988).
- [67] B. T. Thole, P. Carra, F. Sette and G. van der Laan, ‘X-ray circular dichroism as a probe of orbital magnetization’, *Phys. Rev. Lett.* **68**, 1943 (1992).
- [68] P. Carra, B. T. Thole, M. Altarelli and X. Wang, ‘X-ray circular dichroism and local magnetic fields’, *Phys. Rev. Lett.* **70**, 694 (1993).
- [69] R. Wu and A. J. Freeman, ‘Limitation of the magnetic-circular-dichroism spin sum rule for transition metals and importance of the magnetic dipole term’, *Phys. Rev. Lett.* **73**, 1994 (1994).
- [70] J. P. Crocombette, B. T. Thole and F. Jollet, ‘The importance of the magnetic dipole term in magneto-circular X-ray absorption dichroism for 3d transition metal compounds’, *J. Condens. Matter Phys.* **8**, 4095 (1996).
- [71] S. Schumacher, F. Huttmann, M. Petrović, C. Witt, D. F. Förster, C. Vo-Van, J. Coraux, A. J. Martínez-Galera, V. Sessi, I. Vergara, R. Rückamp, M. Grüninger, N. Schleheck, F. Meyer zu Heringdorf, P. Ohresser, M. Kralj, T. O. Wehling and T. Michely, ‘Europium underneath graphene on Ir(111): intercalation mechanism, magnetism, and band structure’, *Phys. Rev. B* **90**, 235437 (2014).
- [72] U. A. Schröder, M. Petrović, T. Gerber, A. J. Martínez-Galera, E. Grånäs, M. A. Arman, C. Herbig, J. Schnadt, M. Kralj, J. Knudsen and T. Michely, ‘Core level shifts of intercalated graphene’, *2D Mater.* **4**, 015013 (2016).
- [73] X.-X. Wang, H.-N. Li, W.-H. Zhang and F.-Q. Xu, ‘Valence band of metal europium studied with synchrotron radiation photoemission spectroscopy’, *J. Condens. Matter Phys.* **19**, 096001 (2007).
- [74] C. Caspers, M. Müller, A. X. Gray, A. M. Kaiser, A. Gloskovskii, C. S. Fadley, W. Drube and C. M. Schneider, ‘Chemical stability of the magnetic oxide EuO directly on silicon observed by hard X-ray photoemission spectroscopy’, *Phys. Rev. B* **84**, 205217 (2011).
- [75] C. Busse, P. Lazić, R. Djemour, J. Coraux, T. Gerber, N. Atodiresei, V. Caciuc, R. Brako, A. T. N’Diaye, S. Blügel, J. Zegenhagen and T. Michely, ‘Graphene on Ir(111): physisorption with chemical modulation’, *Phys. Rev. Lett.* **107**, 036101 (2011).

# Supporting information:

## uniaxially aligned 1D sandwich-molecular wires:

### electronic structure and magnetism

Stefan Kraus<sup>\*1</sup>, Alexander Herman<sup>2</sup>, Felix Huttmann<sup>1</sup>, Marco Bianchi<sup>3</sup>, Raluca-Maria Stan<sup>3</sup>, Ann Julie Holt<sup>3</sup>, Shigeru Tsukamoto<sup>4</sup>, Nico Rothenbach<sup>2</sup>, Katharina Ollefs<sup>2</sup>, Jan Dreiser<sup>5</sup>, Ken Bischof<sup>1</sup>, Heiko Wende<sup>2</sup>, Philip Hofmann<sup>3</sup>, Nicolae Atodiresei<sup>†4</sup>, and Thomas Michely<sup>1</sup>

<sup>1</sup>*II. Physikalisches Institut, Universität zu Köln, Zùlpicher Str. 77, 50937 Köln, Germany*

<sup>2</sup>*Faculty of Physics and Center for Nanointegration Duisburg-Essen (CENIDE), University of Duisburg-Essen, Lotharstraße 1, 47048 Duisburg, Germany*

<sup>3</sup>*Department of Physics and Astronomy, Interdisciplinary Nanoscience Center (iNANO), Aarhus University, 8000 Aarhus C, Denmark*

<sup>4</sup>*Peter Grünberg Institute and Institute for Advanced Simulation, Forschungszentrum Jùlich, Wilhelm-Johnen-StraÙe, 52428 Jùlich, Germany*

<sup>5</sup>*Swiss Light Source, Paul Scherrer Institute, Forschungsstrasse 111, 5232 Villigen PSI, Switzerland*

---

<sup>\*</sup>kraus@ph2.uni-koeln.de (experiment)

<sup>†</sup>n.atodiresei@fz-juelich.de (theory)

**Figure S1: ML EuCot theory calculations comparison for different Hubbard  $U$**

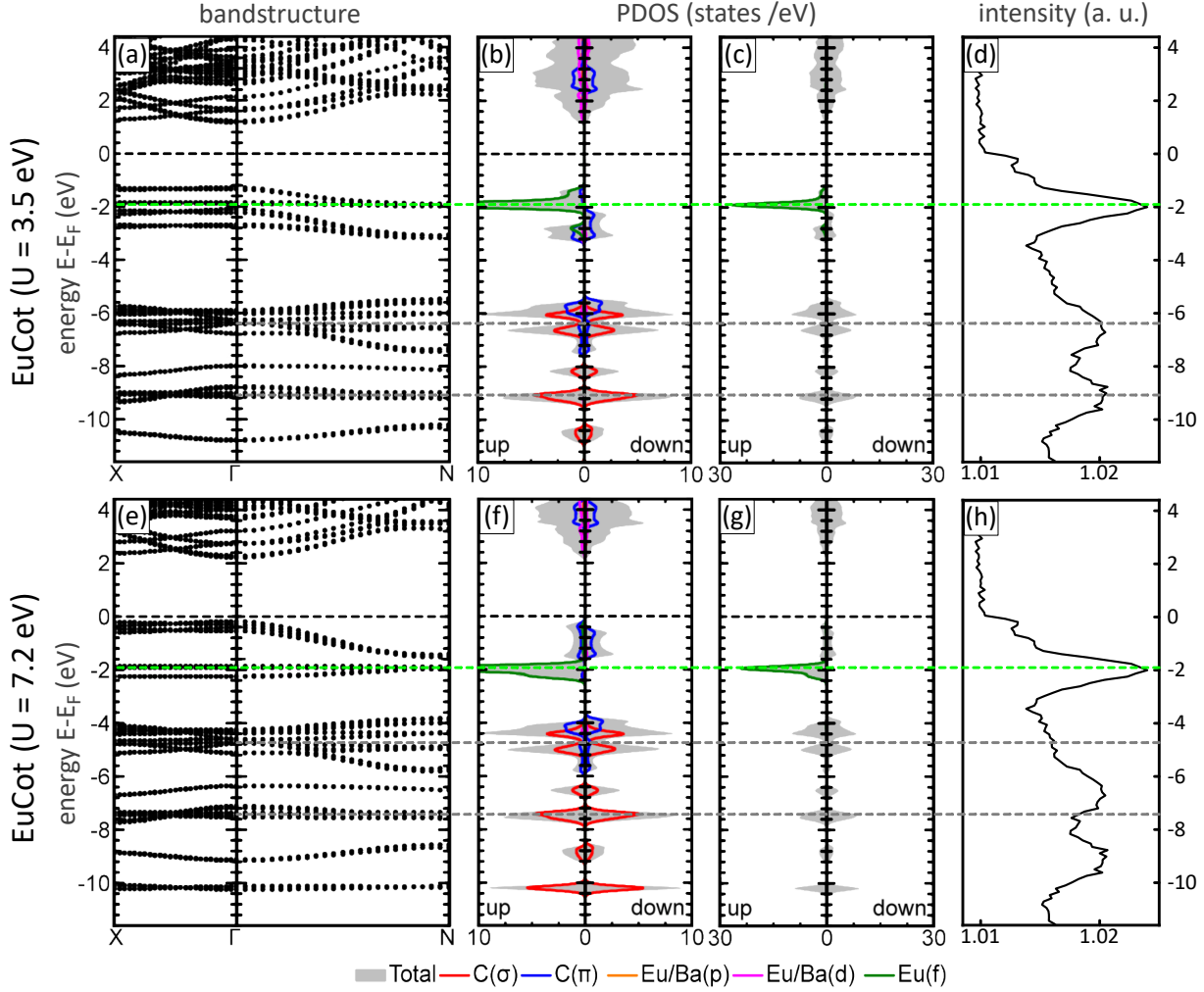


Figure S1: EuCot ML,  $U_{\text{eff}} = 3.5$ : (a) Theoretical band structure along  $X - \Gamma - N$ . (b) Spin-polarized PDOS. (c) Larger scale spin-polarized PDOS. (d) angle-integrated ARPES data of EuCot multilayer ( $\approx 4$  ML). Position of 4f peak is indicated by dotted green line in (a)-(d), the positions of the lower lying  $\sigma$  bands are indicated by grey dotted lines. EuCot ML,  $U_{\text{eff}} = 7.2$ : (e) Theoretical band structure along  $X - \Gamma - N$ . (f) Spin-polarized PDOS. (g) Larger scale spin-polarized PDOS. (h) angle-integrated ARPES data of EuCot multilayer ( $\approx 4$  ML). Position of 4f peak is indicated by dotted green line in (e)-(h), the positions of the lower lying  $\sigma$  bands are indicated by grey dotted lines. ARPES data were obtained at a photon energy  $E_{h\nu} = 130$  eV at  $T = 35$  K. XPS data were obtained at a photon energy  $E_{h\nu} = 1486.6$  eV (Al K- $\alpha$ ) at  $T = 300$  K.

In Figure S1 the band structure and resulting PDOS of ML EuCot is compared for two different values of the effective Hubbard  $U$ . Comparing our angle-integrated ARPES data to the calculations allows us to determine the  $U_{\text{eff}}$  of the ML EuCot system. For  $U_{\text{eff}} = 3.5$  eV, the experimentally observed energetic spacings between the 4f peak (green dotted line) and lower lying  $\sigma$  peaks (grey dotted lines) agree with theory calculations. Therefore, we can conclude, that

an effective  $U_{\text{eff}} = 3.5 \text{ eV}$  correctly describes our system. In contrast, for a value of  $U_{\text{eff}} = 7.2 \text{ eV}$  the measured energy spacings disagree with the calculations, meaning that  $U_{\text{eff}} = 7.2 \text{ eV}$  does not correctly describe the ML EuCot.

**Figure S2: STM and LEED of BaCot wire carpets on Gr/Ir(111)**

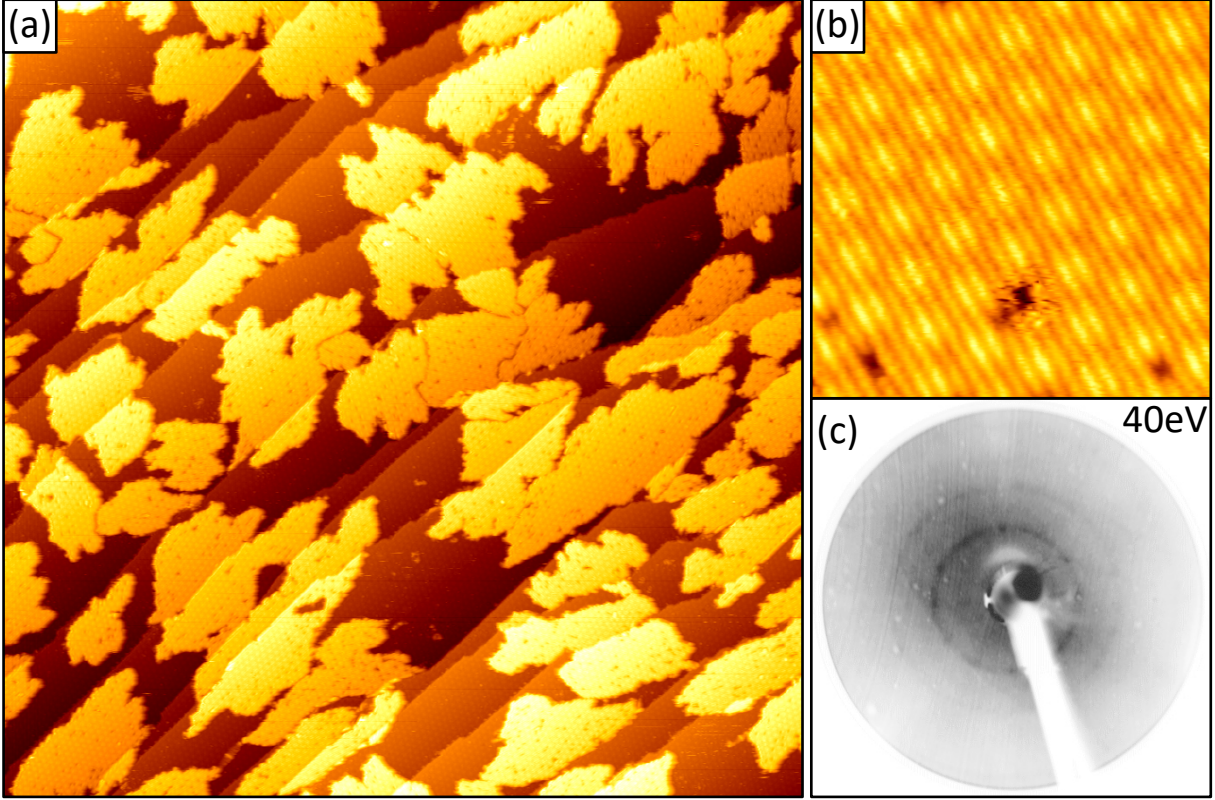


Figure S2: (a) STM topograph ( $3000 \times 3000 \text{ \AA}^2$ ) of a sub-ML BaCot wire carpet on Gr/Ir(111). Crystalline wire carpet islands are visible, which show close-to-random orientation with respect to the substrate. (b) STM topograph ( $165 \times 165 \text{ \AA}^2$ ) of wire carpet, in which parallel aligned wires are visible, as well as the hexagonal moiré of Gr/Ir(111). (c) 40 eV contrast-inverted LEED pattern (MCP LEED) of a ML BaCot wire carpet on Gr/Ir(111). Two rings are visible due to the close-to-random orientation of the wire carpet islands, similar to ref. [1]. STM and LEED were conducted at a temperature of 300 K. Tunneling parameters are (a)  $U_{\text{bias}} = -1.40 \text{ V}$  and  $I_t = 0.07 \text{ nA}$ , (b)  $U_{\text{bias}} = -1.40 \text{ V}$  and  $I_t = 0.21 \text{ nA}$ .

**Figure S3: Magnetization curve of EuCot wires on Gr/Yb/Ir(111)**

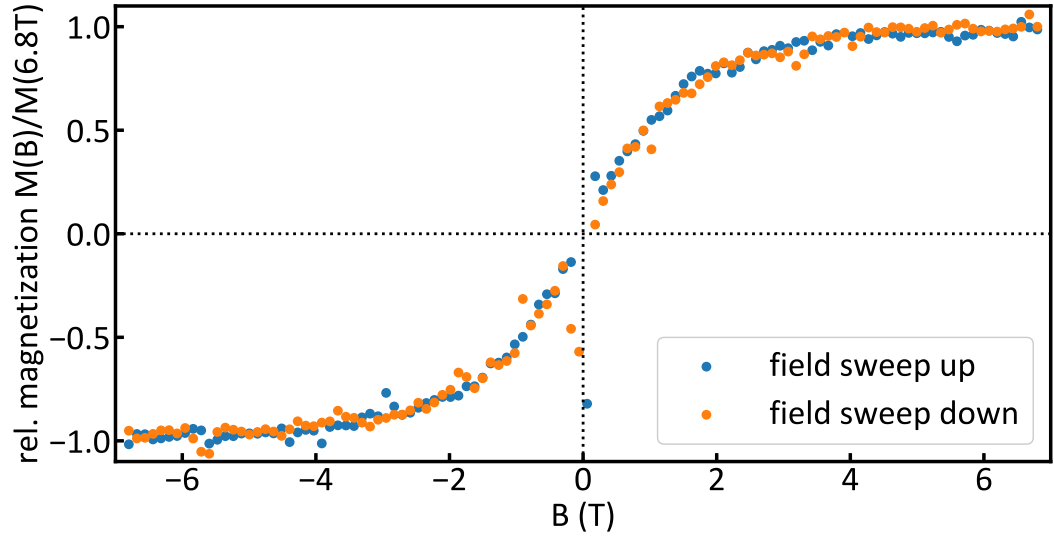


Figure S3: EuCot wires on Gr/Yb/Ir(111): Magnetization curves (field sweep up/down) based on the field dependent XMCD signal of the Eu  $M_5$  edge for grazing incidence ( $\theta = 60^\circ$ ) at  $T = 3$  K. Both curves coincide and no magnetic hysteresis is observed. The outlier values around 0 T are artifacts of the total electron yield method.

## References

- [1] F. Huttmann, N. Rothenbach, S. Kraus, K. Ollefs, L. M. Arruda, M. Bernien, D. Thonig, A. Delin, J. Fransson, K. Kummer, N. B. Brookes, O. Eriksson, W. Kuch, T. Michely and H. Wende, ‘Europium cyclooctatetraene nanowire carpets: a low-dimensional, organometallic, and ferromagnetic insulator’, *J. Phys. Chem. Lett.* **10**, 911 (2019).





## CHAPTER 5

---

# Manuscript 3: From dots to wires: doping-dependent on-surface synthesis of thulium-cyclooctatetraene compounds on graphene

*This chapter wholly consists of the above-named manuscript and its supplement. The manuscript is currently in preparation phase.*

*S.K. conducted the syntheses and the STM and LEED experiments, partially under the guidance of F.H. The TDS experiments were conducted by S.K. and C.K. The XAS/XMCD experiments were conducted by S.K., A.H., N.R., K.O., L.S., T.L., M.B. and L.M.A. The theoretical calculations were conducted by N.A. and S.T. The manuscript was written by S.K. in close collaboration with T.M. and with contributions from N.A.*

*Some of the results in this chapter can be found in the doctoral thesis of F. Huttmann, the Master thesis of S. Kraus, and the Bachelor thesis of C. Krämer.*

# From dots to wires: doping-dependent on-surface synthesis of thulium-cyclooctatetraene compounds on graphene

Stefan Kraus<sup>\*1</sup>, Alexander Herman<sup>2</sup>, Felix Huttmann<sup>1</sup>, Christian Krämer<sup>1</sup>, Shigeru Tsukamoto<sup>3</sup>, Nico Rothenbach<sup>2</sup>, Katharina Ollefs<sup>2</sup>, Lea Spieker<sup>2</sup>, Tobias Lojewski<sup>2</sup>, Matthias Bernien<sup>4</sup>, Lucas M. Arruda<sup>4</sup>, Jan Dreiser<sup>5</sup>, Nick Brookes<sup>6</sup>, Kurt Kummer<sup>6</sup>, Wolfgang Kuch<sup>4</sup>, Heiko Wende<sup>2</sup>, Nicolae Atodiresei<sup>†3</sup>, and Thomas Michely<sup>1</sup>

<sup>1</sup>*II. Physikalisches Institut, Universität zu Köln, Zùlpicher Str. 77, 50937 Köln, Germany*

<sup>2</sup>*Faculty of Physics and Center for Nanointegration Duisburg-Essen (CENIDE), University of Duisburg-Essen, Lotharstraße 1, 47048 Duisburg, Germany*

<sup>3</sup>*Peter Grünberg Institute and Institute for Advanced Simulation, Forschungszentrum Jùlich, Wilhelm-Johnen-StraÙe, 52428 Jùlich, Germany*

<sup>4</sup>*Institut für Experimentalphysik, Freie Universität Berlin, Arnimallee 14, 14195 Berlin, Germany*

<sup>5</sup>*Swiss Light Source, Paul Scherrer Institute, Forschungsstrasse 111, 5232 Villigen PSI, Switzerland*

<sup>6</sup>*European Synchrotron Research Facility (ESRF), Avenue des Martyrs 71, CS 40220, 38043 Grenoble Cedex 9, France*

## Abstract

On-surface synthesis is employed to grow organometallic compounds on graphene/Ir(111) combining the 4f metal thulium (Tm) with the antiaromatic molecule cyclooctatetraene (C<sub>8</sub>H<sub>8</sub>, briefly Cot). Using scanning tunnelling microscopy and thermal desorption spectroscopy we observe the formation of TmCot monomers adsorbed to graphene. For low coverages these monomers form phase pure and orient along the moiré of graphene (Gr) with Ir(111). For higher coverages the formation of a second, island-forming phase is observed that coexists with the monomer phase. Using *ab initio* density functional theory calculations and X-ray magnetic circular dichroism measurements, we find a 4f<sup>12</sup> electronic configuration for the monomers and explain the binding to the substrate via charge transfer to the graphene. Building on this finding, we were able to change the chemical reaction pathway during synthesis by suppressing this charge transfer: While on the undoped substrate monomers are synthesized, n-doping of the Gr enables the growth of sandwich-molecular wires — chains of Tm atoms and Cot molecules in alternating sequence. Furthermore, it is possible to tune the average wire length by changing the ratio Tm/Cot during the on-surface synthesis, going from small wire fragments to long chains exceeding 100 formula units.

---

<sup>\*</sup>kraus@ph2.uni-koeln.de (experiment)

<sup>†</sup>n.atodiresei@fz-juelich.de (theory)

# 1 Introduction

The interplay of metal atoms within a surrounding ligand field of organic molecules is studied in multiple fields between physics and chemistry. In this context, the interaction of 3d and 4f magnetic moments with the molecule  $\pi$  systems is of special interest due to the potential use in spintronic applications [1, 2] that has stimulated research on many different types of such systems. A special case is the on-surface synthesis [3, 4] in which the organometallic reactions are confined to two dimensions, greatly enhancing the reaction efficiency compared to e.g. gas phase methods. The studied organometallic systems can be divided in three main categories: 0D single-molecule magnets, 1D organometallic wires 2D metal-organic networks.

Single-molecule magnets have a stable magnetic moment below their blocking temperature and show a magnetic hysteresis without long-range order [5, 6, 7], which is explained by quantum tunnelling of the magnetization [8]. The magnetic atoms within single-molecule magnets can be build into the molecular structure [8, 5], be enclosed in endohedral fullerenes [9, 7] or more commonly sandwiched by molecules such as phthalocyanines [10, 11, 12, 13, 14]. The widespread use of rare-earth metals in these compounds is due to the robustness of the 4f-generated magnetic moment. Although the interaction of the 4f electrons with the  $\pi$  system is weak, they were still found to be directly involved in electrical transport through a single-molecule magnet containing neodymium [11].

By using single-molecule magnets as building blocks, two-dimensional supramolecular arrays can be assembled [15, 16] and metalation of supramolecular networks can be used to create 2D metal-organic networks [17, 18] in which 2D magnetic ordering and ferromagnetic coupling has been observed [19].

In this work, we focus on 1D sandwich-molecular wires — one-dimensional arrangements of metal atoms and cyclic molecules in alternating sequence — which provide the unique feature of long-range order in just one dimension. Sandwich-molecular wires have been studied extensively by theory, with one of the early systems being short wires containing the 3d metal vanadium (V) and the aromatic benzene (Bz) molecule. VBz wires form through covalent bonding [20, 21] and have been predicted to be ferromagnetic half metals [22], i.e. can act as spin filters. Modifications of these wires were investigated, both on the molecule [23, 24] and the metal side [21, 25] or a combination of both [26]. Experimentally, these wires have been produced in gas phase by laser vaporization [27, 28], electronic properties have been investigated [29, 30, 31] and VBz wires were found to couple ferromagnetically [32] consistent with the theoretical predictions. Due to the aromatic nature of the Bz molecule, all those compounds can only bind covalently. Choosing a molecule which can accept electrons into its  $\pi$  system, predominantly ionically bound complexes can be formed. One example is the use of cyclopentadien ( $\text{C}_5\text{H}_5$ , briefly Cp), which becomes an aromatic  $\text{Cp}^-$  anion within organometallic compounds. Several metal-Cp complexes have been studied [33, 34, 35, 36, 37] which were partly found to be ferromagnetic half metals. Also combinations of Cp and Bz were investigated [38, 39, 40, 41]. On a side note, metal complexes

sandwiched by Cp anions or complexes containing Cp anions form their own field of study — the metallocenes — which find application e.g. in catalysis [42, 43].

For the coordination of lanthanide (Ln) atoms within sandwich-molecular wires the eight-membered carbon ring cyclooctatetraene ( $C_8H_8$ , Cot) is used. While the neutral Cot molecule is antiaromatic, the  $Cot^{2-}$  dianion is aromatic, making 1D wires consisting of  $Ln^{2+}$  dications and  $Cot^{2-}$  dianions energetically highly favorable, allowing the growth of much longer wires as compared to the covalently bound transition-metal–Bz wires. Early *ab initio* calculations for short europium–Cot (briefly EuCot) wires have investigated the magnetization direction [44], and a Eu  $7 \mu_B$  magnetic moment was calculated per formula unit [45]. EuCot wires were predicted to be semiconducting ferromagnets with spin filter properties [46], and modifications of the Cot ring are predicted to shift from semiconducting to half-metallic behavior [47]. Experimentally, EuCot wires were first produced in the liquid phase [48] and more recently in the gas phase [49, 29, 50, 51], achieving maximum wire lengths of up to 30 formula units. Consistent with the theoretical predictions, a magnetic moment of  $7 \mu_B$  per Eu atom was found for EuCot wires in Stern-Gerlach type experiments [52, 53], with the total magnetic moment increasing linearly with wire length. We recently introduced an on-surface synthesis method, in which carpets of interlocking and parallelly aligned EuCot wires are grown on Gr/Ir(111) [54], which allows the formation of very long wires exceeding 1000 formula units. Using this synthesis method, the predicted ferromagnetic and semiconducting behavior was confirmed [55].

Here, we build on the on-surface method to synthesize sandwich-molecular wires containing the late lanthanide thulium (Tm). While Eu possesses only a spin magnetic moment due to its isotropic and half-filled 4f shell, Tm has an additional orbital magnetic moment resulting from its highly anisotropic 4f orbital. This might lead the way to a larger magnetic hysteresis through the additional magnetocrystalline anisotropy, which is absent in EuCot wires.

Intriguingly, we find that using the on-surface synthesis, we can effectively switch the Tm–Cot chemical reaction pathway by n-doping the substrate. On the undoped Gr/Ir(111) the formation of a disperse phase of adsorbed TmCot monomers is observed. Using complementary *ab initio* calculations, we explain the monomer binding mechanism by charge transfer to the Gr. The formation of this disperse phase can be suppressed completely by n-doping the Gr via Eu intercalation [56], leading to the growth of TmCot wire carpets. While in previous experiments only wire lengths below 10 formula units were achieved [53], we were able to synthesize TmCot wires exceeding lengths of 100 formula units, forming large crystalline islands of interlocking and parallelly aligned wires accessible to surface-sensitive techniques. Finally, we find that the average wire length can be tuned by changing the Tm/Cot ratio during on-surface synthesis, allowing to control the synthesis from small wire fragments to wire lengths up to 1000 Å.

## 2 Results and discussion

**TmCot dots – experiment:** Upon deposition of Tm on Gr/Ir(111) in an excess pressure of Cot molecules at 300 K, we observe the formation of point-like objects shown in Figure 1a, forming a disperse phase. Due to the unique height and uniform appearance we call these point-like objects “dots”. Although on a large scale a disperse behavior is observed, in the inset of Figure 1a it can be seen that the dots preferentially bind to the atop sites (compare ref. [57]) of the Gr moiré. For higher coverage as shown in Figure 1b the dots remain disperse, while the dot density increases. The inset in Figure 1b shows how easily the dots interact with the STM tip — as highlighted by the blue arrows — indicating a weak lateral binding strength. Increasing the coverage further moves the dots closer together until a coverage of about one dot per moiré cell is reached. When surpassing this coverage, a second, island-forming phase emerges — white in Figure 1 due to the high contrast — and coexists with the disperse dot phase (the island-forming phase will be discussed later in detail). The inset of Figure 1c shows the round appearance of the dots, while a small depression is visible in their centers. The height profiles in Figures 1d/e show that in both cases the dots are locally separated by approximately one moiré distance ( $25.3 \text{ \AA}$ ), while for coverages above one dot per moiré cell the disperse phase is compressed and the dots move closer as shown in Figure 1f. The apparent height of the dots is  $2 - 3 \text{ \AA}$  and the base width is about  $25 \text{ \AA}$  (significantly larger than the  $8 \text{ \AA}$  van der Waals radius of Cot [58]). Both values depend somewhat on the tunnelling parameters.

In order to determine the composition of the observed dots, only few possibilities need to be considered, because the only two reactants are elemental Tm and Cot molecules. The possible combinations are: (i) single Tm atoms, (ii) single Cot molecules, (iii) TmCot monomers (see Figure 2a) and (iv) TmCot double deckers (see Figure 2b). The first two possibilities can be immediately discarded, because at the growth temperature of 300 K (i) Tm atoms do not form a disperse phase on Gr/Ir(111) but form clusters, and (ii) Cot molecules desorb from Gr well below 300 K (compare Figure S1 and S2 in the Supporting Information).

To distinguish possibilities (iii) and (iv) is more difficult. Cot is electronegative and attracts up to two electrons to form the energetically favorable dianion. Two electrons are easily provided by Tm with the preferred oxidation state  $3+$ . Therefore the binding in both compounds, the TmCot monomer and the TmCot<sub>2</sub> double decker, will predominantly be of ionic character. Charge transfer to Gr or dipole formation explains the dot repulsion, but does not allow one to distinguish between the two possibilities (iii) and (iv). However, the binding strength to the Gr substrate is likely to be different: The TmCot<sub>2</sub> double decker will only be bound by van der Waals interaction, while for the TmCot monomer the formation of an ionic Tm–Gr bond is likely. Therefore, stronger binding to Gr is expected for the latter case.

In Figure 2c TDS data are shown corresponding to a sample as prepared in Figure 1b. No desorption signal is observed for either of both masses (TmCot, 273 amu and TmCot<sub>2</sub>, 377 amu). In a test experiment, we have first deposited several layers of Cot molecules on Gr/Ir(111) and

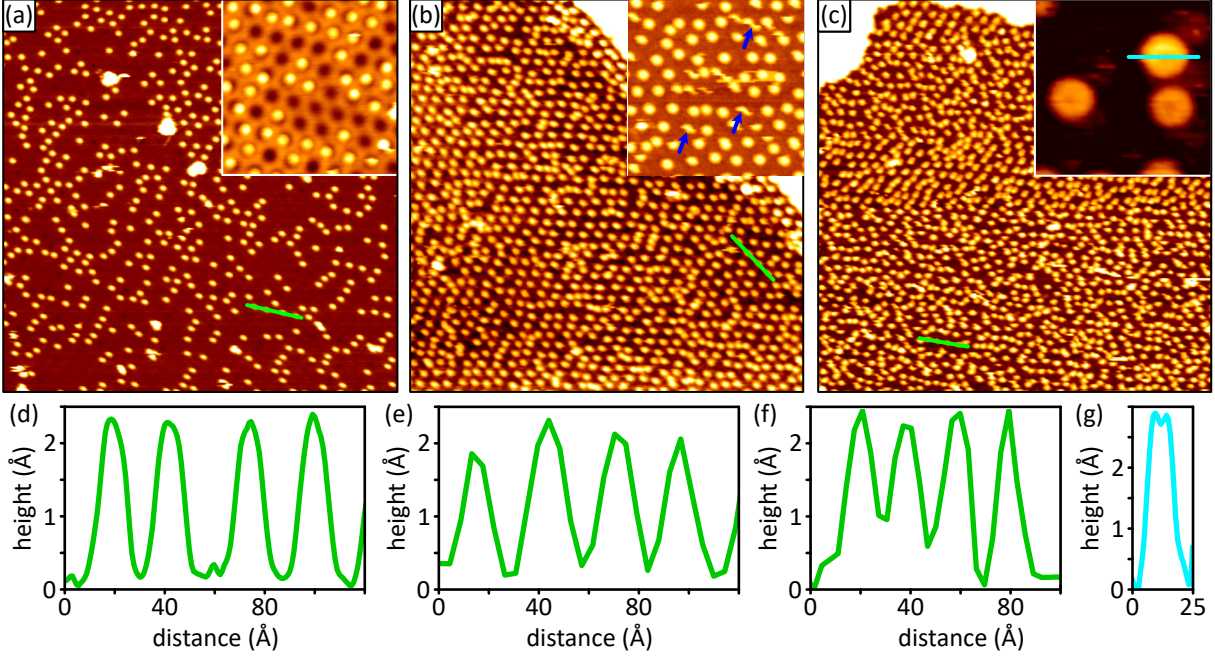


Figure 1: (a)–(c): STM topographs ( $750 \times 750 \text{ Å}^2$ ). (a) TmCot dot phase ( $0.007 \text{ ML Tm}$ ,  $5 \cdot 10^{-9} \text{ mbar Cot}$ ). Point-like objects are visible, which repulse each other and show a dispersive behavior. Inset: The STM topograph ( $200 \times 200 \text{ Å}^2$ ) shows that the dots preferentially adsorb at the atop site of the moiré. (b) TmCot dot phase ( $0.013 \text{ ML Tm}$ ,  $5 \cdot 10^{-9} \text{ mbar Cot}$ ). The disperse phase has increased in density, the repulsive behavior is still observed. Inset: STM topograph ( $200 \times 200 \text{ Å}^2$ ) which shows that the objects can easily be moved with the STM tip (indicated by blue arrows). (c) TmCot dot phase ( $0.08 \text{ ML Tm}$ ,  $5 \cdot 10^{-9} \text{ mbar Cot}$ ). The disperse phase has further increased in density, but now coexists with a distinct island-forming phase. Inset: STM topograph ( $45 \times 45 \text{ Å}^2$ ) with molecular resolution of point-like objects, revealing a small depression at the center. (d) Height profile indicated by green line in (a). The objects keep distance at roughly the moiré periodicity of  $25.3 \text{ Å}$  and show a height slightly above  $2 \text{ Å}$  at the given tunneling conditions. (e) Height profile indicated by green line in (b). Same behavior as in (d) is visible. (f) Height profile indicated by green line in (c). The objects have moved closer, since the density has surpassed one dot per moiré cell. (g) Height profile indicated by cyan line in inset of (c). A small depression is observed in the center of the object. All STM data have been recorded at  $20 \text{ K}$ . Tunneling parameters are (a) [also inset]  $U_{\text{bias}} = -2.9 \text{ V}$  and  $I_t = 8 \text{ pA}$ , (b)  $U_{\text{bias}} = -2.9 \text{ V}$  and  $I_t = 9 \text{ pA}$ , inset:  $U_{\text{bias}} = -2.7 \text{ V}$  and  $I_t = 10 \text{ pA}$ , (c)  $U_{\text{bias}} = -1.7 \text{ V}$  and  $I_t = 7 \text{ pA}$ , inset:  $U_{\text{bias}} = -2.8 \text{ V}$  and  $I_t = 70 \text{ pA}$ .

then deposited elemental Tm into a Cot matrix as depicted in Figure 2c, such that only TmCot<sub>2</sub> double deckers can form. Figure 2e shows the TDS data of this experiment, revealing clear desorption peaks for the mass of TmCot<sub>2</sub> ( $377 \text{ amu}$ ) at  $\approx 160 \text{ K}$ , which increase proportional to the deposited amount of Tm. Concluding from these experiments, the observed dots must be TmCot monomers, because TmCot<sub>2</sub> cannot be present at the growth temperature of  $300 \text{ K}$  since it desorbs at  $160 \text{ K}$ . The absence of a desorption peak for the mass of TmCot ( $273 \text{ amu}$ ) in Figure 2 can be rationalized by the binding strength to Gr through charge transfer. Apparently, the desorption temperature of the TmCot monomer lies above the decomposition temperature,

such that no desorption can be observed.

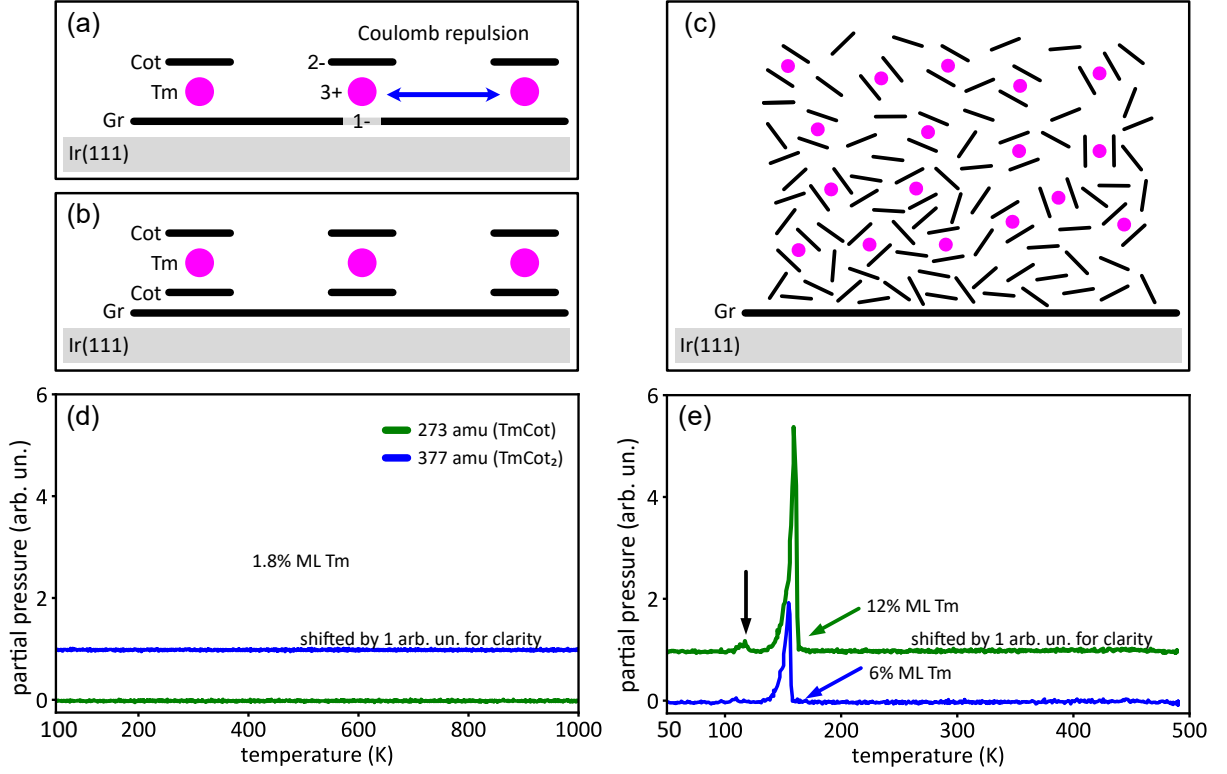


Figure 2: (a) Model of TmCot monomer adsorbed onto Gr/Ir(111). The Tm atoms binds to the Gr and Cot through charge transfer. This charge leads to Coulomb repulsion resulting in a dispersive behavior. (b) Model of TmCot<sub>2</sub> double deckers adsorbed onto Gr/Ir(111). (c) Model of TmCot<sub>2</sub> double deckers embedded into a matrix of Cot molecules. The Tm cannot come into contact with the substrate, because the Gr is first covered with a film of Cot molecules. (d) TDS of masses 273 (TmCot) and 377 (TmCot<sub>2</sub>) after deposition of 0.018 ML Tm at 300 K in excess pressure of Cot. The adsorption of neither of those masses is observed. (e) TDS of mass 377 (TmCot<sub>2</sub>) for 0.06 ML and 0.12 ML Tm. In both cases Tm was deposited into a Cot matrix at 20 K. The desorption peak for 0.06 ML lies at  $(155 \pm 1)$  K, and for 0.12 ML at  $(159 \pm 1)$  K. For 0.12 ML an additional peak at around 117 K is observed, which is presumably due to desorption from the Cot matrix.

We have also investigated the electronic configuration and magnetic properties of both TmCot dots and double-deckers. Figures 3a/b show the XAS and XMCD data for normal ( $0^\circ$ ) and grazing ( $60^\circ$ ) incidence of the X-ray beam with respect to the surface plane, of a TmCot monomer sample as prepared in Figure 1b. Only the  $M_5$  edges are shown here, because the  $M_4$  edges are not observed within the noise levels. While the fine structure varies, in both cases a main peak with two surrounding shoulders is observed, which can be identified as  $4f^{12}$  configuration comparing to literature [59] and the multiplet calculations in Figure S3 of the Supporting Information (SI). The corresponding magnetization curves for both angles of incidence are shown in Figure 3c. While both curves show a saturating behavior, the saturation value at  $60^\circ$  is only  $\approx 60\%$  compared to  $0^\circ$ . Also, the zero field susceptibility at  $0^\circ$  is  $\approx 3.9$  times higher compared to  $60^\circ$ , indicating

an out-of-plane easy-axis magnetization of the TmCot dots. In comparison, Figure 3d shows the XAS and XMCD data for TmCot<sub>2</sub> double deckers embedded in a Cot matrix as depicted in Figure 2d. The data are fully isotropic with respect to the angle of incidence, and in all cases the M<sub>5</sub> and M<sub>4</sub> edges are well visible and clearly indicate a 4f<sup>12</sup> electronic configuration. The isotropic behavior is also visible in the magnetization curves on Figure 3e, which lie on top of each other for both measured angles of incidence and seem close to saturation at 6.8 T. The isotropic behavior is fully consistent with the model in Figure 2c, in which the double deckers are embedded into the Cot matrix in random orientation.

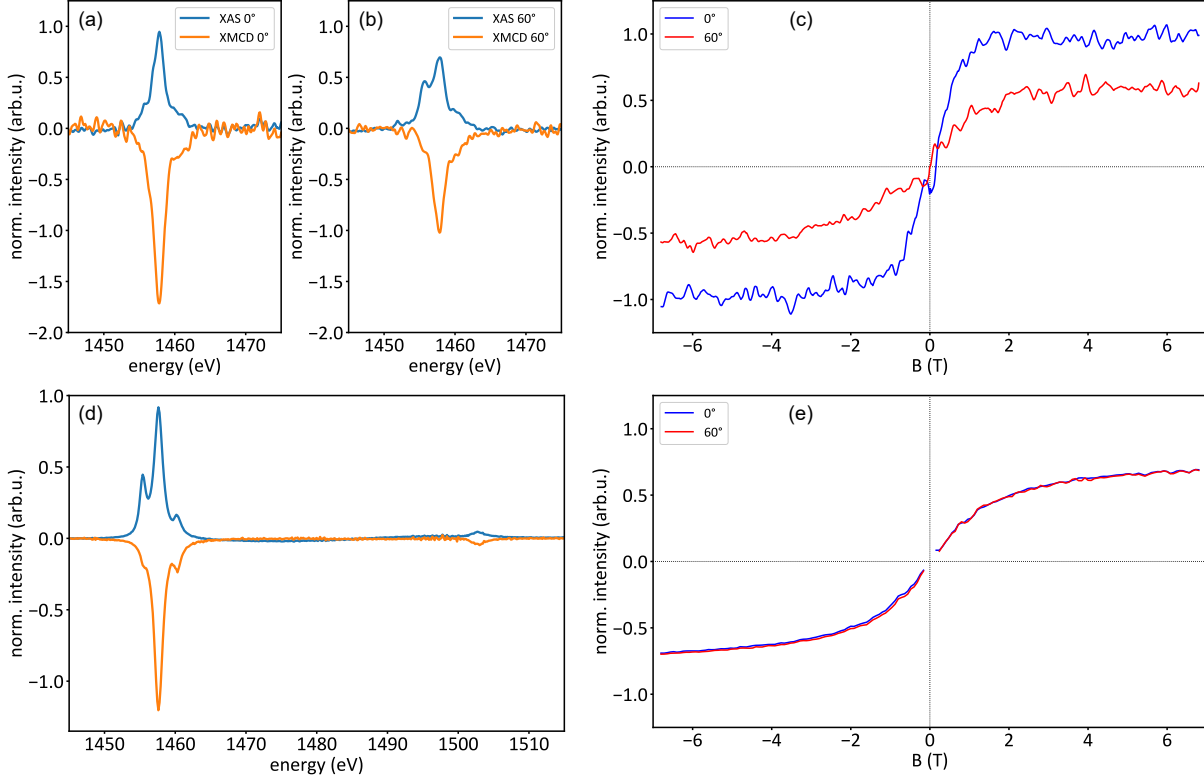


Figure 3: (a) Average XAS and XMCD of TmCot dot phase (0.01 ML Tm) at normal incidence (0°) at the M<sub>5</sub> edge. Two shoulders are visible left and right to the main peak, indicating a 4f<sup>12</sup> electronic configuration. (b) Average XAS and XMCD of TmCot dot phase (0.01 ML Tm) at grazing incidence (60°) at the M<sub>5</sub> edge. The two shoulders are much more pronounced, clearly indicating the 4f<sup>12</sup> electronic configuration. The reduced XMCD signal points to a magnetic anisotropy. (c) Magnetization curves corresponding to (a)/(b). At 0° a much higher zero-field susceptibility is observed, as well as a higher saturation magnetization. This is in agreement with the anisotropic XMCD signal, and the comparison of susceptibilities points to an out-of-plane easy magnetic axis. (d) Average XAS and XMCD of TmCot<sub>2</sub> double decker phase (0.55 ML Tm) averaged over both angles of incidence at the M<sub>5,4</sub> edges. The peak structures with both shoulders and the presence of the M<sub>4</sub> peak clearly indicates a 4f<sup>12</sup> electronic configuration. (e) Magnetization curves corresponding to (d), within accuracy the curves are completely isotropic with respect to the angle of incidence. This is in agreement with the TmCot<sub>2</sub> double deckers being embedded into a Cot matrix at random orientation. All measurements were conducted at  $T = 3$  K.



**TmCot dots – *ab initio* calculations:** Complementary to the experiments, we have employed *ab initio* DFT calculations. Figure 4a shows a top view of the relaxed geometry for a TmCot dot adsorbed on Gr/Ir(111). The adsorption geometry is visible in the side view of Figure 4b, where the Tm atom binds down to the Gr via charge transfer and the Cot molecule binds on top. The resulting adsorption energy of the dot is  $-2.16$  eV, and the relaxed binding distances are  $d(\text{Tm-Cot}) = 1.6$  Å and  $d(\text{Tm-C}_6) = 2.3$  Å. Figures 4c/d show charge-density difference plots (along the red line in Figure 4a), where red indicates electron accumulation and blue electron depletion. In Figure 4c the charge difference is plotted, when a Cot molecule is adsorbed onto Tm/Gr/Ir(111) (Tm atom already adsorbed to the substrate). It is visible, that charge from the Tm-Gr bonds and from the Tm atom moves to the electronegative Cot molecule. In Figure 4d the charge difference is plotted when adsorbing a TmCot dot on the substrate. In this case, some charge from the Cot molecule moves back toward the Tm atom, and a charge transfer to the substrate is observed, in agreement with the assumption made in Figure 2a.

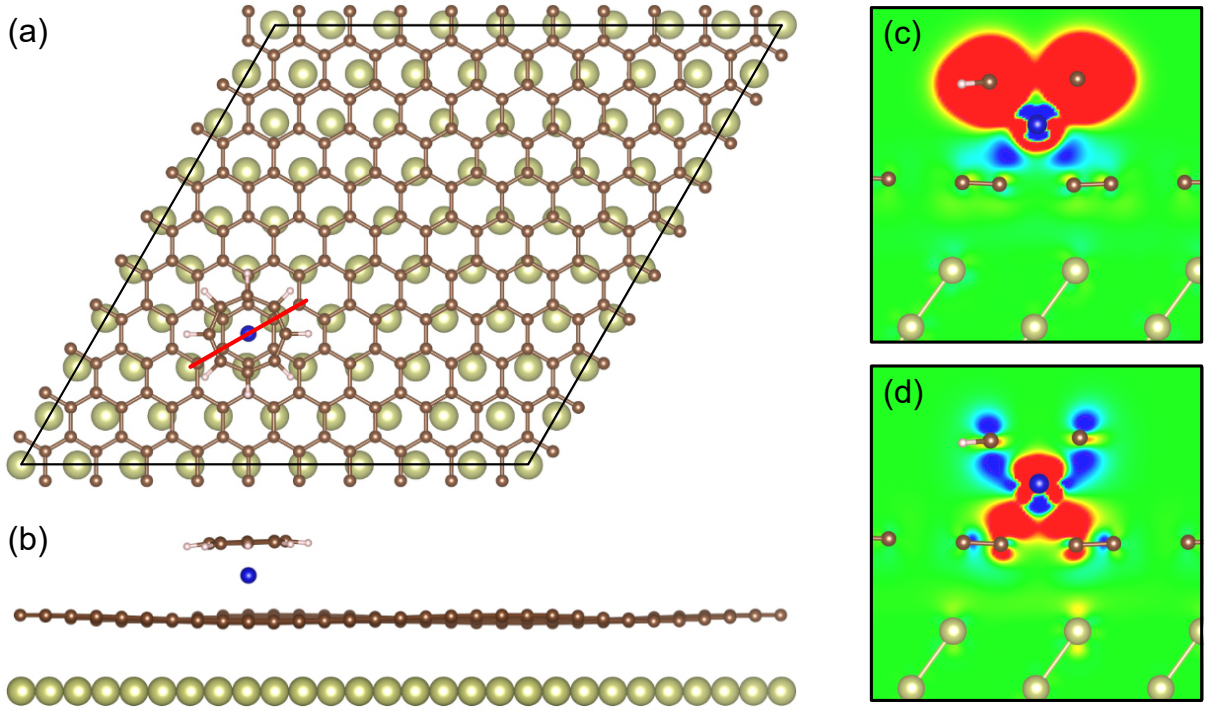


Figure 4: DFT calculated Gr/Ir(111) supercell with adsorbed TmCot dot. (b) Side view of relaxed geometry as shown in (a). (c) Charge-density difference plot along of Cot molecule adsorbed to Tm/Gr/Ir(111). It is visible that charge is transferred from the Tm atom to the Cot molecule. (d) Charge-density difference plot of TmCot monomer adsorbed on Gr/Ir(111). A small portion of charge is removed from the Cot molecule and transferred toward the Tm atom and substrate, forming a monomer-substrate bond. Color scale for all plots ranges from charge accumulation in red ( $+0.015$  electrons/Å<sup>3</sup>) to depletion in blue ( $-0.015$  electrons/Å<sup>3</sup>).

**TmCot coffee beans:** As mentioned for Figure 1c, we observe the formation of a second phase, forming islands when exceeding a TmCot dot coverage of about one dot per moiré cell. This phase coexistence is well visible in the large scale topograph of Figure 5a. The already described dot phase is visible in the zoom-in of Figure 5b (white square), and the island phase is visible in Figure 5c (black square). Additionally, in many areas the island phase is covered with additional species composed of Tm and/or Cot as shown in Figure 5d (blue square). Also apparent from Figure 5b is, that the dot phase has a much higher density compared to the lower-coverage topographs in Figure 1, which means when the island phase increases in coverage, the dot phase is being compressed.

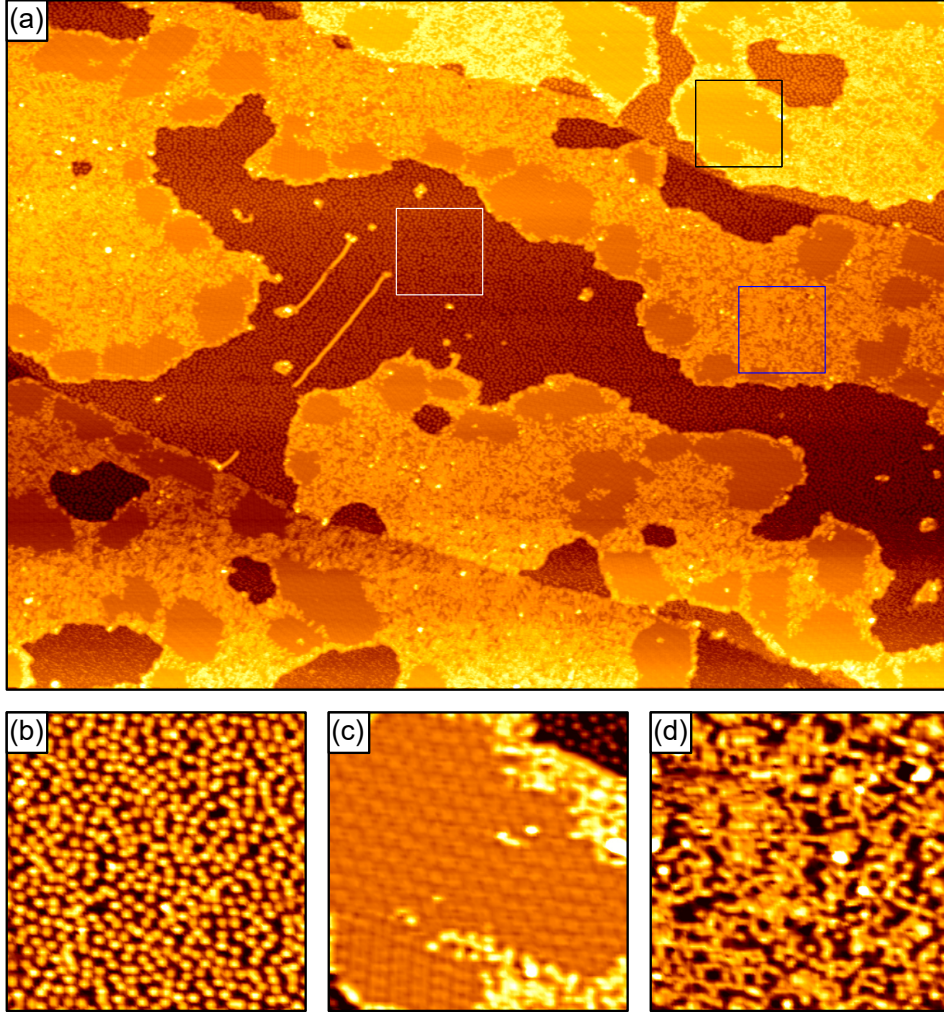


Figure 5: (a) STM topograph ( $3280 \times 2350 \text{ \AA}^2$ ) of coexisting disperse and island phases. (b) STM topograph ( $300 \times 300 \text{ \AA}^2$ ) of dot phase, position indicated by white square in (a). (c) STM topograph ( $300 \times 300 \text{ \AA}^2$ ) of island phase. Two domains are visible with each showing a herringbone structure, position indicated by black square in (a). (d) STM topograph ( $300 \times 300 \text{ \AA}^2$ ) of island which is covered by disordered organometallic compounds, position indicated by blue square in (a). Synthesis recipe: deposition of 0.14 ML Tm in  $4 \cdot 10^{-9}$  mbar Cot on Gr/Ir(111) at 300 K with subsequent short annealing to 400 K. The STM data have been recorded at 20 K. Tunneling parameters for (a)-(d) are  $U_{\text{bias}} = -1.72 \text{ V}$  and  $I_t = 49.0 \text{ pA}$ .

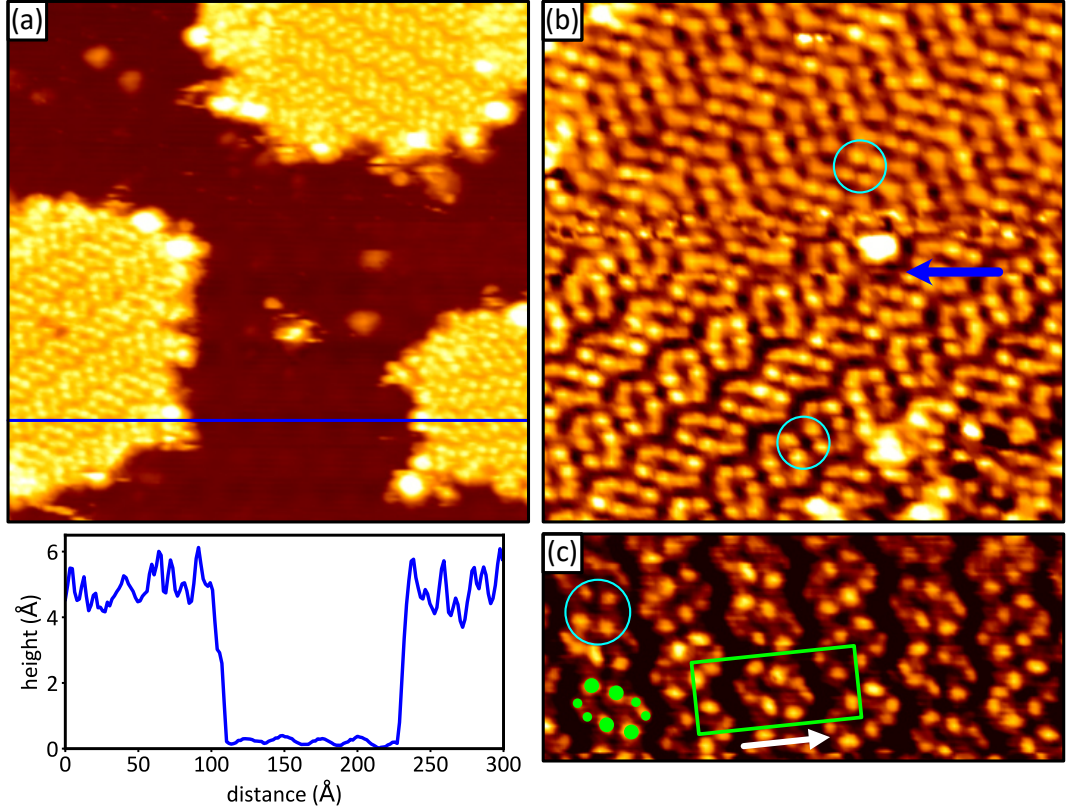


Figure 6: (a) STM topograph ( $300 \times 300 \text{ \AA}^2$ ) of TmCot coffee bean islands on Gr/Ir(111). Position of corresponding height profile indicated by the blue line. (b) STM topograph ( $160 \times 160 \text{ \AA}^2$ ) on top of coffee bean island with two distinct contrasts due to STM tip change, indicated by blue arrow. Cross-like features encircled cyan are visible in both contrasts. (c) STM topograph ( $135 \times 60 \text{ \AA}^2$ ) of coffee bean island. The unit cell is indicated by the green rectangle. Each coffee bean contains four bright and four faint intensities indicated by green dots. Cross-like feature encircled cyan. Synthesis recipe: deposition of 0.08 ML Tm in  $1 \cdot 10^{-9}$  mbar Cot on Gr/Ir(111) at 300 K with subsequent short annealing to 400 K. The STM data have been recorded at 20 K. Tunneling parameters are (a)/(b)  $U_{\text{bias}} = -3.2 \text{ V}$  and  $I_t = 52 \text{ pA}$  and (c)  $U_{\text{bias}} = -2.8 \text{ V}$  and  $I_t = 70 \text{ pA}$ .

A high-resolution topograph of the islands can be seen in Figure 6a (the dots are not visible due to the specific tunneling conditions). Due to the appearance of the building blocks within the islands, we call this the “coffee bean” phase. The apparent height of  $\approx 5 \text{ \AA}$  visible in the height profile of Figure 6a is comparable to the height of EuCot wire islands [54] and thus implies that the Cot molecules are likely to stand upwards with respect to the substrate. The single coffee beans appear in two chiralities and form domains with a herringbone structure. This is also visible in the molecular-resolution topograph in Figure 6b, in which two contrasts are visible due to a STM tip change (indicated by blue arrow). While the periodicities and angles are identical, the upper part appears continuous, whereas the lower part shows the coffee bean herringbone structure. Consistent in all imaging contrasts is the star-like feature encircled in cyan. This feature is also visible in the high-resolution topograph in Figure 6c, in which the herringbone unit cell with dimensions  $40 \times 18 \text{ \AA}^2$  is highlighted by the green rectangle. Each unit cell contains



two coffee beans, and within each coffee bean four bright and four weak intensities are visible, as indicated by the green overlay on the lower left in Figure 6c. It is also visible, that the coffee beans change chirality between the rows along the direction of the white arrow, while the chirality within each row is constant. While the density of Cot molecules is unknown due to the synthesis in Cot excess, the density of Tm atoms within each herringbone unit cell can be calculated using equation (1)

$$\rho_{\text{unit}} = \frac{\rho_{\text{tot}} - \beta \cdot \rho_{\text{dot}}}{\alpha} \quad (1)$$

with the geometrical coverages of the coffee bean ( $\alpha$ ) and dot phase ( $\beta$ ),  $0 \leq \alpha, \beta \leq 1$ , and the Tm atomic density per area for the coffee bean ( $\rho_{\text{unit}}$ ) and dot phase ( $\rho_{\text{dot}}$ ), and  $\rho_{\text{tot}}$  the total density of the deposited Tm. Averaging over several experiments, the resulting Tm density is  $(24 \pm 3)$  atoms per unit cell, which corresponds to 12 Tm atoms per coffee bean.

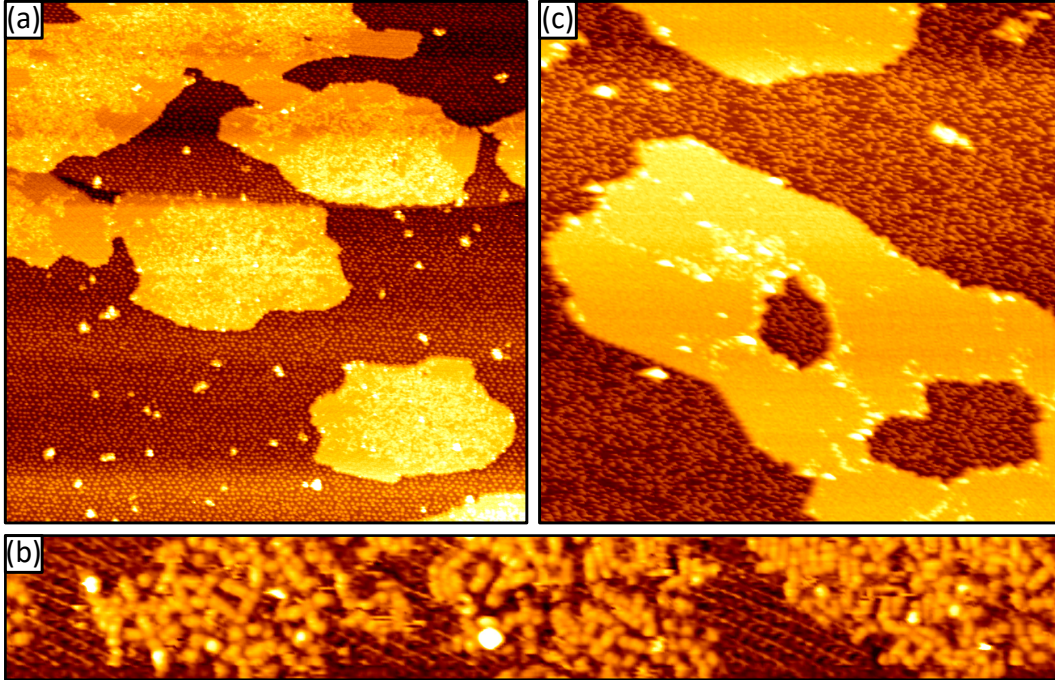


Figure 7: (a) STM topograph ( $1000 \times 1000 \text{ \AA}^2$ ) of TmCot coffee bean islands on Gr/Ir(111) after deposition of 0.08 ML Tm in  $1 \cdot 10^{-9}$  mbar Cot at 300 K. Islands are covered with small organometallic fragments, and the coexistence with the TmCot dot phase is visible. (b) High-resolution STM topograph ( $800 \times 140 \text{ \AA}^2$ ) of island from (a). Small organometallic structures are visible on the islands, most likely small fragments of wires. (c) STM topograph ( $1000 \times 1000 \text{ \AA}^2$ ) of sample in (a) after short annealing to 400 K. Majority of islands are clean, organometallic fragments moved off the islands. The dot phase is still present, but not clearly visible due to strong sample-tip interaction with the tunnelling conditions chosen. The STM data have been recorded at 20 K. Tunneling parameters are (a)  $U_{\text{bias}} = -2.3 \text{ V}$  and  $I_t = 80 \text{ pA}$ , (b)  $U_{\text{bias}} = -2.7 \text{ V}$  and  $I_t = 8 \text{ pA}$ , and  $U_{\text{bias}} = -1.9 \text{ V}$  and  $I_t = 39 \text{ pA}$ .

In Figure 7a the coexistence of the dot and coffee bean phase are well visible. As in Figure 5a, the islands are partly covered by adsorbates. Figure 7b shows a higher-resolution topograph of the adsorbates on a coffee bean island. The observed structures are consistent with small organometallic Tm–Cot fragments — such as  $\text{Tm}_2\text{Cot}_3$  or  $\text{Tm}_3\text{Cot}_4$  — and it is plausible that these have formed during growth on the already existing coffee bean islands. In a consecutive short annealing step to 400 K, this island-covering phase is removed, visible in Figure 7c. During the annealing step, the fragments have either desorbed, or moved off the islands and build themselves into these islands.

We have also conducted XAS measurements on the coffee bean phase as shown in Figures 8a/b. For both measured angles of incidence the  $M_5$  and  $M_4$  peaks are visible and clearly show a  $4f^{12}$  electronic configuration. As apparent from the higher XMCD signal in Figure 8b at grazing incidence a higher magnetization is reached. This is also visible from the corresponding magnetization curve in Figure 8c which shows a strong anisotropy between both angles of incidence. Interestingly, the zero-field susceptibility is equal within few percent for both angles of incidence while the magnetization differs significantly for higher fields. At normal incidence, the magnetization appears close to saturation at 9 T, while at grazing incidence goes to a higher magnetization value and is still far from saturation at 9 T.

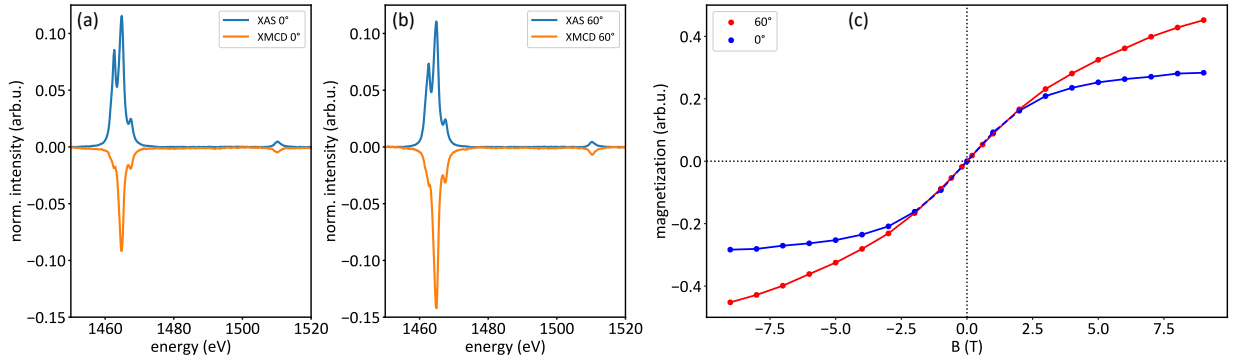


Figure 8: (a)/(b) Average XAS and XMCD of TmCot coffee bean phase (0.08 ML Tm) at normal incidence ( $0^\circ$ ) for (a) and grazing incidence ( $60^\circ$ ) for (b) at the  $M_5$  and  $M_4$  edges. At the  $M_5$  edge a main peak with two clear shoulders is visible, clearly indicating a  $4f^{12}$  electronic configuration. Two light shoulders are visible left and right to the main peak, indicating a  $4f^{12}$  electronic configuration. (c) Magnetization curves corresponding to (a)/(b). The zero-field susceptibility of both curves agrees within few percent. While at normal incidence the magnetization appears close to saturation, it is still far from saturation at grazing incidence. All measurements were conducted at  $T = 5$  K.

**TmCot sandwich-molecular wires – experiment:** The idea of changing the chemical reaction pathway during the on-surface synthesis from TmCot dots to wire growth is depicted in Figure 9. Since the preferred ionization state of Tm in compounds is 3+ and Cot accepts only two electrons, Tm donates charge to Gr and thereby induces an ionic bond to the substrate as shown in Figure 9(a). In order to form sandwich-molecular wires, similar to EuCot, ionic binding of Tm to the substrate needs to be suppressed. An intercalated layer of Eu causes strong n-doping of Gr by about 1.4 eV [56]. N-doping makes additional transfer of electrons to Tm less favorable and thereby weakens the TmCot–Gr bond. This weakening could be sufficient to maintain the 2+ oxidation state of Tm and thereby enable the formation of sandwich-molecular wires depicted in Figure 9b.

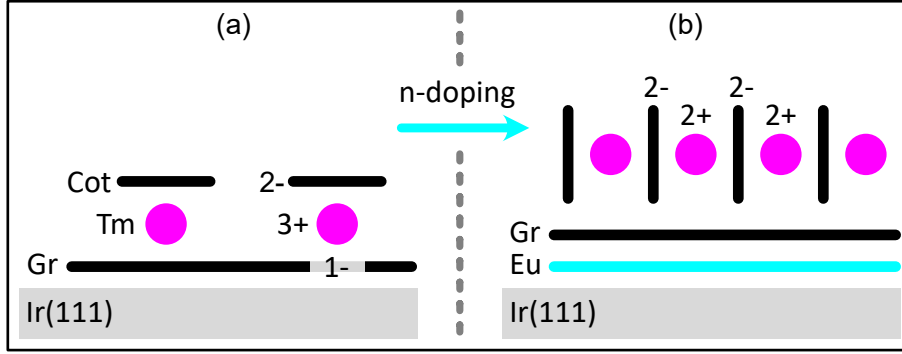


Figure 9: Idea of changing the chemical reaction pathway via substrate doping. (a) On Gr/Ir(111) TmCot monomers can form by charge transfer to the substrate. Tm atoms have the highest binding energy in the monomers, such that wires do not form. (b) By n-doping the substrate via Eu intercalation, the TmCot monomers become significantly less favorable because charge transfer to the substrate is suppressed and TmCot wires can form.

Experimentally we find, that in fact the intercalation of Eu under Gr before the on-surface synthesis completely suppresses the formation of TmCot dots and changes the chemical reaction pathway from the dot phase to polycrystalline islands of TmCot wires as shown in Figure 10a. The observed islands have a height of  $\approx 6 \text{ \AA}$  which is consistent with the height of EuCot wire islands as measured in ref. [54]. The molecular-resolution topograph (position indicated by the blue arrow in Figure 10a) shown in Figure 10b shows the interlocked aligned wires with intra-wire periodicity  $4.3 \pm 0.3 \text{ \AA}$  and inter-wire distance  $6.5 \pm 0.2 \text{ \AA}$ . The unit cell of the wire carpet is indicated by the black rhomboid on top of the ball model of the wires. The topograph of Figure 10c shows the island marked by the black rectangle in Figure 10a in larger magnification, and several domains of aligned wires are visible. The parts within the islands which appear white are consistent with second layer wire growth. The LEED pattern in Figure 10d corresponds to a TmCot wire sample as grown in Figure 1a and the black rhomboid denotes the reciprocal unit cell of the wire carpet. Due to the random orientation of the wire domains the LEED reflections of the reciprocal unit cell are smeared out over all angles and result in the two visible rings consistent with the intra- and inter-wire periodicities determined with STM.

Figure 11 shows a series of experiments, in which the Tm/Cot ratio was increased by a factor

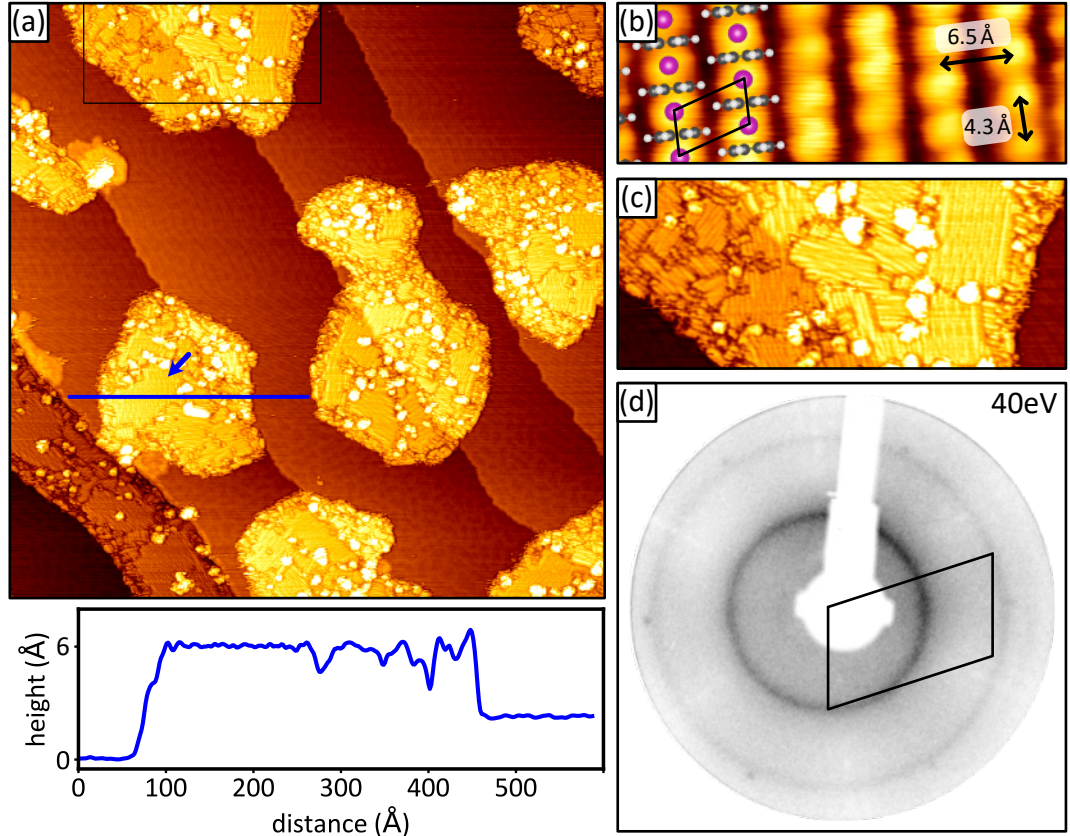


Figure 10: (a) STM topograph ( $1500 \times 1500 \text{ \AA}^2$ ) of TmCot wire islands on Gr/Eu/Ir(111). The islands show several domains of wire carpets, the bright intensities are consistent with second layer wire growth. The position of the corresponding profile is indicated by the green line. An island height of  $\approx 6 \text{ \AA}$  is observed, which is identical to the observed wire heights of EuCot wire islands. (b) Molecular resolution STM topograph ( $42 \times 15 \text{ \AA}^2$ ) of wire carpet at the position indicated by the blue arrow in (a). (c) MCP-LEED pattern (40 eV) of TmCot wire sample as grown in (a). Synthesis recipe (a)–(c): Deposition of 0.12 ML Tm in  $1 \cdot 10^{-9}$  mbar of Cot on Gr/Eu/Ir(111) at 300 K. The STM data have been recorded at 20 K. Tunneling parameters are (a)  $U_{\text{bias}} = -1.7 \text{ V}$  and  $I_t = 47 \text{ pA}$  and (b)  $U_{\text{bias}} = -0.2 \text{ V}$  and  $I_t = 1.4 \text{ nA}$ . Topographs have been superimposed with their derivatives for better visibility.

of 10 from (a)–(c). In Figure 11a only small wire fragments are visible, which can be explained by the large excess of Cot during synthesis. For small values of Tm/Cot, Tm atoms arriving on the substrate rather form short wire fragments — such as  $\text{Tm}_2\text{Cot}_3$  with non-reactive ends — than attaching to an already existing wire, in which the terminal Cot molecule is already in its dianionic charge state. For an increased Tm/Cot ratio parallel wire domains start to form as shown in Figure 11b. Further increasing the Tm/Cot ratio leads to increasingly larger domains visible in Figure 11c. The inset of Figure 11c shows one of the bright intensities (indicated by black square) in a different contrast. The structure and height are fully consistent with second layer wire growth.

Figure 12 shows a series of experiments, in which the Tm/Cot ratio was kept constant from (a)–(c), and the temperature during synthesis was increased from (a)–(d). A similar effect as in



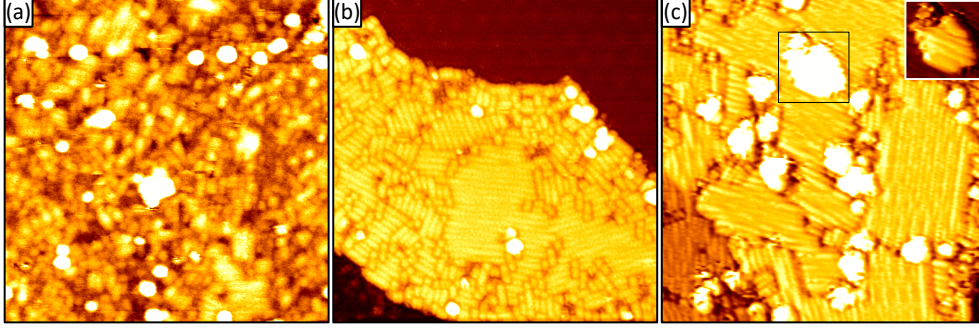


Figure 11: (a)–(c) STM topographs ( $350 \times 350 \text{ \AA}^2$ ) of TmCot wire islands on Gr/Eu/Ir(111) after growth in  $4 \cdot 10^{-9}$  mbar Cot at  $T = 300 \text{ K}$ . (a) 10 min Tm deposition, 0.008 ML/min: Only small wire fragments are visible. (b) 2 min Tm deposition, 0.04 ML/min, subsequent short annealing to 400 K: Still small wire fragments are visible, but also few larger domains of parallel wires are visible. (c) 1.5 min Tm deposition, 0.08 ML/min: The islands consist mostly of extended domains of parallel wires. Inset: STM topograph ( $80 \times 80 \text{ \AA}^2$ ) at position of black square with different contrast. Bright spots on top of the islands are second layer of wires. Tunneling parameters are (a)  $U_{\text{bias}} = -1.8 \text{ V}$  and  $I_t = 11 \text{ pA}$ , (b)  $U_{\text{bias}} = -2.0 \text{ V}$  and  $I_t = 13 \text{ pA}$ , and (c)  $U_{\text{bias}} = -1.7 \text{ V}$  and  $I_t = 47 \text{ pA}$ . Topographs have been superimposed with their derivatives for better visibility.

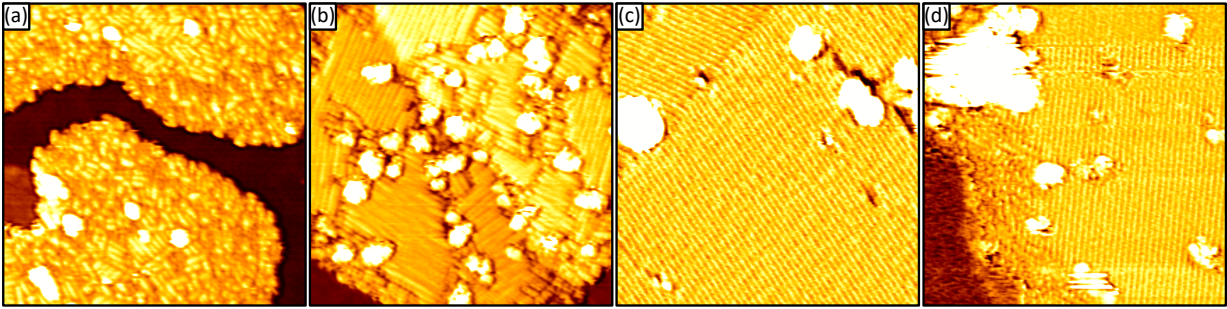


Figure 12: (a)–(d) STM topographs ( $350 \times 350 \text{ \AA}^2$ ) of TmCot wire islands on Gr/Eu/Ir(111), varying temperature  $T$ . (a) 250 K: Only small wire fragments are visible. (b) 300 K: Extended wire domains are visible. (c) 350 K: Large crystalline domains of wires are visible, with wire lengths exceeding 100 formula units. (d) 400 K: Large crystalline domains of wires are visible, but also Tm clusters have formed, e.g. in the upper left of the topograph. Synthesis recipes: (a)–(c) Tm deposition (0.08 ML/min) in  $4 \cdot 10^{-9}$  mbar Cot for 1.5 min, (d) Tm deposition (0.04 ML/min) in  $4 \cdot 10^{-9}$  mbar Cot for 2 min. Tunnelling parameters are (a)  $U_{\text{bias}} = -2.3 \text{ V}$  and  $I_t = 48 \text{ pA}$ , (b)  $U_{\text{bias}} = -1.7 \text{ V}$  and  $I_t = 47 \text{ pA}$ , (c)  $U_{\text{bias}} = -1.8 \text{ V}$  and  $I_t = 11 \text{ pA}$ , and (d)  $U_{\text{bias}} = -2.0 \text{ V}$  and  $I_t = 12 \text{ pA}$ . Topographs have been superimposed with their derivatives for better visibility.

Figure 11 is visible. For  $T = 250 \text{ K}$  in Figure 12a only small wire fragments are observed, while at  $T = 300 \text{ K}$  in Figure 12b larger domains have formed (same synthesis as in Figure 11c). Further increasing the growth temperature to  $T = 350 \text{ K}$  leads to the formation of large crystalline wire islands as visible in Figure 12c, in which wire lengths  $> 200$  formula units are achieved. For the syntheses in Figure 12a–c the observed second layers are consistent with the growth of a second layer of TmCot wires (compare Figure S4a of the SI for the second layer wire growth in Figure 12c). Further increasing the growth temperature to  $T = 400 \text{ K}$  — and also decreasing the deposition rate to 0.04 ML/min — leads to large crystalline islands comparable to Figure 12c,



but also results in the formation of Tm clusters (visible in Figure S4b in the SI). Apparently, the provided amount of Cot at the given temperature was not sufficient to prevent the formation of metal clusters in Figure 12d.

**TmCot sandwich-molecular wires – *ab initio* calculations:**

Complementary to our experiments, we have conducted DFT calculations to explain how n-doping of the substrate can change the chemical reaction pathway during synthesis. Table 1 compares the calculated adsorption energies for the TmCot dot on the undoped and n-doped substrate with the formation of an isolated TmCot 1D chain, i.e. an isolated wire. For the undoped Gr/Ir(111), the adsorbed dot is the energetically favored configuration, preferred by 50 meV over the formation of wires. This situation is reversed on the n-doped substrate, and the formation of TmCot wires is preferred by 600 meV. With this significant energy difference of 600 meV the suppression of the dot phase can be explained. Furthermore, we have calculated the electronic configurations of the different phases observed in experiment. In the infinite wire depicted in Figure 13a, Tm has an electronic configuration of  $4f^{13}$ , fully consistent with the ionic binding picture in which only the 6s electrons take part in binding. In agreement with the XMCD measurements, for the adsorbed monomer depicted in Figure 13b (adsorption geometry as in Figure 4) we find a  $4f^{12}$  configuration, also consistent with the simple ionic picture sketched in Figure 2a, where the Cot molecule accepts two electrons into its  $\pi$  system with the additional transfer of one electron towards the substrate. Finally, for the TmCot<sub>2</sub> double decker shown in Figure 13c we also calculate a  $4f^{12}$  configuration, consistent with XMCD results. Apparently, the two Cot molecules are able to extract and share overall 3 electrons from the Tm atom, but are not electronegative enough to force the Tm into a 4+ oxidation state.

adsorption energy TmCot dot	
on Gr/Ir(111)	−2.16 eV
on Gr/Eu/Ir(111)	−1.51 eV
formation energy TmCot 1D chain	−2.11 eV

Table 1: DFT-calculated adsorption energies for the TmCot dot on Gr/Ir(111) compared to Gr/Eu/Ir(111), and formation energy of isolated TmCot wire.

**Discussion:** On the undoped Gr/Ir(111), we find the adsorption of TmCot dots (monomers) through charge transfer to the Gr. The resulting Coulomb repulsion leads to a disperse behavior of repulsively interacting adsorbants, which has also been observed for the alkaline metal cesium adsorbed on Gr/6H-SiC(0001) [60]. The TmCot dots do not behave as a free 2D gas and are influenced by the substrate moiré with an observed preferential atop binding site. The same behavior was found for cesium adatoms adsorbed on Gr/Ir(111) [61], which are also regulated by the moiré of Gr with Ir(111) with the atop region being the preferred adsorption site. In ref. [62] single Tm atoms were adsorbed to W(110) surface. Although the situation is quite different compared to the adsorption on Gr/Ir(111), also on W(110) the symmetry of the single Tm atom is broken by the presence of the surface plane. Still, the magnetic behavior is similar

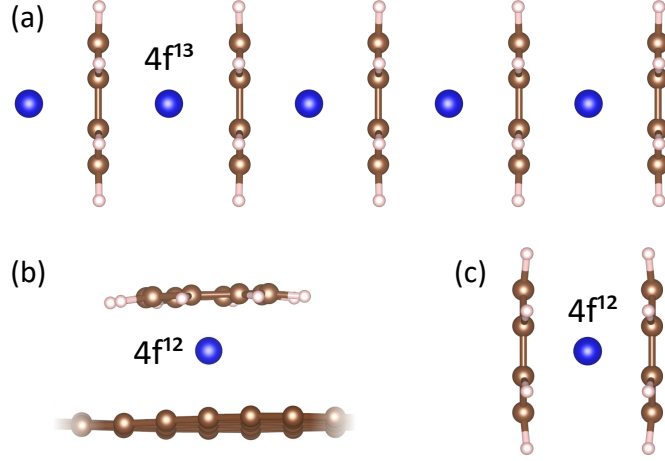


Figure 13: Comparison of DFT geometries and results for different TmCot structures. (a) For the isolated and infinite TmCot wire the electronic configuration of the 4f shell results as  $4f^{13}$ , like for the isolated Tm atom. In the simple ionic picture only the two 6s electrons contribute to the ionic binding. (b) The TmCot monomer adsorbed to Gr/Ir(111) has  $4f^{12}$  configuration, which can be explained by the fact that charge can be transferred to both Gr and the electronegative Cot molecule. (c) The TmCot double decker, i.e. one Tm atom sandwiched between two electronegative Cot molecules, also has a  $4f^{12}$  electronic configuration.

to our situation: The  $4f^{12}$  configuration is found as ground state, and an out-of-plane easy-axis magnetization is found for the single Tm atom.

While the exact molecular structure of the island-forming coffee bean phase remains unclear, the corresponding Tm atomic density of  $(0.033 \pm 0.003)$  atoms/ $\text{\AA}^2$  agrees with the density of the TmCot wires of  $(0.036 \pm 0.004)$  atoms/ $\text{\AA}^2$  within uncertainty. Combined with the observed height of  $\approx 5\text{\AA}$ , this implies that the Tm atoms must be embedded in a similar manner within a matrix of upright standing Cot molecules, comparable to the wire phase. The fact that organometallic wire fragments can be grown on top of the coffee bean islands, and later be removed by mild annealing to 400 K, shows the inertness of the island-forming phase, i.e. all Tm atoms must be encapsulated by Cot molecules and cannot stick out to the vacuum. It is unclear, if the single coffee beans only bind to each other via van der Waals interaction, or whether Tm atoms are bound in between the coffee beans. The fact that coffee beans are never observed in isolated form points towards the latter. Despite its inertness, the Gr can be seen as a catalyst in this instance. The formation of the coffee bean phase is only promoted by the initial TmCot monomer phase, which depends on the Gr as substrate for the charge transfer.

For the TmCot wire growth on the n-doped substrate, we have found that the average wire length depends both on the Tm/Cot ratio and temperature during synthesis, which is in contrast to the findings in ref. [54]. There, EuCot wires were synthesized on Gr/Ir(111), and the wire length was not limited by the Eu/Cot ratio during synthesis, as long as an excess pressure of Cot molecules was provided. The key difference is the preferred oxidation state, which is 2+ in the case of Eu due to its stable and half-filled 4f orbital. The preferred 2+ oxidation state for Eu has the

effect, that EuCot wires are always terminated by either  $\text{Eu}^{1+}$  cations or  $\text{Cot}^{1-}$  anions [50], both of which are chemically reactive and facilitate elongated wire growth. In contrast, Tm prefers a 3+ oxidation state under the same conditions, therefore TmCot wires are always terminated by  $\text{Tm}^{3+}\text{-Cot}^{2-}$ , which is non-reactive and simply terminates the wire growth. Therefore, even the small fragment  $\text{Tm}_2\text{Cot}_3$  is energetically highly favorable, because both Tm atoms can be in a  $\text{Tm}^{3+}$  state, fully saturating the three Cot molecules with electrons. This behavior has also been observed in gas phase experiments for other lanthanides with preferred 3+ oxidation state, described in ref. [49]. Therefore, the synthesis of extended TmCot wire domains can only be achieved by reducing the amount of Cot molecules available during synthesis, i.e. increasing the Tm/Cot ratio. In simple terms, a high Tm/Cot ratio corresponds to fewer Cot molecules present as binding partners, such that reactive Tm atoms are more likely to bind to existing wires. An increased synthesis temperature also results in larger wire domains, which can be explained by two effects: (i) analogous to an increase of the Tm/Cot ratio, the equilibrium density of Cot on Gr decreases for increasing temperature (at fixed Cot pressure) and (ii) an increased temperature leads to higher mobility of the reactants — Tm atoms and Cot molecules — which lowers the energy barrier for rearrangement on the surface, also promoting the growth of larger wire domains.

### 3 Conclusion

The formation of a disperse phase of repulsively interacting TmCot dots is observed on Gr/Ir(111). Using *ab initio* calculations, we explain their binding mechanism through charge transfer from the Tm atom to the Gr, and calculate a  $4f^{12}$  electronic configuration of the Tm. Using XAS and XMCD measurements, we verify the  $4f^{12}$  configuration and find an out-of-plane easy-axis magnetization of the dots.

For coverages exceeding one TmCot dot per moiré cell, an island phase emerges and coexists with the disperse phase. Also here, a  $4f^{12}$  configuration is found, and the Tm atomic density within these islands is similar to the density in the TmCot wire phase.

We find, that by n-doping the Gr via Eu intercalation, the chemical reaction pathway during synthesis is changed. On the n-doped substrate, sandwich-molecular wires are synthesized, forming carpets of interlocking and parallelly aligned wires. The average domain size can be tuned by changing the Tm/Cot ratio and temperature during growth: An increase in either ratio or temperature leads to an increase of the average domain size and thus wire length. Our complementary *ab initio* calculations show, that n-doping of the Gr changes the preferred binding configuration: While on the undoped substrate TmCot monomers adsorbed to Gr are preferred over TmCot wires, this situation is reversed on the n-doped Gr, enabling the growth of sandwich-molecular wires.

## 4 Methods

Scanning tunneling microscopy (STM) measurements and *in situ* sample synthesis were conducted in Cologne in the ultrahigh vacuum system TuMAII with a base pressure below  $1 \cdot 10^{-10}$  mbar. In this system Gr on Ir(111) was synthesized *in situ*. Gases are delivered through a gas dosing tube giving rise to a pressure enhancement by a factor of 50 compared to the pressure measured through a distant ion gauge and specified here. Sample cleaning was accomplished by exposure to  $1 \cdot 10^{-7}$  mbar oxygen at 1200 K when needed, cycles of noble gas sputtering using xenon, and brief annealing to 1500 K. Gr/Ir(111) was grown by room temperature exposure to ethylene until saturation coverage was reached and subsequent thermal decomposition at 1500 K, resulting in well-oriented Gr islands, which are grown to a complete layer through an additional exposure  $1 \cdot 10^{-7}$  mbar ethylene for 600 s at 1200 K [63]. TmCot dots and coffee beans on Gr/Ir(111) were grown by sublimation of elemental Tm from a Knudsen cell with a deposition rate of  $1.0 \cdot 10^{16} \frac{\text{atoms}}{\text{m}^2\text{s}}$  in a background pressure of  $1 \cdot 10^{-8}$  mbar Cot. Similarly, TmCot sandwich-molecular wires on Gr/Eu/Ir(111) were grown by sublimation of elemental Tm from a Knudsen cell with a deposition rate of  $2.0 \cdot 10^{15} - 2.0 \cdot 10^{16} \frac{\text{atoms}}{\text{m}^2\text{s}}$  in a background pressure of  $5 \cdot 10^{-9}$  mbar Cot at temperatures of 250 – 400 K.

STM imaging was conducted at 20 K with a sample bias and tunneling current in the order of  $U_{\text{bias}} \approx -2$  V and  $I_t \approx 0.1$  nA. For STM image processing the software *WSxM* [64] was applied. To ensure Gr quality and for structural characterization low-energy electron diffraction (LEED) was used in an energy range of 30 – 150 eV. LEED patterns are contrast-inverted for better visibility.

X-ray absorption spectroscopy (XAS) and X-ray magnetic circular dichroism (XMCD) measurements of the TmCot dots and double deckers have been conducted at the X-Treme beamline and endstation at the Swiss Light Source (SLS) synchrotron in Villigen (Switzerland [65]). Measurements of the coffee bean phase were performed at the high-field endstation ID32 at the European Synchrotron Research Facility (ESRF) in Grenoble (France). Measurements of the sandwich-molecular wires were performed at the VEKMAG endstation at the ‘Berliner Elektronenspeicherring-Gesellschaft für Synchrotronstrahlung’ (BESSY) in Berlin (Germany). The samples were prepared *in situ* in an ultrahigh vacuum chamber with a base pressure of the order of  $1 \cdot 10^{-10}$  mbar and using the recipes described above. During syntheses, sample cleaning was achieved by oxygen etching and noble-gas sputtering using argon. For consistency with home-lab results, the prepared samples were checked using LEED and a variable-temperature STM. The presented XAS data were recorded at a sample temperature of 3 K (SLS)/5 K (ESRF)/2 K (BESSY) using circularly polarized light in the energy range of 1440 – 1520 eV in the *total electron yield* detection mode.

The shown multiplet calculations were performed with the code in *Crispy* [66], using the standard parameters for Tm.

Our first-principles spin-polarized calculations were performed using the density functional theory

(DFT) [67] and the projector augmented plane wave method [68] as implemented in the VASP code [69, 70]. For the plane wave expansion of the Kohn-Sham wave functions [71] we used a cutoff energy of 500 eV. We carried out the structural relaxation using the vdW-DF2 [72] with a revised Becke (B86b) exchange [73, 74, 75] functional to properly account for the nonlocal correlation effects like van der Waals interactions. The analysis of the electronic structures was done using the PBE exchange-correlation energy functional [76]. We used the GGA + U approach [77] to correctly account for the orbital dependence of the Coulomb and exchange interactions of the Tm 4f states. For the presented calculations, we have used an effective Hubbard  $U$  of  $U_{\text{eff}} = 7.9$  eV.

## Acknowledgements

This work was funded by the Deutsche Forschungsgemeinschaft (DFG, German Research Foundation) within the project 'Sandwich molecular nanowires: on-surface synthesis, structure and magnetism' (MI 581/23-1, AT 109/5-1 and WE 2623/17-1). V. C. and N. A. acknowledge additional DFG support within CRC1238, project no. 277146874 - CRC 1238 (subproject C01). We gratefully acknowledge the Gauss Centre for Supercomputing (GCS) for providing computing time through the John von Neumann Institute for Computing (NIC) on the GCS share of the supercomputer JURECA at Jülich Supercomputing Centre (JSC).

## Supporting information available

Figure S1 shows an STM topograph of Tm clusters on Gr/Ir(111), when Tm is deposited at 300 K. Figure S2 shows the thermal desorption spectrum of a multilayer of Cot adsorbed to Gr/Ir(111). Figure S3 shows multiplet calculations of Tm 4f<sup>12</sup> and 4f<sup>13</sup> configurations. Finally, Figure S4 shows two STM topographs of TmCot wires islands on Gr/Eu/Ir(111), in which depending on growth conditions either additional second layer TmCot wires (Figure S4a) or Tm clusters (Figure S4b) form.

## References

- [1] S. A. Wolf, D. D. Awschalom, R. A. Buhrman, J. M. Daughton, S. von Molnár, M. L. Roukes, A. Y. Chtchelkanova and D. M. Treger, 'Spintronics: a spin-based electronics vision for the future', *Science* **294**, 1488 (2001).
- [2] S. Sanvito, 'Molecular spintronics', *Chem. Soc. Rev.* **40**, 3336 (2011).
- [3] J. Méndez, M. F. López and J. A. Martín-Gago, 'On-surface synthesis of cyclic organic molecules', *Chem. Soc. Rev.* **40**, 4578 (2011).
- [4] R. Lindner and A. Kühnle, 'On-surface reactions', *ChemPhysChem* **16**, 1582 (2015).
- [5] J. D. Rinehart, M. Fang, W. J. Evans and J. R. Long, 'A N<sub>2</sub><sup>3-</sup> radical-bridged terbium complex exhibiting magnetic hysteresis at 14 K', *J. Am. Chem. Soc.* **133**, 14236 (2011).
- [6] D. Klar, A. Candini, L. Joly, S. Klyatskaya, B. Krumme, P. Ohresser, J.-P. Kappler, M. Ruben and H. Wende, 'Hysteretic behaviour in a vacuum deposited submonolayer of single ion magnets', *Dalton Trans.* **43**, 10686 (2014).

- [7] L. Spree, F. Liu, V. Neu, M. Rosenkranz, G. Velkos, Y. Wang, S. Schiemenz, J. Dreiser, P. Gargiani, M. Valvidares, C.-H. Chen, B. Büchner, S. M. Avdoshenko and A. A. Popov, ‘Robust single molecule magnet monolayers on graphene and graphite with magnetic hysteresis up to 28 K’, *Adv. Funct. Mater.* **31**, 2105516 (2021).
- [8] M. Mannini, F. Pineider, C. Danieli, F. Totti, L. Sorace, P. Saintavrit, M.-A. Arrio, E. Otero, L. Joly, J. C. Cezar, A. Cornia and R. Sessoli, ‘Quantum tunnelling of the magnetization in a monolayer of oriented single-molecule magnets’, *Nature* **468**, 417 (2010).
- [9] R. Westerström, A.-C. Uldry, R. Stania, J. Dreiser, C. Piamonteze, M. Muntwiler, F. Matsui, S. Rusponi, H. Brune, S. Yang, A. Popov, B. Büchner, B. Delley and T. Greber, ‘Surface aligned magnetic moments and hysteresis of an endohedral single-molecule magnet on a metal’, *Phys. Rev. Lett.* **114**, 087201 (2015).
- [10] N. Ishikawa, M. Sugita, T. Ishikawa, S.-y. Koshihara and Y. Kaizu, ‘Lanthanide double-decker complexes functioning as magnets at the single-molecular level’, *J. Am. Chem. Soc.* **125**, 8694 (2003).
- [11] S. Fahrenndorf, N. Atodiresei, C. Besson, V. Caciuc, F. Matthes, S. Blügel, P. Kögerler, D. E. Bürgler and C. M. Schneider, ‘Accessing 4f-states in single-molecule spintronics’, *Nat. Commun.* **4**, 2425 (2013).
- [12] D. Klar, A. Candini, L. Joly, S. Klyatskaya, B. Krumme, P. Ohresser, J.-P. Kappler, M. Ruben and H. Wende, ‘Hysteretic behaviour in a vacuum deposited submonolayer of single ion magnets’, *Dalton Trans.* **43**, 10686 (2014).
- [13] Y. Lan, S. Klyatskaya, M. Ruben, O. Fuhr, W. Wernsdorfer, A. Candini, V. Corradini, A. Lodi Rizzini, U. del Pennino, F. Troiani, L. Joly, D. Klar, H. Wende and M. Affronte, ‘Magnetic interplay between two different lanthanides in a tris-phthalocyaninato complex: a viable synthetic route and detailed investigation in the bulk and on the surface’, *J. Mater. Chem. C* **3**, 9794 (2015).
- [14] C. Wäckerlin, F. Donati, A. Singha, R. Baltic, S. Rusponi, K. Diller, F. Patthey, M. Pivetta, Y. Lan, S. Klyatskaya, M. Ruben, H. Brune and J. Dreiser, ‘Giant hysteresis of single-molecule magnets adsorbed on a nonmagnetic insulator’, *Adv. Mater.* **28**, 5195 (2016).
- [15] D. Écija, W. Auwärter, S. Vijayaraghavan, K. Seufert, F. Bischoff, K. Tashiro and J. V. Barth, ‘Assembly and manipulation of rotatable cerium porphyrinato sandwich complexes on a surface’, *Angew. Chem. Int. Ed.* **50**, 3872 (2011).
- [16] C. Wäckerlin, J. Nowakowski, S.-X. Liu, M. Jaggi, D. Siewert, J. Girovsky, A. Shchyrba, T. Hählen, A. Kleibert, P. M. Oppeneer, F. Nolting, S. Decurtins, T. A. Jung and N. Ballav, ‘Two-dimensional supramolecular electron spin arrays’, *Adv. Mater.* **25**, 2404 (2013).
- [17] K. Schouteden, T. Ivanova, Z. Li, V. Iancu, E. Janssens and C. Van Haesendonck, ‘Probing magnetism in 2D molecular networks after *in situ* metalation by transition metal atoms’, *J. Phys. Chem. Lett.* **6**, 1048 (2015).
- [18] J. I. Urgel, D. Eciija, W. Auwärter, D. Stassen, D. Bonifazi and J. V. Barth, ‘Orthogonal insertion of lanthanide and transition-metal atoms in metal-organic networks on surfaces’, *Angew. Chem. Int. Ed.* **54**, 6163 (2015).
- [19] T. R. Umbach, M. Bernien, C. F. Hermanns, A. Krüger, V. Sessi, I. Fernandez-Torrente, P. Stoll, J. I. Pascual, K. J. Franke and W. Kuch, ‘Ferromagnetic coupling of mononuclear Fe centers in a self-assembled metal-organic network on Au(111)’, *Phys. Rev. Lett.* **109**, 267207 (2012).
- [20] J. Wang, P. H. Acioli and J. Jellinek, ‘Structure and magnetism of  $V_nBz_{n+1}$  sandwich clusters’, *J. Am. Chem. Soc.* **127**, 2812 (2005).
- [21] Y. Mokrousov, N. Atodiresei, G. Bihlmayer and S. Blügel, ‘Magnetic anisotropy energies of metal-benzene sandwiches’, *Int. J. Quantum Chem.* **106**, 3208 (2006).
- [22] V. V. Maslyuk, A. Bagrets, V. Meded, A. Arnold, F. Evers, M. Brandbyge, T. Bredow and I. Mertig, ‘Organometallic benzene-vanadium Wire: a one-dimensional half-metallic ferromagnet’, *Phys. Rev. Lett.* **97**, 097201 (2006).

- [23] W. B. Tan, J. Hongmei, S.-W. Yang and G. Q. Xu, ‘Boratabenzene-vanadium sandwich molecular wire and its properties’, *Nanoscale* **4**, 7557 (2012).
- [24] L. Zhu and J. Wang, ‘*Ab initio* study of structural, electronic, and magnetic properties of transition metal-borazine molecular wires’, *J. Phys. Chem. C* **113**, 8767 (2009).
- [25] T. Masubuchi, T. Iwasa and A. Nakajima, ‘Multiple-decker and ring sandwich formation of manganese-benzene organometallic cluster anions:  $\text{Mn}_n\text{Bz}_n^-$  ( $n=1-5$  and 18)’, *Phys. Chem. Chem. Phys.* **18**, 26049 (2016).
- [26] Y. H. Lu, H. Jin, H. Zhu, S.-W. Yang, C. Zhang, J. Z. Jiang and Y. P. Feng, ‘A possible reaction pathway to fabricate a half-metallic wire on a silicon surface’, *Adv. Funct. Mater.* **23**, 2233 (2013).
- [27] K. Hoshino, T. Kurikawa, H. Takeda, A. Nakajima and K. Kaya, ‘Structures and ionization energies of sandwich clusters ( $\text{V}_n(\text{benzene})_m$ )’, *J. Phys. Chem. C* **99**, 3053 (1995).
- [28] A. Nakajima and K. Kaya, ‘A novel network structure of organometallic clusters in the gas phase’, *J. Phys. Chem. A* **104**, 176 (2000).
- [29] T. Kurikawa, H. Takeda, M. Hirano, K. Judai, T. Arita, S. Nagao, A. Nakajima and K. Kaya, ‘Electronic properties of organometallic metal-benzene complexes  $[\text{M}_n(\text{benzene})_m]$  ( $\text{M} = \text{Sc-Cu}$ )’, *Organometallics* **18**, 1430 (1999).
- [30] H. Xiang, J. Yang, J. G. Hou and Q. Zhu, ‘One-dimensional transition metal-benzene sandwich polymers: possible ideal conductors for spin transport’, *J. Am. Chem. Soc.* **128**, 2310 (2006).
- [31] T. Masubuchi, K. Ohi, T. Iwasa and A. Nakajima, ‘Experimental and theoretical studies on the electronic properties of vanadium-benzene sandwich cluster anions,  $\text{V}_n\text{Bz}_{n+1}^-$  ( $n = 1-5$ )’, *J. Chem. Phys.* **137**, 224305 (2012).
- [32] K. Miyajima, A. Nakajima, S. Yabushita, M. B. Knickelbein and K. Kaya, ‘Ferromagnetism in one-dimensional vanadium-benzene sandwich clusters’, *J. Am. Chem. Soc.* **126**, 13202 (2004).
- [33] L. Zhou, S.-W. Yang, M.-F. Ng, M. B. Sullivan, Tan and L. Shen, ‘One-dimensional iron-cyclopentadienyl sandwich molecular wire with half metallic, negative differential resistance and high-spin filter efficiency properties’, *J. Am. Chem. Soc.* **130**, 4023 (2008).
- [34] L. Shen, S.-W. Yang, M.-F. Ng, V. Ligatchev, L. Zhou and Y. Feng, ‘Charge-transfer-based mechanism for half-metallicity and ferromagnetism in one-dimensional organometallic sandwich molecular wires’, *J. Am. Chem. Soc.* **130**, 13956 (2008).
- [35] H. Da, H. M. Jin, K. H. Lim and S.-W. Yang, ‘Half-metallic spintronic switch of bimetallic sandwich molecular wire via the control of external electrical field’, *J. Phys. Chem. C* **114**, 21705 (2010).
- [36] X. Zhang, Z. Tian, S.-W. Yang and J. Wang, ‘Magnetic manipulation and half-metal prediction of one-dimensional bimetallic organic sandwich molecular wires  $[\text{CpTM}_1\text{CpTM}_2]$  ( $\text{TM}_1 = \text{Ti, Cr, Fe}$ ;  $\text{TM}_2 = \text{Sc-Co}$ )’, *J. Phys. Chem. C* **115**, 2948 (2011).
- [37] C. Morari, H. Allmaier, F. Beiuşeanu, T. Jurcuţ and L. Chioncel, ‘Electronic structure and magnetic properties of metallocene multiple-decker sandwich nanowires’, *Phys. Rev. B* **85**, 085413 (2012).
- [38] L. Wang, Z. Cai, J. Wang, J. Lu, G. Luo, L. Lai, J. Zhou, R. Qin, Z. Gao, D. Yu, G. Li, W. N. Mei and S. Sanvito, ‘Novel one-dimensional organometallic half metals: vanadium-cyclopentadienyl, vanadium-cyclopentadienyl-benzene, and vanadium-anthracene wires’, *Nano Lett.* **8**, 3640 (2008).
- [39] X. Zhang and J. Wang, ‘*Ab initio* study of bond characteristics and magnetic properties of mixed-sandwich  $\text{V}_n\text{Bz}_m\text{Cp}_k$  clusters’, *J. Phys. Chem. A* **114**, 2319 (2010).
- [40] Y. Li, G. Zhou, J. Li, J. Wu, B.-L. Gu and W. Duan, ‘*Ab initio* study of half-metallicity and magnetism of complex organometallic molecular wires’, *J. Phys. Chem. C* **115**, 7292 (2011).
- [41] X. Zhang, M. Cao, L. Liu and Y. Liu, ‘Tunable electronic and magnetic properties of boron/nitrogen-doped  $\text{BzTMCp}^*\text{TMBz/CpTMCp}^*\text{TMCp}$  clusters and one-dimensional infinite molecular wires’, *J. Phys. Chem. C* **118**, 11620 (2014).

- [42] W. Kaminsky, ‘The discovery of metallocene catalysts and their present state of the art’, *J. Polym. Sci. A Polym. Chem.* **42**, 3911 (2004).
- [43] M. R. Machat, A. Fischer, D. Schmitz, M. Vöst, M. Drees, C. Jandl, A. Pöthig, N. P. M. Casati, W. Scherer and B. Rieger, ‘Behind the scenes of group 4 metallocene catalysis: examination of the metal-carbon bond’, *Organometallics* **37**, 2690 (2018).
- [44] N. Atodiresei, P. H. Dederichs, Y. Mokrousov, L. Bergqvist, G. Bihlmayer and S. Blügel, ‘Controlling the magnetization direction in molecules via their oxidation state’, *Phys. Rev. Lett.* **100**, 117207 (2008).
- [45] X. Zhang, M.-F. Ng, Y. Wang, J. Wang and S.-W. Yang, ‘Theoretical studies on structural, magnetic, and spintronic characteristics of sandwiched  $\text{Eu}_n\text{COT}_{n+1}$  ( $n = 1-4$ ) clusters’, *ACS Nano* **3**, 2515 (2009).
- [46] K. Xu, J. Huang, S. Lei, H. Su, F. Y. C. Boey, Q. Li and J. Yang, ‘Efficient organometallic spin filter based on europium-cyclooctatetraene wire’, *J. Chem. Phys.* **131**, 104704 (2009).
- [47] X. Yao, S. Yuan and J. Wang, ‘Theoretical studies of sandwich molecular wires with europium and boratacyclooctatetraene ligand and the structure on a H-Ge(001)-2x1 surface’, *J. Phys. Chem. C* **120**, 7088 (2016).
- [48] R. G. Hayes and J. L. Thomas, ‘Synthesis of cyclooctatetraenyleuropium and cyclooctatetraenylterbium’, *J. Am. Chem. Soc.* **91**, 6876 (1969).
- [49] T. Kurikawa, Y. Negishi, F. Hayakawa, S. Nagao, K. Miyajima, A. Nakajima and K. Kaya, ‘Multiple-decker sandwich complexes of lanthanide-1,3,5,7-cyclooctatetraene  $[\text{Ln}_n(\text{C}_8\text{H}_8)_m]$  ( $\text{Ln} = \text{Ce}, \text{Nd}, \text{Eu}, \text{Ho}, \text{and Yb}$ ); localized ionic bonding structure’, *J. Am. Chem. Soc.* **120**, 11766 (1998).
- [50] N. Hosoya, R. Takegami, J.-i. Suzumura, K. Yada, K. Koyasu, K. Miyajima, M. Mitsui, M. B. Knickelbein, S. Yabushita and A. Nakajima, ‘Lanthanide organometallic sandwich nanowires: formation mechanism’, *J. Phys. Chem. A* **109**, 9 (2005).
- [51] N. Hosoya, R. Takegami, J.-i. Suzumura, K. Yada, K. Miyajima, M. Mitsui, M. B. Knickelbein, S. Yabushita and A. Nakajima, ‘Formation and electronic structures of organoeuropium sandwich nanowires’, *J. Phys. Chem. A* **118**, 8298 (2014).
- [52] K. Miyajima, M. B. Knickelbein and A. Nakajima, ‘Magnetic properties of lanthanide organometallic sandwich complexes produced in a molecular beam’, *Polyhedron* **24**, 2341 (2005), proceedings of the 9th International Conference on Molecule-based Magnets (ICMM 2004).
- [53] K. Miyajima, M. B. Knickelbein and A. Nakajima, ‘Stern-Gerlach study of multidecker lanthanide-cyclooctatetraene sandwich clusters’, *J. Phys. Chem. A* **112**, 366 (2008).
- [54] F. Huttmann, N. Schleheck, N. Atodiresei and T. Michely, ‘On-surface synthesis of sandwich molecular nanowires on graphene’, *J. Am. Chem. Soc.* **139**, 9895 (2017).
- [55] F. Huttmann, N. Rothenbach, S. Kraus, K. Ollefs, L. M. Arruda, M. Bernien, D. Thonig, A. Delin, J. Fransson, K. Kummer, N. B. Brookes, O. Eriksson, W. Kuch, T. Michely and H. Wende, ‘Europium cyclooctatetraene nanowire carpets: a low-dimensional, organometallic, and ferromagnetic insulator’, *J. Phys. Chem. Lett.* **10**, 911 (2019).
- [56] S. Schumacher, F. Huttmann, M. Petrović, C. Witt, D. F. Förster, C. Vo-Van, J. Coraux, A. J. Martínez-Galera, V. Sessi, I. Vergara, R. Rückamp, M. Grüninger, N. Schleheck, F. Meyer zu Heringdorf, P. Ohresser, M. Kralj, T. O. Wehling and T. Michely, ‘Europium underneath graphene on Ir(111): intercalation mechanism, magnetism, and band structure’, *Phys. Rev. B* **90**, 235437 (2014).
- [57] A. T. N'Diaye, J. Coraux, T. N. Plasa, C. Busse and T. Michely, ‘Structure of epitaxial graphene on Ir(111)’, *New J. Phys.* **10**, 043033 (2008).
- [58] J. A. Lau, I. Calvo-Almazán, P. S. M. Townsend, D. J. Ward, A. P. Jardine, W. Allison, J. Ellis, B. J. Hinch and N. Avidor, ‘Structural evolution of a cyclooctatetraene adlayer on Cu(111) during isothermal desorption’, *J. Phys. Chem. C* **122**, 8941 (2018).



- [59] J. B. Goedkoop, B. T. Thole, G. van der Laan, G. A. Sawatzky, F. M. F. de Groot and J. C. Fuggle, ‘Calculations of magnetic X-ray dichroism in the 3d absorption spectra of rare-earth compounds’, *Phys. Rev. B* **37**, 2086 (1988).
- [60] C.-L. Song, B. Sun, Y.-L. Wang, Y.-P. Jiang, L. Wang, K. He, X. Chen, P. Zhang, X.-C. Ma and Q.-K. Xue, ‘Charge-transfer-induced cesium superlattices on graphene’, *Phys. Rev. Lett.* **108**, 156803 (2012).
- [61] M. Petrović, P. Lazić, S. Runte, T. Michely, C. Busse and M. Kralj, ‘Moiré-regulated self-assembly of cesium adatoms on epitaxial graphene’, *Phys. Rev. B* **96**, 085428 (2017).
- [62] C. Nistor, A. Mugarza, S. Stepanow, P. Gambardella, K. Kummer, J. L. Diez-Ferrer, D. Coffey, C. de la Fuente, M. Ciria and J. I. Arnaud, ‘Structure and magnetism of Tm atoms and monolayers on W(110)’, *Phys. Rev. B* **90**, 064423 (2014).
- [63] R. van Gastel, A. T. N’Diaye, D. Wall, J. Coraux, C. Busse, N. M. Buckanie, F.-J. Meyer zu Heringdorf, M. Horn von Hoegen, T. Michely and B. Poelsema, ‘Selecting a single orientation for millimeter sized graphene sheets’, *Appl. Phys. Lett.* **95**, 121901 (2009).
- [64] I. Horcas, R. Fernández, J. M. Gómez-Rodríguez, J. Colchero, J. Gómez-Herrero and A. M. Baro, ‘WSXM: A software for scanning probe microscopy and a tool for nanotechnology’, *Rev. Sci. Instrum.* **78**, 013705 (2007).
- [65] C. Piamonteze, U. Flechsig, S. Rusponi, J. Dreiser, J. Heidler, M. Schmidt, R. Wetter, M. Calvi, T. Schmidt, H. Pruchova, J. Krempasky, C. Quitmann, H. Brune and F. Nolting, ‘X-Treme beamline at SLS: X-ray magnetic circular and linear dichroism at high field and low temperature’, *J. Synchrotron Radiat.* **19**, 661 (2012).
- [66] M. Retegan, ‘Crispy: v0.7.3’, (2019).
- [67] P. Hohenberg and W. Kohn, ‘Inhomogeneous electron gas’, *Phys. Rev.* **136**, B864 (1964).
- [68] P. E. Blöchl, ‘Projector augmented-wave method’, *Phys. Rev. B* **50**, 17953 (1994).
- [69] G. Kresse and J. Hafner, ‘*Ab initio* molecular dynamics for liquid metals’, *Phys. Rev. B* **47**, 558 (1993).
- [70] G. Kresse and J. Furthmüller, ‘Efficient iterative schemes for *ab initio* total-energy calculations using a plane-wave basis set’, *Phys. Rev. B* **54**, 11169 (1996).
- [71] W. Kohn and L. J. Sham, ‘Self-consistent equations including exchange and correlation effects’, *Phys. Rev.* **140**, A1133 (1965).
- [72] K. Lee, E. D. Murray, L. Kong, B. I. Lundqvist and D. C. Langreth, ‘Higher-accuracy van der Waals density functional’, *Phys. Rev. B* **82**, 081101 (2010).
- [73] A. D. Becke, ‘On the large-gradient behavior of the density functional exchange energy’, *J. Chem. Phys.* **85**, 7184 (1986).
- [74] I. Hamada, ‘Van der Waals density functional made accurate’, *Phys. Rev. B* **89**, 121103 (2014).
- [75] F. Huttmann, A. J. Martínez-Galera, V. Caciuc, N. Atodiresei, S. Schumacher, S. Standop, I. Hamada, T. O. Wehling, S. Blügel and T. Michely, ‘Tuning the van der Waals interaction of graphene with molecules via doping’, *Phys. Rev. Lett.* **115**, 236101 (2015).
- [76] J. P. Perdew, K. Burke and M. Ernzerhof, ‘Generalized gradient approximation made simple’, *Phys. Rev. Lett.* **77**, 3865 (1996).
- [77] V. I. Anisimov, F. Aryasetiawan and A. I. Lichtenstein, ‘First-principles calculations of the electronic structure and spectra of strongly correlated systems: the LDA + U method’, *J. Condens. Matter Phys.* **9**, 767 (1997).

**Supporting information:**  
**from dots to wires:**  
**doping-dependent on-surface synthesis of**  
**thulium-cyclooctatetraene compounds on graphene**

Stefan Kraus<sup>\*1</sup>, Alexander Herman<sup>2</sup>, Felix Huttmann<sup>1</sup>, Christian Krämer<sup>1</sup>, Shigeru Tsukamoto<sup>3</sup>, Nico Rothenbach<sup>2</sup>, Katharina Ollefs<sup>2</sup>, Lea Spieker<sup>2</sup>, Tobias Lojewski<sup>2</sup>, Matthias Bernien<sup>4</sup>, Lucas M. Arruda<sup>4</sup>, Jan Dreiser<sup>5</sup>, Nick Brookes<sup>6</sup>, Kurt Kummer<sup>6</sup>, Wolfgang Kuch<sup>4</sup>, Heiko Wende<sup>2</sup>, Nicolae Atodiresei<sup>†3</sup>, and Thomas Michely<sup>1</sup>

<sup>1</sup>*II. Physikalisches Institut, Universität zu Köln, Zùlpicher Str. 77, 50937 Köln, Germany*

<sup>2</sup>*Faculty of Physics and Center for Nanointegration Duisburg-Essen (CENIDE), University of Duisburg-Essen, Lotharstraße 1, 47048 Duisburg, Germany*

<sup>3</sup>*Peter Grünberg Institute and Institute for Advanced Simulation, Forschungszentrum Jùlich, Wilhelm-Johnen-StraÙe, 52428 Jùlich, Germany*

<sup>4</sup>*Institut für Experimentalphysik, Freie Universität Berlin, Arnimallee 14, 14195 Berlin, Germany*

<sup>5</sup>*Swiss Light Source, Paul Scherrer Institute, Forschungsstrasse 111, 5232 Villigen PSI, Switzerland*

<sup>6</sup>*European Synchrotron Research Facility (ESRF), Avenue des Martyrs 71, CS 40220, 38043 Grenoble Cedex 9, France*

---

<sup>\*</sup>kraus@ph2.uni-koeln.de (experiment)

<sup>†</sup>n.atodiresei@fz-juelich.de (theory)

**Figure S1: Tm deposited on Gr/Ir(111) at T= 300 K**

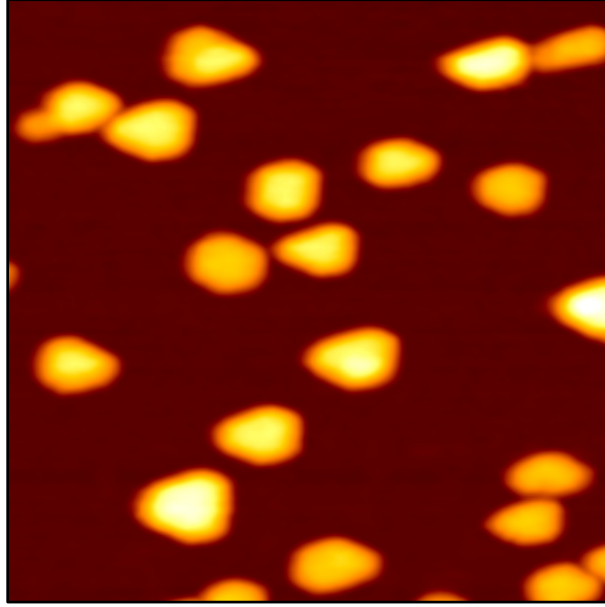


Figure S1: STM topograph ( $700 \times 700 \text{ \AA}$ ) of 0.35 ML Tm deposited on Gr/Ir(111) at  $T = 300 \text{ K}$ . All Tm forms clusters, the Gr in between is clean. STM taken at  $T = 20 \text{ K}$ . Tunnelling parameters are  $U_{\text{bias}} = -2.0 \text{ V}$  and  $I_t = 0.7 \text{ nA}$

**Figure S2: TDS of multiayer Cot adsorbed to Gr/Ir(111)**

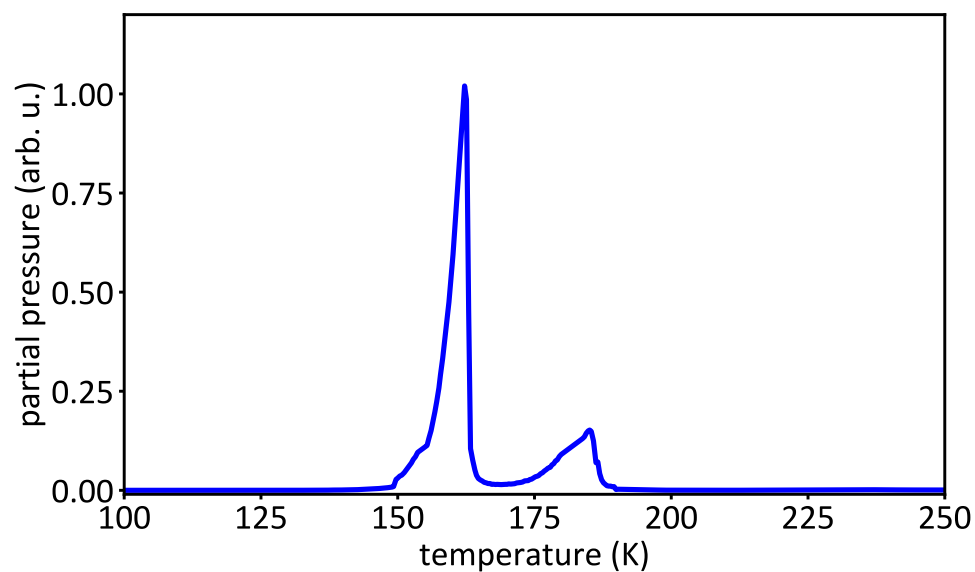


Figure S2: Thermal desorption spectrum (TDS) of multilayer Cot adsorbed to Gr/Ir(111). The multilayer desorption peak is located at  $(162 \pm 3)$  K and the monolayer desorption peak at  $(185 \pm 5)$  K. The annealing rate during desorption was 2 K/s.

**Figure S3: Multiplet calculations for Tm  $4f^{12}$  and  $4f^{13}$  configuration**

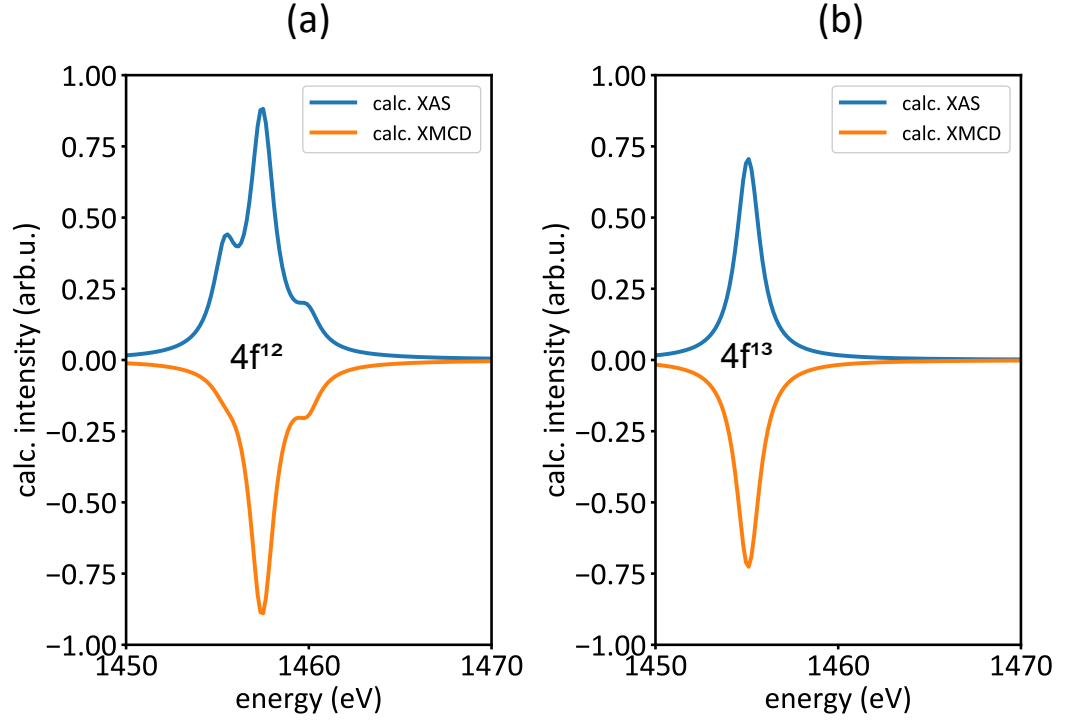


Figure S3: Multiplet calculations of the XAS and XMCD for (a) Tm  $4f^{12}$  and (b) Tm  $4f^{13}$  configurations. The calculations were performed using the Crispy code with parameters  $T = 3$  K and  $B = 6.8$  T.

**Figure S4: TmCot wires on Gr/Eu/Ir(111)**

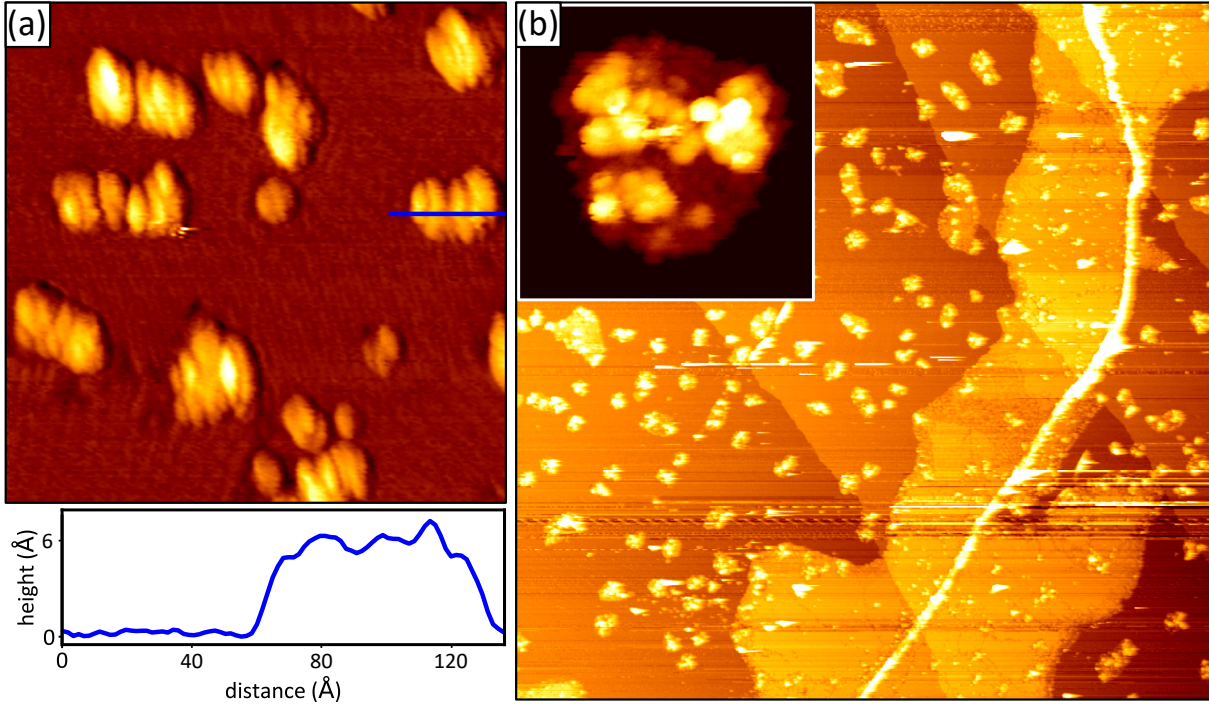


Figure S4: (a) STM topograph ( $400 \times 400 \text{ \AA}$ ) of TmCot wire island on Gr/Eu/Ir(111) after growth in  $4 \cdot 10^{-9}$  mbar Cot with Tm deposition rate 0.08 ML/min for 90 s at  $T = 350 \text{ K}$ . The ground level is the first layer of a wire island, the second layer shows a substructure and height (compare the corresponding profile) which is consistent with second layer wire growth. (b) STM topograph ( $5000 \times 5000 \text{ \AA}$ ) of TmCot wire island on Gr/Eu/Ir(111) after growth in  $4 \cdot 10^{-9}$  mbar Cot with Tm deposition rate 0.08 ML/min for 90 s at  $T = 400 \text{ K}$ . Large wire islands are visible, especially along the wrinkle in the Gr which appears as the white stripe. Also many Tm clusters have formed under these growth conditions. Inset: STM topograph ( $150 \times 150 \text{ \AA}$ ) of small island in (b). The island structure is undefined and consistent with the growth of Tm clusters. STM taken at  $T = 20 \text{ K}$ . Tunnelling parameters are (a)  $U_{\text{bias}} = -1.8 \text{ V}$  and  $I_t = 11 \text{ pA}$ , (b)  $U_{\text{bias}} = -2.0 \text{ V}$  and  $I_t = 10 \text{ pA}$ , and (b) [inset]  $U_{\text{bias}} = -1.1 \text{ V}$  and  $I_t = 10 \text{ pA}$ .

## CHAPTER 6

---

# Reactant and substrate variation in on-surface synthesis

*S.K. and K.B. conducted the experiments shown in this chapter under the guidance of T. Michely. The interpretations of the tetramethyl-Cot experiments were developed in discussions between S.K. and T.M.*

*In this chapter, the on-surface synthesis of sandwich-molecular wires is extended to metal reactants beyond europium and thulium. Further, the tetramethyl-Cot molecule is introduced to the on-surface synthesis and the feasibility of a metal oxide substrate is investigated for the on-surface reactions.*

### Motivation

In this chapter, the different components during the on-surface synthesis of sandwich-molecular wires are varied. These are (i) the metal reactant, (ii) the cyclic molecule, and (iii) the substrate.

Regarding (i) it was already shown in the previous chapter, that it is possible to synthesize TmCot wires, although only by suitable substrate doping and precise control of the growth conditions. In order to demonstrate that the on-surface synthesis of sandwich-molecular wires is not limited to elements from the lanthanide series, but can be generalized to other elements, the alkaline-earth metal barium (Ba) is introduced to the synthesis. Moreover, the feasibility of the on-surface synthesis of wires containing elements beyond Eu, Tm, and Ba will be investigated, which showed promising results in gas phase experiments [83, 119], and the feasibility of their on-surface synthesis will be investigated.

Furthermore, regarding (ii) the Cot molecule used during synthesis will be exchanged to tetramethyl-Cot. In the case of tetramethyl-Cot, four methyl groups are symmetrically attached to the Cot ring. While the antiaromaticity is not changed, some charge is donated to the  $\pi$  system [120], which corresponds to a lower electronegativity. Therefore, within Ln–tetramethyl-Cot wires containing Ln atoms preferring a 3+ oxidation state, this 3+ oxidation state could possibly be suppressed due to the lower electronegativity of tetramethyl-Cot. Then, the wire ends would be reactive, similar to EuCot wires, and the growth of long Ln–tetramethyl-Cot wires

could be achieved. Further, a change in the molecular  $\pi$  system could lead to different electronic and magnetic behavior. Since the coupling of the metal atoms within the wires is mediated by the molecular  $\pi$  orbitals, changing these orbitals is expected to modify the interaction along the wire. In the theoretical study in ref. [29] a modification of the Cot molecule in EuCot wires has resulted in a transition from a semiconducting to a half-metallic state.

Finally, concerning (iii) another substrate is chosen for the synthesis of the prototypical EuCot wires. In chapter 3 EuCot wires were already grown on the more strongly bound Gr/Ir(110). Still, it was shown that molecules bind only weakly to Gr/Ir(110) *via* van der Waals interaction, comparable to Gr/Ir(111) [116]. The synthesis on polar Eu oxide on Ir(111) is introduced and compared to the synthesis on Gr substrates. In literature, metal-oxide layers have been used as substrate for organometallic compounds, for example in refs. [67, 107, 121].

## Results

### 6.0.1 Barium-cyclooctatetraene wires on graphene/Ir(111)

The alkaline-earth metal Ba ( $[\text{Xe}]6s^2$ ) is chemically similar to the rare-earth metal Eu ( $[\text{Xe}]4f^76s^2$ ). This is largely due to their electronic structures and their resulting oxidation state: Compared to Eu, Ba lacks only the 4f electrons, which are close to the core and provide little chemical reactivity. Hence, the favored oxidation state of both chemical elements is 2+. For the growth of sandwich-molecular wires, Ba is a logical choice since its ionic radius is only slightly larger compared to Eu.

Using the on-surface synthesis method under the same growth conditions as for Eu (*i.e.* deposition of elemental Ba on Gr/Ir(111) in a background pressure of the Cot molecules at 300 K) yields BaCot wire carpets shown in Figure 6.1a. The BaCot islands have a random orientation with respect to the substrate. The corresponding height profile shows an apparent height of  $(6.0 \pm 0.3)$  Å, similar to the EuCot wire height [32]. It is expected that BaCot and EuCot wires have the same apparent height, because in both cases the metal atoms are encapsulated by Cot dianions which stand upright with respect to the surface.

While for EuCot wires the islands are typically elongated and have a racetrack-like appearance, this is not the case for BaCot. The BaCot island shown in the topograph of Figure 6.1b consists of only one direction of parallel wires and no bending angles or winding wires are observed, in contrast to EuCot. The substrate moiré is well visible through the wire island. As characteristic feature the edges of the island are not straight, but decorated with small wire segments which are roughly spaced by the moiré periodicity. Finally, the molecular-resolution topograph in Figure 6.1c shows the interlocking and parallelly aligned BaCot wires as indicated by the overlaid atomic structure model with an intra-wire periodicity of  $(4.8 \pm 0.2)$  Å and an inter-wire distance of  $(6.9 \pm 0.2)$  Å.



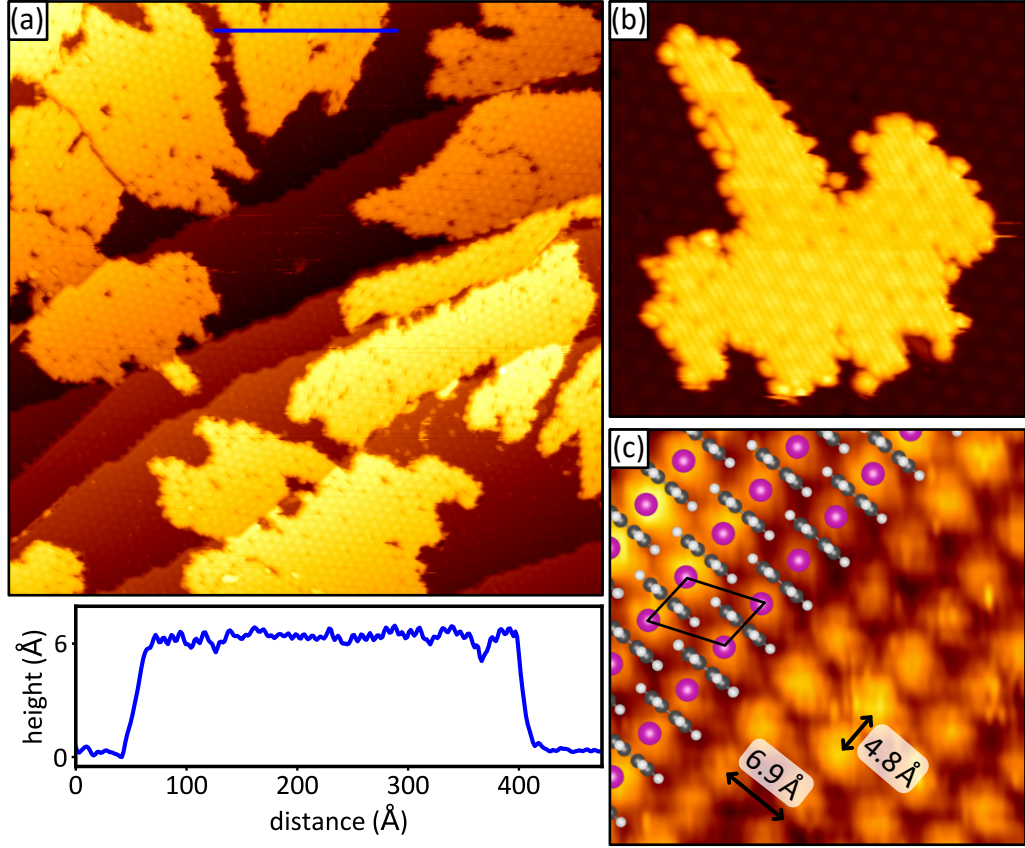


**Figure 6.1:** (a) STM topograph ( $1400 \times 1400 \text{ \AA}^2$ ) of BaCot wire islands. The position of the corresponding height profile is indicated by the blue line. (b) STM topograph ( $150 \times 150 \text{ \AA}^2$ ) of single BaCot wire islands. The moiré of Gr/Ir(111) is well visible through the island. (c) Molecular-resolution STM topograph ( $30 \times 30 \text{ \AA}^2$ ) on top of a BaCot island. The parallel wires are well visible and overlaid with an atomic structure model. The BaCot unit cell is indicated by the black rhomboid. Synthesis recipe: deposition of (a)/(c) 0.1 ML Ba, (b) 0.025 ML Ba in  $1 \cdot 10^{-8}$  mbar Cot on Gr/Ir(111) at 300 K. The STM data have been recorded at 300 K. Tunneling parameters are (a)  $U_{\text{bias}} = -1.4 \text{ V}$  and  $I_t = 70 \text{ pA}$ , (b)  $U_{\text{bias}} = -2.4 \text{ V}$  and  $I_t = 82 \text{ pA}$  and (c)  $U_{\text{bias}} = -1.8 \text{ V}$  and  $I_t = 84 \text{ pA}$ .

### 6.0.2 Ytterbium-cyclooctatetraene wires on graphene/Ir(111)

The rare-earth metal Yb with  $[\text{Xe}]4f^{14}$  electronic configuration shares the favored 2+ oxidation state with Eu [119]. In this sense, Eu and Yb stand out within the elements of the lanthanide series, because most other lanthanides favor a higher oxidation state [8, 119]. The reason for this is the occupancy of the 4f orbital: Eu has a half-filled 4f shell, while the 4f shell of Yb is fully occupied. This leads to a spheric symmetry and stabilization of the 4f orbital such that higher energies are needed to withdraw an extra electron beyond the two 6s electrons, resulting in the favored 2+ state. Therefore the use of Yb promises a very similar growth behavior to that of Eu during on-surface synthesis.

As shown in Figure 6.2a, indeed islands of YbCot wires are formed under the same growth

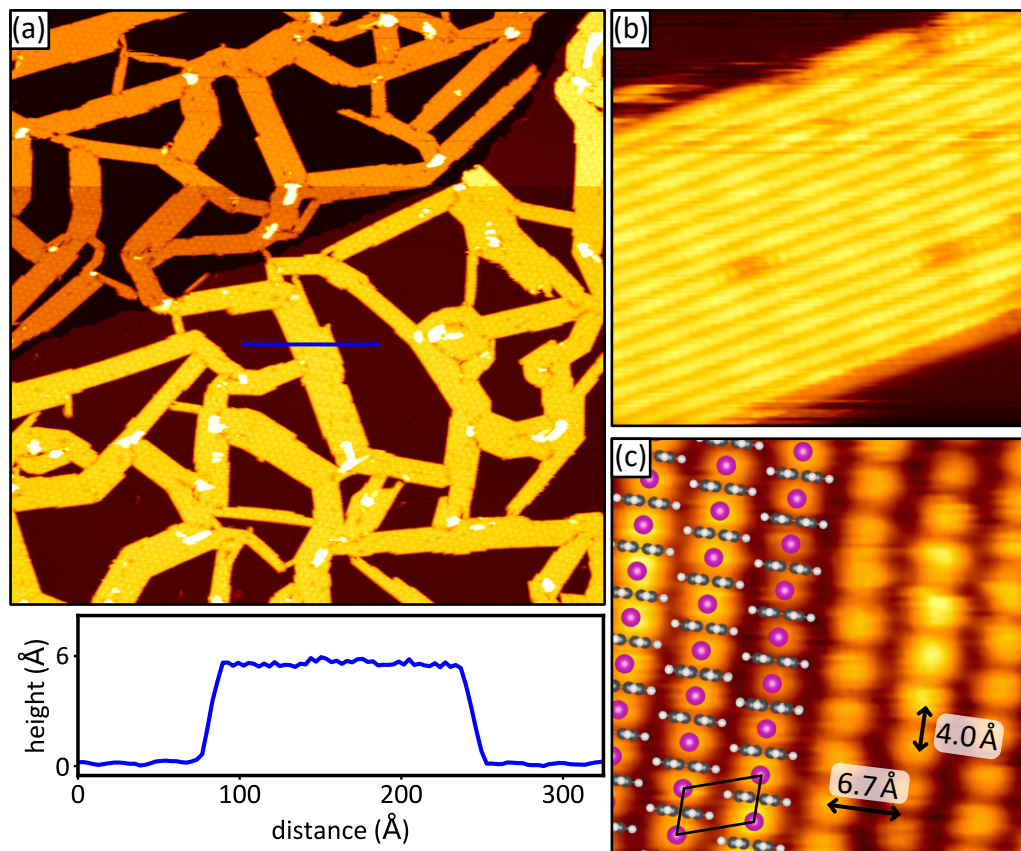


**Figure 6.2:** (a) STM topograph ( $1400 \times 1400 \text{ \AA}^2$ ) of YbCot wire islands. The position of the corresponding height profile is indicated by the blue line. (b) STM topograph ( $150 \times 150 \text{ \AA}^2$ ) on top of single YbCot wire islands. (c) Molecular-resolution STM topograph ( $35 \times 35 \text{ \AA}^2$ ) on top of YbCot island, the parallel wires are well visible and overlaid with an atomic structure model. The YbCot unit cell is indicated by the black rhomboid. Synthesis recipe: deposition of (a)/(b) 0.1 ML Yb, (b) 0.05 ML Yb in  $1 \cdot 10^{-8}$  mbar Cot on Gr/Ir(111) at 300 K. The STM data have been recorded at 300 K. Tunneling parameters are (a)  $U_{\text{bias}} = -1.9 \text{ V}$  and  $I_t = 94 \text{ pA}$ , (b)  $U_{\text{bias}} = -1.1 \text{ V}$  and  $I_t = 70 \text{ pA}$  and (c)  $U_{\text{bias}} = -1.9 \text{ V}$  and  $I_t = 0.9 \text{ nA}$ .

conditions as for EuCot and BaCot. The YbCot islands appear elongated with straight edges and form a network of all-connected islands. Apparently, during growth the islands do not move around each other and collide. Recurring bending angles are observed in Figure 6.2a, which are multiples of  $(34 \pm 3)^\circ$ . On top of the first layer of wire islands, small second layer islands are formed visible as bright protrusions. The corresponding height profile indicated by the blue line shows an apparent island height of  $(5.9 \pm 0.2) \text{ \AA}$ , similar to the heights observed for EuCot and BaCot. The topograph in Figure 6.2b clearly shows the parallel wires within the island, which is of high crystalline quality. A few depressions with a lower apparent height are visible in the STM topograph. Presumably, these stem from defects present in the substrate before growth which are visible through the wire film. In contrast to BaCot, the edges of the islands are very sharp without any fringes. The molecular resolution topograph in Figure 6.2c shows the

interlocking wires as indicated by the overlaid structure model, with an intra-wire periodicity of  $(4.0 \pm 0.2) \text{ \AA}$  and an inter-wire distance of  $(6.7 \pm 0.3) \text{ \AA}$ .

### 6.0.3 Europium-ytterbium-cyclooctatetraene wires on graphene/Ir(111)

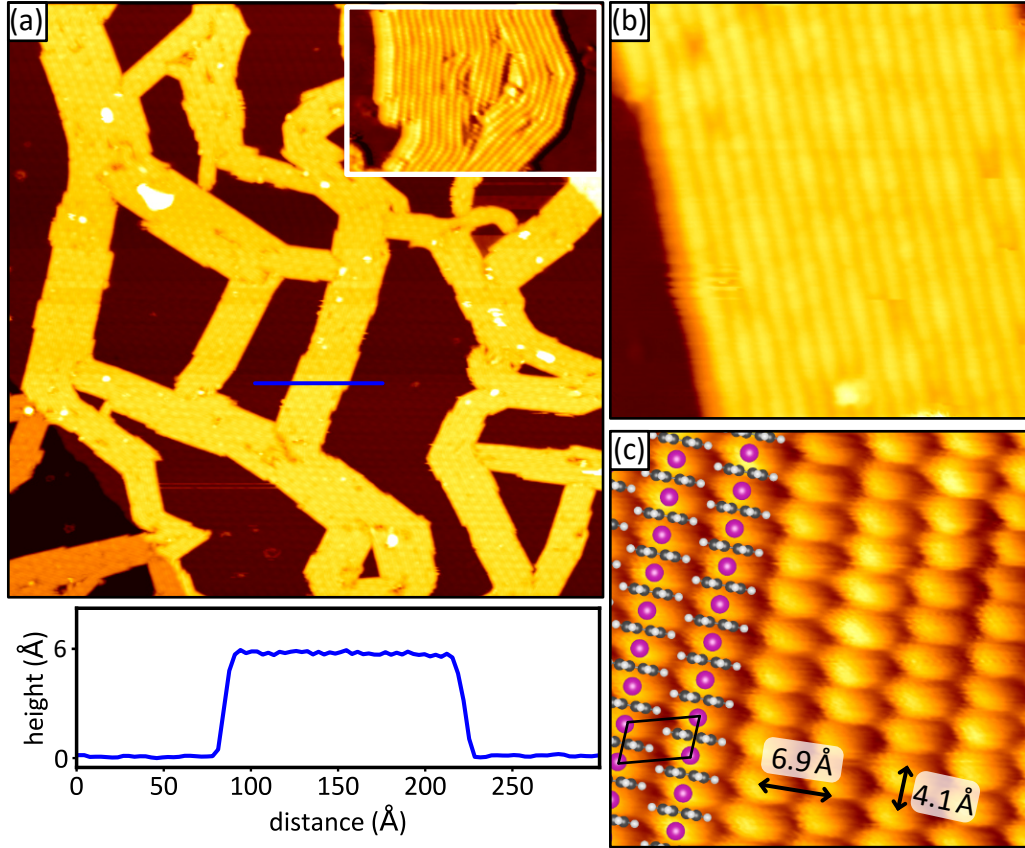


**Figure 6.3:** (a) STM topograph ( $1400 \times 1400 \text{ \AA}^2$ ) of EuYbCot wire islands. The position of the corresponding height profile is indicated by the blue line. Inset: STM topograph ( $160 \times 240 \text{ \AA}^2$ ) of bending wires in an EuYbCot island. (b) STM topograph ( $150 \times 150 \text{ \AA}^2$ ) on top of single EuYbCot wire islands. (c) Molecular-resolution STM topograph ( $45 \times 45 \text{ \AA}^2$ ) on top of EuYbCot island, the parallel wires are well visible and overlaid with an atomic structure model. The unit cell is indicated by the black rhomboid. Synthesis recipe: co-deposition of 0.05 ML Eu and 0.05 ML Yb in  $1 \cdot 10^{-8}$  mbar Cot on Gr/Ir(111) at 300 K. The STM data have been recorded at 300 K. Tunneling parameters are (a)  $U_{\text{bias}} = -2.1 \text{ V}$  and  $I_t = 59 \text{ pA}$ , (b)  $U_{\text{bias}} = -2.0 \text{ V}$  and  $I_t = 0.1 \text{ nA}$  and (c)  $U_{\text{bias}} = -1.5 \text{ V}$  and  $I_t = 35 \text{ pA}$ . The inset of (a) is superimposed with its derivative for better visibility.

The on-surface synthesis of bi-metallic sandwich-molecular wires was investigated using Eu and Yb. For this, both elements were co-evaporated (with equal amounts) on Gr/Ir(111) in a background pressure of  $1 \cdot 10^{-8}$  mbar Cot at 300 K. This synthesis results in the formation of homogeneous wires islands shown in the topograph of Figure 6.3a. The island morphology is very similar to YbCot wires and all islands are connected to each other. Generally, the bending

angles are less well defined compared to EuCot and YbCot. The inset of Figure 6.3a shows an islands position where the wires are bending. It appears that there is strain within the wire islands, which can be released at the position of wire bends. The island height of  $(5.9 \pm 0.2)$  Å visible in the line profile in Figure 6.3 is similar to the island heights of the other synthesized LnCot islands. The topograph of Figure 6.3b shows the parallel wires within an island. The moiré of Gr with Ir(111) is weakly visible through the island. The wires within the island appear homogeneous. Therefore, the position of the Eu and Yb atoms within the wire film cannot be distinguished. Also in the molecular-resolution topograph in Figure 6.3c, the wires appear continuous and homogeneous. The wire geometry is indicated by the overlaid structure model. The average intra-wire periodicity is given by  $(4.1 \pm 0.2)$  Å and the inter-wire distance is  $(6.9 \pm 0.4)$  Å.

#### 6.0.4 Europium-tetramethyl-cyclooctatetraene wires on graphene/Ir(111)

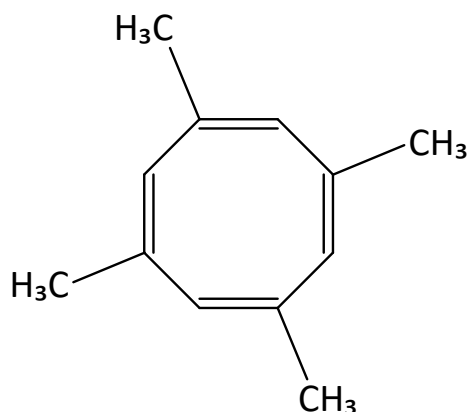


**Figure 6.4:** Structure of 1,3,5,7-tetramethyl-2,4,5,8-cyclooctatetraene, a Cot molecule with symmetrically attached methyl groups.

During on-surface synthesis of sandwich-molecular wires, the choice of the organic molecule is as crucial as that of the metal reactant. In order to further investigate the formation mechanism of organometallic wires, we introduce here a different molecule: 1,3,5,7-tetramethyl-2,4,5,8-cyclooctatetraene, abbreviated to tetramethyl-Cot (compare Figure 6.4). The methyl groups donate some charge to the Cot  $\pi$  system [120] and promise to enable synthesis of elongated Ln-tetramethyl-Cot wires, as outlined in the motivation. Additionally, the methyl groups could serve as separators, isolating the wire from the substrate and reduce inter-wire interactions. As a paradigm for the feasibility of metal-tetramethyl-Cot wire growth, Eu is used as metal reactant as its growth within sandwich-molecular wires has been extensively studied.

The on-surface synthesis under comparable conditions to EuCot growth (*i.e.* deposition of elemental Eu on Gr/Ir(111) in a background pressure of tetramethyl-Cot at  $T = 300 - 400$  K)



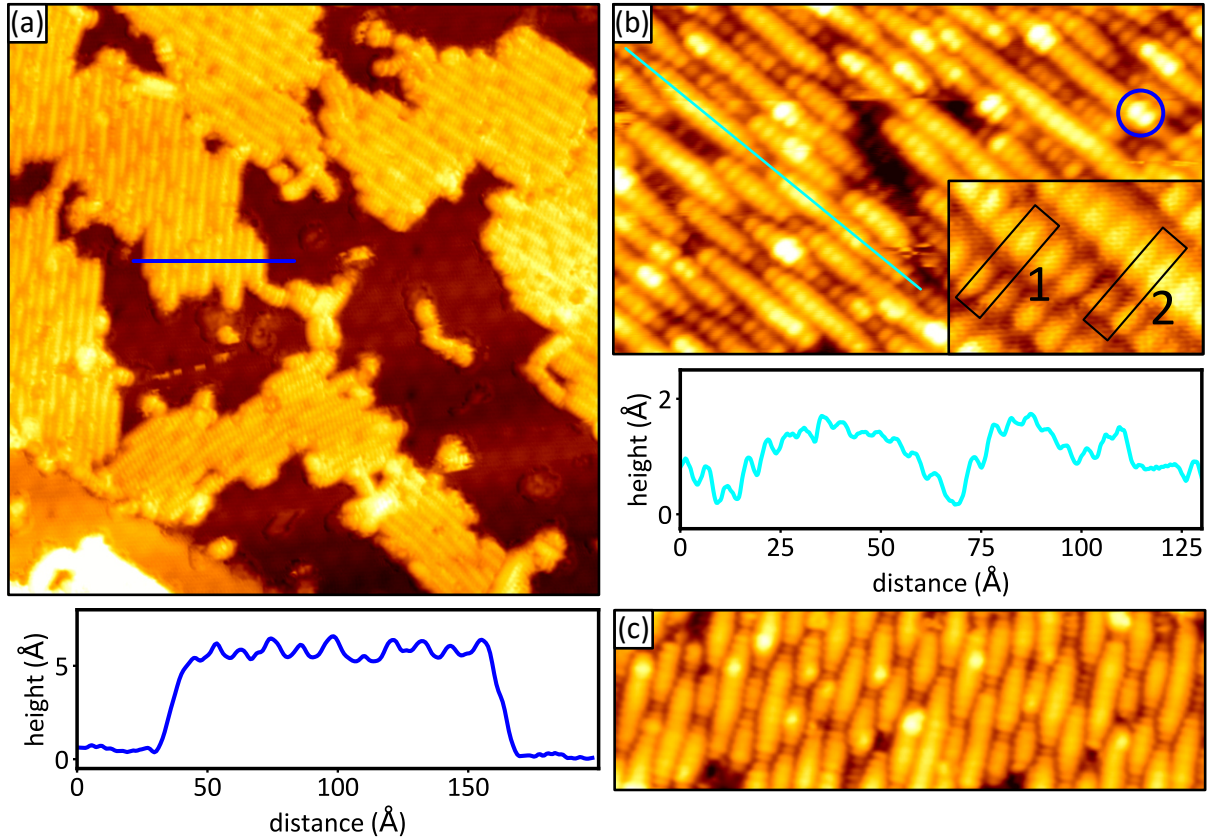


**Figure 6.5:** (a) STM topograph ( $650 \times 650 \text{ \AA}^2$ ) of Eu-tetramethyl-Cot wire islands. The position of the corresponding height profile is indicated by the blue line. (b) Molecular-resolution STM topograph ( $120 \times 200 \text{ \AA}^2$ ) of a Eu-tetramethyl-Cot wire island. The corresponding height profile is indicated by the cyan line. The blue circle indicates a protrusion. Inset: enlarged STM topograph ( $30 \times 45 \text{ \AA}^2$ ) of parallel wires. At position 1, the neighboring molecules are shifted by half a formula unit. At position 2, the neighboring molecules are adjacent to each other. (c) STM topograph ( $85 \times 275 \text{ \AA}^2$ ) of island. The height modulations are very well visible. Synthesis recipe: deposition of (a) 0.06 ML Eu, (b) 0.07 ML Eu in  $1 \cdot 10^{-8}$  mbar tetramethyl-Cot on Gr/Ir(111) at 350 K. The STM data have been recorded at 20 K. Tunneling parameters are (a)  $U_{\text{bias}} = -1.9 \text{ V}$  and  $I_t = 0.1 \text{ nA}$ , (b)  $U_{\text{bias}} = -2.2 \text{ V}$  and  $I_t = 76 \text{ pA}$  (also inset) and (c)  $U_{\text{bias}} = -2.4 \text{ V}$  and  $I_t = 47 \text{ pA}$ .

yields the formation of sandwich-molecular wires shown in the topograph of Figure 6.5a. The formation of islands without distinct bending angles is observed. The corresponding height profile shows an apparent base height of  $\approx 6 \text{ \AA}$ , which is similar to the EuCot wire height. The apparent height is significantly modulated, oscillating between  $6 - 7 \text{ \AA}$  under the given tunnelling conditions. This modulation is very well visible in the topograph of Figure 6.5b and the corresponding height profile. An apparent height modulation of  $(1.5 \pm 0.1) \text{ \AA}$  is observed. The apparent height varies continuously along the wire direction and the periodicities range between  $20 - 100 \text{ \AA}$ . Additional to the continuous height variation, local bright protrusions are observed. One of those protrusions is encircled blue in the topograph of Figure 6.5b. These protrusions always appear as pairs of two and are located between two depressions of the neighboring wires.

In the inset of Figure 6.5b, the relative positions of neighboring molecules are indicated with black rectangles at two positions. At position 1, molecules of neighboring wires are shifted by half a formula unit. At position 2, the molecules of neighboring wires are directly adjacent to each other. This implies that there is no strict interlocking, as it is the case for EuCot. In the topograph of Figure 6.5c, the height variation along the wires is well visible. The high points of the variation are typically adjacent to the lowest points of the neighboring wires. For the case of Eu-tetramethyl-Cot, the intra-wire periodicity is  $(4.7 \pm 0.5) \text{ \AA}$  and the inter-wire distance is  $(10 \pm 1) \text{ \AA}$ . The inter-wire distance is significantly larger compared to the EuCot wires which is plausible due to the additional methyl groups.

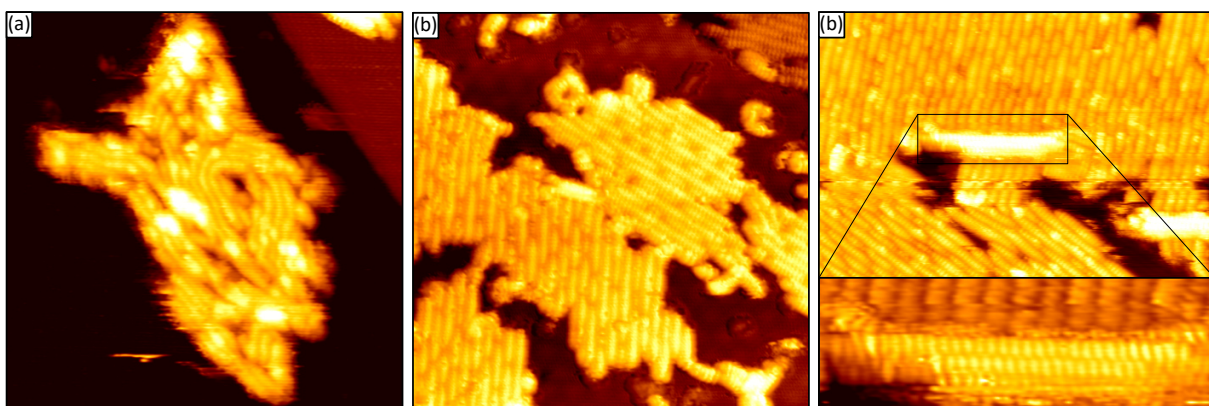


**Figure 6.6:** Growth temperature dependence of Eu-tetramethyl-Cot wire islands: (a)  $T = 300 \text{ K}$ , (b)  $T = 350 \text{ K}$ , (c)  $T = 400 \text{ K}$ . (a)–(c) STM topographs ( $400 \times 400 \text{ \AA}^2$ ) of Eu-tetramethyl-Cot wire islands. (a) The island appears disordered and curled up. (b) The islands are well ordered with parallel aligned wires. (c) The island appears ordered, but a second phase on top of the first layer islands appears. Inset: STM topograph ( $50 \times 150 \text{ \AA}^2$ ) of second layer wire-like phase. Synthesis recipe: deposition of (a) 0.03 ML Eu at  $T = 300 \text{ K}$ , (b) 0.06 ML Eu at  $T = 350 \text{ K}$  and (c) 0.07 ML  $T = 400 \text{ K}$  in  $1 \cdot 10^{-8} \text{ mbar}$  tetramethyl-Cot on Gr/Ir(111). The STM data have been recorded at 20 K. Tunneling parameters are (a)  $U_{\text{bias}} = -1.4 \text{ V}$  and  $I_t = 98 \text{ pA}$ , (b)  $U_{\text{bias}} = -1.9 \text{ V}$  and  $I_t = 0.1 \text{ nA}$  and (c)  $U_{\text{bias}} = -2.1 \text{ V}$  and  $I_t = 55 \text{ pA}$  (inset: superimposed with derivative for better visibility).

The growth temperature dependence was investigated in Figure 6.6, where the substrate temperature during synthesis was varied from 300 – 400 K. As shown in Figure 6.6a, the synthesis at 300 K results in the formation of disordered islands of first and second layer Eu-tetramethyl-Cot wires. This appearance reminds of the two-step synthesis of EuCot wires at low temperature described in the supporting information of ref. [32]. A reasonable explanation for this behavior is the lower mobility of the pure tetramethyl-Cot molecule, which has a significantly higher adsorption energy compared to Cot (compare the thermal desorption spectra of Cot in Figure A.3 and tetramethyl-Cot in Figure A.5 of the scientific appendix). By elevating the growth temperature to 350 K, highly ordered wire islands are formed shown in Figure 6.6b, as discussed in the previous paragraph. This can be explained by the increased mobility during growth, such that the wires can easily move and re-arrange. It also means that the aligned phase is most likely

---

energetically favorable. As shown in Figure 6.6c, increasing the growth temperature further to 400 K yields highly ordered islands. Additionally, the formation of a second phase on top of the first layer wire islands is observed. A closer look to the molecular resolution topograph in the inset of Figure 6.6c reveals that the second phase appears to consist of sandwich-molecular wires with perpendicular orientation with respect to the first layer. The periodicities of the second wire phase are consistent with EuCot wires, which are embedded onto the Eu-tetramethyl-Cot wire film. A plausible explanation could be the partial decomposition of tetramethyl-Cot molecules at the elevated temperature in form of methyl group dissociation. The dissociation of four of methyl groups from tetramethyl-Cot results in a Cot ring, which combined with Eu could form the EuCot wires observed on top of the first layer islands. Additionally, the dissociation of tetramethyl-Cot could explain the pairs of protrusions described above. If a dissociated (or partly dissociated with 1 – 3 methyl groups missing) molecule is bound within a wire, it would have a distinct imaging contrast. As explained in ref. [32], using STM the electrons tunnel into the  $\pi$  molecular orbitals which have their nodal point in the molecular plane. The orbitals extend from the nodal point into both directions and would therefore be imaged twice.

Next, the origin of the observed modulation observed in Figure 6.5b needs to be addressed. First, it should be noted that the apparent height modulation is consistent with methyl-carbon bond lengths of  $\approx 1.5 \text{ \AA}$  [122], meaning how far the methyl groups stick out from the Cot ring. Therefore, it is plausible that the high/low points along the wires correspond to different rotations of the molecules around the wire axis. In the following, two possible scenarios are described:

(i) At the imaging temperature of 20 K the molecular rotations are frozen and neighboring molecules cannot rotate with respect to each other due to the methyl groups. Therefore, neighboring molecules cannot have the same orientation because the methyl groups would collide. By cooling down the system to 20 K the observed pattern freezes out.

(ii) Neighboring methyl groups do not block each other, but can still rotate close to freely at 20 K. Then it is conceivable, that at some locations the tetramethyl-Cot molecules bind down to the substrate where a certain rotation leads to an increased physisorption, possibly at defects. In between these fixed positions, the molecular chains can rotate and behave like strained wires of a violin, with the highest oscillation amplitude in the center between two fixed points. The STM would then image the average of all rotations, and the average height decreases towards the fixed points visible as dark depressions.

Given the obtained data, it cannot be clearly determined whether (i) or (ii) is more plausible. However, the rather large inter-wire distance of  $10 \text{ \AA}$  makes it implausible that methyl groups of adjacent wires substantially impede each other's rotations. This is also consistent with the observation, that no strict interlocking behavior is visible between the wires. Further temperature-dependent experiments could help to distinguish between those two possibilities.

## 6.0.5 Terbium-tetramethyl-cyclooctatetraene wires on graphene/Ir(111)

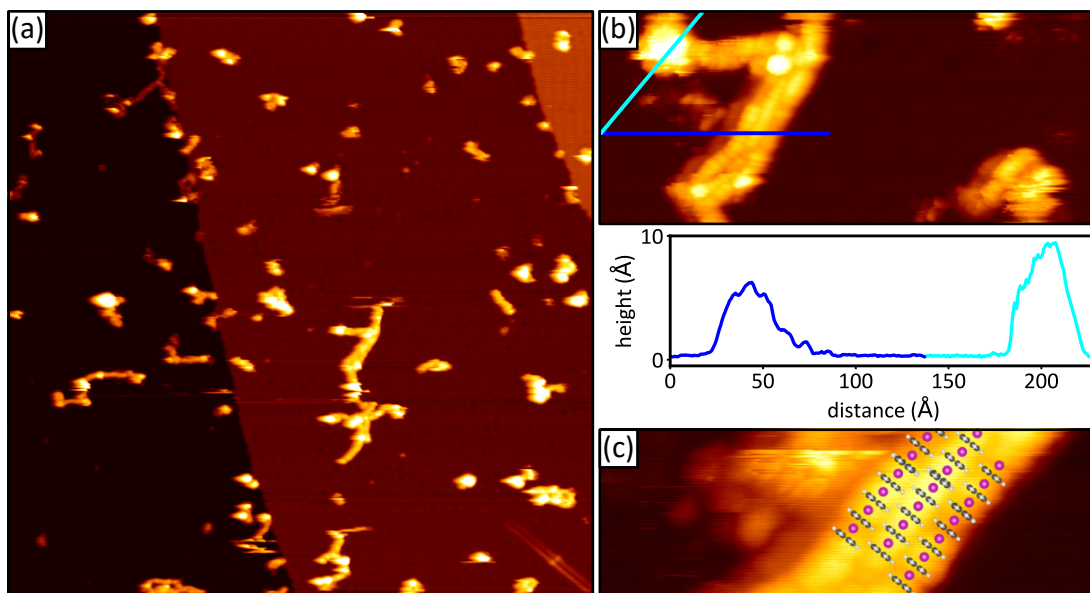


**Figure 6.7:** (a) STM topograph ( $1340 \times 1340 \text{ Å}^2$ ) of a Tb-tetramethyl-Cot structures coexisting with Tb clusters. (b) STM topograph ( $130 \times 300 \text{ Å}^2$ ) of a wire-like structure, the corresponding height profile is indicated by the blue and cyan line. (c) Molecular-resolution STM topograph ( $33 \times 100 \text{ Å}^2$ ) of a wire-like structure overlaid with an atomic model. Synthesis recipe: deposition of 0.1 ML Tb in  $1 \cdot 10^{-8}$  mbar tetramethyl-Cot on Gr/Ir(111) at 400 K. The STM data have been recorded at 20 K. Tunneling parameters are (a)  $U_{\text{bias}} = -2.5 \text{ V}$  and  $I_t = 8 \text{ pA}$ , (b)/(c)  $U_{\text{bias}} = -2.5 \text{ V}$  and  $I_t = 17 \text{ pA}$ .

In the following, the tetramethyl-Cot molecule introduced in the previous section is combined with the rare-earth metal Tb during the on-surface synthesis on Gr/Ir(111). In contrast to Eu and Yb, Tb prefers a 3+ oxidation state [98] and is therefore chemically more similar to Tm. While TmCot wires could only be produced on n-doped Gr, the more electronegative tetramethyl-Cot molecule could possibly facilitate the growth of wires containing metal atoms with a preferred 3+ oxidation state.

Figure 6.7a presents an STM topograph after deposition of elemental Tb on Gr/Ir(111) in a background pressure of  $1 \cdot 10^{-8}$  mbar tetramethyl-Cot at 400 K. As visible in the topograph, essentially no elongated islands are observed. Instead, most of the surface consists of broad protrusions surrounded by clean Gr. The topograph provided in Figure 6.7b reveals an apparent height of the protrusion well over the expected wire height of  $\approx 6 \text{ Å}$  (cyan line profile) and consistent with a Tb metal cluster. No internal structure can be detected. In contrast to that, the elongated feature shows the expected structure of sandwich-molecular wires. The structure appears to consist of three parallel wires with a typical intra-wire periodicity of  $4 - 5 \text{ Å}$ . The measured apparent height of  $\approx 6 \text{ Å}$  (cyan line profile) is similar to that of other sandwich-molecular wires on Gr/Ir(111), from which we can conclude these shapes to be short Tb-tetramethyl-Cot



wires. In the further magnified view in Figure 6.7c the proposed sandwich-molecular structure is indicated by the overlaid atomic model.

### 6.0.6 Europium-cyclooctatetraene wires on polar europium oxide on Ir(111)

Finally, the synthesis of EuCot sandwich-molecular wires on a metal-oxide surface is investigated. Here, epitaxial polar europium oxide on Ir(111) is used as a substrate [123]. The on-surface synthesis under typical growth conditions, *i.e.* deposition of elemental Eu in a background pressure of  $1 \cdot 10^{-8}$  mbar Cot at 300 K yields the formation of disordered EuCot wire islands as visible in Figure 6.8a. The islands are less ordered compared to the synthesis on Gr/Ir(111) [32]. The topograph in Figure 6.8b shows that the islands consist of only a few parallelly aligned wires. The observed apparent height of  $(6.1 \pm 0.2) \text{ \AA}$ , in good agreement with the expected apparent height on Gr/Ir(111). The inset of Figure 6.8b shows that the structure in the second layer are consistent with second layer wires, which appear as bright protrusions in Figure 6.8a. The molecular structure is visible in the high-resolution topograph in Figure 6.8c. The defect density within the wires is low, but at the island edges several fringes of small wire segments are visible, which are absent for EuCot/Gr/Ir(111).

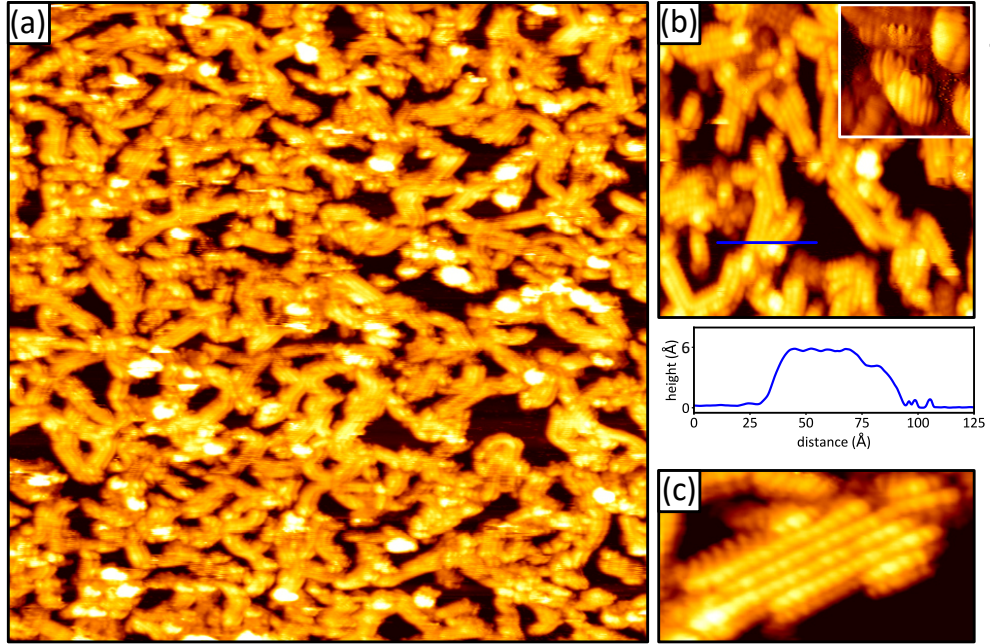


**Figure 6.8:** EuCot wire islands on polar EuO/Ir(111). (a) STM topograph ( $1000 \times 100 \text{ \AA}^2$ ) of a disordered network of EuCot wire island. The bright intensities are consistent with second layer wires. (b) STM topograph ( $350 \times 350 \text{ \AA}^2$ ) of EuCot wires. The wires form small islands and the corresponding height profile is consistent with the EuCot wire height on Gr/Ir(111). (c) STM topograph ( $55 \times 100 \text{ \AA}^2$ ) of parallelly aligned EuCot wires in single island. Synthesis recipe: deposition of 0.1 ML Eu in  $1 \cdot 10^{-8}$  mbar Cot on polar EuO/Ir(111) at 300 K. The STM data have been recorded at 300 K. Tunneling parameters are (a)  $U_{\text{bias}} = -2.0 \text{ V}$  and  $I_t = 0.2 \text{ nA}$ , (b)  $U_{\text{bias}} = -2.3 \text{ V}$  and  $I_t = 18 \text{ pA}$  and (c)  $U_{\text{bias}} = -2.5 \text{ V}$  and  $I_t = 39 \text{ pA}$  (superimposed with derivative for better visibility).

### Discussion

Through the synthesis of BaCot wires it is demonstrated that the on-surface synthesis of sandwich-molecular wires using Cot is not limited to metal reactants from the lanthanide series, but represents a generalized growth scheme applicable to elements which can assume a 2+ oxidation state within the wire. This finding is in agreement with previous gas phase experiments, in which several different metal atoms — such as Eu, Yb, Tm, Tb and Ba — were successfully synthesized [83, 119].

The slightly larger lattice parameters of BaCot wires compared to EuCot can be explained by the larger ionic radius of Ba, which can also explain the absence of distinct bending angles observed for EuCot [32]. With an increasing bending angle, the resulting wire deformation energy is increased. Therefore it is plausible, that for BaCot the energy penalty of bending is high enough to prevent the formation of bending wires at the given growth conditions. The fringe-like decoration of the BaCot island edges with small wire fragments indicates that the binding energy within BaCot wires is lower compared to EuCot, which in turn allows the formation of small fragments due to the lower energy penalty of wire termination.

Further, the on-surface synthesis of YbCot wires has confirmed the favored Yb 2+ oxidation state which has previously been reported in gas phase experiments [8]. The inter- and intra-wire periodicities of YbCot wires on Gr/Ir(111) found to be smaller than for EuCot. This can be explained by the lower ionic radius of Yb. The small periodicities lead to even more elongated and linearly growing wire islands compared to EuCot. Due to the preferred linear growth the islands appear to grow into each other during synthesis, thus forming a connected network of wires with no isolated islands present. The observed bending angles agree with the expected 33° calculated from the bending angle formula introduced in ref. [32], but appear to be less favorable compared to EuCot.

The synthesis of bi-metallic sandwich-molecular wires is demonstrated using the lanthanides Eu and Yb combined with Cot. Using this synthesis, the formation of homogeneous EuYbCot islands was observed on Gr/Ir(111). It was not possible to distinguish between Eu and Yb within the wires, which consist of continuous wires. Possible strain within the wire islands was observed at positions of ill-defined bending angles. It is plausible that strain is caused within the islands by the slightly different lattice parameters of EuCot and YbCot wires. Although the distribution of Eu and Yb within the wires is unclear, it is demonstrated that the on-surface synthesis of bi-metallic wires is generally possible. Several theoretical studies have predicted bi-metallic sandwich-molecules wires to be half-metallic using Bz and Cp molecules [17, 26, 48, 91]. It is plausible, that also the electronic and magnetic properties of metal-Cot wires can be strongly influenced through bi-metallic synthesis.

By introducing the synthesis of Eu-tetramethyl-Cot wires it is shown, that also modified cyclic molecules are feasible for the growth of sandwich-molecular wires. This result is a proof of concept and paves the way for studies with other potentially more complex molecules. Examples

---

for such studies have been proposed theoretically, *e.g.* with Cot modifications. [29], modified Bz rings [22] or other proposed molecules [124]. The weak interaction of the Eu-tetramethyl-Cot wire islands with the substrate indicates that the attached methyl groups isolate the wires from the substrate. In this sense the methyl groups could be viewed as stilts, somewhat lifting the wires from the substrate. This strategy could be used to maintain an unperturbed intra-wire coupling, which might otherwise be disturbed on more strongly interacting substrates.

The successful growth of small fragments of Tb-tetramethyl-Cot wires on on Gr/Ir(111) is a promising finding in itself. In contrast, wire growth could not be achieved for the chemically similar Tm with the Cot molecule. Therefore, the synthesis of Tb-tetramethyl-Cot fragments suggests that also other lanthanide elements preferring 3+ oxidation can be formed using tetramethyl-Cot. The fact that only small fragments are formed while at the same time Tb clusters are present at the surface can be rationalized by the high cohesive energy of Tb compared to Tm [125]. The use of 4f elements with lower cohesive energy might result in longer wires in the absence of clusters.

Finally, the growth of EuCot wires on the epitaxial Eu oxide on Ir(111) has demonstrated, that the on-surface synthesis of sandwich-molecular wires is not limited to Gr substrates, but can be expanded to metal oxide surfaces. The observed wire islands are disordered, which is typically a sign of low mobility during the chemical on-surface reactions. Therefore it is plausible, that increasing the growth temperature can lead to well-ordered wire islands. Even a uniaxial wire alignment is conceivable, if a two-fold symmetric oxide surface is used. Since the charge transfer from/to oxide layers is typically significantly weaker compared to Gr, this type of synthesis is expected to result in even more isolated sandwich-molecular wires.



## CHAPTER 7

---

### Discussion

*S.K. conducted the experiment of naphthalene adsorption on Gr/Ir(110) shown in this chapter, under the guidance of T.M. S.K. and K.B. conducted the Ba-Dibenzo-Cot experiment on Gr/Ir(111) shown in this chapter, under the guidance of T.M. The DFT calculations were conducted by S.T. and N.A.*

*In this chapter, the main lessons learned from the experimental results will be discussed. This concerns the problem of irradiation damage of organometallic systems and the conditions for successful on-surface synthesis of sandwich-molecular wires, with respect to the substrate and chemical reactants. Finally, the magnetic properties of the investigated systems are discussed, along with possible ways to modify these properties.*

#### 7.1 Irradiation damage

Investigating sandwich-molecular wires with irradiating techniques has shown, that the effects of irradiation damage need to be carefully considered. In ref. [126] the problem of irradiation damage has already been described in the context of photoelectron spectroscopy of organic systems. In the context of this thesis irradiation damage of both EuCot and TmCot sandwich-molecular wires were observed, which will be discussed in the following.

When EuCot wires are exposed to low-energy electrons (20 – 100 eV) of a conventional LEED setup, the observed rings described in ref. [84] fade away on a time scale of 60 s. This implies that the structural integrity of the wires is immediately damaged by electron irradiation, most likely through the decomposition of the organic molecules. With typical sample currents of 100 nA and an electron beam diameter of a few mm, the approximate electron flux is given by  $1 \frac{e^-}{\text{nm}^2\text{s}}$ , which means EuCot sandwich-molecular wires are decomposed after the exposure to  $\approx 60 \frac{e^-}{\text{nm}^2}$ . This rapid decomposition can be avoided by the use of a microchannelplate-LEED setup, which uses typical beam currents of 10 – 100 pA, thereby increasing the time to full decomposition by three to four orders of magnitude.

The effect of irradiation damage through high-energy (1000 – 1250 eV) photons (ph) in XAS and XMCD measurements of EuCot wires has been described in the supporting information

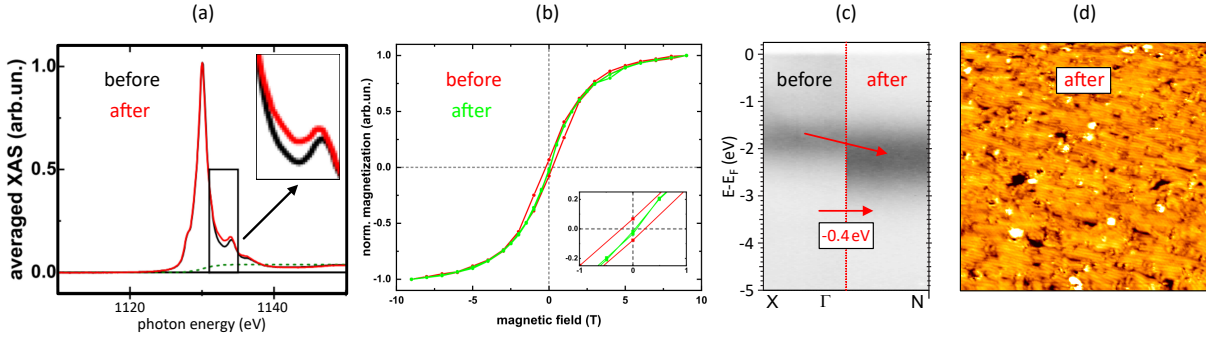


**Figure 7.1:** (a) Average XAS at the Eu M<sub>5</sub> edge of EuCot wires on Gr/Ir(111) before and after irradiation damage, from the supporting information of ref. [84]. The irradiation damage induces changes in the fine structure. (b) Magnetization curves of EuCot wires on Gr/Ir(111) before (red) and after (green) irradiation damage from ref. [84] ( $T = 5$  K and measured at grazing incidence). The irradiation damage causes the observed hysteresis loop to close. (c) Superimposed angle-resolved photo emission spectrum along  $X - \Gamma - N$  for a 1 ML (left)/4 ML (right) EuCot film recorded at a photon energy of 110 eV (left)/110 eV (right). Left: The photon beam is not moved over the sample and the integrated photon dose at the measurement location is  $\approx 1.2 \cdot 10^7 \frac{\text{ph}}{\text{nm}^2}$ . The apparent irradiation damage causes the observed flat band to shift down by 0.4 eV with respect to the Fermi level. (d) STM topograph ( $500 \times 500 \text{ \AA}^2$ ) of a 1 ML thick EuCot wire carpet after a photon dose of  $\approx 6 \cdot 10^3 \frac{\text{ph}}{\text{nm}^2}$  in each sample location. Tunneling parameters are  $U_{\text{bias}} = -2.12$  V and  $I_t = 0.14$  nA. (a)–(b) Adapted with permission from ref. [84] © 2019 ACS.

of ref. [84]. In Figure 7.1a the Eu M<sub>5</sub> edge of EuCot wires is shown where the black curve corresponds to the measurement directly after synthesis. Prolonged exposure leads to small changes in the M<sub>5</sub> fine structure, such that the minimum between the main peak and the right shoulder moves up (see red curve). Although the fine structure is changed, the M<sub>5,4</sub> edges are still of characteristic  $4f^7$  shape, meaning the Eu stays in its divalent state ( $\text{Eu}^{2+}$ ). Severe changes are observed in the recorded magnetization curve of the wires, shown in Figure 7.1b. While the undamaged sample exhibits a clear hysteresis (red curve) which is attributed to the intra-wire coupling of Eu, irradiation damage leads to the closing of the magnetization curve (green curve). This observation is consistent with the assumption that the wires are decomposed through the irradiation, since only the intact wires are expected to couple ferromagnetically. It remains unclear whether the decomposition is mainly caused directly through the high-energy photons, or through the exposure to secondary electrons. LEED measurements have shown that even low-energy electrons cause damage to the wire film, which makes both assumptions plausible. In order to minimize the effects of irradiation damage, the photon flux should be reduced as much as possible above the acceptable noise level. Additionally, the photon beam should be defocused over a larger fraction of the irradiated sample, which is possible at most XAS beamlines. For the XAS measurements presented in chapter 4 and acquired at the *Swiss Light Source* in Villigen (Switzerland) the photon beam was defocused to an area of  $0.3 \times 2.5 \text{ mm}^2$  on the sample while using a photon flux of  $3 \cdot 10^{-3} \frac{\text{ph}}{\text{nm}^2 \text{ s}}$ . No significant irradiation damage was observed over a time span of the order of one hour. This means an acceptable high-

energy photon exposure beyond which irradiation damage becomes relevant for EuCot wires is roughly  $10 \frac{\text{ph}}{\text{nm}^2}$ .

Similarly, for the ARPES measurements presented in the manuscript of chapter 4 strong effects of irradiation damage through low-energy (70 – 110 eV) photons were observed. As can be seen in Figure 7.1c, on the undamaged EuCot wires sample a flat band at  $-1.85 \text{ eV}$  was observed, which quickly shifts down to  $-2.25 \text{ eV}$  under photon exposure for both mono- and multilayer samples. It was found, that by scanning the photon beam over the sample during the measurements, severe irradiation damage can be avoided and ARPES measurements of the intact wires can be acquired (compare left side of Figure 7.1c). During the measurements, a photon flux of  $3 \cdot 10^2 \frac{\text{ph}}{\text{nm}^2 \text{s}}$  was used, and the integration time at each position during scanning was 20 s. To investigate the irradiation effects on EuCot with STM, the whole sample was intentionally irradiated using the scan mode prior to STM imaging. The corresponding STM topograph is shown in Figure 7.1d. Directly after the successful *in situ* synthesis, EuCot wires are of high quality and low defect density. After the exposure to  $6 \cdot 10^3 \frac{\text{ph}}{\text{nm}^2}$ , the appearance of dark spots and bright protrusions in the film is observed. According to earlier analysis, the former are most likely holes in the wires, while the latter are identified as Eu clusters. As already discussed in the manuscript, the Cot molecules decompose under irradiation and it is plausible that the exposed Eu partly intercalates and forms clusters, causing the flat band to broaden and shift down. Although the wire film in Figure 7.1d is visibly damaged, in many areas the wires are still intact. Therefore, the exposure to  $6 \cdot 10^3 \frac{\text{ph}}{\text{nm}^2}$  of low-energy photons is a reasonable limit, below which measurements of the intact organometallic film are acquired. In analogy to the XAS irradiation damage, both photons and electrons are expected to contribute to the molecule decomposition.

Similar to EuCot wires on Gr, also TmCot wires described in the manuscript of chapter 5 are prone to irradiation damage under measuring conditions. Under the irradiation of low-energy electrons in a conventional LEED setup, TmCot wires are quickly damaged and the corresponding rings in the LEED pattern fade away within approximately one minute, similar to EuCot. Here, the same strategy of using a microchannelplate-LEED setup is applicable to reduce irradiation damage.

XAS and XMCD measurements of TmCot wires on Gr/Eu/Ir(111) were conducted at the end-station VEGMAK of the *Berliner Elektronenspeicherring-Gesellschaft für Synchrotronstrahlung* in Berlin, Germany. Photon energies of 1440 – 1520 eV were used with a lower photon flux compared to the measurements at the *Swiss Light Source*. The synthesis recipe of a sample similar to the one in Figure 7.2a was used, *i.e.* a sample of medium sized wire islands such that the formation of metallic Tm clusters during synthesis can be excluded. The MCP-LEED pattern of the *in situ* synthesized TmCot wires is shown in Figure 7.2b. The visible Eu ( $\sqrt{3} \times \sqrt{3}$ )R30° intercalation reflections are encircled in black. Furthermore, a ring around the (0,0) reflection appears, indicated by a black arrow. The emergence of this ring proves the successful synthesis

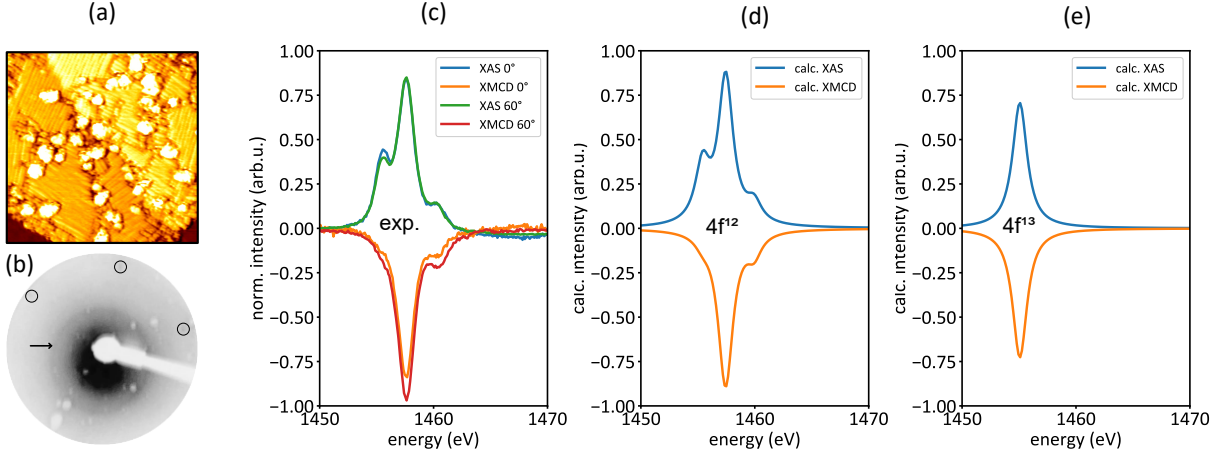


**Figure 7.2:** (a) STM topograph ( $350 \times 350 \text{ \AA}^2$ ) of TmCot wire islands on Gr/Eu/Ir(111) after Tm deposition ( $0.08 \text{ ML/min}$ ) in  $4 \cdot 10^{-9} \text{ mbar}$  Cot for 1.5 min at 300 K. STM data recorded at  $T = 20 \text{ K}$ . (b) MCP-LEED pattern of TmCot wire sample similar to (a) and corresponding to the data in (c). LEED pattern taken after the *in situ* synthesis and before transfer to the XAS measurement chamber. The ring indicated by the black arrow proves that TmCot wires have successfully been synthesized. The Eu ( $\sqrt{3} \times \sqrt{3}$ )R30° reflections are encircled black. (c) Experimentally measured XAS and XMCD signals at the  $M_5$  edge for normal ( $0^\circ$ ) and grazing incidence ( $60^\circ$ ) of the X-ray beam. For both angles of incidence a main peak with two surrounding shoulders is observed. The comparison to multiplet calculations of the XAS and XMCD for Tm in  $4f^{12}$  (d) and  $4f^{13}$  (e) electronic configuration unambiguously shows that in the experiment a clear  $4f^{12}$  configuration is measured. The XAS/XMCD experiments and calculations were performed at  $T = 3 \text{ K}$  and at a  $B$  field of 6.8 T.

of TmCot wires at the endstation. After the *in situ* synthesis the sample was directly transferred to the measurement setup and the resulting XAS and XMCD data of the  $M_5$  peak for normal ( $0^\circ$ ) and grazing ( $60^\circ$ ) incidence of the X-ray beam with respect to the surface normal are shown in Figure 7.2c. The fine structure varies only slightly between both angles of incidence and are unambiguously assigned to a  $4f^{12}$  electronic configuration, by comparing to multiplet calculations of  $4f^{12}$  (compare Figure 7.2d) and  $4f^{13}$  (compare Figure 7.2e). The characteristic shape of the Tm  $M_5$  edge for  $4f^{12}$  is the observed main peak, with a large shoulder to the left and weaker shoulder to the right [127,128]. The measured  $4f^{12}$  occupancy is completely inconsistent with the formation of TmCot wires, both from an ionic binding picture and with respect to our *ab initio* calculations. Neutral Tm has an electronic configuration of  $[\text{Xe}]4f^{13}6s^2$ , and within a wire both 6s electrons move towards the molecules, leading to a  $\text{Tm}^{2+}\text{-Cot}^{2-}$  ionic binding motif. Within this binding motif, there is simply no possibility for further charge transfer of any electrons, leaving a Tm  $4f^{13}$  configuration as the only possible state. Although Tm atoms at the wire terminals are in a  $4f^{12}$  state (discussed in the manuscript of chapter 5), the observed ring in LEED implies the synthesis of extended wire islands, such that the corresponding spectrum should be dominated by the central Tm atoms. Combined with the fact, that the ring in LEED has vanished after the XAS measurements, we conclude that the synthesized wires were decomposed before or during the XAS measurements. For EuCot wires, X-ray irradiation damage



induces changes in the  $M_5$  fine structure over the time scale of hours. In contrast, these types of changes were not found for irradiated TmCot wires. Indeed, the first spectrum, the second spectrum (acquired  $\approx 1$  min later), and the last measured spectrum (after hours of irradiation) show no changes in the  $M_5$  fine structure. This can be interpreted in two ways: (i) the wires are decomposed by the irradiation damage within a time span of  $< 1$  min, such that during the first spectrum they are completely decomposed, thus no changes can be observed afterwards. (ii) The wires were already decomposed during the transfer process, which takes about 30 min. In the transfer chamber, the wires were exposed to  $\approx 1 \times 10^{-7}$  mbar background pressure containing water, since the chamber was not baked out. The adsorption of  $H_2O$  on the wires could induce oxidation and thus a decomposition of the molecular structure.

Both possibilities (i) and (ii) or the combination of both seem plausible, when considering the differences between EuCot and TmCot wires: EuCot wires form carpets of closed and mostly single-domain islands with low defect density, and the Eu atoms are in their preferred dianionic state. Within these closed carpets, the Eu atoms are well isolated from the environment through the encapsulation by Cot molecules. In contrast, within the TmCot wires, the Tm atoms are not in their preferred oxidation state of  $3+$ , and the formation is only possible through substrate doping and precise tuning of growth conditions. The resulting islands have mostly disordered edges and consist of many domains visible in Figure 7.2a. Therefore, TmCot wire islands have significantly more nucleation points for oxygen etching and the resulting decomposition. In conclusion, it is simply not possible to investigate TmCot wires using X-ray techniques without significant decomposition.

To the contrary, the other observed TmCot phases — *i.e.* dots and coffee beans — are the preferred configurations on Gr/Ir(111). Therefore, it is plausible that for both of these cases irradiation damage is significantly weaker and comparable to EuCot wires, justifying the validity of the measured spectra.

## 7.2 On-surface synthesis

**Naphthalene:** In the manuscript of chapter 3, the orienting effect of the two-fold-symmetric Gr/Ir(110) was demonstrated through the uniaxial alignment of EuCot sandwich-molecular wires. Moreover, *ab initio* calculations were presented for the adsorption of the small anisotropic naphthalene molecule on Gr/Ir(110). Several local minima were found for the site-dependent adsorption energy, with the lowest energy state adsorbed to the trough position, where the highest amount of charge is transferred to the Gr. This finding is consistent with naphthalene adsorption experiments on Gr/Ir(111) [116], in which a higher adsorption energy was reported on n-doped Gr. Also, the calculations show that the preferred orientation of the molecules is with the long axis along the [001] direction of the substrate, *i.e.* a uniaxial alignment effect is expected. In contrast, the naphthalene molecules on Gr/Ir(111) were found to form randomly-oriented 2D carpets [116].

In Figure 7.3 the results of initial naphthalene adsorption experiments on Gr/Ir(110) are presented. Figure 7.3a shows a close-to-monolayer film of adsorbed naphthalene molecules on Gr/Ir(110), which was achieved through deposition of a few multilayers at 40 K and a subsequent temperature-programmed desorption step above the multilayer desorption temperature. A strong templating effect on the film is observed, in which the molecules order in rows along the [001] direction. The characteristic 10 Å stripe pattern along  $[1\bar{1}0]$  is indicated by blue lines in Figure 7.3b, which are aligned to the missing rows in the film. The missing rows are presumably the crests, where the molecules have the highest binding energy. Most molecules form close-packed rows, presumably through van der Waals interactions. Single molecules in troughs where the neighboring crests are empty appear elongated in [001] direction, consistent with the *ab initio* calculations. In the corresponding LEED pattern in Figure 7.3c most substrate reflections are suppressed by the molecular film, but the reflections corresponding to the 10 Å periodicity are very pronounced and encircled in black. The additional reflections encircled in blue are caused by the molecular film and correspond to a 6.5 Å periodicity, consistent with the close-packed row distance observed in STM.

Summarizing, a strong templating effect on the close-to-monolayer film is observed in STM and LEED, and it is plausible that for low coverages a uniaxial alignment is imposed onto the molecules with the long axis oriented along the [001] direction. Due to the weak physisorption of the molecular film to Gr, further investigations at a low-temperature STM setup would be beneficial.

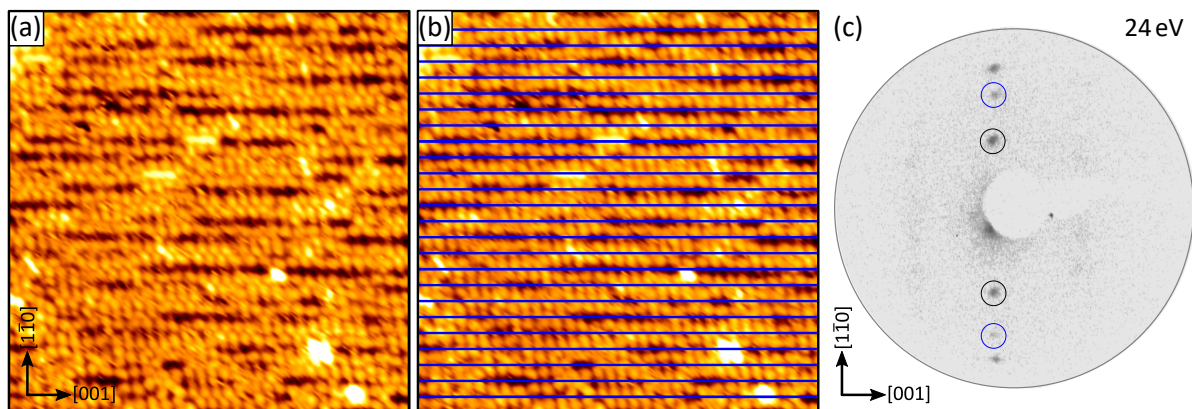


**Figure 7.3:** (a) STM topograph ( $250 \times 250 \text{ Å}^2$ ) of  $\text{C}_{10}\text{H}_8$  adsorbed at 100 K to Gr/Ir(110). (b) Topograph shown in (a) in which the 10 Å moiré periodicity of Gr/Ir(110) is highlighted by blue lines. (c) Contrast-inverted LEED pattern (24 eV) corresponding to (a), the 10 Å moiré reflections are encircled in black. Two additional reflections originating from the adsorbed naphthalene molecules are encircled in blue and correspond to a periodicity of  $\approx 6.5 \text{ Å}$ . STM and LEED data were recorded at 40 K. Tunneling parameters are  $U_{\text{bias}} = -2.4 \text{ V}$  and  $I_t = 0.9 \text{ nA}$ .

**TmCot:** In the manuscript of chapter 5 the formation of TmCot wires on n-doped Gr/Ir(111) was reported. It was found that the average wire length depends on the ratio of Tm to Cot

during the on-surface synthesis. Figure 7.4 shows a sequence of TmCot syntheses for varying flux ratios. In the following, the ratio will be discussed in terms of Cot molecules available during synthesis per Tm atom, *i.e.* the ratio will be given as Cot/Tm. The Tm deposition rate is already known from the calibration, and the Cot flux was calculated using the Hertz-Knudsen formula (7.1) as the number  $N$  of incoming Cot molecules per time  $t$  and surface area  $A$ :

$$\frac{N}{A \cdot t} = \frac{pN_A}{\sqrt{2\pi MRT}} \quad (7.1)$$

with  $p \hat{=}$  local Cot pressure,  $N_A = 6.022 \cdot 10^{23} \text{ mol}^{-1} \hat{=}$  Avogadro constant,  $M = 104.15 \hat{=}$  molar mass of Cot,  $R = 8.314 \text{ JK}^{-1}\text{mol}^{-1} \hat{=}$  universal gas constant and  $T = 300 \text{ K} \hat{=}$  temperature of Cot gas. In Figure 7.4a/b/d/e the local pressure  $p$  corresponds to the background pressure of Cot, and in Figure 7.4c/f — where Cot was supplied through a gas dosing tube — the local pressure  $p$  was calculated by multiplying the Cot background pressure with the pressure enhancement factor of  $\approx 20$ .

Going from left to right in Figure 7.4a–f, the flux dependence can be easily explained: In Figure 7.4a the flux ratio was Cot/Tm  $< 1$ , meaning on average less than one molecule is available per Tm atom during synthesis. Therefore, the Tm atoms form Tm–Tm bonds due to the lack of molecules and the formation of metal clusters is observed. The corresponding LEED pattern shows the substrate reflections [intercalated Eu ( $\sqrt{3} \times \sqrt{3}$ )R30°] and no additional Tm or TmCot reflections. With the stoichiometric ratio Cot/Tm  $\approx 4$  represented in Figure 7.4b, enough molecules are available during synthesis for the formation of wires, but still not enough to fully suppress the formation of Tm clusters, which are visible as bright intensities on top of the wire islands. The formation of randomly oriented wire domains results in a ring observed in the corresponding LEED pattern. Further increasing the ratio to values of Cot/Tm  $\approx 6 - 7$  as shown in Figure 7.4c/d leads the formation of extended wire domains with some second layer wire coverage. Due to the larger domains, the rings in LEED are very pronounced. If the ratio is further increased to Cot/Tm  $\approx 37$  in Figure 7.4e the wire domain sizes start to shrink due to the high surplus of Cot molecules, until for ratios of Cot/Tm  $\approx 60$  represented in Figure 7.4f mostly small wire fragments are formed and the ring in LEED has consequently vanished. This means that there is only a small window of ratios, Cot/Tm  $\approx 6 - 37$ , in which extended wire domains can be successfully synthesized (Figure 7.4c–e). Below that window – Cot/Tm  $< 6$  Tm – clusters are formed due to the low Cot flux (Figure 7.4a/b) and above that window only small wire fragments are formed (Figure 7.4f).

It is plausible, that this window of successful wire synthesis also holds true also for other rare-earth metals preferring a 3+ oxidation state, and the size of that window presumably depends on the cohesive energy of the used element. If the cohesive energy is high, the metal–metal bond becomes more favorable compared to the binding within wires. Therefore, if the cohesive energy

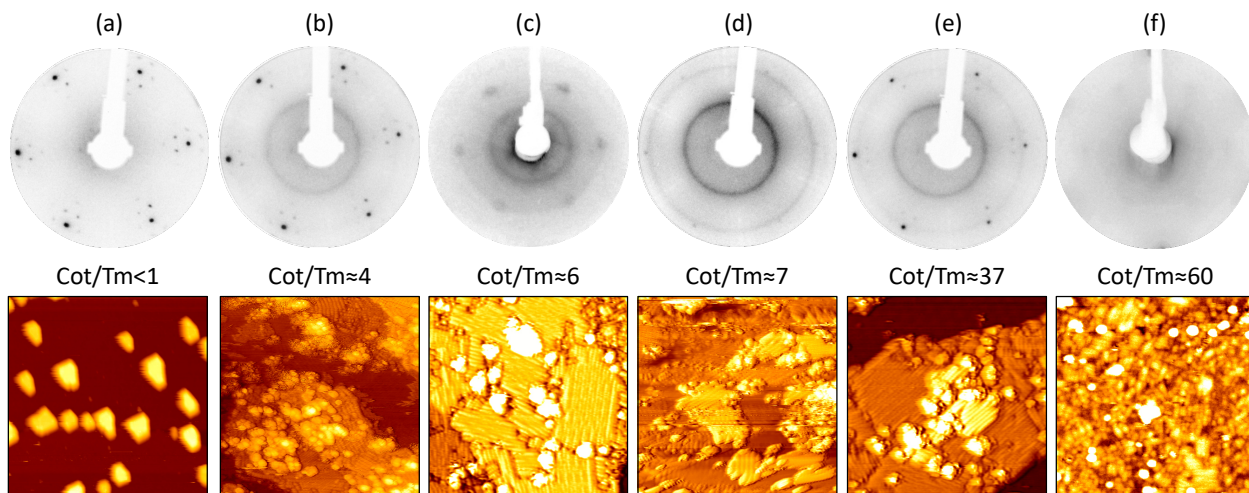


**Figure 7.4:** (a)–(f) Contrast-inverted LEED patterns and corresponding STM topographs ( $350 \times 350 \text{ \AA}^2$ ) after TmCot synthesis on Gr/Eu/Ir(111) with Tm deposition rate 0.08 ML/min [(a)–(e)]/0.008 ML/min [(f)] in local Cot pressure of (a)  $1 \cdot 10^{-8}$  mbar, (b)  $5 \cdot 10^{-8}$  mbar, (c)  $8 \cdot 10^{-8}$  mbar, (d)  $1 \cdot 10^{-7}$  mbar, (e)  $5 \cdot 10^{-7}$  mbar, (f)  $8 \cdot 10^{-8}$  mbar. The given Cot/Tm flux ratios were calculated using the Hertz-Knudsen formula. For  $\text{Cot/Tm} < 1$  metal clusters are formed and no ring in LEED is observed. For  $\text{Cot/Tm} \approx 1$  wires and clusters coexist, a ring in LEED appears. For  $3 < \text{Cot/Tm} < 19$  extended wire islands are formed and a clear ring is visible in LEED. For  $\text{Cot/Tm} \approx 30$  small wire fragments are formed and the ring in LEED has disappeared. The visible LEED reflections correspond to the  $\sqrt{3} \times \sqrt{3} \text{R}30^\circ$  Eu intercalation structure. LEED energies: (a) 40 eV, MCP-LEED, (b) 40 eV, MCP-LEED, (c) 44 eV, conventional LEED, (d) 40 eV, MCP-LEED, (e) 40 eV, MCP-LEED, (f) 60 eV, conventional LEED. All STM and LEED data were acquired at  $T = 20 \text{ K}$ . Tunneling parameters are (a)  $U_{\text{bias}} = -1.7 \text{ V}$  and  $I_t = 9 \text{ pA}$ , (b)  $U_{\text{bias}} = -2.0 \text{ V}$  and  $I_t = 10 \text{ pA}$ , (c)  $U_{\text{bias}} = -1.7 \text{ V}$  and  $I_t = 47 \text{ nA}$ , (d)  $U_{\text{bias}} = -2.0 \text{ V}$  and  $I_t = 9 \text{ pA}$ , (e)  $U_{\text{bias}} = -2.0 \text{ V}$  and  $I_t = 11 \text{ pA}$ , (f)  $U_{\text{bias}} = -1.8 \text{ V}$  and  $I_t = 11 \text{ nA}$ .

is to high, the phase-pure formation of large wire domains might not be possible. For avoiding metal clusters high molecule/metal ratios are needed, which in turn lead to the formation of small wire fragments. The limit with respect to the cohesive energy is unclear, but several rare-earth metals have a cohesive energy similar to Tm [125]. These elements could be promising candidates for the on-surface synthesis.

**Tetramethyl-Cot:** The use of the molecule tetramethyl-Cot for the on-surface synthesis of organometallic wires has shown, that their successful growth is not limited to Cot molecules (compare chapter 6). The Eu–tetramethyl-Cot wires appear to be more isolated from the substrate due to the methyl groups. Furthermore, the synthesis of small Tb–tetramethyl-Cot wire fragments was demonstrated on undoped Gr/Ir(111). This is presumably not possible using the simple Cot molecule — in analogy to TmCot wires described in chapter 5. The calculated flux ratio of the Eu–tetramethyl-Cot experiment in chapter 6 is tetramethyl-Cot/Tb  $\approx 23$ . For TmCot this ratio is well within the window of a successful synthesis. The already discussed argument regarding the cohesive energy can explain the fact, that mostly clusters are formed.

While Tm has a cohesive energy of  $\approx 2.5$  eV [129], the cohesive energy of Tb is significantly larger with a value of  $\approx 4.0$  eV [129], thus favoring the formation of Tb–Tb bonds.

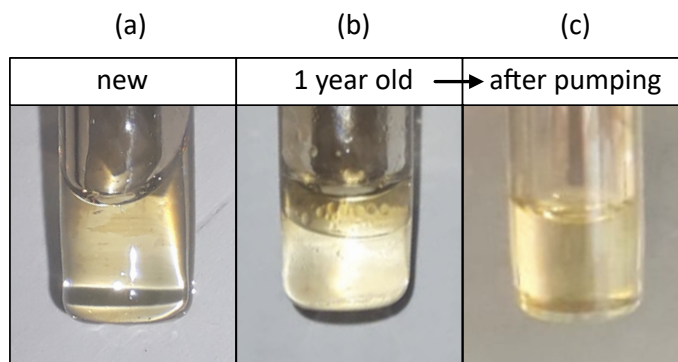


**Figure 7.5:** Liquid tetramethyl-Cot in glas vial: (a) Shortly after purchase (and synthesis), the liquid appears transparent and light yellow. (b) vial refilled with tetramethyl-Cot which was stored at  $\approx -30^\circ\text{C}$  for one year, the liquid has separated in two phases. (c) After pumping the vial for few minutes, the upper liquid phase has disappeared.

Regarding the use of tetramethyl-Cot it should be mentioned, that during the time span of  $\approx$  one year, the molecules have significantly decomposed. As a consequence, the successful synthesis of Eu–tetramethyl-Cot wires could not no longer be achieved after one year. Tetramethyl-Cot is liquid at room temperature and solidifies when stored in a common freezer. Figure 7.5a shows the liquid filled into a glas vial directly after purchase. As apparent from the photograph, the liquid appears transparent and light yellow. After storing the molecules for one year in the freezer and refilling the vial, the liquid has separated into two phases visible in Figure 7.5b. This could be explained by the dissociation of methyl groups from tetramethyl-Cot, leaving a mixture of tetramethyl-Cot, Cot and other fragments. This assumption seems plausible when considering that in the Eu–tetramethyl-Cot experiments in chapter 6 the molecules also appear to decompose at a synthesis temperature of 400 K. Pumping on the two-phase liquid results in a single phase again (compare Figure 7.5c). However, synthesis with this liquid was not clean either. The acquired mass spectra corresponding to Figure 7.5a/c are shown in Figure A.5a of the scientific appendix and support the finding of decomposition. While in the blue spectrum (directly after purchase) the tetramethyl-Cot mass (160 amu) is well visible together with fragments thereof, both are no more visible after one year of storage, even at a ten times higher provided gas pressure. In conclusion, tetramethyl-Cot can only be used for a short timespan after its synthesis by the manufacturer, before significant decomposition occurs, even when storing at temperatures of  $\approx -40^\circ\text{C}$ .

**Dibenzo-Cot:** During the course of this thesis, the use of the Cot derivative Dibenzo-Cot (compare Figure 7.6) was tested in on-surface synthesis combined with the alkaline-metal Ba on Gr/Ir(111). The topograph of Figure 7.7a shows Ba–Dibenzo-Cot organometallic compounds



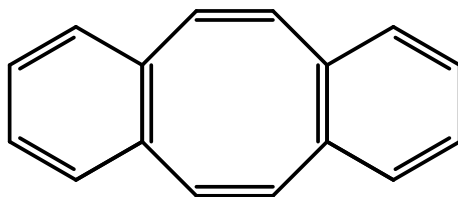


**Figure 7.6:** Structural formula of Dibenzo-Cot ( $C_{16}H_{12}$ ). Two benzene rings are attached to the Cot molecule symmetrically.

after on-surface synthesis on Gr/Ir(111) at 300 K under excess pressure of Dibenzo-Cot. The compounds form a disordered network, and the molecular resolution topograph in Figure 7.7b shows wire-like complexes forming disordered islands. Also the average height of  $\approx 5 \text{ \AA}$  visible in the corresponding height profile is consistent with the formation of small wire fragments. A plausible explanation for the disordered behavior is the more complex geometry of the Dibenzo-Cot molecule. Dibenzo-Cot is only of two-fold symmetry, while Cot is of eight-fold and tetramethyl-Cot still of four-fold symmetry. The benzene rings of two neighboring Dibenzo-Cot molecules within a wire are likely to attract each other through physisorption. A significant attraction could lead to bending of the Ba–Dibenzo-Cot wires. It is plausible, that this bending would occur randomly to both directions along a wire. Thereby, the disordered network could be explained.

In conclusion, Dibenzo-Cot is not a good candidate for the on-surface synthesis of ordered and high-quality films of sandwich-molecular wires.

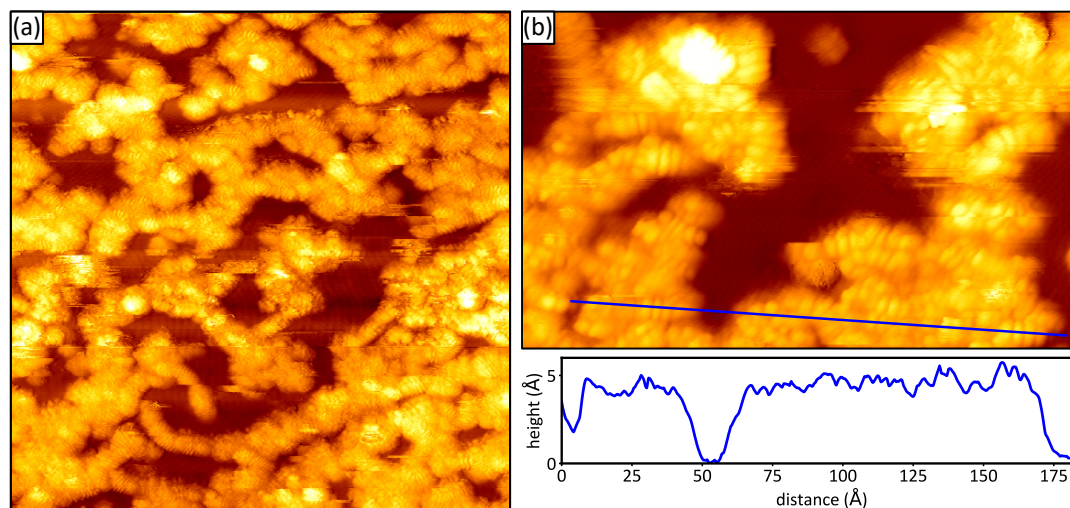


**Figure 7.7:** Ba–di-benzo-Cot organometallic structures on Gr/Ir(111): (a) STM topograph ( $400 \times 400 \text{ \AA}^2$ ) of disordered structures are visible. (b) STM topograph ( $120 \times 200 \text{ \AA}^2$ ) with organometallic structures which appear like disordered short wire fragments. The corresponding height profile reveals an apparent height of  $\approx 5 \text{ \AA}$  which is consistent with the growth of sandwich-molecular fragments of upright standing molecules, with the long axis parallel to the surface. Synthesis recipe: deposition of 0.1 ML Ba in  $2 \times 10^{-10}$  mbar di-benzo-Cot on Gr/Ir(111) at  $T = 300 \text{ K}$ . STM topographs were recorded at  $T = 20 \text{ K}$ . Tunnelling parameters are (a)  $U_{\text{bias}} = -2.2 \text{ V}$  and  $I_t = 43 \text{ pA}$  and (b)  $U_{\text{bias}} = -1.1 \text{ V}$  and  $I_t = 16 \text{ pA}$  (both superimposed with their derivatives for better visibility).

### 7.3 Magnetic ordering

In the manuscript of chapter 4 the magnetic behavior of EuCot wires on Gr/Ir(110) was investigated and compared to EuCot wires on Gr/Ir(111). As discussed in ref. [84], a ML of EuCot on Gr/Ir(111) was reported to be ferromagnetic with a magnetic hysteresis below 7 K. Surprisingly, on the two-fold symmetric substrate Gr/Ir(110) the magnetic hysteresis of EuCot has vanished even at 3 K. In the manuscript it was speculated, that the charge transfer to Gr in the trough locations could be the reason for the suppression of the hysteresis. This explanation is consistent with the finding, that also on the n-doped (Yb intercalated) Gr/Ir(111) the magnetic hysteresis is suppressed (compare supporting information of chapter 4). These speculations are solidified with *ab initio* calculations presented in Figure 7.8. Therein, the effects of doping of the Cot ring on the magnetic coupling were studied. Due to computational constraints, the substrate doping was simulated by symmetrically exchanging four H atoms of the Cot ring by electron donating ( $X=\text{NH}_2$ ) or withdrawing groups ( $X=\text{BH}_2$ ), visualized in Figure 7.8.

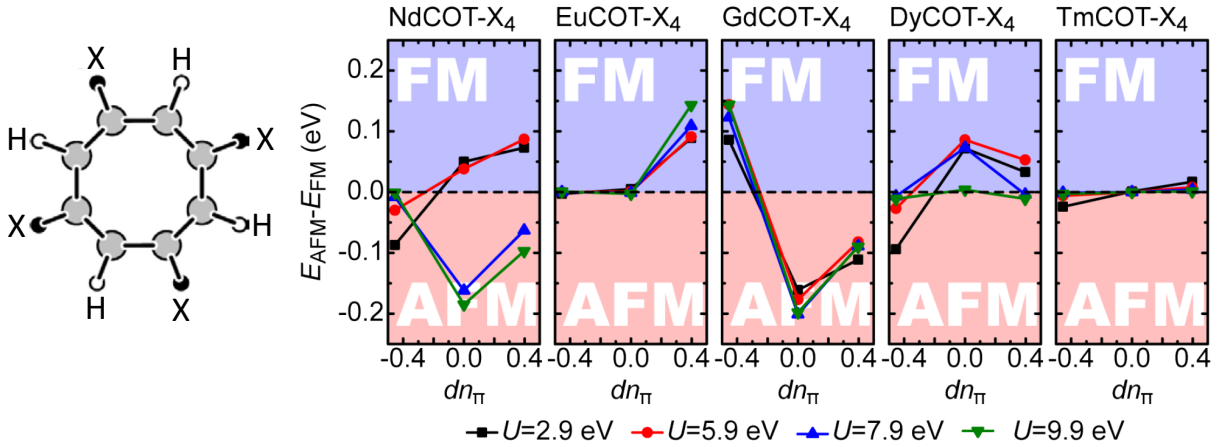


**Figure 7.8:** *Ab initio* calculations of doping effects on the ferromagnetic (FM) and antiferromagnetic (AFM) coupling in LnCot wires (Ln=Nd, Eu, Gd, Dy, Tm) for different values of the effective Hubbard  $U$ . The substrate doping effects are simulated by symmetrically replacing four H atoms of the Cot ring by electron donating ( $X=\text{NH}_2$ ) and withdrawing groups ( $X=\text{BH}_2$ ). Negative  $dn_\pi$  corresponds to electron donation to the Cot  $\pi$  system.

The *ab initio* calculations find, that the rare-earth atoms within the wires form 4f–5d hybrid orbitals which can interact with the extended molecular  $\pi$  system. This interaction mediates the magnetic coupling within the wires and therefore changes in the  $\pi$  and 4f–5d hybrid occupancy have a direct effect onto the intra-wire coupling. The energy differences between antiferromagnetic and ferromagnetic ordering for periodic LnCot- $X_4$  wires (Ln=Nd, Eu, Gd, Dy and Tm) were calculated, and the doping is found to severely change the magnetic behavior through the explained mechanism. In the graphs of Figure 7.8, negative  $dn_\pi$  corresponds to charge donation into the Cot ring, which can be achieved by n-doping of the substrate. The graph for the EuCot

wires shows, that p-doping (positive axis) promotes ferromagnetic coupling within the wires, whereas for n-doping the suppression of ferromagnetic coupling is observed. These results are in agreement with our experimental findings that on the slightly p-doped Gr/Ir(111) EuCot wires couple ferromagnetically, while on n-doped Gr/Ir(111) the coupling is suppressed. The same behavior is found in the calculations for TmCot wires. This implies that for the TmCot wires on n-doped Gr/Ir(111) described in chapter 5 no ferromagnetic coupling is to be expected, but rather weak antiferromagnetic coupling. In contrast, for GdCot wires ferromagnetic coupling is strongly favored on n-doped substrates, according to the theoretical calculations. These results show, that magnetic coupling in sandwich-molecular wires can be easily tuned *via* substrate doping and promise a variety of electronic and magnetic behaviors that could be investigated in future experiments.



## CHAPTER 8

---

### Summary and outlook

#### Single-crystal graphene on Ir(110)

In the first manuscript of this thesis, the growth of a single-crystal sheet of Gr on the two-fold symmetric substrate Ir(110) was presented. The adsorbed Gr layer is able to suppress the surface reconstructions present on the bare Ir(110) substrate and flat terraces are formed. The two-fold symmetry of Ir(110) is imprinted onto the moiré creating a wave pattern of nm wavelength. This wave pattern is associated with a modulation of the electronic properties and charge transfer into Gr is observed in the trough locations of the moiré. The resulting binding strength varies between strong physisorption and weak chemisorption, suppressing the Dirac cone of the electronic band structure characteristic to freestanding Gr. In DFT calculations the adsorption of the naphthalene molecule to the Gr was studied and no hybridization was found, *i.e.* the molecule purely binds through physisorption. Therefore, Gr/Ir(110) can be regarded as inert and adsorbed molecular species bind only weakly, *i.e.* their electronic properties are not perturbed through substrate hybridization. Finally it is shown, that Gr/Ir(110) is able to uniaxially align sandwich-molecular wires and template the adsorption of aromatic molecules.

In future experiments, other sandwich-molecular wires could be uniaxially aligned using Gr/Ir(110) as template, if they do not rely on n-doping of the substrate. This includes BaCot and YbCot wires described in this thesis, which were shown to have a similar growth behavior to EuCot wires. Also the synthesis of another two-fold symmetric Gr/metal substrate is conceivable using the Pt(110) surface. While in ref. [43] the formation of multiple domains was found at a growth temperature of 1000 K, Gr growth above the roughening temperature of Pt might lead to the formation of single-crystal Gr/Pt(110).

#### Uniaxially aligned 1D sandwich-molecular wires: electronic structure and magnetism

In the second manuscript of this thesis, the two-fold symmetric moiré of Gr/Ir(110) was used for the uniaxial alignment of EuCot sandwich-molecular wires with the goal to use spatially

averaging techniques for the investigation of electronic and magnetic properties. The electronic band structure of EuCot is dominated by a flat band 1.85 eV below the Fermi energy which was found to originate from the localized Eu 4f states. By matching the relative distance of the EuCot  $\pi$  and  $\sigma$  bands observed in ARPES to DFT calculations, the effective Hubbard  $U$  of this system is found to be  $\approx 3.5$  eV. In the calculated PDOS of an isolated EuCot wire the formation of 4f–5d hybrid orbitals is observed, which can interact with the extended molecular  $\pi$  system and mediate magnetic coupling of the 4f-generated moments. While EuCot wires on Gr/Ir(111) couple ferromagnetically below 7 K, they show a paramagnetic behavior on Gr/Ir(110) down to 3 K with an easy-axis magnetization along the wires. It is speculated that the ferromagnetic coupling is suppressed due to the more strongly interacting Gr/Ir(110) and the related modification of its electronic structure.

For future experiments, the 1D band structure investigation of BaCot wires aligned on Gr/Ir(110) using ARPES could allow the observation of dispersing  $\pi$  bands within the wire. For EuCot only a 4f-derived flat band was observed, which has by far the highest intensity in the corresponding calculated PDOS. Therefore it is plausible that  $\pi$ -related bands simply cannot be resolved in ARPES due to the superposition with the intense flat band. In BaCot wires the 4f states are not occupied, and ARPES measurements might be able to resolve  $\pi$ -derived bands using the scanning technique explained in the manuscript.

The growth of Eu-tetramethyl-Cot wires on Gr/Ir(110) could allow ferromagnetic coupling within the sandwich-molecular wires, as they were found to be more isolated from Gr/Ir(111) compared to EuCot. If this isolation is strong enough to decouple the wires from the Gr/Ir(110), the unperturbed magnetic ordering could be probed using XAS and XMCD measurements.

## From dots to wires: doping-dependent on-surface synthesis of thulium-cyclooctatetraene compounds on graphene

In the third manuscript of this thesis, the on-surface synthesis of TmCot compounds on Gr/Ir(111) was studied and it was found that the chemical reaction pathway can be changed through substrate doping. On the undoped substrate the formation of the TmCot dot phase is observed, which consists of repulsively interacting TmCot monomers bound to Gr through charge transfer. The dots have a 4f<sup>12</sup> electronic configuration and an out-of-plane easy axis magnetization. For higher coverages the dot phase coexists with the coffee bean phase. The latter forms islands of Tm and Cot, in which the molecules presumably stand upright with respect to Gr. The coffee bean phase also has a 4f<sup>12</sup> configuration and a peculiar magnetic behavior. For low magnetic fields the in- and out-of-plane susceptibility agrees within few percent, while for higher fields the in-plane magnetization saturates to a much lower value compared to out-of-plane. On n-doped Gr/Ir(111) interlocking and parallelly aligned TmCot sandwich-molecular wires were synthesized, forming multi-domain islands. The average wire length can be controlled by the Tm/Cot

---

flux ratio during organometallic synthesis, going from small wire fragments to long wires of more than 100 formula units.

In future experiments Tm could be combined with the more reactive tetramethyl-Cot. It is plausible that due to the higher reactivity, Tm–tetramethyl-Cot wires grow longer compared TmCot. It can also be speculated, that on Gr/Ir(111) other metal–Cot monomers could be synthesized, specifically dysprosium–Cot. Similar to Tm, dysprosium (Dy) prefers an oxidation state of 3+. In ref. [130] a superlattice of Dy atoms is reported on Gr/Ir(111) at low temperatures, and the Dy atoms were found to be a single-atom magnets with an open magnetization curve at 2.5 K. While the single atoms of Dy adsorbed to Gr/Ir(111) would immediately form clusters at 300 K, this would not be the case for repulsively interacting DyCot monomers which bind to Gr through charge transfer. The adsorbed Cot ring could further protect the Dy from oxidation and modify the magnetic behavior.

## Reactant and substrate variation in on-surface synthesis

Finally, in chapter 6 the use of different atomic species and molecules in the on-surface synthesis of sandwich-molecular wires was investigated and the growth substrate was varied. BaCot and YbCot on Gr/Ir(111) follow the same growth mechanism as EuCot, and form large islands of interlocking and parallelly aligned wires, with some differences in the growth morphology. This demonstrates that the formation of sandwich-molecular wires using Cot is not limited to metal reactants from the lanthanide series, but also applies to other metal atoms favoring a +2 oxidation state. Eu was combined with tetramethyl-Cot in the on-surface synthesis on Gr/Ir(111) and also here the formation of sandwich-molecular wires was observed, which are parallelly aligned within islands. The island height is significantly modulated which is explained by the rotation of the attached methyl groups. These side groups further lead to a larger inter-wire distance and a weaker binding to the substrate compared to EuCot. When combining Tb with tetramethyl-Cot on Gr/Ir(111), small wire fragments were synthesized in coexistence with Tb clusters. Since Tb prefers a 3+ oxidation state, the wire formation on Gr/Ir(111) indicates a higher reactivity of tetramethyl-Cot during the chemical reactions. Lastly, on-surface synthesis of EuCot wires on polar Eu oxide on Ir(111) was demonstrated, though at the cost of reduced order.

For future experiments, tetramethyl-Cot could be combined with other lanthanide elements on undoped and n-doped Gr/Ir(111). By choosing lanthanides with lower cohesive energy compared to Tb — *e.g.* Nd, Gd, Dy, Ho, Er — the formation of clusters can possibly be suppressed. Additionally, each of these lanthanide elements has a different 4f occupation and resulting magnetic moment, which could lead to a variety of different magnetic behaviors. Also other Cot derivatives could be used for the on-surface synthesis, preferably with higher reactivity. Finally, the growth of sandwich-molecular wires on metal oxide surfaces could be further investigated. Since oxides have an even lower ability to take up charge compared to n-doped Gr/Ir(111), it is

possible that TmCot and other lanthanide–Cot wires could be directly grown on *e.g.* polar Eu oxide on Ir(111). As a secondary effect, the wires might be even more isolated electronically, which would enable the investigation of their unperturbed electronic and magnetic properties.

## APPENDIX A

### Scientific appendix

*S. Kraus and K. Bischof conducted the experiments shown in this chapter under the guidance of T. Michely.*

#### A.1 Ytterbium intercalation under graphene/Ir(111)

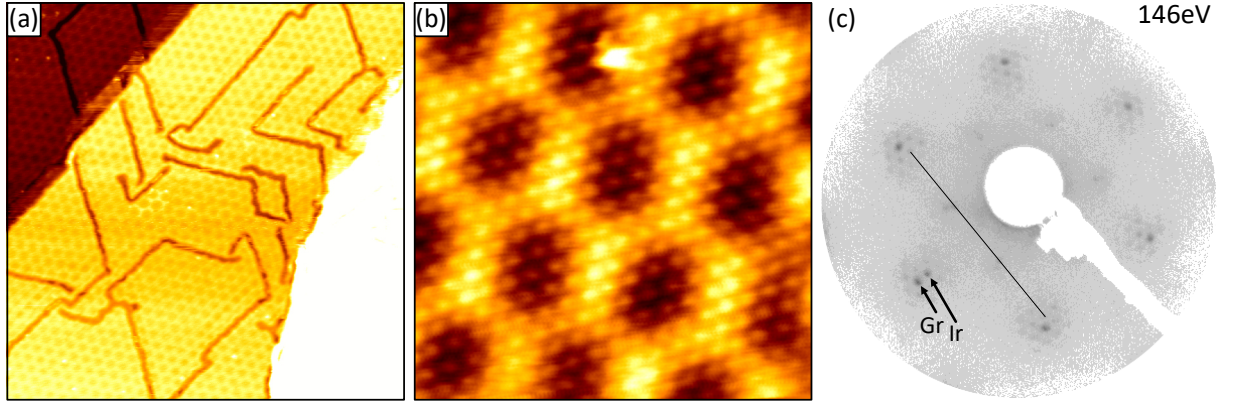


**Figure A.1:** Yb intercalated under Gr/Ir(111): (a) STM topograph ( $820 \times 820 \text{ Å}^2$ ) of an almost full intercalation layer, only the dark stripes are non-intercalated. (b) STM topograph ( $150 \times 150 \text{ Å}^2$ ). The moiré of Gr with Ir(111) and the  $(\sqrt{3} \times \sqrt{3})R30^\circ$  intercalated Yb lattice is visible. (c) Contrast-inverted 146 eV LEED pattern corresponding to (a)/(b). The moiré reflections are still visible and the  $(\sqrt{3} \times \sqrt{3})R30^\circ$  intercalation structure (with respect to Ir) is weakly visible. Intercalation recipe: deposition of  $\approx 1 \text{ ML}$  Yb on Gr/Ir(111) at 450 K sample temperature,  $\Delta t = 600 \text{ s}$ . The STM data have been recorded at 300 K. Tunnelling parameters are (a)  $U_{\text{bias}} = -0.5 \text{ V}$  and  $I_t = 0.3 \text{ nA}$  and (b)  $U_{\text{bias}} = -0.7 \text{ V}$  and  $I_t = 2.9 \text{ nA}$  (superimposed with derivative for better visibility).

The intercalation of Gr/Ir(111) has already been studied for different species, *e.g.* for cesium [131] or Eu [132, 133]. Intercalation can lead to the decoupling of the Gr sheet from its substrate, the doping of Gr and in the case of Eu [133] was found to form a magnetic layer. Here, the rare-earth metal Yb is intercalated under Gr/Ir(111) at a temperature of 450 K, significantly lower compared to the required 720 K for the effective intercalation of Eu [133]. Similar to Eu, the described deposition of Yb results in a homogeneous intercalation layer shown in the topograph of Figure A.1a. The observed non-intercalated stripes have a very similar appearance

to those of the Eu intercalation layer described in ref. [132]. Although the intercalation layer is almost closed, the moiré of Gr with Ir(111) is still well visible through the layer, indicating a weaker decoupling effect compared to Eu, where the moiré is weakened through the intercalation. In the topograph of Figure A.1b the moiré is very well visible, along with a  $(\sqrt{3} \times \sqrt{3})R30^\circ$  intercalation pattern of Yb. The corresponding LEED pattern in Figure A.1c both the Gr and Ir reflections are still visible with additional moiré reflections, and also the  $(\sqrt{3} \times \sqrt{3})R30^\circ$  reflections are weakly visible. As indicated by the black line between two Ir reflections in Figure A.1c, the  $(\sqrt{3} \times \sqrt{3})R30^\circ$  structure is formed with respect to the Ir(111) substrate. The weak appearance of the intercalation layer reflections is consistent with the strong moiré of the fully intercalated regions. It should be mentioned that upon Yb intercalation immediately the  $(\sqrt{3} \times \sqrt{3})R30^\circ$  structure is observed, up to the full intercalation layer. This is in contrast to Eu, which first forms a  $(2 \times 2)R0^\circ$  structure until 0.25 ML Eu has been intercalated, and beyond that starts to form the more densely packed  $(\sqrt{3} \times \sqrt{3})R30^\circ$  structure up to full intercalation.

## A.2 Barium intercalation under graphene/Ir(111)

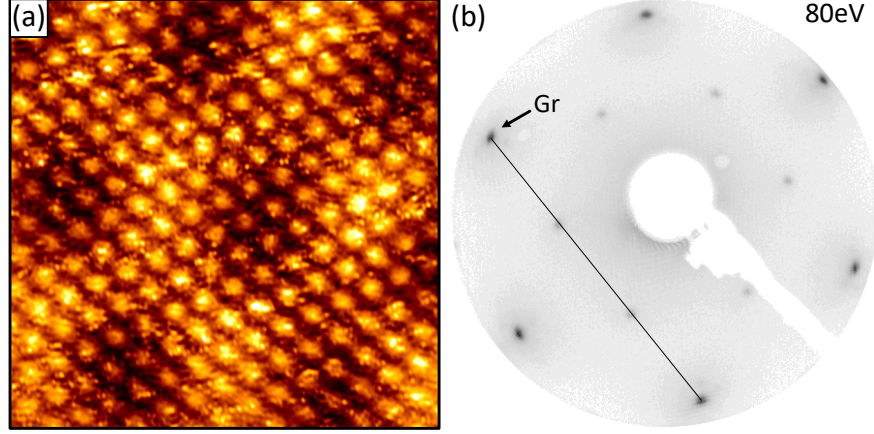


**Figure A.2:** Ba intercalated under Gr/Ir(111): (a) STM topograph ( $56 \times 56 \text{ \AA}^2$ ) of an intercalated area. The moiré of Gr with Ir(111) and the  $(\sqrt{3} \times \sqrt{3})\text{R}30^\circ$  intercalated Ba lattice are visible. (b) Contrast-inverted 80 eV LEED pattern corresponding to (a). The moiré reflections are suppressed, and the  $(\sqrt{3} \times \sqrt{3})\text{R}30^\circ$  intercalation structure (with respect to Gr) is well visible. Intercalation recipe: deposition of  $\approx 0.5 \text{ ML}$  Ba on Gr/Ir(111) at 600 K,  $\Delta t = 1400 \text{ s}$ . The STM data have been recorded at 300 K. Tunnelling parameters are  $U_{\text{bias}} = -0.5 \text{ V}$  and  $I_t = 0.3 \text{ nA}$  (superimposed with derivative for better visibility).

Similar to Yb, also the non-magnetic alkaline-earth metal Ba can be intercalated under Gr/Ir(111), but a higher substrate temperature compared to Yb is needed for effective intercalation. Upon deposition of Ba on Gr/Ir(111) at 600 K until saturation, the  $(\sqrt{3} \times \sqrt{3})\text{R}30^\circ$  intercalation layer shown in the topograph of Figure A.2a is formed. Here, the moiré appears much weaker, and in the corresponding LEED pattern in Figure A.2b the Ir as well as the moiré reflections are no more visible, while the  $(\sqrt{3} \times \sqrt{3})\text{R}30^\circ$  intercalation reflections are very pronounced and with respect to Gr. This indicates a strong decoupling effect of the intercalated Ba layer, which in contrast to Eu is non-magnetic. It should be mentioned that similar to Eu, also Ba intercalation first goes through a  $(2 \times 2)\text{R}0^\circ$  phase until finally the more dense  $(\sqrt{3} \times \sqrt{3})\text{R}30^\circ$  phase is formed as shown in Figure A.2.

### A.3 Cyclooctatetraene

Figure A.3a shows the mass spectrum of Cot ( $\text{C}_8\text{H}_8$ , 104 amu). The main mass peak at 104 amu is well visible, along with fragments of lower masses. Figure A.3b shows the thermal desorption spectrum of a multilayer of Cot adsorbed to Gr/Ir(111) at 20 K. The multilayer peak is located at  $\approx 162$  K and the monolayer peak at 185 K.

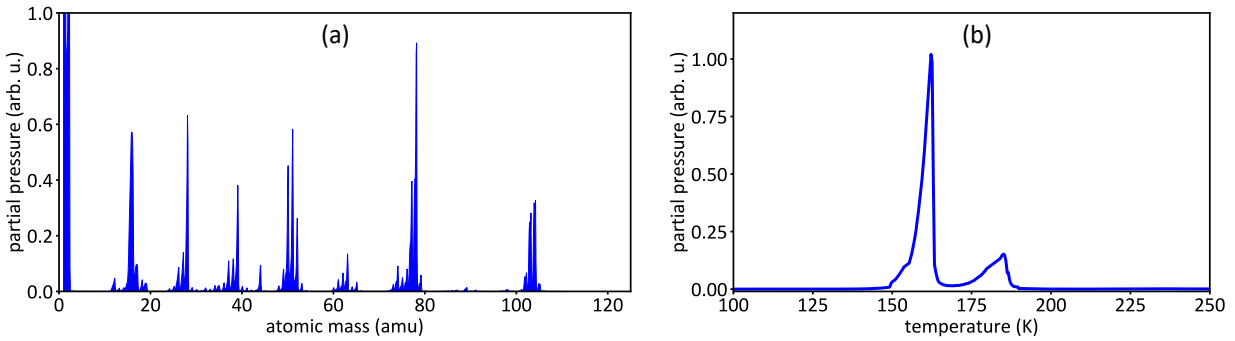


**Figure A.3:** (a) Mass spectrum of Cot (mass 104). Additional to the mass of Cot, also Cot fragments are detected. (b) Thermal desorption spectrum of mass 104 (Cot) of multilayer film Cot adsorbed to Gr/Ir(111) at  $T = 20$  K. The monolayer peak is positioned at  $(185 \pm 5)$  K and the multilayer peak at  $(162 \pm 3)$  K. Ramp rate 2 K/s.

The topograph Figure A.4a shows a sub-monolayer coverage of Cot adsorbed to Gr/Ir(111) at 20 K. The Cot molecules order along the moiré of Gr with Ir(111) with a periodicity of  $\approx 25$  Å visible in the corresponding height profile. The apparent height at the given tunnelling conditions is  $\approx 1$  Å. The STM topograph in Figure A.4b shows a close-to-monolayer film of Cot adsorbed to Gr/Ir(111) at 20 K and the formation of islands with a herringbone structure is observed, with intra-row periodicity  $\approx 7$  Å and inter-row distance  $\approx 8$  Å. The corresponding line profile shows an average height of  $< 2$  Å and suggests that the Cot molecules are adsorbed flat to the Gr. They appear elongated, which can be explained by the tub-like shape in their neutral configuration.



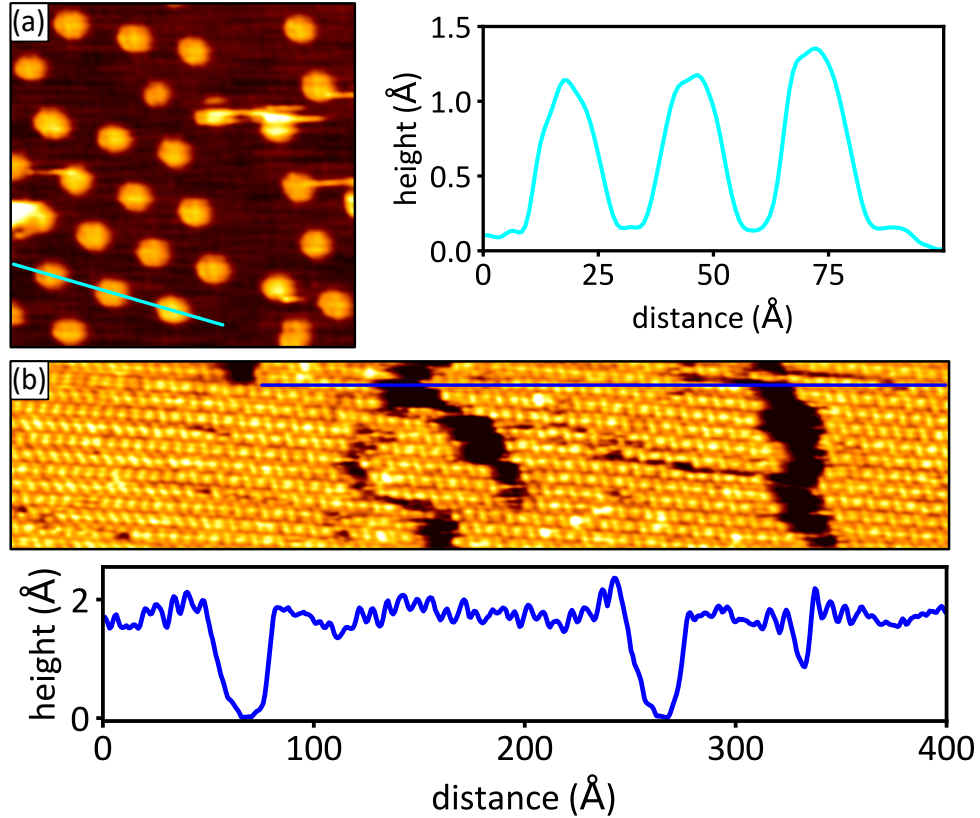


**Figure A.4:** (a) STM topograph ( $150 \times 150 \text{ Å}^2$ ) of sub-monolayer coverage Cot adsorbed to Gr/Ir(111) at  $T = 20 \text{ K}$ , the Cot molecules are arranged with the moiré periodicity of the substrate and have an apparent height of  $\approx 1 \text{ Å}$  shown in corresponding height profile (position indicated by cyan line). (b) STM topograph ( $100 \times 500 \text{ Å}^2$ ) of close-to-monolayer coverage Cot adsorbed to Gr/Ir(111). Within the Cot island a herringbone structure is observed, and the apparent island height is  $\approx 2 \text{ Å}$  (position of height profile indicated by blue line). The observed intra-row spacing is  $8.0 \pm 0.4 \text{ Å}$  and the inter-row spacing is  $7.0 \pm 0.2 \text{ Å}$ . STM topographs were recorded at  $T = 20 \text{ K}$ . Tunnelling parameters are (a)  $U_{\text{bias}} = -1.8 \text{ V}$  and  $I_t = 11 \text{ pA}$  and (b)  $U_{\text{bias}} = -1.8 \text{ V}$  and  $I_t = 8 \text{ pA}$  (superimposed with reversed Fourier transform of Cot superstructure for better visibility).

## A.4 Tetramethyl-cyclooctatetraene

Figure A.5 shows the mass spectrum of tetramethyl-Cot directly after purchase (blue) and after one year of storage (orange). The mass of tetramethyl-Cot ( $160 \text{ amu}$ ) is well visible in the blue spectrum, as well as molecular fragments. In the orange spectrum a ten times higher gas pressure was provided, but still the mass of  $160 \text{ amu}$  is below the noise level. Therefore it is concluded, that after storage, the molecules are decomposed. Figure A.5b shows the thermal desorption spectrum of few multilayers of intact tetramethyl-Cot adsorbed to Gr/Ir(111) at  $20 \text{ K}$ . The multilayer peak lies at  $\approx 177 \text{ K}$  and the monolayer peak at  $\approx 221 \text{ K}$ . Compared to Cot, tetramethyl-Cot has a  $36 \text{ K}$  higher desorption temperature.

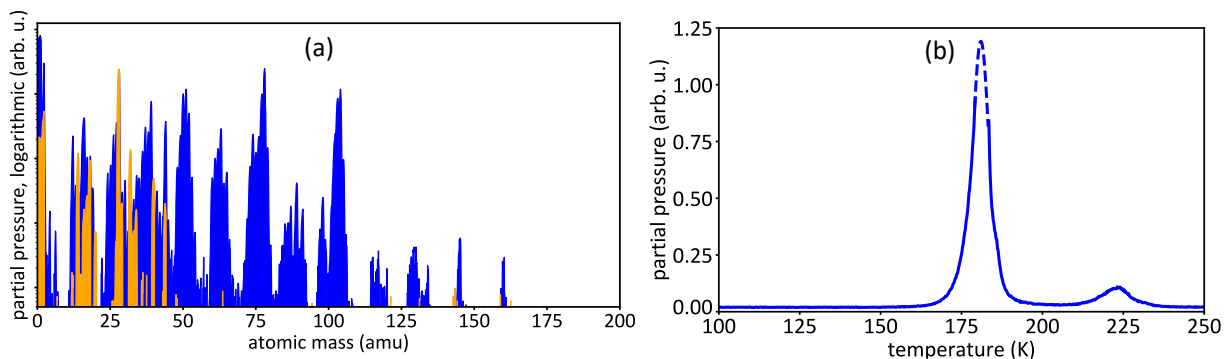


**Figure A.5:** (a) Mass spectra of tetramethyl-Cot. Blue: After purchase, in pressure of  $1 \times 10^{-8}$  mbar tetramethyl-Cot. Orange: stored for one year after purchase, in a pressure of  $1 \times 10^{-7}$  mbar tetramethyl-Cot. (b) Thermal desorption spectrum of mass 160 (tetramethyl-Cot) of multilayer film tetramethyl-Cot adsorbed to Gr/Ir(111) at  $T = 20$  K. The monolayer peak is positioned at  $(221 \pm 4)$  K and the multilayer peak at  $(177 \pm 3)$  K. Ramp rate 2 K/s.

## A.5 Dibenzo-cyclooctatetraene

In Figure A.6a the mass spectrum of Dibenzo-Cot is shown, which has a mass of 204 amu. The main peak is not visible, but only fragments such as Cot (104 amu). The absence of the main peak is probably due to the low sensitivity of the spectrometer at high masses. Therefore, the fragment mass of 57 amu has been used for the thermal desorption spectrum of multilayer Dibenzo-Cot adsorbed to Gr/Ir(111) in ref.A.6b. The multilayer desorption peak is located at  $\approx 136$  K and the monolayer peak at  $\approx 187$  K, which is very close to the monolayer desorption temperature of Cot.

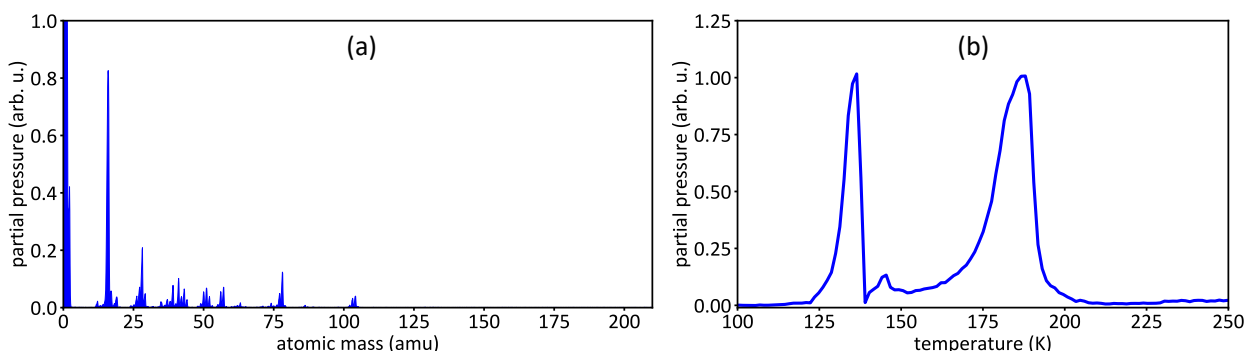


**Figure A.6:** (a) Mass spectrum of Dibenzo-Cot, in a background pressure of  $5 \times 10^{-5}$  mbar dibenzo-Cot. The mass of Dibenzo-Cot (204) is not visible in the spectrum, most likely due to the low sensitivity of the spectrometer at high masses. (b) Thermal desorption spectrum of mass 57 (fragment of mass 204 for Dibenzo-Cot) of multilayer film Dibenzo-Cot adsorbed to Gr/Ir(111) at  $T = 20$  K. The monolayer peak is positioned at  $(187 \pm 3)$  K and the multilayer peak at  $(136 \pm 2)$  K. Ramp rate 4 K/s.

Figure A.7a shows the topograph of a closed monolayer film of Dibenzo-Cot adsorbed to Gr/Ir(111) at 20 K, which was achieved by the adsorption of a mulilayer film and subsequent thermally programmed desorption to 160 K. In the molecular-resolution topograph of Figure A.7b, it is visible that the molecules arrange in rows with two distinct molecular orientations. The intra-row distance is given by  $\approx 5.6 \text{ \AA}$  and the inter-row spacing is given by  $\approx 8.9 \text{ \AA}$ .

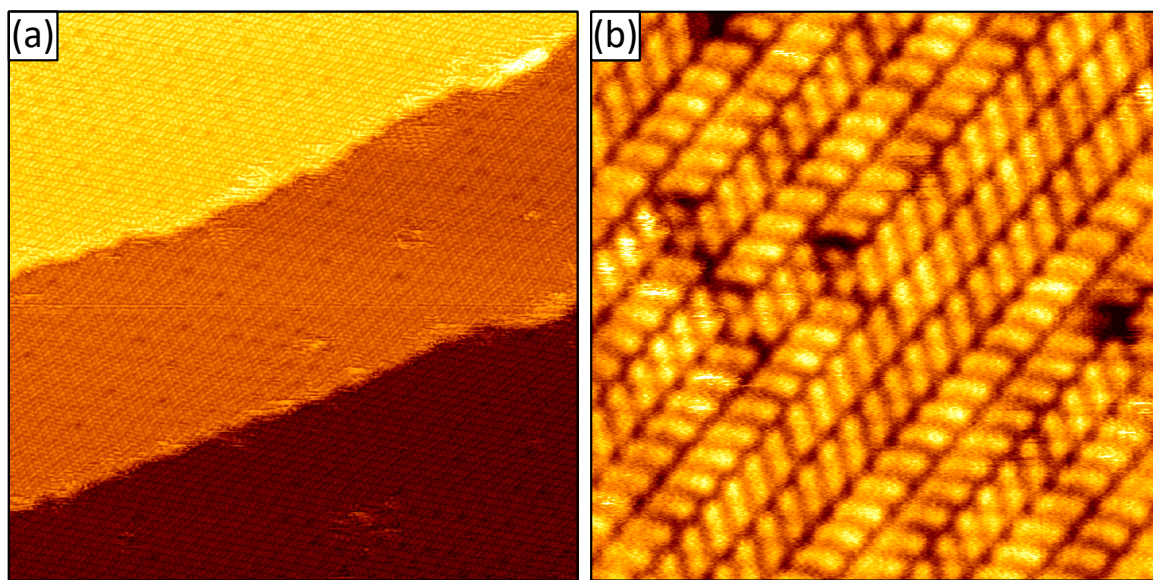


**Figure A.7:** (a) STM topograph ( $820 \times 820 \text{ \AA}^2$ ) of a closed monolayer di-benzo-Cot film adsorbed to Gr/Ir(111) at  $T = 20 \text{ K}$ . (b) STM topograph ( $100 \times 500 \text{ \AA}^2$ ) closed monolayer of di-benzo-Cot adsorbed to Gr/Ir(111), rows of elongated objects are observed with two distinct orientations. The observed intra-row spacing is  $5.6 \pm 0.3 \text{ \AA}$  and the inter-row spacing is  $8.9 \pm 0.4 \text{ \AA}$ . Recipe: Deposition of multilayer film di-benzo-Cot on Gr/Ir(111) at  $T = 20 \text{ K}$  with subsequent short annealing to  $T = 160 \text{ K}$  to desorb the multilayers. STM topographs were recorded at  $T = 20 \text{ K}$ . Tunnelling parameters are (a)  $U_{\text{bias}} = -1.6 \text{ V}$  and  $I_t = 8 \text{ pA}$  and (b)  $U_{\text{bias}} = -1.6 \text{ V}$  and  $I_t = 4 \text{ pA}$  (both superimposed with derivative for better visibility).

## APPENDIX B

---

### List of Publications (*Liste der Teilpublikationen*)

---

The results presented in this thesis can be found in the following publications:

*Teile dieser Arbeit wurden als Bestandteil der folgenden Artikel in Fachzeitschriften bereits veröffentlicht:*

- [118] **Stefan Kraus**, Felix Huttman, Jeison Fischer, Timo Knispel, Ken Bischof, Alexander Herman, Marco Bianchi, Raluca-Maria Stan, Ann Julie Holt, Vasile Caciuc, Shigeru Tsukamoto, Heiko Wende, Philip Hofmann, Nicolae Atodiresei, and Thomas Michely  
*Single-crystal graphene on Ir(110)*  
manuscript, submitted to Physical Review B, available as preprint [118]
- n/a **Stefan Kraus**, Alexander Herman, Felix Huttman, Marco Bianchi, Raluca-Maria Stan, Ann Julie Holt, Shigeru Tsukamoto, Nico Rothenbach, Katharina Ollefs, Jan Dreiser, Ken Bischof, Heiko Wende, Philip Hofmann, Nicolae Atodiresei, and Thomas Michely  
*Uniaxially aligned 1D sandwich-molecular wires: electronic structure and magnetism*  
manuscript, submitted to the Journal of Physical Chemistry C
- n/a **Stefan Kraus**, Alexander Herman, Felix Huttman, Christian Krämer, Shigeru Tsukamoto, Nico Rothenbach, Katharina Ollefs, Lea Spieker, Tobias Lojewski, Matthias Bernien, Lucas M. Arruda, Jan Dreiser, Nick Brookes, Kurt Kummer, Wolfgang Kuch, Heiko Wende, Nicolae Atodiresei, and Thomas Michely  
*From dots to wires: doping-dependent on-surface synthesis of thulium-cyclooctatetraene compounds on graphene*  
manuscript, in preparation phase

---

### Further publications:

#### *Weitere Publikationen:*

- [84] Felix Huttmann, Nico Rothenbach, **Stefan Kraus**, Katharina Ollefs, Lucas M. Arruda, Matthias Bernien, Danny Thonig, Anna Delin, Jonas Fransson, Kurt Kummer, Nicholas B. Brookes, Olle Eriksson, Wolfgang Kuch, Thomas Michely, and Heiko Wende  
*Europium cyclooctatetraene nanowire carpets: a low-dimensional, organometallic, and ferromagnetic insulator*  
J. Phys. Chem. Lett. 2019, **10**, 911-917
- [134] Camiel van Efferen, Jan Berges, Joshua Hall, Erik van Loon, **Stefan Kraus**, Arne Schobert, Tobias Wekking, Felix Huttmann, Eline Plaar, Nico Rothenbach, Katharina Ollefs, Lucas M. Arruda, Nick Brookes, Gunnar Schönhoff, Kurt Kummer, Heiko Wende, Tim Wehling, and Thomas Michely  
*A full gap above the Fermi level: the charge density wave of monolayer VS<sub>2</sub>*  
Nature Commun. 2021, **12**, 6837
- n/a Alexander Herman, **Stefan Kraus**, Shigeru Tsukamoto, Lea Spieker, Vasile Caciuc, Tobias Lojewski, Damian Günzing, Tobias Hartl, Jan Dreiser, Bernard Delley, Katharina Ollefs, Thomas Michely, Nicolae Atodiresei, and Heiko Wende  
*Tailoring magnetic anisotropy by graphene induced skyhook effect of 4f-metals*  
manuscript, submitted to Nature Communications

## Appendix B List of publications (*Liste der Teilpublikationen*)

---

### Conference contributions as presenting author:

*Konferenzbeiträge als präsentierender Autor:*

- 2017** QMol Conference, Ascona (CH), *Nanostructures of Cyclooctatetraene with Thulium on Graphene on Ir(111)*. Poster
- 2018** EWEG/2D (European Workshop on Epitaxial Graphene and 2D Materials), Salamanca (ES), *Nanostructures of Cyclooctatetraene with Rare-Earth Metals on Graphene*. Talk
- 2018** OSS18 (International workshop *On-Surface Synthesis*), Sant Feliu de Guíxols (ES), *Nanostructures of Cyclooctatetraene with Rare-Earth Metals on Graphene*. Talk
- 2020** DPG Spring Meeting, Dresden (DE) *Electronic and magnetic structure of oriented sandwich-molecular wires on graphene/Ir(110)*. Poster, postponed due to COVID-19 pandemic.
- 2020** EWEG/2D (European Workshop on Epitaxial Graphene and 2D Materials), Sankt Moritz (CH), *Graphene/Ir(110) as growth substrate for oriented sandwich-molecular wires*. Talk, postponed due to COVID-19 pandemic.
- 2021** virtual DPG Spring Meeting, *Single-crystal graphene on Ir(110): a uniaxial template*. Poster

# Bibliography

- [1] G. Wilkinson, M. Rosenblum, M. C. Whiting and R. B. Woodward, ‘The structure of iron bis-cyclopentadienyl’, *J. Am. Chem. Soc.* **74**, 2125 (1952). Cited on page(s) 1
- [2] E. O. Fischer and W. Pfab, ‘Cyclopentadien-Metallkomplexe, ein neuer Typ metallorganischer Verbindungen’, *Z. Naturforsch. B* **7**, 377 (1952). Cited on page(s) 1
- [3] P. L. Pauson, ‘Ferrocene and related compounds’, *Q. Rev. Chem. Soc.* **9**, 391 (1955). Cited on page(s) 1
- [4] W. Kaminsky, ‘The discovery of metallocene catalysts and their present state of the art’, *J. Polym. Sci. A Polym. Chem.* **42**, 3911 (2004). Cited on page(s) 1
- [5] E. O. Fischer and W. Hafner, ‘Di-benzol-chrom: Über Aromatenkomplexe von Metallen I’, *Z. Naturforsch. B* **10**, 665 (1955). Cited on page(s) 1
- [6] A. Streitwieser and U. Müller-Westerhoff, ‘Bis(cyclooctatetraenyl)uranium (uranocene). A new class of sandwich complexes that utilize atomic f orbitals’, *J. Am. Chem. Soc.* **90**, 7364 (1968). Cited on page(s) 1
- [7] R. G. Hayes and J. L. Thomas, ‘Synthesis of cyclooctatetraenyleuropium and cyclooctatetraenylterbium’, *J. Am. Chem. Soc.* **91**, 6876 (1969). Cited on page(s) 2
- [8] A. Nakajima and K. Kaya, ‘A novel network structure of organometallic clusters in the gas phase’, *J. Phys. Chem. A* **104**, 176 (2000). Cited on page(s) 2, 111, and 120
- [9] K. Xu, J. Huang, S. Lei, H. Su, F. Y. C. Boey, Q. Li and J. Yang, ‘Efficient organometallic spin filter based on europium-cyclooctatetraene wire’, *J. Chem. Phys.* **131**, 104704 (2009). Cited on page(s) 2 and 14
- [10] S. A. Wolf, D. D. Awschalom, R. A. Buhrman, J. M. Daughton, S. von Molnár, M. L. Roukes, A. Y. Chtchelkanova and D. M. Treger, ‘Spintronics: a spin-based electronics vision for the future’, *Science* **294**, 1488 (2001). Cited on page(s) 2 and 9
- [11] S. Sanvito, ‘Molecular spintronics’, *Chem. Soc. Rev.* **40**, 3336 (2011). Cited on page(s) 2 and 9
- [12] A. Hirohata and K. Takanashi, ‘Future perspectives for spintronic devices’, *J. Phys. D Appl. Phys.* **47**, 193001 (2014). Cited on page(s) 2
- [13] M. N. Baibich, J. M. Broto, A. Fert, F. N. Van Dau, F. Petroff, P. Etienne, G. Creuzet, A. Friederich and J. Chazelas, ‘Giant magnetoresistance of (001)Fe/(001)Cr magnetic superlattices’, *Phys. Rev. Lett.* **61**, 2472 (1988). Cited on page(s) 2
- [14] G. Binasch, P. Grünberg, F. Saurenbach and W. Zinn, ‘Enhanced magnetoresistance in layered magnetic structures with antiferromagnetic interlayer exchange’, *Phys. Rev. B* **39**, 4828 (1989). Cited on page(s) 2
- [15] Z. Yang, B. L. Zhang, X. G. Liu, Y. Z. Yang, X. Y. Li, S. J. Xiong and B. S. Xu, ‘Spin-valve giant magnetoresistance in scandium-benzene sandwich cluster’, *EPL* **104**, 50006 (2013). Cited on page(s) 2
- [16] D. Li and A. Smogunov, ‘Giant magnetoresistance due to orbital-symmetry mismatch in transition metal benzene sandwich molecules’, *Phys. Rev. B* **103**, 085432 (2021). Cited on page(s) 2

## Bibliography

---

- [17] H. Da, H. M. Jin, K. H. Lim and S.-W. Yang, 'Half-metallic spintronic switch of bimetallic sandwich molecular wire via the control of external electrical field', *J. Phys. Chem. C* **114**, 21705 (2010). Cited on page(s) 2, 13, and 120
- [18] M. Wu and X. Cheng Zeng, 'Transition-metal-molecular sandwich nanowires as magnetic on/off switch', *Appl. Phys. Lett.* **99**, 053121 (2011). Cited on page(s) 2
- [19] V. V. Maslyuk, A. Bagrets, V. Meded, A. Arnold, F. Evers, M. Brandbyge, T. Bredow and I. Mertig, 'Organometallic benzene-vanadium wire: a one-dimensional half-metallic ferromagnet', *Phys. Rev. Lett.* **97**, 097201 (2006). Cited on page(s) 2 and 12
- [20] H. Xiang, J. Yang, J. G. Hou and Q. Zhu, 'One-dimensional transition metal-benzene sandwich polymers: possible ideal conductors for spin transport', *J. Am. Chem. Soc.* **128**, 2310 (2006). Cited on page(s) 2
- [21] S. Zhu, H. Fu, G. Gao, S. Wang, Y. Ni and K. Yao, 'A first principles study of novel one-dimensional organic half-metal vanadium-cyclooctatetraene wire', *J. Chem. Phys.* **139**, 024309 (2013). Cited on page(s) 2
- [22] W. B. Tan, J. Hongmei, S.-W. Yang and G. Q. Xu, 'Boratabenzene-vanadium sandwich molecular wire and its properties', *Nanoscale* **4**, 7557 (2012). Cited on page(s) 2, 12, and 121
- [23] T. Masubuchi, K. Ohi, T. Iwasa and A. Nakajima, 'Experimental and theoretical studies on the electronic properties of vanadium-benzene sandwich cluster anions,  $V_nBz_{n+1}^-$  ( $n = 1-5$ )', *J. Chem. Phys.* **137**, 224305 (2012). Cited on page(s) 2
- [24] Y. H. Lu, H. Jin, H. Zhu, S.-W. Yang, C. Zhang, J. Z. Jiang and Y. P. Feng, 'A possible reaction pathway to fabricate a half-metallic wire on a silicon surface', *Adv. Funct. Mater.* **23**, 2233 (2013). Cited on page(s) 2, 12, and 13
- [25] K. Lu, W. Gao, M. Xu, Y. Sun, J. Li, X. Yao, Y. Liu and X. Zhang, 'Spin transport properties of one-dimensional benzene ligand organobimetallic sandwich molecular wires', *ACS Omega* **5**, 5534 (2020). Cited on page(s) 2
- [26] L. Wang, Z. Cai, J. Wang, J. Lu, G. Luo, L. Lai, J. Zhou, R. Qin, Z. Gao, D. Yu, G. Li, W. N. Mei and S. Sanvito, 'Novel one-dimensional organometallic half metals: vanadium-cyclopentadienyl, vanadium-cyclopentadienyl-benzene, and vanadium-anthracene wires', *Nano Lett.* **8**, 3640 (2008). Cited on page(s) 2, 13, and 120
- [27] L. Zhou, S.-W. Yang, M.-F. Ng, M. B. Sullivan, Tan and L. Shen, 'One-dimensional iron-cyclopentadienyl sandwich molecular wire with half metallic, negative differential resistance and high-spin filter efficiency properties', *J. Am. Chem. Soc.* **130**, 4023 (2008). Cited on page(s) 2 and 13
- [28] R. Farzadi and H. Milani Moghaddam, 'Half-metallic behavior in ruthenium-cyclopentadienyl organometallic sandwich molecules', *Phys. Chem. Chem. Phys.* **21**, 22475 (2019). Cited on page(s) 2
- [29] X. Yao, S. Yuan and J. Wang, 'Theoretical studies of sandwich molecular wires with europium and boratacyclooctatetraene ligand and the structure on a H-Ge(001)-2x1 surface', *J. Phys. Chem. C* **120**, 7088 (2016). Cited on page(s) 2, 14, 110, and 121
- [30] X. Liu, Y. Tan, G. Zhang and Y. Pei, 'Electronic structure and spin transport properties of a new class of semiconductor surface-confined one-dimensional half-metallic  $[Eu-(C_nH_{n-2})]_N$  ( $n = 7-9$ ) sandwich compounds and molecular wires: first principle studies', *J. Phys. Chem. C* **122**, 16168 (2018). Cited on page(s) 2
- [31] W. Gao, X. Yao, Y. Sun, W. Sun, H. Liu, J. Liu, Y. Liu and X. Zhang, 'Theoretical study on sandwich-like transition-metal-cyclooctatetraene clusters and one-dimensional infinite molecular wires', *ACS Omega* **4**, 9739 (2019). Cited on page(s) 2



- 
- [32] F. Huttmann, N. Schleheck, N. Atodiresi and T. Michely, ‘On-surface synthesis of sandwich molecular nanowires on graphene’, *J. Am. Chem. Soc.* **139**, 9895 (2017). Cited on page(s) 2, 14, 16, 17, 110, 116, 117, 119, and 120
- [33] M. Batzill, ‘The surface science of graphene: Metal interfaces, CVD synthesis, nanoribbons, chemical modifications, and defects’, *Surf. Sci. Rep.* **67**, 83 (2012). Cited on page(s) 5
- [34] L. Gao, J. R. Guest and N. P. Guisinger, ‘Epitaxial graphene on Cu(111)’, *Nano Lett.* **10**, 3512 (2010). Cited on page(s) 5
- [35] T. A. Land, T. Michely, R. J. Behm, J. C. Hemminger and G. Comsa, ‘Direct observation of surface reactions by scanning tunneling microscopy: Ethylene→ethynidyne→carbon particles→graphite on Pt(111)’, *J. Chem. Phys.* **97**, 6774 (1992). Cited on page(s) 5
- [36] S. Marchini, S. Günther and J. Wintterlin, ‘Scanning tunneling microscopy of graphene on Ru(0001)’, *Phys. Rev. B* **76**, 075429 (2007). Cited on page(s) 5
- [37] D. Martoccia, M. Björck, C. M. Schlepütz, T. Brugger, S. A. Pauli, B. D. Patterson, T. Greber and P. R. Willmott, ‘Graphene on Ru(0001): a corrugated and chiral structure’, *New J. Phys.* **12**, 043028 (2010). Cited on page(s) 5
- [38] A. T. N'Diaye, J. Coraux, T. N. Plasa, C. Busse and T. Michely, ‘Structure of epitaxial graphene on Ir(111)’, *New J. Phys.* **10**, 043033 (2008). Cited on page(s) 5 and 16
- [39] A. T. N'Diaye, M. Engler, C. Busse, D. Wall, N. Buckanie, F.-J. M. zu Heringdorf, R. van Gastel, B. Poelsema and T. Michely, ‘Growth of graphene on Ir(111)’, *New J. Phys.* **11**, 023006 (2009). Cited on page(s) 5 and 16
- [40] N. A. Vinogradov, A. A. Zakharov, V. Kocevski, J. Ruzs, K. A. Simonov, O. Eriksson, A. Mikkelsen, E. Lundgren, A. S. Vinogradov, N. Mårtensson and A. B. Preobrajenski, ‘Formation and structure of graphene waves on Fe(110)’, *Phys. Rev. Lett.* **109**, 026101 (2012). Cited on page(s) 5, 6, 7, and 8
- [41] O. Dugerjav, G. Duvjir, L. Tapasztó and C. Hwang, ‘Growth of graphene on the Cu(110) surface’, *J. Phys. Chem. C* **124**, 12106 (2020). Cited on page(s) 6 and 8
- [42] T. Chagas, T. H. R. Cunha, M. J. S. Matos, D. D. dos Reis, K. A. S. Araujo, A. Malachias, M. S. C. Mazzoni, A. S. Ferlauto and R. Magalhaes-Paniago, ‘Room temperature observation of the correlation between atomic and electronic structure of graphene on Cu(110)’, *RSC Adv.* **6**, 98001 (2016). Cited on page(s) 6, 7, and 8
- [43] S. Achilli, E. Cavaliere, T. H. Nguyen, M. Cattelan and S. Agnoli, ‘Growth and electronic structure of 2D hexagonal nanosheets on a corrugated rectangular substrate’, *Nanotechnology* **29**, 485201 (2018). Cited on page(s) 6, 7, 8, and 135
- [44] A. J. Martínez-Galera and J. M. Gómez-Rodríguez, ‘Influence of metal support in-plane symmetry on the corrugation of hexagonal boron nitride and graphene monolayers’, *Nano Res.* **11**, 4643 (2018). Cited on page(s) 6, 7, and 8
- [45] D. Usachov, A. M. Dobrotvorskii, A. Varykhalov, O. Rader, W. Gudat, A. M. Shikin and V. K. Adamchuk, ‘Experimental and theoretical study of the morphology of commensurate and incommensurate graphene layers on Ni single-crystal surfaces’, *Phys. Rev. B* **78**, 085403 (2008). Cited on page(s) 6, 7, and 8
- [46] A. Fedorov, A. Varykhalov, A. Dobrotvorskii, A. Chikina, V. Adamchuk and D. Usachov, ‘Structure of graphene on the Ni(110) surface’, *Phys. Solid State* **53**, 1952 (2011). Cited on page(s) 7 and 8
- [47] J. Dai, D. Wang, M. Zhang, T. Niu, A. Li, M. Ye, S. Qiao, G. Ding, X. Xie, Y. Wang, P. K. Chu, Q. Yuan, Z. Di, X. Wang, F. Ding and B. I. Yakobson, ‘How graphene islands are unidirectionally aligned on the Ge(110) surface’, *Nano Lett.* **16**, 3160 (2016). Cited on page(s) 7 and 8

## Bibliography

---

- [48] Y. Li, G. Zhou, J. Li, J. Wu, B.-L. Gu and W. Duan, ‘*Ab initio* study of half-metallicity and magnetism of complex organometallic molecular wires’, *J. Phys. Chem. C* **115**, 7292 (2011). Cited on page(s) 7, 8, 13, and 120
- [49] J.-H. Lee, E. K. Lee, W.-J. Joo, Y. Jang, B.-S. Kim, J. Y. Lim, S.-H. Choi, S. J. Ahn, J. R. Ahn, M.-H. Park, C.-W. Yang, B. L. Choi, S.-W. Hwang and D. Whang, ‘Wafer-scale growth of single-crystal monolayer graphene on reusable hydrogen-terminated germanium’, *Science* **344**, 286 (2014). Cited on page(s) 7 and 8
- [50] L. Nilsson, M. Andersen, R. Balog, E. Lægsgaard, P. Hofmann, F. Besenbacher, B. Hammer, I. Stensgaard and L. Hornekær, ‘Graphene coatings: probing the limits of the one atom thick protection layer’, *ACS Nano* **6**, 10258 (2012). Cited on page(s) 8
- [51] L. Nilsson, M. Andersen, J. Bjerre, R. Balog, B. Hammer, L. Hornekær and I. Stensgaard, ‘Preservation of the Pt(100) surface reconstruction after growth of a continuous layer of graphene’, *Surf. Sci.* **606**, 464 (2012). Cited on page(s) 8
- [52] K. M. McElhinny, R. M. Jacobberger, A. J. Zaug, M. S. Arnold and P. G. Evans, ‘Graphene-induced Ge (001) surface faceting’, *Surf. Sci.* **647**, 90 (2016). Cited on page(s) 8
- [53] L. Di Gaspere, A. Scaparro, M. Fanfoni, L. Fazi, A. Sgarlata, A. Notargiacomo, V. Miseikis, C. Coletti and M. De Seta, ‘Early stage of CVD graphene synthesis on Ge(001) substrate’, *Carbon* **134**, 183 (2018). Cited on page(s) 8
- [54] L. Persichetti, L. Di Gaspere, F. Fabbri, A. Scaparro, A. Notargiacomo, A. Sgarlata, M. Fanfoni, V. Miseikis, C. Coletti and M. De Seta, ‘Abrupt changes in the graphene on Ge(001) system at the onset of surface melting’, *Carbon* **145**, 345 (2019). Cited on page(s) 8
- [55] D. Steiner, F. Mittendorfer and E. Bertel, ‘Quasiliquid layer Promotes hexagonal boron nitride (h-BN) single-domain growth: h-BN on Pt(110)’, *ACS Nano* **13**, 7083 (2019). Cited on page(s) 8 and 9
- [56] A. J. Martínez-Galera and J. M. Gómez-Rodríguez, ‘Structural and electronic properties of 3,4,9,10-perylene tetracarboxylic dianhydride on h-BN/Rh(110)’, *J. Phys. Chem. C* **123**, 1866 (2019). Cited on page(s) 8 and 9
- [57] J. Yano and V. K. Yachandra, ‘X-ray absorption spectroscopy’, *Photosynth. Res.* **102**, 241 (2009). Cited on page(s) 9
- [58] H. Wende, ‘Recent advances in X-ray absorption spectroscopy’, *Rep. Prog. Phys.* **67**, 2105 (2004). Cited on page(s) 9
- [59] T. Funk, A. Deb, S. J. George, H. Wang and S. P. Cramer, ‘X-ray magnetic circular dichroism—a high energy probe of magnetic properties’, *Coord. Chem. Rev* **249**, 3 (2005), synchrotron Radiation in Inorganic and Bioinorganic Chemistry. Cited on page(s) 9
- [60] G. van der Laan and A. I. Figueroa, ‘X-ray magnetic circular dichroism - a versatile tool to study magnetism’, *Coord. Chem. Rev* **277-278**, 95 (2014), following Chemical Structures using Synchrotron Radiation. Cited on page(s) 9
- [61] J. Stöhr and H. C. Siegmann, ‘Magnetism’ (Springer, 2006). Cited on page(s) 10
- [62] C. M. Sorensen, in ‘Nanoscale materials in chemistry’ (John Wiley and Sons, Ltd, 2001), Chap. 6, Pages 169–221. Cited on page(s) 10
- [63] L. Thomas, F. Lioni, R. Ballou, D. Gatteschi, R. Sessoli and B. Barbara, ‘Macroscopic quantum tunnelling of magnetization in a single crystal of nanomagnets’, *Nature* **383**, 145 (1996). Cited on page(s) 10

- [64] M. Mannini, F. Pineider, C. Danieli, F. Totti, L. Sorace, P. Sainctavit, M.-A. Arrio, E. Otero, L. Joly, J. C. Cezar, A. Cornia and R. Sessoli, ‘Quantum tunnelling of the magnetization in a monolayer of oriented single-molecule magnets’, *Nature* **468**, 417 (2010). Cited on page(s) 10 and 11
- [65] J. D. Rinehart, M. Fang, W. J. Evans and J. R. Long, ‘A  $N_2^{3-}$  radical-bridged terbium complex exhibiting magnetic hysteresis at 14 K’, *J. Am. Chem. Soc.* **133**, 14236 (2011). Cited on page(s) 10 and 11
- [66] R. Westerström, A.-C. Uldry, R. Stania, J. Dreiser, C. Piamonteze, M. Muntwiler, F. Matsui, S. Rusponi, H. Brune, S. Yang, A. Popov, B. Büchner, B. Delley and T. Greber, ‘Surface aligned magnetic moments and hysteresis of an endohedral single-molecule magnet on a metal’, *Phys. Rev. Lett.* **114**, 087201 (2015). Cited on page(s) 10 and 11
- [67] C. Wäckerlin, F. Donati, A. Singha, R. Baltic, S. Rusponi, K. Diller, F. Patthey, M. Pivetta, Y. Lan, S. Klyatskaya, M. Ruben, H. Brune and J. Dreiser, ‘Giant hysteresis of single-molecule magnets adsorbed on a nonmagnetic insulator’, *Adv. Mater.* **28**, 5195 (2016). Cited on page(s) 10, 11, and 110
- [68] E.-C. Yang, D. N. Hendrickson, W. Wernsdorfer, M. Nakano, L. N. Zakharov, R. D. Sommer, A. L. Rheingold, M. Ledezma-Gairaud and G. Christou, ‘Cobalt single-molecule magnet’, *J. Appl. Phys.* **91**, 7382 (2002). Cited on page(s) 11
- [69] S. Osa, T. Kido, N. Matsumoto, N. Re, A. Pochaba and J. Mrozinski, ‘A tetranuclear 3d-4f single molecule magnet:  $[Cu^{II}LTb^{III}(hfac)_2]_2$ ’, *J. Am. Chem. Soc.* **126**, 420 (2004). Cited on page(s) 11
- [70] C. J. Milios, A. Vinslava, W. Wernsdorfer, S. Moggach, S. Parsons, S. P. Perlepes, G. Christou and E. K. Brechin, ‘A record anisotropy barrier for a single-molecule magnet’, *J. Am. Chem. Soc.* **129**, 2754 (2007). Cited on page(s) 11
- [71] V. M. Mereacre, A. M. Ako, R. Clérac, W. Wernsdorfer, G. Filoti, J. Bartolomé, C. E. Anson and A. K. Powell, ‘A bell-shaped  $Mn_{11}Gd_2$  single-molecule magnet’, *J. Am. Chem. Soc.* **129**, 9248 (2007). Cited on page(s) 11
- [72] F.-S. Guo, B. M. Day, Y.-C. Chen, M.-L. Tong, A. Mansikkamäki and R. A. Layfield, ‘Magnetic hysteresis up to 80 kelvin in a dysprosium metallocene single-molecule magnet’, *Science* **362**, 1400 (2018). Cited on page(s) 11
- [73] L. Spree, F. Liu, V. Neu, M. Rosenkranz, G. Velkos, Y. Wang, S. Schiemenz, J. Dreiser, P. Gargiani, M. Valvidares, C.-H. Chen, B. Büchner, S. M. Avdoshenko and A. A. Popov, ‘Robust single molecule magnet monolayers on graphene and graphite with magnetic hysteresis up to 28 K’, *Adv. Funct. Mater.* **31**, 2105516 . Cited on page(s) 11
- [74] H. Wende, M. Bernien, J. Luo, C. Sorg, N. Ponpandian, J. Kurde, J. Miguel, M. Piantek, X. Xu, P. Eckhold, W. Kuch, K. Baberschke, P. M. Panchmatia, B. Sanyal, P. M. Oppeneer and O. Eriksson, ‘Substrate-induced magnetic ordering and switching of iron porphyrin molecules’, *Nat. Mater.* **6**, 516 (2007). Cited on page(s) 11
- [75] M. Bernien, J. Miguel, C. Weis, M. E. Ali, J. Kurde, B. Krumme, P. M. Panchmatia, B. Sanyal, M. Piantek, P. Srivastava, K. Baberschke, P. M. Oppeneer, O. Eriksson, W. Kuch and H. Wende, ‘Tailoring the nature of magnetic coupling of Fe-porphyrin molecules to ferromagnetic substrates’, *Phys. Rev. Lett.* **102**, 047202 (2009). Cited on page(s) 11
- [76] D. Écija, W. Auwärter, S. Vijayaraghavan, K. Seufert, F. Bischoff, K. Tashiro and J. V. Barth, ‘Assembly and manipulation of rotatable cerium porphyrinato sandwich complexes on a surface’, *Angew. Chem. Int. Ed.* **50**, 3872 (2011). Cited on page(s) 11 and 15

- [77] N. Ishikawa, M. Sugita, T. Ishikawa, S.-y. Koshihara and Y. Kaizu, ‘Lanthanide double-decker complexes functioning as magnets at the single-molecular level’, *J. Am. Chem. Soc.* **125**, 8694 (2003). Cited on page(s) 11
- [78] S. Fahrenndorf, N. Atodiresei, C. Besson, V. Caciuc, F. Matthes, S. Blügel, P. Kögerler, D. E. Bürgler and C. M. Schneider, ‘Accessing 4f-states in single-molecule spintronics’, *Nat. Commun.* **4**, 2425 (2013). Cited on page(s) 11
- [79] D. Klar, A. Candini, L. Joly, S. Klyatskaya, B. Krumme, P. Ohresser, J.-P. Kappler, M. Ruben and H. Wende, ‘Hysteretic behaviour in a vacuum deposited submonolayer of single ion magnets’, *Dalton Trans.* **43**, 10686 (2014). Cited on page(s) 11
- [80] Y. Lan, S. Klyatskaya, M. Ruben, O. Fuhr, W. Wernsdorfer, A. Candini, V. Corradini, A. Lodi Rizzini, U. del Pennino, F. Troiani, L. Joly, D. Klar, H. Wende and M. Affronte, ‘Magnetic interplay between two different lanthanides in a tris-phthalocyaninato complex: a viable synthetic route and detailed investigation in the bulk and on the surface’, *J. Mater. Chem. C* **3**, 9794 (2015). Cited on page(s) 11
- [81] T. R. Umbach, M. Bernien, C. F. Hermanns, A. Krüger, V. Sessi, I. Fernandez-Torrente, P. Stoll, J. I. Pascual, K. J. Franke and W. Kuch, ‘Ferromagnetic coupling of mononuclear Fe centers in a self-assembled metal-organic network on Au(111)’, *Phys. Rev. Lett.* **109**, 267207 (2012). Cited on page(s) 11, 12, and 14
- [82] P. Gambardella, S. Stepanow, A. Dmitriev, J. Honolka, F. M. F. de Groot, M. Lingenfelder, S. S. Gupta, D. D. Sarma, P. Bencok, S. Stanescu, S. Clair, S. Pons, N. Lin, A. P. Seitsonen, H. Brune, J. V. Barth and K. Kern, ‘Supramolecular control of the magnetic anisotropy in two-dimensional high-spin Fe arrays at a metal interface’, *Nat. Mat.* **8**, 189 (2009). Cited on page(s) 11, 12, and 14
- [83] K. Miyajima, M. B. Knickelbein and A. Nakajima, ‘Stern-Gerlach study of multidecker lanthanide-cyclooctatetraene sandwich clusters’, *J. Phys. Chem. A* **112**, 366 (2008). Cited on page(s) 13, 14, 109, and 120
- [84] F. Huttmann, N. Rothenbach, S. Kraus, K. Ollefs, L. M. Arruda, M. Bernien, D. Thonig, A. Delin, J. Fransson, K. Kummer, N. B. Brookes, O. Eriksson, W. Kuch, T. Michely and H. Wende, ‘Europium cyclooctatetraene nanowire carpets: a low-dimensional, organometallic, and ferromagnetic insulator’, *J. Phys. Chem. Lett.* **10**, 911 (2019). Cited on page(s) 13, 14, 123, 124, 133, and 147
- [85] J. Wang, P. H. Acioli and J. Jellinek, ‘Structure and magnetism of  $V_nBz_{n+1}$  sandwich clusters’, *J. Am. Chem. Soc.* **127**, 2812 (2005). Cited on page(s) 12
- [86] Y. Mokrousov, N. Atodiresei, G. Bihlmayer and S. Blügel, ‘Magnetic anisotropy energies of metal–benzene sandwiches’, *Int. J. Quantum Chem.* **106**, 3208 (2006). Cited on page(s) 12
- [87] L. Zhu and J. Wang, ‘*Ab initio* study of structural, electronic, and magnetic properties of transition metal-borazine molecular wires’, *J. Phys. Chem. C* **113**, 8767 (2009). Cited on page(s) 12
- [88] T. Masubuchi, T. Iwasa and A. Nakajima, ‘Multiple-decker and ring sandwich formation of manganese-benzene organometallic cluster anions:  $Mn_nBz_n^-$  ( $n=1-5$  and 18)’, *Phys. Chem. Chem. Phys.* **18**, 26049 (2016). Cited on page(s) 12
- [89] K. Miyajima, A. Nakajima, S. Yabushita, M. B. Knickelbein and K. Kaya, ‘Ferromagnetism in one-dimensional vanadium-benzene sandwich clusters’, *J. Am. Chem. Soc.* **126**, 13202 (2004). Cited on page(s) 13
- [90] L. Shen, S.-W. Yang, M.-F. Ng, V. Ligatchev, L. Zhou and Y. Feng, ‘Charge-transfer-based mechanism for half-metallicity and ferromagnetism in one-dimensional organometallic sandwich molecular wires’, *J. Am. Chem. Soc.* **130**, 13956 (2008). Cited on page(s) 13
- [91] X. Zhang, Z. Tian, S.-W. Yang and J. Wang, ‘Magnetic manipulation and half-metal prediction of one-dimensional bimetallic organic sandwich molecular wires  $[CpTM_1CpTM_2]$  ( $TM_1 = Ti, Cr, Fe$ ;  $TM_2 = Sc-Co$ )’, *J. Phys. Chem. C* **115**, 2948 (2011). Cited on page(s) 13 and 120

- [92] C. Morari, H. Allmaier, F. Beiușeanu, T. Jurcuț and L. Chioncel, ‘Electronic structure and magnetic properties of metallocene multiple-decker sandwich nanowires’, *Phys. Rev. B* **85**, 085413 (2012). Cited on page(s) 13
- [93] X. Zhang and J. Wang, ‘*Ab initio* study of bond characteristics and magnetic properties of mixed-sandwich  $V_nBz_mCp_k$  clusters’, *J. Phys. Chem. A* **114**, 2319 (2010). Cited on page(s) 13
- [94] X. Zhang, M. Cao, L. Liu and Y. Liu, ‘Tunable electronic and magnetic properties of boron/nitrogen-doped  $BzTMCp^*TMBz/CpTMCp^*TMCp$  clusters and one-dimensional infinite molecular wires’, *J. Phys. Chem. C* **118**, 11620 (2014). Cited on page(s) 13
- [95] P. B. Karadakov, ‘Aromaticity and antiaromaticity in the low-lying electronic states of cyclooctatetraene’, *J. Phys. Chem. A* **112**, 12707 (2008). Cited on page(s) 13
- [96] K. H. Claus and C. Krüger, ‘Structure of cyclooctatetraene at 129 K’, *Acta crystallogr. C* **44**, 1632 (1988). Cited on page(s) 13
- [97] N. Atodiresei, P. H. Dederichs, Y. Mokrousov, L. Bergqvist, G. Bihlmayer and S. Blügel, ‘Controlling the magnetization direction in molecules via their oxidation state’, *Phys. Rev. Lett.* **100**, 117207 (2008). Cited on page(s) 14
- [98] K. Miyajima, M. B. Knickelbein and A. Nakajima, ‘Magnetic properties of lanthanide organometallic sandwich complexes produced in a molecular beam’, *Polyhedron* **24**, 2341 (2005). Cited on page(s) 14 and 118
- [99] M. Lackinger, ‘On-surface polymerization - a versatile synthetic route to two-dimensional polymers’, *Polym. Int.* **64**, 1073 (2015). Cited on page(s) 14 and 15
- [100] M. Lackinger, ‘Surface-assisted Ullmann coupling’, *Chem. Commun.* **53**, 7872 (2017). Cited on page(s) 14
- [101] L. Dong, P. N. Liu and N. Lin, ‘Surface-activated coupling reactions confined on a surface’, *Acc. Chem. Res.* **48**, 2765 (2015). Cited on page(s) 14
- [102] U. Schlickum, R. Decker, F. Klappenberger, G. Zoppellaro, S. Klyatskaya, M. Ruben, I. Silanes, A. Arnau, K. Kern, H. Brune and J. V. Barth, ‘Metal-organic honeycomb nanomeshes with tunable cavity size’, *Nano Lett.* **7**, 3813 (2007). Cited on page(s) 14
- [103] Q. Fan, J. M. Gottfried and J. Zhu, ‘Surface-catalyzed C-C covalent coupling strategies toward the synthesis of low-dimensional carbon-based nanostructures’, *Acc. Chem. Res.* **48**, 2484 (2015). Cited on page(s) 14
- [104] F. Klappenberger, Y.-Q. Zhang, J. Björk, S. Klyatskaya, M. Ruben and J. V. Barth, ‘On-surface synthesis of carbon-based scaffolds and nanomaterials using terminal alkynes’, *Acc. Chem. Res.* **48**, 2140 (2015). Cited on page(s) 14
- [105] K. Schouteden, T. Ivanova, Z. Li, V. Iancu, E. Janssens and C. Van Haesendonck, ‘Probing magnetism in 2D molecular networks after *in situ* metalation by transition metal atoms’, *J. Phys. Chem. Lett.* **6**, 1048 (2015). Cited on page(s) 14 and 15
- [106] J. I. Urgel, D. Eciija, W. Auwärter, D. Stassen, D. Bonifazi and J. V. Barth, ‘Orthogonal insertion of lanthanide and transition-metal atoms in metal-organic networks on surfaces’, *Angew. Chem. Int. Ed.* **54**, 6163 (2015). Cited on page(s) 14
- [107] C. Wäckerlin, J. Nowakowski, S.-X. Liu, M. Jaggi, D. Siewert, J. Girovsky, A. Shchyrba, T. Hählen, A. Kleibert, P. M. Oppeneer, F. Nolting, S. Decurtins, T. A. Jung and N. Ballav, ‘Two-dimensional supramolecular electron spin arrays’, *Adv. Mater.* **25**, 2404 (2013). Cited on page(s) 15 and 110
- [108] L. Talirz, P. Ruffieux and R. Fasel, ‘On-surface synthesis of atomically precise graphene nanoribbons’, *Adv. Mater.* **28**, 6222 (2016). Cited on page(s) 15

## Bibliography

---

- [109] C. J. Villagómez, T. Sasaki, J. M. Tour and L. Grill, ‘Bottom-up assembly of molecular wagons on a surface’, *J. Am. Chem. Soc.* **132**, 16848 (2010). Cited on page(s) 15
- [110] Z. Yang, C. Lotze, K. J. Franke and J. I. Pascual, ‘Metal-organic superlattices induced by long-range repulsive interactions on a metal surface’, *J. Phys. Chem. C* **125**, 18494 (2021). Cited on page(s) 15
- [111] D. Zhong, J.-H. Franke, S. K. Podiyanachari, T. Blömker, H. Zhang, G. Kehr, G. Erker, H. Fuchs and L. Chi, ‘Linear alkane polymerization on a gold surface’, *Science* **334**, 213 (2011). Cited on page(s) 15
- [112] D. Moreno, B. Cirera, S. O. Parreiras, J. I. Urgel, N. Giménez-Agulló, K. Lauwaet, J. M. Gallego, J. R. Galán-Mascarós, J. I. Martínez, P. Ballester, R. Miranda and D. Écija, ‘Dysprosium-directed metallosupramolecular network on graphene/Ir(111)’, *Chem. Commun.* **57**, 1380 (2021). Cited on page(s) 15 and 16
- [113] J. Klinkhammer, D. F. Förster, S. Schumacher, H. P. Oepen, T. Michely and C. Busse, ‘Structure and magnetic properties of ultra thin textured EuO films on graphene’, *Appl. Phys. Lett.* **103**, 131601 (2013). Cited on page(s) 16
- [114] J. Hall, B. Pilić, C. Murray, W. Jolie, T. Wekking, C. Busse, M. Kralj and T. Michely, ‘Molecular beam epitaxy of quasi-freestanding transition metal disulphide monolayers on van der Waals substrates: a growth study’, *2D Mater.* **5**, 025005 (2018). Cited on page(s) 16
- [115] C. Murray, W. Jolie, J. A. Fischer, J. Hall, C. van Efferen, N. Ehlen, A. Grüneis, C. Busse and T. Michely, ‘Comprehensive tunneling spectroscopy of quasifreestanding MoS<sub>2</sub> on graphene on Ir(111)’, *Phys. Rev. B* **99**, 115434 (2019). Cited on page(s) 16
- [116] F. Huttmann, A. J. Martínez-Galera, V. Caciuc, N. Atodiresei, S. Schumacher, S. Standop, I. Hamada, T. O. Wehling, S. Blügel and T. Michely, ‘Tuning the van der Waals interaction of graphene with molecules via doping’, *Phys. Rev. Lett.* **115**, 236101 (2015). Cited on page(s) 16, 110, and 127
- [117] N. Hosoya, R. Takegami, J.-i. Suzumura, K. Yada, K. Koyasu, K. Miyajima, M. Mitsui, M. B. Knickelbein, S. Yabushita and A. Nakajima, ‘Lanthanide organometallic sandwich nanowires: formation mechanism’, *J. Phys. Chem. A* **109**, 9 (2005). Cited on page(s) 17
- [118] S. Kraus, F. Huttmann, J. Fischer, T. Knispel, K. Bischof, A. Herman, M. Bianchi, R.-M. Stan, A. J. Holt, V. Caciuc, S. Tsukamoto, H. Wende, P. Hofmann, N. Atodiresei and T. Michely, ‘Single-crystal graphene on Ir(110)’, **arXiv:2109.04198**, (2021). Cited on page(s) 19 and 146
- [119] T. Kurikawa, Y. Negishi, F. Hayakawa, S. Nagao, K. Miyajima, A. Nakajima and K. Kaya, ‘Multiple-decker sandwich complexes of lanthanide-1,3,5,7-cyclooctatetraene [Ln<sub>n</sub>(C<sub>8</sub>H<sub>8</sub>)<sub>m</sub>] (Ln = Ce, Nd, Eu, Ho, and Yb); localized ionic bonding structure’, *J. Am. Chem. Soc.* **120**, 11766 (1998). Cited on page(s) 109, 111, and 120
- [120] M. Saberinasab, S. Salehzadeh, Y. Maghsoud and M. Bayat, ‘The significant effect of electron donating and electron withdrawing substituents on nature and strength of an intermolecular Se- $\pi$  interaction. A theoretical study’, *Comput. Theor. Chem.* **1078**, 9 (2016). Cited on page(s) 109 and 114
- [121] D. Chylarecka, C. Wäckerlin, T. K. Kim, K. Müller, F. Nolting, A. Kleibert, N. Ballav and T. A. Jung, ‘Self-assembly and superexchange coupling of magnetic molecules on oxygen-reconstructed ferromagnetic thin film’, *J. Phys. Chem. Lett.* **1**, 1408 (2010). Cited on page(s) 110
- [122] A. A. Zavitsas, ‘The relation between bond lengths and dissociation energies of carbon-carbon bonds’, *J. Phys. Chem. A* **107**, 897 (2003). Cited on page(s) 117
- [123] S. Schumacher, D. F. Förster, F. Hu, T. Frauenheim, T. O. Wehling and T. Michely, ‘Polar EuO(111) on Ir(111): a two-dimensional oxide’, *Phys. Rev. B* **89**, 115410 (2014). Cited on page(s) 119

- [124] M. Joshi and T. K. Ghanty, ‘Prediction of a nine-membered aromatic heterocyclic 1,4,7-triazacyclononatetraenyl anion and its sandwich complexes with divalent lanthanides’, *Chemistry-Select* **4**, 9940 (2019). Cited on page(s) 121
- [125] O. C. Trulson, ‘Cohesive energies of some rare earth metals’, *Retrospective Theses and Dissertations* **2166**, (1959). Cited on page(s) 121 and 130
- [126] Y. Nakayama, S. Kera and N. Ueno, ‘Photoelectron spectroscopy on single crystals of organic semiconductors: experimental electronic band structure for optoelectronic properties’, *J. Mater. Chem. C* **8**, 9090 (2020). Cited on page(s) 123
- [127] J. B. Goedkoop, B. T. Thole, G. van der Laan, G. A. Sawatzky, F. M. F. de Groot and J. C. Fuggle, ‘Calculations of magnetic X-ray dichroism in the 3d absorption spectra of rare-earth compounds’, *Phys. Rev. B* **37**, 2086 (1988). Cited on page(s) 126
- [128] C. Nistor, A. Mugarza, S. Stepanow, P. Gambardella, K. Kummer, J. L. Diez-Ferrer, D. Coffey, C. de la Fuente, M. Ciria and J. I. Arnaud, ‘Structure and magnetism of Tm atoms and monolayers on W(110)’, *Phys. Rev. B* **90**, 064423 (2014). Cited on page(s) 126
- [129] O. C. Trulson, D. E. Hudson and F. H. Spedding, ‘Cohesive energies of europium, gadolinium, holmium, and erbium’, *J. Chem. Phys.* **35**, 1018 (1961). Cited on page(s) 131
- [130] R. Baltic, M. Pivetta, F. Donati, C. Wäckerlin, A. Singha, J. Dreiser, S. Rusponi and H. Brune, ‘Superlattice of single atom magnets on graphene’, *Nano Lett.* **16**, 7610 (2016). Cited on page(s) 137
- [131] M. Petrović, I. Šrut Rakić, S. Runte, C. Busse, J. T. Sadowski, P. Lazić, I. Pletikosić, Z.-H. Pan, M. Milun, P. Pervan, N. Atodiresei, R. Brako, D. Šokčević, T. Valla, T. Michely and M. Kralj, ‘The mechanism of caesium intercalation of graphene’, *Nat. Commun.* **4**, 2772 (2013). Cited on page(s) 139
- [132] S. Schumacher, D. F. Förster, M. Rösner, T. O. Wehling and T. Michely, ‘Strain in epitaxial graphene visualized by intercalation’, *Phys. Rev. Lett.* **110**, 086111 (2013). Cited on page(s) 139 and 140
- [133] S. Schumacher, F. Huttman, M. Petrović, C. Witt, D. F. Förster, C. Vo-Van, J. Coraux, A. J. Martínez-Galera, V. Sessi, I. Vergara, R. Rückamp, M. Grüninger, N. Schleheck, F. Meyer zu Heringdorf, P. Ohresser, M. Kralj, T. O. Wehling and T. Michely, ‘Europium underneath graphene on Ir(111): intercalation mechanism, magnetism, and band structure’, *Phys. Rev. B* **90**, 235437 (2014). Cited on page(s) 139
- [134] C. van Efferen, J. Berges, J. Hall, E. van Loon, S. Kraus, A. Schobert, T. Wekking, F. Huttman, E. Plaar, N. Rothenbach, K. Ollefs, L. M. Arruda, N. Brookes, G. Schönhoff, K. Kummer, H. Wende, T. Wehling and T. Michely, ‘A full gap above the Fermi level: the charge density wave of monolayer VS<sub>2</sub>’, *Nat. Commun.* **12**, 6837 (2021). Cited on page(s) 147





# Acknowledgements

## (*Danksagung*)

---

Schließlich folgt der vielleicht schwierigste Teil dieser Arbeit — die Danksagung an alle Menschen, mit denen ich während der Zeit meiner Promotion zusammenarbeiten durfte. Genauso geht natürlich ein Dank an alle Personen, welche mich während dieser Zeit durchweg unterstützt haben oder für mich da waren.

Zunächst einmal gilt mein ganz besonderer Dank meinem Doktorvater Prof. Thomas Michely, welcher es mir ermöglicht hat, meine Promotion in seiner Arbeitsgruppe durchzuführen. Thomas hat mich immer sehr unterstützt, und das auch zu Zeiten, in denen es mal nicht so gut lief. Sehr gerne erinnere ich mich an Zeiten, in welchen wir über wissenschaftliche Probleme gemeinsam gegrübelt haben, wie beispielsweise über die nach wie vor mysteriösen Kaffeebohnen. Auch die Strahlzeit an der *Swiss Light Source* werde ich nie vergessen, bei welcher wir gemeinsam bis in die Nacht experimentiert und Proben hergestellt haben. Vielen Dank für diese wirklich schöne Zeit!

Als nächstes bedanke ich mich bei Priv.-Doz. Daniel Bürgler, welcher sich bereit erklärt hat die Zweitkorrektur meiner Arbeit zu übernehmen. Ich bedanke mich auch für die sehr freundliche Einladung ins Forschungszentrum Jülich, bei welcher ich die Gelegenheit hatte, über die Themen meiner Arbeit zu berichten.

Auch geht mein Dank natürlich an Prof. Hans-Günther Schmalz, welcher sich ohne Umschweife dazu bereit erklärt hat, den Vorsitz der Prüfungskommission für diese Arbeit zu übernehmen.

Ebenfalls bedanke ich mich sehr bei meinem Kollegen Jeison Fischer, welcher sich dazu bereit erklärt hat, den Beisitz für meine Disputation zu übernehmen.

Mein Dank geht auch an meinen früheren Betreuer Felix Huttmann, der mich durch meine Masterarbeit geleitet hat und von wem ich unglaublich viel gelernt habe.

Auch bedanke ich mich für die gute Zusammenarbeit mit Ken Bischof, den ich während seiner Masterarbeit betreut habe.

Die Betreuung von Christian Krämer während seiner Bachelorarbeit wird mir auch in sehr guter Erinnerung bleiben. Es hat wirklich viel Spaß gemacht, gemeinsam im Labor zu arbeiten, und ich freue mich, dass wir im Rahmen unserer Zusammenarbeit Freunde geworden sind.

Ich bedanke mich auch besonders bei Camiel van Efferen, Wouter Jolie, Moritz Will und Timo Knispel für das Korrekturlesen meiner Arbeit, ihr habt mir sehr geholfen!

## Acknowledgements (*Danksagung*)

---

Als nächstes bedanke ich mich bei der ganzen Gruppe Michely für die gemeinsame Zeit mit Jeison Fischer, Wouter Jolie, Moritz Will, Philipp Valerius, Camiel van Efferen, Clifford Murray, Joshua Hall, Carsten Speckmann, Tobias Hartl, Timo Knispel, Christian Krämer, Daniela Mohrenstecher, Nicolas Georgopoulos und Felix Oberbauer. Es war schön mit euch in der Gruppe zusammenzuarbeiten. Hervorheben möchte ich die angenehme Zusammenarbeit mit meinem früheren Laborpartner Joshua Hall bei TuMAIL.

Ich bedanke mich sehr bei unserem früheren Techniker Norbert Henn, welcher jederzeit gerne mit uns technische Probleme gelöst hat. Ebenfalls bedanke ich mich sehr bei unserem aktuellen Techniker Pascal Hurth. Danke, dass du dich immer mit unseren technischen Problemen herumschlägst! Es macht sehr viel Spaß mit dir zusammenzuarbeiten und auch den ein oder anderen Kaffeeclatsch zu halten.

Ich bedanke mich für die Kollaboration mit Marco Bianci, Raluca-Maria Stan, Ann Julie Holt und Philip Hofmann. Die gemeinsame ARPES-Messzeit hat sehr viel Spaß gemacht.

Genauso bedanke ich mich bei allen Kollaborationspartnern meiner XAS/XMCD-Strahlzeiten aus den Arbeitsgruppen Heiko Wende und Wolfgang Kuch. Die Arbeit mit Alexander Herman, Nico Rothenbach, Katharina Ollefs, Lea Spieker, Tobias Lojewski, Matthias Bernien und Lucas M. Arruda hat viel Spaß gemacht. Besonders möchte ich Alexander Herman hervorheben. Wir haben viele gemeinsame Strahlzeiten bestritten, und dabei immer eine gute Zeit gehabt, das werde ich nie vergessen! Auch bedanke ich mich bei den Beamline-Wissenschaftlern oder Technikern, mit welchen ich im Rahmen dieser Arbeit auf Strahlzeiten zusammenarbeiten durfte. Das sind Jan Dreiser, Stefan Zeugin, Nick Brookes und Kurt Kummer.

I also want to thank Nicolae Atodiresei, Shigeru Tsukamoto and Vasile Caciuc for our fruitful collaboration. Thank you for our joint work on projects and the many scientific discussions!

Es fehlt hier natürlich noch mein ganz besonderer Dank an meine früheren Bürokollegen Moritz Will und Philipp Valerius. Wir sind in unserem Büro wortwörtlich durch dick und dünn gegangen, durch Hitzeperioden oder auch arktische Winter. Ebenfalls die Internetverhältnisse waren zuletzt wie in der Arktis. Vielen Dank für die unglaublich unterhaltsame und schöne Zeit in unserem Büro und die vielen Liter gemeinsam getrunkenen Kaffee.

Ebenfalls bedanke ich mich sehr bei meinem aktuellen Bürokollegen und Leidensgenossen Timo Knispel. Gemeinsam haben wir uns die letzten Monate durch die Zustände im Büro und das Verfassen unserer Manuskripte und Arbeiten gekämpft. Die vielen gemeinsam verzehrten Zuckerwerke und Aufheiterungen haben mir in der letzten Phase des Schreibens immer sehr geholfen!

Ich möchte meinem früheren Bürokollegen Moritz Will nochmal ganz besonders danken. Zuerst sind wir im Büro Freunde geworden und seit ein paar Jahren auch Mitbewohner. Ich bedanke mich sehr für den vielen Quatsch, den wir uns bei vermilchtem Kaffee und Löblichen's Gebäckstücken erzählt haben. Wenn mich etwas beschäftigt, weiß ich immer, dass ich zu dir kommen kann. Dafür bin ich dir sehr dankbar!

---

Natürlich geht ein ganz besonderer Dank an meine Freunde, welche mich immer unterstützen und auch in der Zeit meiner Promotion immer für mich da waren und mich aufgeheitert haben. Ich freue mich auf viele weitere Koch- und Erlebnisabende mit Mario Josupeit und Eva Mix. Danke, dass ihr auch immer für mich da wart, als ich „gestresst“ war. Ich freue mich auf viele weitere gemeinsame Abenteuer in fremden Welten und Minenschächten! Ich bedanke mich auch bei Shayoni Panja, welche während meiner Zeit des Schreibens immer wieder nachgehört hat, wie es mir geht. Ich freue mich auf unseren nächsten Kaffeeklatsch. Natürlich auch einen ganz großen Dank an Benedikt „Bernd“ Rings, mit welchem ich glücklicherweise seit meiner Schulzeit befreundet sein darf. Auch vielen Dank für deine Unterstützung während der Zeit meiner Promotion, und die häufigen Aufheiterungen. Ich bedanke mich auch sehr bei Jan Attig, welcher ebenfalls während der Zeit meines Schreibens oft nach meinem Wohlbefinden gefragt hat. Auch die gemeinsamen PhD-Treffen mit Severin Kopatz haben mir beim Finalisieren meiner Arbeit geholfen. Ich entschuldige mich schonmal im Voraus bei jeder nicht namentlich genannten Person in meinem Freundeskreis, den ich sehr schätze!

Ich bedanke mich auch ganz herzlich bei meiner Familie. Ich bedanke ich mich bei meinen Großeltern Josef und Leni Kraus, welche immer für mich da waren und mir stets gut zugeredet haben. I also want to thank my guest family — the “Morrin Clan” — which I now know for ten years already. You are also part of my family and I am looking forward to many future joint vacations!

Ich bedanke mich ganz besonders bei meinen Eltern Johannes und Therese Kraus. Ohne euch wäre mein Studium nie möglich gewesen. Ihr habt meinen Weg des Physikstudiums von Anfang an gefördert. Ich weiß es sehr zu schätzen, dass ihr immer für mich da seid, und hoffe, dass ihr wisst wie dankbar ich dafür bin!

Schließlich bedanke ich mich ganz herzlich bei meiner Freundin Lena Schüller, welche in den Jahren meiner Promotion immer für mich da gewesen ist und mich unterstützt hat. Ich bin unglaublich glücklich dich zu haben, und freue mich sehr auf unsere gemeinsame Zukunft!



# Erklärung zur Dissertation

gemäß der Promotionsordnung vom 12. März 2020

---

Hiermit versichere ich an Eides statt, dass ich die vorliegende Dissertation selbstständig und ohne die Benutzung anderer als der angegebenen Hilfsmittel und Literatur angefertigt habe. Alle Stellen, die wörtlich oder sinngemäß aus veröffentlichten und nicht veröffentlichten Werken dem Wortlaut oder dem Sinn nach entnommen wurden, sind als solche kenntlich gemacht. Ich versichere an Eides statt, dass diese Dissertation noch keiner anderen Fakultät oder Universität zur Prüfung vorgelegen hat; dass sie - abgesehen von unten angegebenen Teilpublikationen und eingebundenen Artikeln und Manuskripten - noch nicht veröffentlicht worden ist sowie, dass ich eine Veröffentlichung der Dissertation vor Abschluss der Promotion nicht ohne Genehmigung des Promotionsausschusses vornehmen werde. Die Bestimmungen dieser Ordnung sind mir bekannt. Darüber hinaus erkläre ich hiermit, dass ich die Ordnung zur Sicherung guter wissenschaftlicher Praxis und zum Umgang mit wissenschaftlichem Fehlverhalten der Universität zu Köln gelesen und sie bei der Durchführung der Dissertation zugrundeliegenden Arbeiten und der schriftlich verfassten Dissertation beachtet habe und verpflichte mich hiermit, die dort genannten Vorgaben bei allen wissenschaftlichen Tätigkeiten zu beachten und umzusetzen. Ich versichere, dass die eingereichte elektronische Fassung der eingereichten Druckfassung vollständig entspricht.

Teilpublikationen:

- [118] **Stefan Kraus**, Felix Huttman, Jeison Fischer, Timo Knispel, Ken Bischof, Alexander Herman, Marco Bianchi, Raluca-Maria Stan, Ann Julie Holt, Vasile Caciuc, Shigeru Tsukamoto, Heiko Wende, Philip Hofmann, Nicolae Atodiresei, and Thomas Michely  
*Single-crystal graphene on Ir(110)*  
manuscript, submitted to Physical Review B, available as preprint [118]
- n/a **Stefan Kraus**, Alexander Herman, Felix Huttman, Marco Bianchi, Raluca-Maria Stan, Ann Julie Holt, Shigeru Tsukamoto, Nico Rothenbach, Katharina Ollefs, Jan Dreiser, Ken Bischof, Heiko Wende, Philip Hofmann, Nicolae Atodiresei, and Thomas Michely  
*Uniaxially aligned 1D sandwich-molecular wires: electronic structure and magnetism*  
manuscript, submitted to the Journal of Physical Chemistry C

## Erklärung zur Dissertation

---

n/a **Stefan Kraus**, Alexander Herman, Felix Huttmann, Christian Krämer, Shigeru Tsukamoto, Nico Rothenbach, Katharina Ollefs, Lea Spieker, Tobias Lojewski, Matthias Bernien, Lucas M. Arruda, Jan Dreiser, Nick Brookes, Kurt Kummer, Wolfgang Kuch, Heiko Wende, Nicolae Atodiresei, and Thomas Michely

*From dots to wires: doping-dependent on-surface synthesis of thulium-cyclooctatetraene compounds on graphene*

manuscript, in preparation phase

Köln, den 16.12.2021

Stefan Kraus



### Datenverfügbarkeit

Die in dieser Dissertation gezeigten Primärdaten sind bei der Arbeitsgruppe von Prof. Dr. Thomas Michely am II. Physikalischen Institut der Universität zu Köln hinterlegt.

# Lebenslauf (*Curriculum Vitae*)

---

## Persönliche Daten

Name	Kraus
Vorname	Stefan
Geburtstag	18.02.1992
Geburtsort	Aachen
Staatsangehörigkeit	Deutsch

## Ausbildung

07/2017 – 12/2021	Promotionsstudium II. Physikalisches Institut, Universität zu Köln Arbeitsgruppe Prof. Dr. Thomas Michely
10/2014 – 05/2017	Master of Science in Physics Universität zu Köln Durchschnittsnote: 1,6 Masterarbeit “Nanostructures of Cyclooctatetraene with Rare Earth Metals: Growth and Magnetism” (Note: sehr gut 1,0) II. Physikalisches Institut, Universität zu Köln Arbeitsgruppe Prof. Dr. Thomas Michely
10/2011 – 09/2014	Bachelor of Science in Physics Universität zu Köln Durchschnittsnote: 1,8 Bachelorarbeit “STM Rausch-Detektion” (Note: sehr gut 1,0) II. Physikalisches Institut, Universität zu Köln Arbeitsgruppe Prof. Dr. Thomas Michely, betreut durch Priv.-Doz. Dr. Carsten Busse
07/2011	Allgemeine Hochschulreife, Gymnasium Haus Overbach, Jülich, Durchschnittsnote: gut (2,4)